UNIVERSITY OF CALIFORNIA, SAN DIEGO

Field-based Atmospheric Oxygen Measurements and the Ocean Carbon Cycle

A dissertation submitted in partial satisfaction of the
Requirements for the degree Doctor of Philosophy in

Oceanography

by

Britton Bruce Stephens

Committee in charge:
Professor Ralph F. Keeling, Chair
Professor Andrew G. Dickson
Professor Richard C. J. Somerville
Professor Mark H. Thiemens
Professor Ray F. Weiss

1999

The dissertation of Britton B. Stephens is approved, and it is acceptable in quality and form for publication on microfilm:

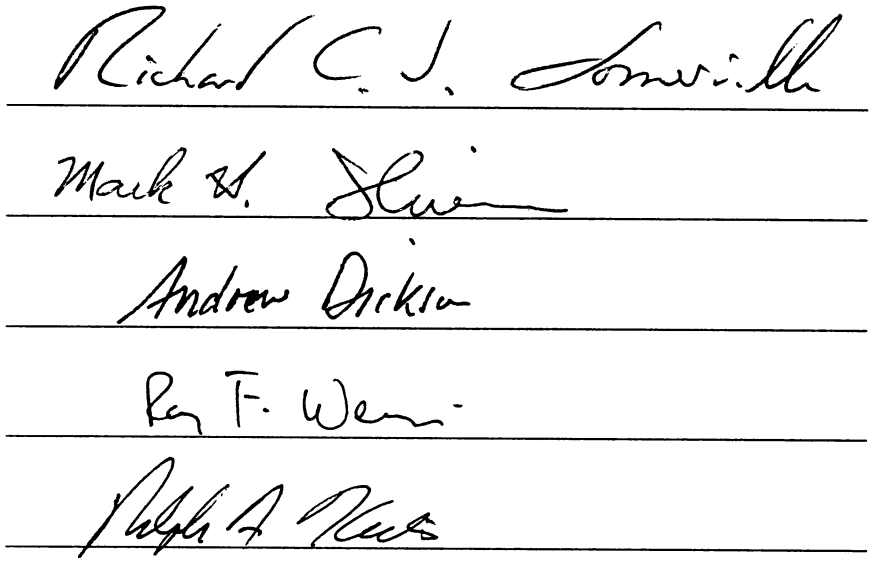

Chair

University of California, San Diego

1999

TABLE OF CONTENTS

LIST OF FIGURES AND TABLES

ACKNOWLEDGEMENTS

I am very grateful for the mentoring and support provided by my advisor, Ralph Keeling. Ralph is absolutely overflowing with ideas about the global carbon cycle and climate system, and I have been very fortunate to spend four years in the catch basin. At times I feel I may have taken advantage of Ralph's generosity, by stopping by his office for a quick question and then staying for a several-hour discussion. However, I have learned more through these informal conversations than I could ever have hoped in a classroom setting. In addition to being the original source of many of the insights presented in this dissertation, Ralph also provided the original conception of the VUV instrument and invaluable technical advice during its incarnation.

The development of the VUV instrument would also not have been possible without the initial efforts and continued assistance from Bill Paplawsky. Bill's expert technical support, unselfishly offered to a multitude of graduate students, is a great asset to Scripps. Elizabeth McEvoy performed the flask analyses presented in this dissertation, and provided vital assistance around the lab. I would like to thank Steve Piper and Martin Heimann for their guidance in using the TM2 atmospheric transport model, and Jorge Sarmiento, Richard Murnane, Ernst Maier-Reimer, Katharina Six, and Ken Caldeira for providing me with output from the biogeochemical ocean models used in Chapter 2. Discussions with Robert Toggweiler were very helpful in formulating the ideas on ocean circulation presented in Chapters 2 and 6. I would like

to thank Darin Toohey for the extended loan of a key piece of equipment, and for early instrumentation advice.

I would like to acknowledge NOAA, Richard Feely, Michael McPhaden, and crew of the Ka'imimoana for their assistance in making the measurements presented in Chapter 4; NSF and crew of the Lawrence M. Gould for their assistance in making the measurements presented in Chapter 5; and Team Snapper and crew of the Robert G. Sproul for their assistance during a shakedown cruise. I was supported by a NSF Graduate Research Fellowship and an Achievement Rewards for College Scientists Fellowship while conducting the research presented in this dissertation.

Chapter 2 appeared in full as Stephens, B. B., R. F. Keeling, M. Heimann, K. D. Six, R. Murnane, and K. Caldeira, Testing global ocean carbon cycle models using measurements of atmospheric O_2 and CO_2 concentration, *Global Biogeochemical Cycles*, *12*, 213-230, 1998. I was the primary investigator and lead author for this paper, and conducted all of the analyses presented therein. Chapter 7 includes an update to the discussion and conclusions of Chapter 2 based on more recent observations. Portions of Chapter 6 have been submitted as Stephens, B. B., and R. F. Keeling, The influence of Antarctic sea ice on glacial-interglacial CO_2 variations, submitted to *Nature*, 1999. I was the primary investigator and lead author for this paper, and conducted all of the analyses presented therein.

My fellow students at Scripps have contributed immensely to my graduate experience. In particular, I would like to thank Andrew Manning for many educational late-night discussions on the subtleties of measuring atmospheric oxygen,

and for the implicit moral support that comes from knowing someone else is awake at that hour. The other two members of the old men's discussion group, Martin Vollmer and Rob Rhew, were valuable sources of geochemical wisdom and academic levity. Among many others, Kara Lavender, Kim Cobb, Bruce Anderson, Chris Blackburn, and Alex De Robertis have provided a great deal of scientific inspiration over the past four years, and much needed encouragement during the writing of this dissertation.

Finally I would like to thank my family, who has been incredibly supportive on the road leading up to, and throughout my time at Scripps. From a very early age, and primarily by example, my parents Anne and Brad Stephens have taught me the value of hard work, hard play, and a lifelong education, all the while encouraging me to pursue my interests and dreams in whatever direction they may lead. Thank you.

Vita

1993	A.B. Magna Cum Laude, Harvard University
1993 - 1995	ECO Associate, United States Geological Survey, Woods Hole, Massachusetts
1995 - 1998	NSF Graduate Research Fellow University of California, San Diego
1998 - 1999	Achievement Rewards for College Scientists Scholar University of California, San Diego
1999	Ph.D., Scripps Institution of Oceanography, University of California, San Diego

PUBLICATIONS

Winston, G. C., B. B. Stephens, and E. T. Sundquist, Seasonal variability in CO_2 transport through snow in a boreal forest, *Biogeochemistry of Seasonally Snow-Covered Catchments*, IAHS publ. no. 228, 61-70, 1995.

Winston, G. C., E. T. Sundquist, B. B. Stephens, and S. E. Trumbore, Winter CO_2 fluxes in a boreal forest, *Journal of Geophysical Research*, 102, 28795-28804, 1997.

Keeling, R. F., B. B. Stephens, R. G. Najjar, S. C. Doney, D. Archer, and M. Heimann, Seasonal variations in the atmospheric O_2/N_2 ratio in relation to the kinetics of air-sea gas exchange, *Global Biogeochemical Cycles*, 12, 141-163, 1998.

Stephens, B. B., R. F. Keeling, M. Heimann, K. D. Six, and R. Murnane, Testing global biological ocean models using measurements of atmospheric O_2 and CO_2 concentration, *Global Biogeochemical Cycles*, 12, 213-230, 1998.

Stephens, B. B., S. C. Wofsy, R. F. Keeling, P. P. Tans, and M. J. Potosnak, The CO_2 Budget and Rectification Airborne Study: Strategies for measuring rectifiers and regional fluxes, accepted to the AGU Monograph, *Inverse Methods in Global Biogeochemical Cycles*, 1999.

ABSTRACT OF THE DISSERTATION

Field-based Atmospheric Oxygen Measurements and the Ocean Carbon Cycle

by

Britton B. Stephens

Doctor of Philosophy in Oceanography

University of California, San Diego, 1999

Professor Ralph F. Keeling, Chair

Atmospheric oxygen variations are a sensitive measure of biological and thermal processes in the oceans. Chapter 2 presents a modeling study in which I chemically coupled three ocean carbon cycle models to an atmospheric transport model and compared the results to flask station O_2 and CO_2 measurements. The large discrepancies between the coupled-model predictions and the observations may result from physical problems in the underlying coarse-resolution ocean models, specifically the overestimation of low-latitude deep-water upwelling rates.

To improve upon the resolution of the existing O_2 data set, I developed an instrument for making field-based measurements of atmospheric O_2 variations using a vacuum ultraviolet (VUV) absorption technique. Chapter 3 presents a technical

description of the instrument and its performance. The VUV analyzer has a precision of 6 per meg (5 per meg ≈ 1 ppm) over 10 seconds and 1 per meg for a 5 minute average, comparable to existing laboratory techniques. I have implemented this analyzer aboard two research vessels to make the first field-based O_2 measurements.

Chapter 4 presents atmospheric O_2 and CO_2, and surface ΔO_2 data collected from the NOAA ship Ka'imimoana in the equatorial Pacific during April/May 1998. These measurements reveal significant short-term variations in atmospheric O_2, resulting from variations in atmospheric mixing relative to the strong interhemispheric gradient. Chapter 5 presents atmospheric O_2 and CO_2 measurements made from the NSF ship Lawrence M. Gould in the Southern Ocean during October 1998. Correlations between the O_2 and CO_2 observations from this cruise allow the separate identification of oceanic and industrial influences on these gases, and provide evidence that the Southern Ocean is a source for CO_2 at this time of year.

Together, the measurements from these two cruises lend support to the hypotheses from Chapter 2, that ocean carbon cycle models overestimate the equatorial outgassing and high-southern-latitude ingassing of O_2 and CO_2. In Chapter 6, I make use of these indications to investigate oceanic controls on glacial-interglacial atmospheric CO_2 concentrations in the case where deep-water upwelling is confined to the oceans around Antarctica.

Chapter 1

Introduction

The international community is beginning to confront increasing evidence that past and present human activities may have dramatic effects on the future climate of our planet. Chief among the concerns is the possibility that carbon dioxide (CO_2) and other industrial gases will trap excess heat in the atmosphere and warm the surface of the Earth. Of critical importance to predicting climatic and ecosystem responses to present human activities are improvements to our currently limited understanding of modern and past global biogeochemical processes. This dissertation is directed at making such improvements through a combination of experimental, numerical, and theoretical studies. These include 1) the development of a new instrument capable of measuring variations in atmospheric oxygen (O_2) from ships and remote field sites, 2) the implementation of this instrument on two research cruises, 3) the application of these shipboard and existing laboratory O_2 measurements to investigate ocean biogeochemistry and to constrain numerical ocean models, and 4) the use of inferences derived from these model-observation comparisons to develop new theories for past changes in ocean carbon cycling.

Presently, we are dumping over 6 billion tons of carbon into the atmosphere as CO_2 each year [Andres *et al.,* 1999]. It is apparent from atmospheric measurements that only approximately half of this emitted CO_2 is remaining in the atmosphere, the other half presumably being absorbed by the oceans or taken up by land plants [e.g. Schimel *et al.,* 1995]. Numerical computer simulations indicate that approximately one half of the absorbed CO_2 is being stored in the oceans. However, the process responsible for the remaining apparent CO_2 uptake on land has yet to be found. After

accounting for land use changes, including the vast burning of tropical forests, this CO_2 budgeting imbalance becomes worse. Resolving the present partitioning between terrestrial and oceanic CO_2 sinks is necessary before we can identify the processes most important for future CO_2 uptake.

A second carbon-cycle uncertainty, which similarly limits our ability to predict future atmospheric CO_2 trends, is that associated with the unexplained changes in atmospheric CO_2 over glacial cycles. Ice core measurements show that CO_2 concentrations were consistently 30% lower during each of the last 4 glacial periods than they were during interglacial periods and before the Industrial Revolution [Petit *et al.,* 1999]. Though these large concentration shifts have been recognized for over 15 years, a mechanism for their occurrence that is consistent with all observations has not yet been identified. Our inability to explain the close linkage between global temperature and atmospheric CO_2 in the past casts doubt on our ability to predict future CO_2 trends in the presence of the expected global warming.

The question of how much anthropogenic CO_2 will stay in the atmosphere is not academic. For example, if we knew that a relatively large fraction of future CO_2 emissions were going to be absorbed by the oceans and land plants, we could either look forward to a smaller climate perturbation or burn more fossil fuels, depending on our priorities. Conversely, if we were able to anticipate a relatively small CO_2 uptake, it might provide more motivation to make the presently-contemplated changes in energy consumption. In addition to the absolute amount of future CO_2 uptake from the atmosphere, its ocean-land partitioning will also be important. If CO_2 is taken up

by a growing tree, it is re-released to the atmosphere when that tree dies and decomposes, on average about 30 years later. In contrast, because of the slow mixing time of the oceans, the CO_2 that is currently being absorbed may not return to the atmosphere for 1,000 years. Thus, on time scales of 50 to 100 years, oceanic uptake may play a more significant role in mitigating human CO_2 emissions.

Unfortunately, heterogeneities in oceanic and terrestrial CO_2 fluxes make it difficult to estimate their regional or global values from direct measurements on small-scales. Instead, global carbon budgets are typically estimated using spatial gradients in atmospheric CO_2 and its isotopes [e.g Ciais, *et al.,* 1995]. Recently, the development of methods to measure atmospheric O_2 variations on flask samples collected at remote sites [Keeling, 1988; Bender *et al.,* 1994] has provided more rigid constraints. The value of measuring atmospheric O_2 stems from the fact that the relationship between O_2 and CO_2 exchange is very different for oceanic, terrestrial, and industrial processes. For example, assuming that the oceans have relatively little influence on long-term interannual atmospheric O_2 trends, and correcting for the relatively well-known fossil-fuel influence, trends in atmospheric O_2 can provide a direct measure of changes in terrestrial biomass [Keeling *et al.*, 1993; 1996].

Furthermore, because the O_2:CO_2 ratio for terrestrial photosynthesis and respiration is relatively well-known, measurements of CO_2 can be used to account for terrestrial influences on both seasonal and spatial O_2 variations. For seasonal O_2 variations, the resulting oceanic signals can be used as a measure of hemispheric marine productivity [Keeling and Shertz, 1992], and as a constraint on global air-sea

gas exchange rates [Keeling *et al.,* 1998]. For spatial O_2 variations, correcting for terrestrial influences using concurrent measurements of CO_2 produces signals closely related to global-scale oceanic processes. The work presented in this dissertation focuses primarily on measuring and interpreting these spatial variations.

Air-sea fluxes of O_2 are sensitive to biological and solubility-driven changes in O_2 saturation. Because the ocean's deepest waters are formed at high latitudes, where it is cold and where the biological utilization of surface nutrients is incomplete, these waters can drive significant thermal and biological O_2 fluxes when they return to the surface. As a result, spatial gradients in atmospheric O_2 can provide valuable information on the global overturning circulation, such as the primary locations where deep-water upwelling occurs. Because the vertical rain and decomposition of biological material results in vast amounts of carbon being stored in the deep oceans, the upwelling of deep waters can also have a dominant impact on air-sea CO_2 exchange and atmospheric CO_2 concentrations. Current questions about the specifics of ocean overturning have large implications for ocean carbon cycling, and are dealt with throughout this dissertation.

Global biogeochemical ocean models are potentially powerful tools for unraveling the carbon cycle. However, it is important to validate them using available data before we can extend their predictions with confidence. Previous studies that have used such models to predict terms in the global carbon budget find relatively little southward transport of CO_2 in the oceans [e.g. Sarmiento *et al.,* 1995]. By subtraction, this requires a relatively large terrestrial CO_2 sink in the Northern

Hemisphere to account for the observed spatial gradients in atmospheric CO_2. In Chapter 2, I chemically couple three ocean carbon cycle models to an atmospheric transport model and compare the predicted atmospheric O_2 and CO_2 gradients to existing measurements from the Scripps atmospheric O_2 laboratory. These comparisons suggest that the models overestimate the outgassing of O_2 and CO_2 at low latitudes, possibly as a result of overpredicting the upwelling of deep waters in these regions. These results imply greater southward transport of CO_2 in the oceans than predicted by models, and consequently greater oceanic CO_2 uptake at high northern latitudes. Chapter 2 also includes a discussion of ocean biogeochemical controls on CO_2 and O_2 that provides a basis for the discussions in Chapters 4-7.

Existing atmospheric O_2 measurements are limited to biweekly flask samples from a relatively sparse network of background stations. To improve the spatial and temporal resolution of our O_2 measuring capability, I have designed and built a continuous O_2 analyzer that is capable of making field-based measurements with a precision as good or better than other laboratory techniques. The difficulty in measuring O_2 precisely results from the fact that there is so much of it in the atmosphere. Mole fraction changes that are relatively large for trace gases such as CO_2 are very small relative to the absolute O_2 concentration. The instrument I have built overcomes this challenge by measuring changes in the absorption of vacuum ultraviolet (VUV) light by O_2 in a sample gas, using optical, electronic, and gas-handling components that are stable at the required level of one part per million. I describe this VUV O_2 instrument in detail in Chapter 3.

In Chapters 4 and 5, I describe the implementation of this instrument during research cruises in the equatorial Pacific and Southern Ocean, respectively. These are the two regions where it has been suggested that deep waters upwell, and also where there have been few atmospheric O_2 measurements. Correlations between the shipboard O_2 and CO_2 measurements allow the identification of oceanic signals in these gases, while relationships to the origin of the sampled air reveal a strong influence from atmospheric transport on both short-term O_2 variability and annual-mean O_2 concentrations. Seasonal and interannual variability somewhat limit comparisons between these initial measurements and the climatological-mean model predictions. However, as with the background records, the shipboard data are suggestive that the coarse-resolution ocean models overestimate deep-water upwelling at low latitudes, and underestimate deep-water upwelling in the Southern Ocean.

In Chapter 6, I take this suggestion and apply it to the glacial-interglacial CO_2 problem. By assuming that deep waters upwell predominately in the Southern Ocean and not at low latitudes, I show that increases in Antarctic sea ice during glacial times could block the outgassing of CO_2 in this region and thus produce the observed low atmospheric CO_2 concentrations. This mechanism does not produce unrealistic deep O_2 concentrations or Antarctic surface $^{13}C/^{12}C$ ratios, as previous theories do. Measurements of silica production and ^{14}C concentrations in the surface oceans provide further evidence for the lack of deep-water upwelling at low latitudes, and the limited data available suggests that Antarctic sea ice was greatly expanded during glacial times. Though it is difficult to validate this theory directly, further

measurements such as those presented in Chapters 4 and 5, that constrain the large-scale overturning of the ocean, have the potential to test the premises on which it is based. Future VUV measurements of spatial and temporal variations in atmospheric O_2 would also help to refine our understanding of the present day global carbon cycle, and improve predictions of future atmospheric CO_2 trends and climate change.

1.1 References

Andres, R. J., G. Marland, T. Boden, and S. Bischoff, Carbon dioxide emissions from fossil fuel combustion and cement manufacture 1751-1991 and an estimate of their isotopic composition and latitudinal distribution, in *1993 Global Change Institute*, edited by T. Wigley and D. Schimel, in press, Cambridge Univ. Press, New York, 1999.

Bender, M. L., P. P. Tans, J. T. Ellis, J. Orchardo and K. Habfast, A high precision ratio mass spectrometry method for measuring the O_2/N_2 ratio of air, *Geochimica et Cosmochimica Acta*, *58*, 4751-4758, 1994.

Ciais, P., P. P. Tans, J. W. C. White, M. Trolier, R. J. Francey, J. A. Berry, D. R. Random, P. J. Sellers, G. J. Collatz, and D. S. Schimel, Partitioning of ocean and land uptake of CO_2 as inferred by $\delta^{13}C$ measurements from the NOAA Climate Monitoring and Diagnostics Laboratory global air sampling network. *J. Geophys. Res.*, 100, 5051-5070, 1995.

Keeling, R. F., Development of an interferometric oxygen analyzer for precise measurement of the atmospheric O_2 mole fraction, Ph.D. thesis, 178 pp., Harvard Univ., Cambridge, Mass., 1988.

Keeling, R. F., and S. R. Shertz, Seasonal and interannual variations in atmospheric oxygen and implications for the global carbon cycle, *Nature*, *358*, 723-727, 1992.

Keeling, R. F., R. G. Najjar, M. L. Bender, and P. P. Tans, What atmospheric oxygen measurements can tell us about the global carbon cycle, *Global Biogeochem. Cycles*, *7*, 37-67, 1993.

Keeling, R. F., S. C. Piper, and M. Heimann, Global and hemispheric CO_2 sinks deduced from changes in atmospheric O_2 concentration, *Nature*, *381*, 218-221, 1996.

Keeling, R. F., B. B. Stephens, R. G. Najjar, S. C. Doney, D. Archer, and M. Heimann, Seasonal variations in the atmospheric O_2/N_2 ratio in relation to the kinetics of air-sea gas exchange, *Global Biogeochem. Cycles*, 12, 141-163, 1998.

Petit, J. R., J. Jouzel, D. Raynaud, N. I. Barkov, J.-M. Barnola, I. Basile, M. Bender, J. Chappellaz, M. Davis, G. Delaygue, M. Delmotte, V. M. Kotlyakov, M. Legrand, V. Y. Lipenkov, C. Lorious, L. Pépin, C. Ritz, E. Saltzman, and M. Stievenard, Climate and atmospheric history of the past 420,000 years from the Vostok ice core, Antarctica, *Nature*, *399*, 429-436, 1999.

Sarmiento, J. L., R. Murnane and C. Le Quéré, Air-sea CO_2 transfer and the carbon budget of the North Atlantic, *Philos. Trans. R. Soc. London Ser. B*, *348*, 211-219, 1995

Schimel, D., I. G. Enting, M. Heimann, T. M. L. Wigley, D. Raynaud, D. Alves, and U. Siegenthaler, CO_2 and the carbon cycle. In *Climate Change 1994, Radiative Forcing of Climate Change and an Evaluation of the IPCC IS92 Emission Scenarios* (Houghton, J.T., L.G. Meira Filho, J. Bruce, et al., eds.), Cambridge University Press, Cambridge, pp. 35-71, 1995.

Chapter 2

Testing Global Ocean Carbon Cycle Models Using Measurements of Atmospheric O_2 and CO_2 Concentration

Abstract

We present a method for testing the performance of global ocean carbon cycle models using measurements of atmospheric O_2 and CO_2 concentration. We combine these measurements to define a tracer, atmospheric potential oxygen (APO $\approx O_2 + CO_2$), which is conservative with respect to terrestrial photosynthesis and respiration. We then compare observations of APO to the simulations of an atmospheric transport model which uses ocean-model air-sea fluxes and fossil fuel combustion estimates as lower boundary conditions. We present observations of the annual-average concentrations of CO_2, O_2, and APO at 10 stations in a north-south transect. The observations of APO show a significant interhemispheric gradient decreasing towards the north. We use air-sea CO_2, O_2, and N_2 fluxes from the Princeton ocean biogeochemistry model, the Hamburg model of the ocean carbon cycle, and the Lawrence Livermore ocean biogeochemistry model to drive the TM2 atmospheric transport model. The latitudinal variations in annual-average APO predicted by the combined models are distinctly different from the observations. All three models significantly underestimate the interhemispheric difference in APO, suggesting that they underestimate the net southward transport of the sum of O_2 and CO_2 in the oceans. Uncertainties in the model-observation comparisons include uncertainties associated with the atmospheric measurements, the atmospheric transport model, and the physical and biological components of the ocean models. Potential deficiencies in the physical components of the ocean models, which have previously been suggested

as causes for anomalously large heat fluxes out of the Southern Ocean, may contribute to the discrepancies with the APO observations. These deficiencies include the inadequate parameterization of subgrid-scale isopycnal eddy mixing, a lack of subgrid-scale vertical convection, too much Antarctic sea-ice formation, and an overestimation of vertical diffusivities in the main thermocline.

2.1 Introduction

Global ocean carbon cycle models, consisting of ocean general circulation models with biological parameterizations or submodels, are becoming valuable tools for investigating and quantifying organic matter cycling, new production, and the uptake of anthropogenic CO_2 on regional and global scales [Sarmiento *et al.*, 1995; Six and Maier-Reimer, 1996]. Initial comparisons between such models and observations, which indicated an unrealistic buildup of nutrients in the equatorial region, contributed to an increased awareness of the importance of dissolved organic carbon (DOC) in nutrient transport [Sarmiento *et al.*, 1988; Bacastow and Maier-Reimer, 1991; Najjar *et al.*, 1992]. These models have also produced significantly increased estimates of global new production, of the order of 10 Gt C yr^{-1} [Sarmiento *et al.*, 1993; Six and Maier-Reimer, 1996]. Ocean carbon cycle models have recently been applied toward estimating how much anthropogenic CO_2 has been taken up by the oceans [Sarmiento *et al.*, 1995; Heimann and Maier-Reimer, 1996] and predicting how climate change might affect future uptake [Sarmiento and Le Quéré, 1996; Maier-Reimer *et al.*, 1996].

The regional predictions of global carbon cycle models have a bearing on a controversy involving the relative importance of the northern terrestrial biota and the northern hemisphere oceans, particularly the North Atlantic, in absorbing anthropogenic CO_2 [Keeling *et al.*, 1989b; Tans *et al.*, 1990]. The atmospheric CO_2 and $^{13}CO_2/^{12}CO_2$ measurements of Keeling *et al.* [1989b], when compared to results

from an atmospheric transport model, indicated a 1 Gt C yr^{-1} sink in the North Atlantic Ocean. However, Tans *et al.* [1990], also using an atmospheric transport model, found that surface pCO_2 measurements were inconsistent with such a sink and concluded that a large sink in northern terrestrial biota was required to explain the interhemispheric CO_2 gradient. More recently, the ocean carbon cycle model of Sarmiento *et al.* [1995] predicted that the Atlantic Ocean north of 18°S is currently taking up 0.4 Gt C yr^{-1}, which by subtraction implies a relatively large northern terrestrial CO_2 sink. The surface pCO_2 values in this model were in good agreement with the measurements of Takahashi *et al.* [1995]. However, as Sarmiento *et al.* [1995] discussed, the balance between the implied atmospheric CO_2 sink, riverine inputs, and the observed southward transport of dissolved inorganic carbon (DIC) in the Atlantic [Brewer *et al.*, 1989; Broecker and Peng, 1992] is not well understood.

We have examined output from three models, the Princeton ocean biogeochemistry model (POBM) [Sarmiento *et al.*, 1995; Najjar, 1990], the Hamburg model of the ocean carbon cycle (HAMOCC3.1) [Six and Maier-Reimer, 1996; Maier-Reimer, 1993], and the Lawrence Livermore ocean biogeochemistry model (LLOBM) (K. Caldeira et al., manuscript in preparation, 1998), in this study. Because these models are under active development and because of their wide reaching and often unique predictions, there is a strong need to test these models against observed data sets. These models have been extensively compared to observed ocean nutrient and tracer distributions [Bacastow and Maier-Reimer, 1991; Najjar *et al.*, 1992; Gruber *et al.*, 1996; K. Caldeira et al., manuscript in preparation, 1998]. Although the biological

parameterizations are highly simplified and the physical models are relatively coarse, the model predictions are in qualitative agreement with oceanic nutrient and tracer data such as ^{14}C [Toggweiler *et al.*, 1989a, b], PO_4 [Anderson and Sarmiento, 1995; Six and Maier-Reimer, 1996], and apparent oxygen utilization [Anderson and Sarmiento, 1995]. Resolving the quantitative discrepancies with these data, however, will not necessarily improve the representation of air-sea fluxes. If there are any errors in the hydrographic transports, optimizing the models to match oceanic observations would actually produce errors in air-sea exchange. Thus a sensitive validation of these models also requires a means of testing the predicted air-sea fluxes themselves.

Our approach to testing these air-sea fluxes is to compare the variations they produce in an atmospheric transport model to observations of a composite tracer approximately equal to the sum of atmospheric O_2 and CO_2. In an ideal world in which atmospheric carbon existed only as CO_2 and modern and fossil terrestrial carbon existed only as CH_2O, the sum of atmospheric CO_2 and O_2 would be conservative with respect to terrestrial photosynthesis, respiration, and fossil fuel combustion and only sensitive to air-sea exchange [Keeling and Shertz, 1992; Keeling *et al.*, 1998b]. Thus observations of the sum of CO_2 and O_2 can be used to test atmosphere-ocean model predictions irrespective of terrestrial CO_2 and O_2 exchange. We refer to this sum, which is effectively the amount of O_2 that would be left in an air parcel after all of its CO_2 was reduced through photosynthesis, as atmospheric potential oxygen (APO). We present a more explicit definition of APO below, in which we account for complexities due to variations in the reduction of nitrogen and

other species during photosynthesis and to the oxidation of CO and CH_4 in the atmosphere.

Six and Maier-Reimer [1996] recently presented a favorable comparison between the results of an atmospheric transport model driven by HAMOCC3.1 O_2 fluxes and seasonal observations of atmospheric O_2 at Cape Grim, Tasmania. Here we emphasize primarily the test of the nonseasonal component of the modeled atmospheric concentrations. We find large discrepancies between the observed latitudinal APO gradients and those predicted by all three ocean models. This result may be consistent with postulated problems in the models' hydrographic tracer transports. These comparisons represent a method for independently testing the models' representations of physical and biological processes and a means to target aspects of the models which may require future improvement. Because the biogeochemical controls on APO are somewhat more complicated than for CO_2 or O_2 alone, we will briefly discuss the relevant oceanic processes before presenting the model-observation comparison.

2.2 Ocean Biogeochemical Controls on CO_2 and O_2

The regional fluxes of CO_2 and O_2 across the air-sea interface are driven by three distinct processes: (1) temperature- and salinity-related solubility effects known as the solubility pump, (2) biological production and respiration known as the biological pump, and (3) atmospheric buildup of anthropogenic CO_2. Where waters

near the surface are warmed, such as at low latitudes in association with equatorial upwelling, the decreasing solubilities lead to net effluxes of CO_2 and O_2 into the atmosphere. Conversely, where waters near the surface are cooled, for example, at high latitudes or in association with poleward current systems such as the Gulf Stream, increasing solubilities lead to net CO_2 and O_2 influx. Because salinity influences are relatively small, air-sea fluxes due to the solubility pump are primarily the result of temperature changes closely associated with air-sea heat fluxes. These thermally driven CO_2 and O_2 fluxes are superimposed on biologically driven fluxes that are closely associated with changes in preformed nutrients [Keeling *et al.*, 1993]. Along the equator and at high latitudes, the supply of DIC, O_2 deficit, and nutrients to the surface exceeds the rate of local productivity, leading to net CO_2 efflux, net O_2 influx, and the creation of preformed nutrients. Conversely, as these waters spread laterally into the subtropical gyres and their preformed nutrients are consumed, they take up CO_2 and give off O_2.

The effects of the solubility and biological pumps on air-sea CO_2 fluxes have been discussed extensively [Volk and Hoffert, 1985; Sarmiento *et al.*, 1995]. The interaction of these processes is somewhat different for O_2. In high-latitude regions, where DIC rich, O_2-depleted waters are brought to the surface and cooled, the biological and solubility pumps have opposing effects on air-sea CO_2 fluxes but have reinforcing effects on O_2 fluxes. In the equatorial upwelling zones, the effects of the solubility and biological pumps on air-sea exchange tend to reinforce for CO_2 and counteract for O_2 because of the warming of the upwelled water. However, as this

water spreads laterally and nutrients are depleted through photosynthesis, the two pumps tend to reinforce for O_2 and counteract for CO_2 over the broader equatorial region. The reinforcing tendency of the solubility and biological pumps on the large-scale air-sea O_2 exchanges, which occurs over most of the ocean surface, makes atmospheric O_2 particularly sensitive to large-scale patterns of ocean circulation. The effects of the solubility and biological pumps on air-sea APO fluxes will be a complex combination of their effects on O_2 and CO_2 individually. Because the solubility pump affects air-sea CO_2 and O_2 fluxes in the same direction, it will have a strong effect on APO in the sense of outgassing at low latitudes where the oceans are warmed and ingassing in high-latitude regions where the ocean is cooled. Because the biological pump affects CO_2 and O_2 in opposite directions, it will have a weaker effect on APO. We do not expect the biological CO_2 and O_2 fluxes to perfectly cancel, however, because of the reduction of nitrogen during marine photosynthesis, alkalinity changes which affect CO_2 but not O_2, and differences between the rates of CO_2 and O_2 gas exchange. The greater influence of the solubility pump on APO fluxes implies that variations in APO will be particularly sensitive to oceanic heat fluxes.

2.3 Observations and Fossil Fuel Predictions

We have measured CO_2 and O_2 concentrations in air which was collected in flasks approximately biweekly at a global network of 10 stations as shown in Table 2.1 and Figure 2.1. We measure CO_2 using a nondispersive infrared analyzer and O_2 by an

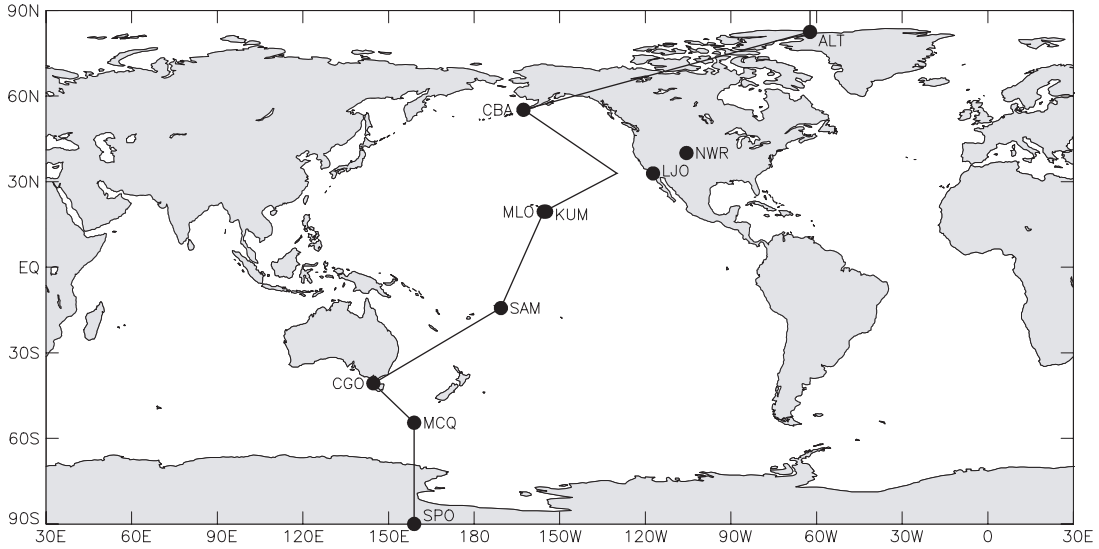

Figure 2.1. Showing the locations of the stations in the Scripps O_2/N_2 sampling network as listed in Table 2.1. The solid line indicates the surface transect used to present the model predictions in Figure 2.2 and Figures 2.4-2.7.

interferometric technique [Keeling, 1988, Keeling *et al.*, 1998a]. We report O_2 concentrations as changes in O_2/N_2 ratio in units of per meg (see definition in Section 3.2.1). We fit the observed records at each station with the sum of a stiff-spline interannual trend and a four-harmonic seasonal cycle. Owing to the shortness of the records at Cold Bay, Niwot Ridge, and Macquarie Island, we use fixed trends and a two-harmonic fit at these stations. For seasonal cycle comparisons, we look only at the harmonic fits. To derive relative concentration or ratio differences between stations, we first adjust each observed value to the 15th of its month by sliding it parallel to the combined stiff-spline and harmonic fit. We then average the

Table 2.1. Sampling Stations in the Scripps O_2/N_2 Network

Station Code	Site	Latitude	Longitude	Elevation (m)	Time Period
ALT	Alert, Northwest Territories	82°27'N	62°31'W	210	Nov. to Dec. 1989 Apr. 1991 to Oct. 1996
CBA	Cold Bay, Alaska	55°12'N	162°43'W	25	Aug. 1995 to Nov. 1996
NWR	Niwot Ridge, Colorado	40°03'N	105°38'W	3749	Apr. 1991 to Apr. 1993
LJO	La Jolla, California	32°52'N	117°15'W	20	May 1989 to Oct. 1996
MLO	Mauna Loa, Hawaii	19°32'N	155°35'W	3397	Aug. 1993 to Nov. 1996
KUM	Kumukahi, Hawaii	19°31'N	154°49'W	40	June 1993 to Oct. 1996
SMO	Cape Matatula, American Samoa	14°15'S	170°34'W	42	June 1993 to Oct. 1996
CGO	Cape Grim, Tasmania	40°41'S	144°41'E	94	Jan. 1991 to Oct. 1996
MCQ	Macquarie Island	54°29'S	158°58'E	94	Sept. 1992 to Jan. 1994
SPO	South Pole Station	89°59'S	24°48'W	2810	Nov. 1991 to Feb. 1996

observations for each month and subtract the harmonic fit from these monthly values to deseasonalize the data. We compute relative CO_2 and O_2/N_2 differences between stations by averaging the differences between these deseasonalized monthly values over the period of overlapping observations. Although we observe meaningful inter-annual variations in these relative differences [Keeling *et al.*, 1996], our focus here is on the averages of the differences over the several years of observation, as we are comparing to models with no interannual variations. We do not have long enough records to calculate meaningful estimates of the uncertainty in our comparisons due to natural interannual variability. Although more observations are needed to characterize the stability of the observed patterns over longer time frames, the dominant patterns presented here were stable over the periods shown in Table 2.1.

2.3.1 CO_2 Gradients

As Enting and Mansbridge [1989] point out, the relationship between atmospheric concentrations and surface sources of CO_2 is sensitive to the photochemical oxidation of CO to CO_2 and CH_4 to CO in the atmosphere. This same sensitivity applies to O_2. Recent studies [Enting *et al.*, 1995; Erickson *et al.*, 1996] have attempted to estimate the relative CO contributions from incomplete combustion of fossil fuels and biomass and the oxidation of CH_4, in order to correct their model CO_2 concentrations so that they could be directly compared to observations. Instead of correcting our model values, we correct our observations, using observed CH_4 and CO concentrations. To correct our CO_2 observations, we compute total atmospheric carbon (TAC) as

$$\text{TAC (ppm)} = [CO_2] + [CH_4] + [CO] \qquad (2.1)$$

where the brackets indicate a measurement in units of μmole/mole of dry air. TAC is an atmospheric tracer that is conservative with respect to photochemical CH_4 and CO oxidation. We can then compare modeled and observed TAC values without having to estimate the extent of oxidation which occurs during fossil fuel and biomass combustion and organic matter respiration.

Figure 2.2a shows the latitudinal variations in TAC, computed by correcting our CO_2 observations using CH_4 and CO measurements from the National Oceanic and Atmospheric Administration / Climate Monitoring and Diagnostics Laboratory (NOAA/CMDL) [Dlugokencky *et al.*, 1994; Novelli *et al.*, 1992]. Where CH_4 or CO measurements were not available for our stations, we used estimates based on

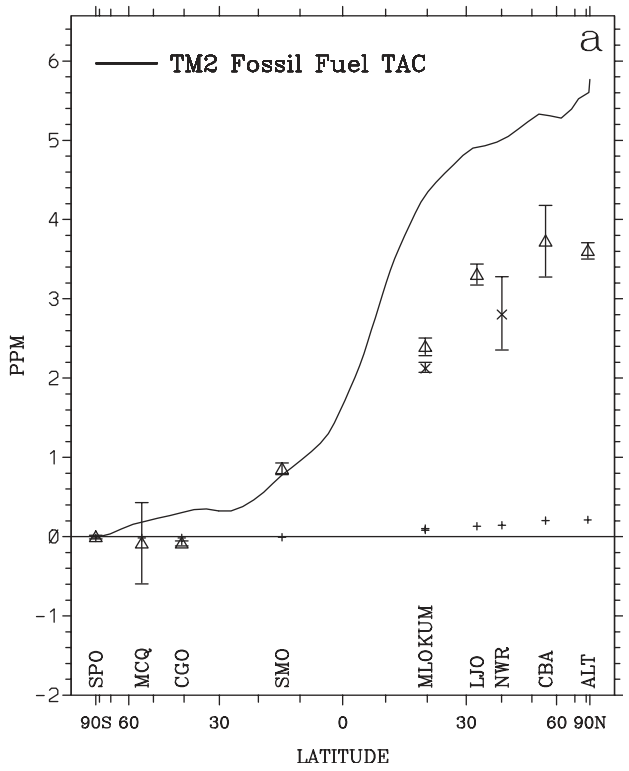

Figure 2.2. (a) Observed annual mean latitudinal variations in total atmospheric carbon (TAC) (Δ). Values were calculated from the average difference between the deseasonalized monthly values at each station and those at La Jolla, then plotted with the South Pole value set to zero. The vertical bars are the standard errors of the deseasonalized monthly residuals with respect to the stiff-spline or fixed trend fits at each station (equal to ± 0.01 ppm at South Pole). The solid curve shows the TAC variations predicted along the transect in Figure 2.1 by a 6.1 Gt C yr^{-1} fossil fuel source run on TM2. This transect provides a direct comparison at all of the stations except Mauna Loa and Niwot Ridge which are represented here by cross symbols. (b) Same but for $\delta(O_2/N_2)_{corr}$. (c) Same but for APO. Vertical bars include the influence of allowing the terrestrial oxidative ratio to vary over the range 1.1 ± 0.05. The plus symbols in Figures 2.2a, 2.2b, and 2.2c represent the combined contribution of the CO and CH_4 terms in Equations 2.1, 2.2, and 2.3, respectively. The vertical axes have been scaled so that Figure 2.2c is graphically the sum of Figures 2.2a and 2.2b.

measurements from the one or two closest available stations. We calculated the value for each station relative to La Jolla, the station with the longest and most consistent record, but plot these values with South Pole Station set to zero for visualization purposes. The error bars in Figure 2.2a represent the standard errors of the deseasonalized monthly residuals with respect to the stiff-spline or fixed-trend fits. This error accounts for measurement imprecision and synoptic variability in the observed differences but not for interannual variability which is taken up by the stiff spline. Because of CO_2 sampling problems at Macquarie Island, we have assumed that its CO_2 value is 0.0 ± 0.5 ppm relative to Cape Grim (R. Francey, personal communication, 1996). These observations define a relatively smooth northward increasing gradient, as we expect due to fossil fuel burning.

We also show in Figure 2.2a the TAC variations relative to South Pole Station predicted by forcing the TM2 atmospheric transport model (described below) with a 6.1 Gt C yr^{-1} fossil fuel source [Marland *et al.*, 1985; Andres *et al.*, 1999]. We interpolate the atmospheric model results along a surface transect as shown in Figure 2.1. We compare the La Jolla observations to model predictions one gridbox to the west, because the TM2 gridbox which contains La Jolla has strong fossil fuel sources, whereas the sampling times at this station are selected to coincide with wind conditions that deliver clean marine boundary layer air. This surface transect thus allows direct comparisons at all stations except for Mauna Loa and Niwot Ridge. For TAC, this comparison shows (Figure 2.2a) a significant discrepancy between the modeled and observed gradients which has previously been used to infer that a large

unaccounted CO_2 sink must exist in the northern hemisphere [Keeling *et al.*, 1989b; Tans *et al.*, 1990].

2.3.2 O_2 Gradients

We have accounted for the interference and dilution effects of CO_2, CH_4, and CO on our interferometric O_2 measurements using concurrent CO_2 measurements and NOAA/CMDL CH_4 and CO values [Dlugokencky *et al.*, 1994; Novelli *et al.*, 1992]. To correct our O_2 observations for the influence of photochemical CH_4 and CO oxidation, we define corrected O_2/N_2 as

$$\delta(O_2/N_2)_{corr} \text{ (per meg)} = \delta(O_2/N_2) - (2.0/X_{O_2})[CH_4] - (0.5/X_{O_2})[CO] \qquad (2.2)$$

where the O_2 mole fraction ($X_{O_2} = 0.2095$) is needed to convert from "ppm" to "per meg" units [Keeling *et al.*, 1998a] (see Section 3.2.1). Ignoring the relatively small absolute variations in other molecules that undergo photochemical oxidation, reduction, or heterogeneous loss, the tracer $\delta(O_2/N_2)_{corr}$ represents the atmospheric O_2/N_2 that one would measure after CH_4 and CO were both fully oxidized.

Figure 2.2b shows the observed latitudinal variations in $\delta(O_2/N_2)_{corr}$ along with the fossil fuel predictions. These fossil fuel predictions account for the different oxidative ratios and spatial distributions of gas, liquid, and solid fuel combustion, gas-flaring, and cement manufacture [Marland *et al.*, 1985; Keeling, 1988; Andres *et al.*, 1999]. To obtain the annual mean value from the limited observations at Macquarie Island, we compared the observations to the fitted curve for Cape Grim and computed

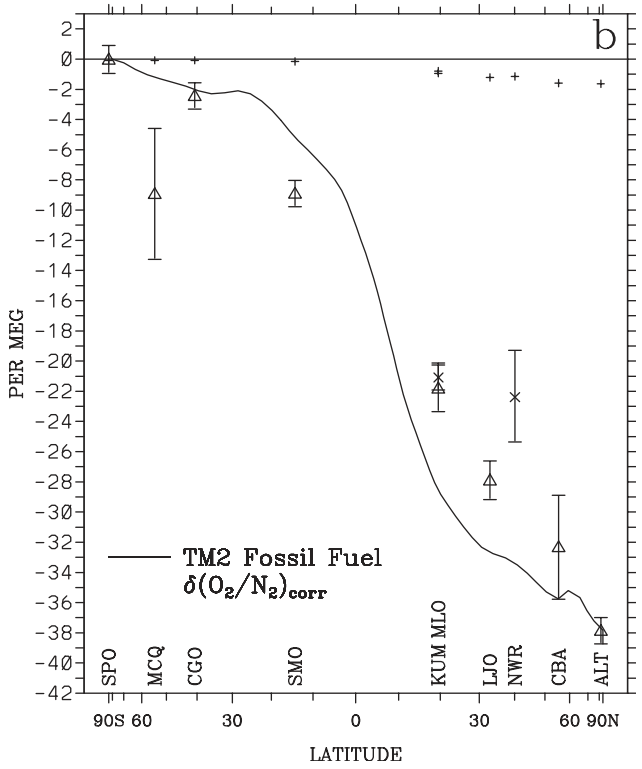

Figure 2.2. (continued)

the Macquarie Island - Cape Grim difference. The relatively large error bars for Macquarie Island result from the inclusion or exclusion of several possible outliers. The $\delta(O_2/N_2)_{corr}$ value at Niwot Ridge may be anomalously high, and the TAC value may be low, because of the influence of local vegetation on daytime samples.

The interhemispheric $\delta(O_2/N_2)_{corr}$ gradient decreases toward the northern hemisphere, as we would expect from fossil fuel combustion. However, similarly to the TAC case and as shown previously by Keeling *et al.* [1996], the fossil fuel source run on TM2 overpredicts the difference in $\delta(O_2/N_2)_{corr}$ between northern and southern

midlatitudes. It is clear that terrestrial and oceanic exchanges of CO_2, O_2, and N_2 must also be affecting the latitudinal variations of these species.

2.3.3 Derivation of Atmospheric Potential Oxygen

Because the relationships between air-sea CO_2 and O_2 exchanges are complex, it is not possible to use atmospheric CO_2 and O_2 measurements alone to separate the terrestrial and oceanic components of the observed latitudinal variations unless other constraints on the air-sea fluxes are invoked [e.g., Keeling *et al.*, 1996]. However, if we had a global ocean carbon cycle model that could predict the oceanic component of the atmospheric variations, we could determine the terrestrial CO_2 and O_2 components by subtraction, and furthermore we would expect these CO_2 and O_2 components to be stoichiometrically consistent with terrestrial processes. Here we instead reverse this concept by combining the TAC and $\delta(O_2/N_2)_{corr}$ measurements to eliminate any terrestrial influences and checking to see if the results are consistent with ocean model predictions.

To do this, we define atmospheric potential oxygen as

$$\begin{aligned} \text{APO (per meg)} &= \delta(O_2/N_2)_{corr} + (1.1/X_{O_2})\text{TAC} \\ &= \delta(O_2/N_2) + (1.1/X_{O_2})[CO_2] - (0.9/X_{O_2})[CH_4] \\ &\quad + (0.6/X_{O_2})[CO] \end{aligned} \tag{2.3}$$

where X_{O_2} again converts from "ppm" to "per meg" units and the factor of 1.1 represents the O_2:CO_2 exchange ratio for terrestrial photosynthesis and respiration as

determined by Severinghaus [1995]. This value, which exceeds unity because of the reduction and oxidation of nitrogen and other elements, was estimated based on an analysis of elemental abundances and direct measurements [Severinghaus, 1995; Keeling, 1988]. The tracer APO represents the atmospheric O_2/N_2 ratio one would measure if all CH_4 and CO molecules were oxidized to CO_2 and then all CO_2 was converted to O_2 through terrestrial photosynthesis (comparable to "Oceanic O_2/N_2" of Keeling and Shertz [1992] and Keeling *et al.* [1998b]). This tracer is thus conservative with respect to the oxidation of CH_4 and CO and with respect to terrestrial exchange. Variations in APO can be caused only by air-sea exchange of CO_2, O_2, and N_2 and a fossil fuel effect resulting from the higher O_2:C oxidative ratios for fossil fuels than for terrestrial organic matter.

To model changes in APO in an air parcel due to changes in the number of moles of an individual species (e.g., ΔO_2, ΔN_2, and ΔCO_2), we can write

$$\begin{aligned}\Delta APO &= (\partial APO/\partial O_2)\Delta O_2 + (\partial APO/\partial N_2)\Delta N_2 \\ &\quad + (\partial APO/\partial CO_2)\Delta CO_2 \\ &= [(1.0/X_{O_2})\Delta O_2 - (1.0/X_{N_2})\Delta N_2 \\ &\quad + (1.1/X_{O_2})\Delta CO_2]/M \end{aligned} \qquad (2.4)$$

where M represents the initial number of moles in the air parcel and X_{N_2}, the N_2 mole fraction, is equal to 0.7808. Figure 2.2c shows the observed latitudinal variations in APO, along with those predicted for the fossil fuel effect, where the fossil fuel effect is calculated according to the first and last terms in Equation 2.4. The observed error

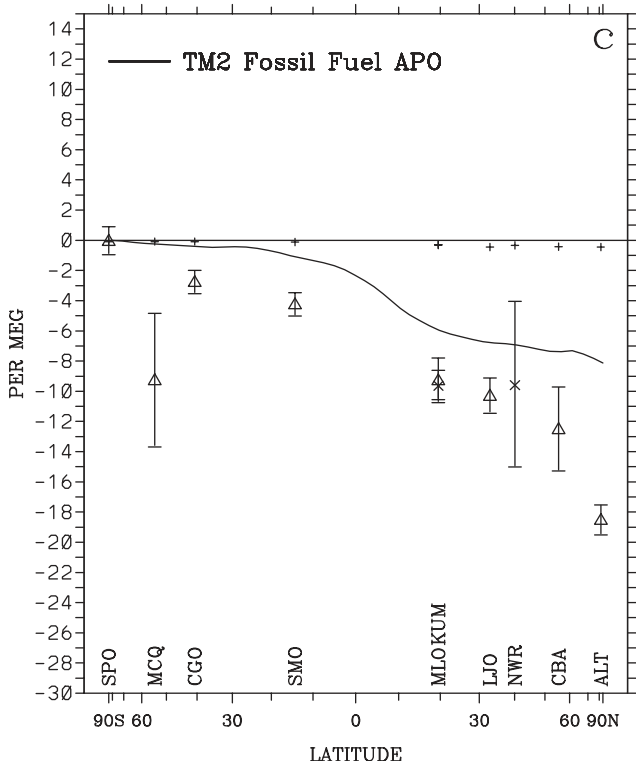

Figure 2.2. (continued)

bars here represent a quadrature sum of the statistical error and the variation produced by allowing the terrestrial oxidative ratio to vary over the range 1.1 ± 0.05 per Severinghaus [1995]. Figure 2.2 also indicates that the CH_4 and CO photochemical correction terms sum to approximately 5% of the TAC and $\delta(O_2/N_2)_{corr}$ signals but that their contributions are less significant to APO.

With local terrestrial influences removed, the APO value at Niwot Ridge is closer to the values for La Jolla and Cold Bay. Fossil fuel combustion has a significant effect on APO because of the higher oxidative ratio in fossil fuels, of around 1.4, relative to terrestrial biotic matter. However, the predicted fossil fuel

effect on APO does not account for the Cold Bay - Alert difference, the South Pole - Cape Grim difference, nor the Macquarie Island depression. We expect these features in APO are primarily due to latitudinal variations in air-sea CO_2, O_2, and N_2 exchange.

Before presenting the ocean model predictions of such variations, we can make a few general inferences based on our observations. The APO gradient in excess of fossil fuel burning is of the order of 5 per meg (Figure 2.2c). Allowing for the oceanic uptake of anthropogenic CO_2, which is expected to increase the interhemispheric CO_2 gradient by 0.4 ppm because of the larger ocean area in the southern hemisphere [Keeling *et al.*, 1996], this implies a preindustrial gradient in APO of the order of 7 per meg. If we assume as per Keeling *et al.* [1996] that this steady state difference is entirely due to transport in the Atlantic thermohaline circulation and use similar O_2:CO_2 scaling factors [Keeling and Peng, 1995], we compute a preindustrial southward transport of 0.35 Gt C yr^{-1}. This estimate is in disagreement with the POBM prediction of 0.0 ± 0.2 Gt C yr^{-1} [Sarmiento *et al.*, 1995]. It is, however, consistent with that of Keeling *et al.* [1996], showing that their results are not sensitive to the selection of a few stations and similarly pointing to the need for model revisions in the sense of increased southward oceanic transport of CO_2.

2.4 Ocean Models

The temperature, salinity, and velocity fields for POBM are generated by the Geophysical Fluid Dynamics Laboratory (GFDL) nonseasonal circulation model [Toggweiler *et al.,* 1989a, b]. This model has a horizontal resolution of 3.75° longitude by 4.5° latitude, has 12 levels in the vertical, and qualitatively reproduces the thermohaline forced solubility pump [Sarmiento *et al.,* 1995]. The formation of organic carbon is parameterized in POBM by using a fixed C:P ratio and by forcing the surface phosphate (PO_4) concentrations toward annual-average observations on a 100-day timescale. Half of this production goes into particulate organic matter (POM) which sinks and is remineralized with a depth distribution based on sediment trap observations, while the other half goes into dissolved organic matter (DOM) which is transported and remineralized with a decay time of 11.2 years. This approach produces realistic biological pump driven vertical and horizontal variations in DIC [Sarmiento *et al.*, 1995].

Figure 2.3a shows the preindustrial air-sea CO_2 fluxes predicted by POBM, which are influenced by a combination of the solubility and biological pumps. The cooling and sinking of northward moving water leads to strong CO_2 sinks in the northwestern Atlantic and the Greenland and Norwegian Seas, while the strongest CO_2 source is in the equatorial Pacific where cold, DIC rich waters are brought to the surface and warmed. The alternating pattern of CO_2 influx and efflux across the Southern Ocean reflects variations in the strength of convection in the physical model.

Figure 2.3. (a) The preindustrial sea-air CO_2 flux in mol CO_2 m^{-2} yr^{-1} as predicted by the Princeton ocean biogeochemistry model (POBM). The grid spacing of these fluxes is 3.75° longitude by 4.5° latitude. (b) Same but for sea-air O_2 flux in mol O_2 m^{-2} yr^{-1}. (c) Same as Figure 2.3a but as predicted by the Hamburg model of the ocean carbon cycle (HAMOCC3.1). The original 3.5° by 3.5° diagonal grid was interpolated onto a 2.5° by 2.5° rectangular grid before contouring. (d) Same as Figure 2.3b but as predicted by HAMOCC3.1. (e) Same as Figure 2.3a but as predicted by the Lawrence Livermore ocean biogeochemistry model (LLOBM). These fluxes have a resolution of 4° longitude by 2° latitude. (f) Same as Figure 2.3b but as predicted by LLOBM. Note the similar contour levels, with the exception of the extreme values, between Figures 2.3a, 2.3c, and 2.3e, and between Figures 2.3b, 2.3d, and 2.3f.

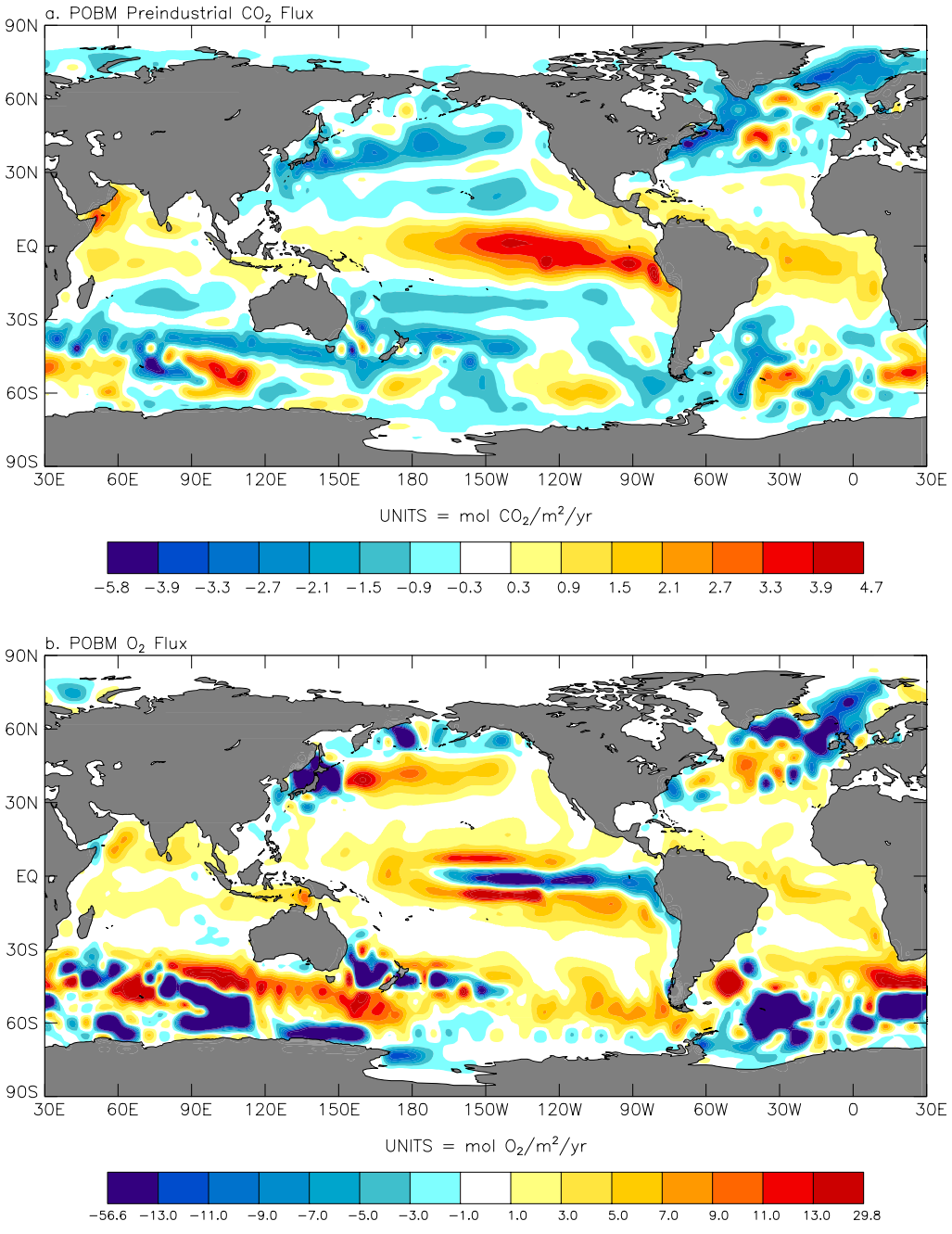
a. POBM Preindustrial CO_2 Flux
90N
60N
30N
EQ
30S
60S
90S
30E
60E
90E
120E
150E
180
150W
120W
90W
60W
30W
0
30E
UNITS = mol $CO_2/m^2/yr$
−5.8 −3.9 −3.3 −2.7 −2.1 −1.5 −0.9 −0.3 0.3 0.9 1.5 2.1 2.7 3.3 3.9 4.7
b. POBM O_2 Flux
90N
60N
30N
EQ
30S
60S
90S
30E
60E
90E
120E
150E
180
150W
120W
90W
60W
30W
0
30E
UNITS = mol $O_2/m^2/yr$
−56.6 −13.0 −11.0 −9.0 −7.0 −5.0 −3.0 −1.0 1.0 3.0 5.0 7.0 9.0 11.0 13.0 29.8

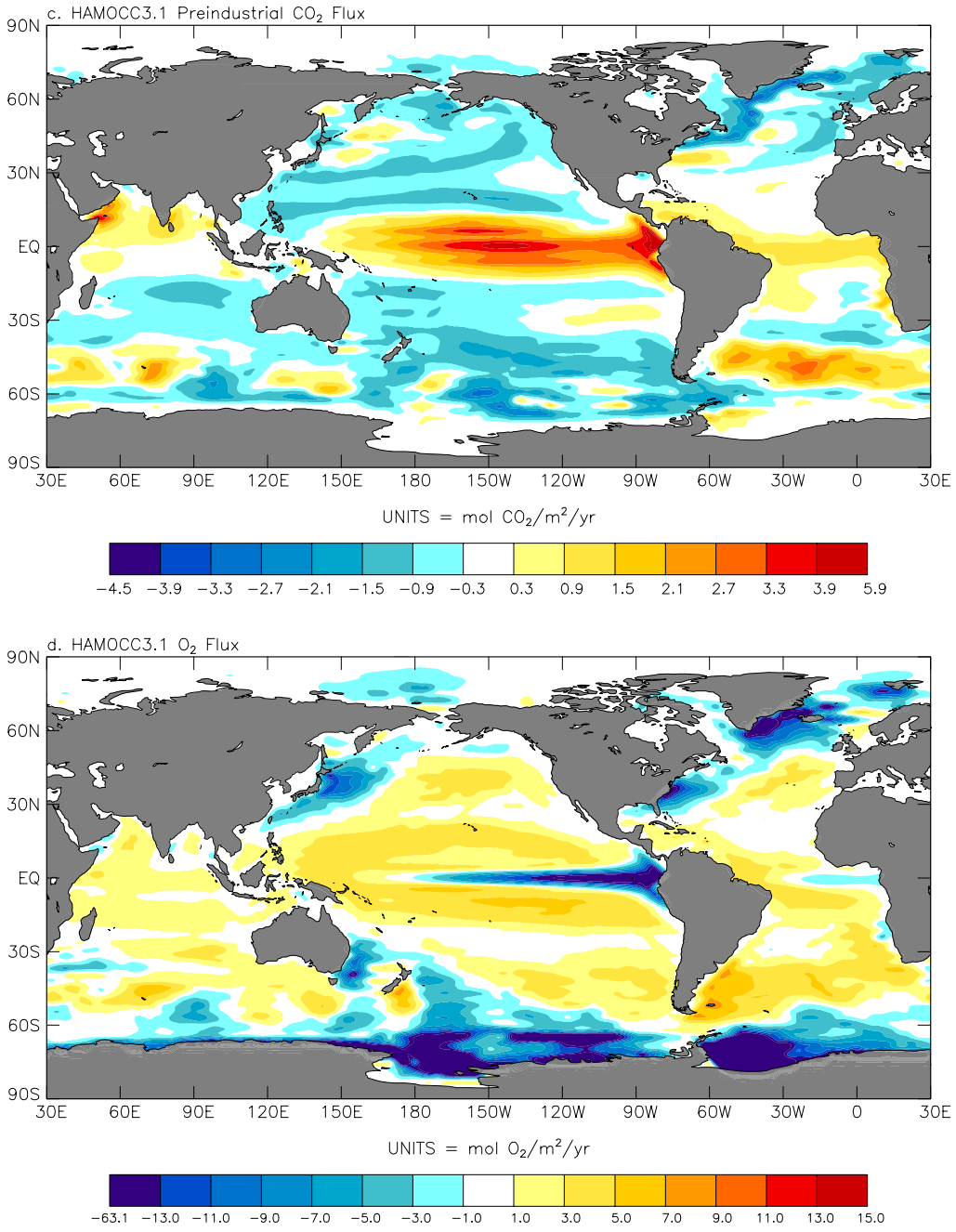

Figure 2.3. (continued)

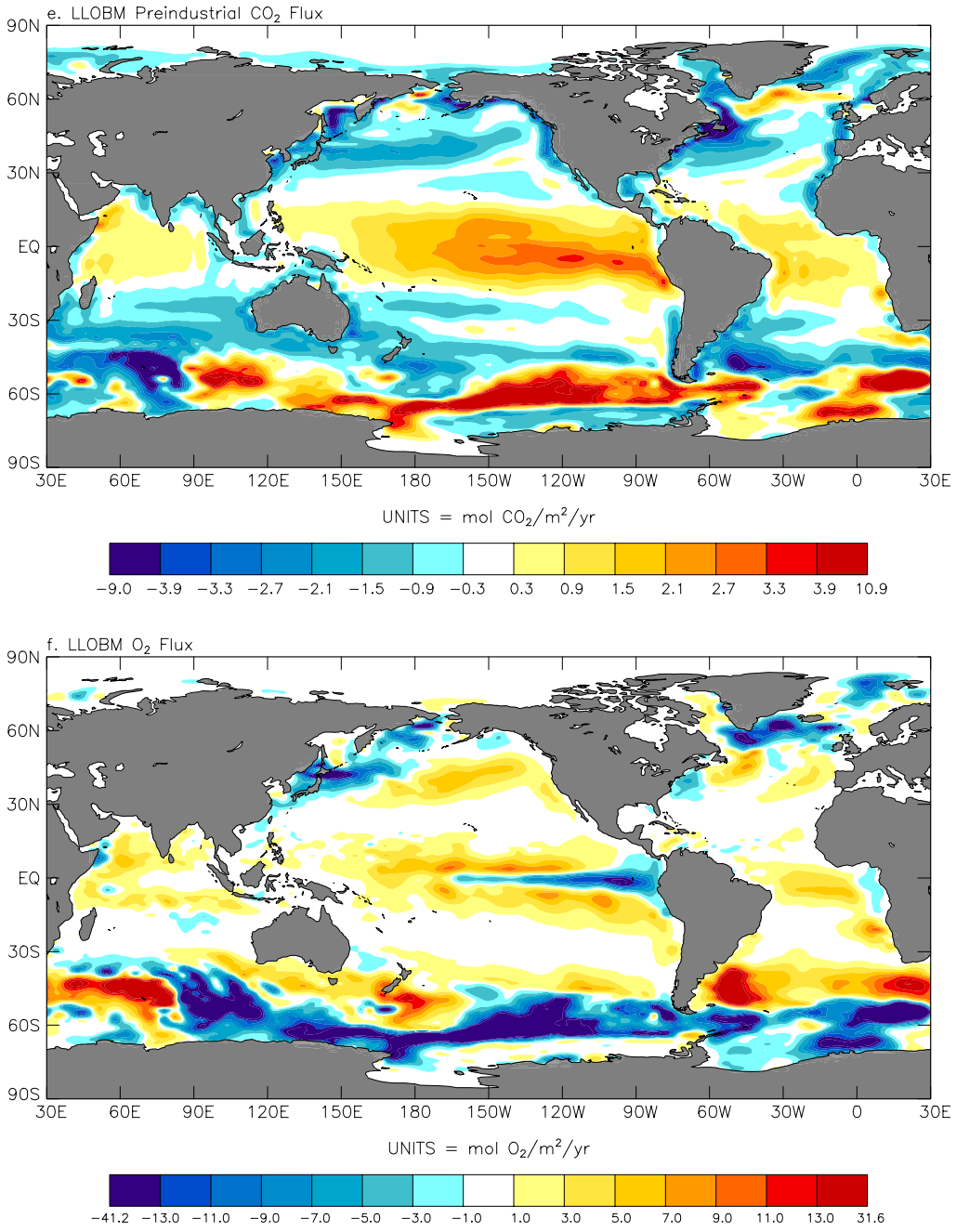

Figure 2.3. (continued)

Figure 2.3b shows the O_2 flux predicted by POBM. Similar to CO_2, the North Atlantic regions of deep water formation are sinks for O_2. In the equatorial Pacific, the biological depletion of O_2 in the upwelling waters produces a sink along the equator. However, as these nutrient rich waters spread outward from the equator, enhanced new production and warming lead to a net source of O_2 for the equatorial region. The strong Southern Ocean O_2 sinks appear to correspond to regions of CO_2 efflux, indicating the supply of DIC rich, O_2-depleted waters to the surface through model convection on the scale of a grid cell.

The physical fields for HAMOCC3.1 are taken from the large-scale geostrophic circulation model (LSG) [Maier-Reimer *et al.*, 1993]. This model has a horizontal resolution of 3.5° by 3.5° and 15 layers in the vertical and resolves the seasonal cycle on a 1-month time step. This model represents an improvement over earlier HAMOCC versions in that it includes a plankton model which allows nutrient uptake rates to vary seasonally thereby improving agreements with seasonal surface pCO_2 variations [Six and Maier-Reimer, 1996]. The model tracks PO_4, phytoplankton, zooplankton, POM, and DOC. New production in HAMOCC3.1 is parameterized by a Michaelis-Menton kinetics equation, based on simulated surface PO_4 concentrations and modified by light, temperature, vertical mixing, and phytoplankton abundance. The predicted latitudinal variations in annual-average PO_4 and O_2 saturation are generally in good agreement with observations.

Figure 2.3c shows the annual-average, preindustrial air-sea CO_2 fluxes predicted by HAMOCC3.1. The distribution of these fluxes is similar to that of the POBM CO_2 fluxes, with the exception of a slightly reduced CO_2 sink in the North Atlantic and a distinctly different pattern in the Southern Ocean. Figure 2.3d shows the annual-average O_2 flux predicted by HAMOCC3.1. This flux pattern is also similar to that of POBM, however, with a somewhat larger equatorial sink. In addition, HAMOCC3.1 predicts a very large O_2 sink in the Weddell Sea which is less strongly predicted by POBM. The HAMOCC3.1 heat fluxes indicate that this sink is primarily due to solubility forcing through the modeled convective formation of deep water.

The physical fields for LLOBM are based on a modified version of the GFDL model [Duffy *et al.*, 1997], which in the simulations used here had a resolution of 4° longitude by 2° latitude and 23 levels in the vertical. This model also has a similar biological parameterization to that of POBM. Productivity in LLOBM is simulated by forcing to seasonal PO_4 observations with a timescale of 2 weeks. Because it is known that this approach does not produce realistic seasonal variations in air-sea CO_2 and O_2 fluxes [Six and Maier-Reimer, 1996], we have only used the annual-average fluxes here. Of the new production in LLOBM, 80% is assumed to be in the form of POM which sinks and is remineralized using an exponential depth scale, while the other 20% goes into DOM which is remineralized with a decay constant of 25 years.

Figures 2.3e and 2.3f show the annual-average, preindustrial CO_2 and O_2 fluxes, respectively, predicted by LLOBM. The large-scale patterns are similar to the other two models, again with the exception of the Southern Ocean. There are several

similarities between the LLOBM and POBM fluxes, such as the CO_2 source / O_2 sink southwest of Australia and the CO_2 sink/O_2 source east of Argentina, which indicate that these two GFDL-based models are predicting grid-scale convection in many of the same regions. It is apparent from the molar magnitude of the fluxes shown in Figure 2.3 that the largest air-sea O_2 fluxes are an order of magnitude greater than the largest air-sea CO_2 fluxes. This is due to the reinforcing tendencies of the solubility and biological pumps as discussed above and to the more rapid gas exchange of O_2. When zonally integrated, however, the largest O_2 fluxes are only twice as large as the largest CO_2 fluxes; thus both significantly influence the meridional variations in APO.

2.5 Predicted Atmospheric Potential Oxygen Gradients

We used the preindustrial CO_2 (Figures 2.3a, 2.3c, and 2.3e), anthropogenic perturbation CO_2 (not shown), O_2 (Figures 2.3b, 2.3d, and 2.3f) , and N_2 (not shown) ocean model fluxes as lower boundary conditions in the TM2 atmospheric tracer transport model [Heimann, 1995]. For the anthropogenic CO_2 flux, we used years 1990, 1987, and 1989 for POBM, HAMOCC3.1, and LLOBM, respectively. Only HAMOCC3.1 explicitly calculates air-sea N_2 fluxes. For POBM, we estimated the N_2 fluxes by scaling the solubility-driven O_2 fluxes according to the ratio of N_2 and O_2 solubilities. For LLOBM, we estimated N_2 fluxes based on solubility changes calculated from model heat fluxes. The TM2 model solves the tracer continuity equation using wind fields generated by the European Centre for Medium-Range

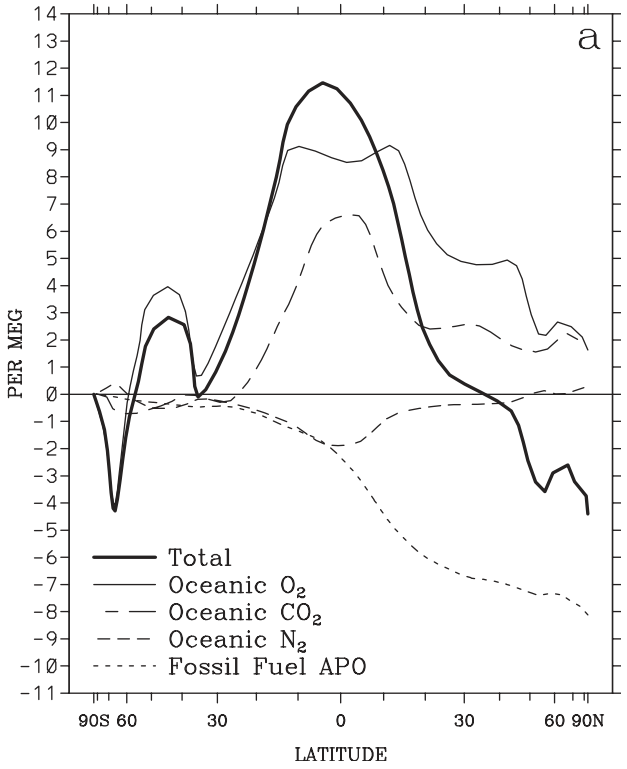

Figure 2.4. (a) The latitudinal APO variations as predicted by POBM-TM2 along the transect in Figure 2.1 and relative to the prediction at South Pole, along with the components. (b) Same as Figure 2.4a but as predicted by HAMOCC3.1-TM2. (c) Same as Figure 2.4a but as predicted by LLOBM-TM2.

Weather Forecasting analyses and a subgrid-scale vertical convection parameterization. In this study, we used analyzed winds from 1987. This model has a resolution of 8° latitude by 10° longitude with nine sigma layers in the vertical and a time step of 4 hours. The ocean model output fields were regridded onto the TM2 horizontal grid. We ran the model for 4 years, at which point the spatial concentration gradients are quasi-stationary, and used annual average values from the fourth year. Because the transport is linearly related to tracer concentration, various source

components can be run separately, and the results can be combined for comparison to atmospheric observations.

Figure 2.4a shows the interhemispheric variation in APO and its components as predicted by POBM-TM2. The total curve is graphically the sum of the component curves and is calculated according to Equation 2.4. The fossil fuel component is the same as that shown in Figure 2.2c. The oceanic components show greater structure than the fossil fuel component because of the proximity of the sources to the surface transect (Figure 2.1) used for the model predictions, while the oceanic O_2 component shows the most structure for the reasons discussed above. The oceanic CO_2 component reflects the strong equatorial outgassing shown in Figure 2.3a. Because of the greater ocean area in the southern hemisphere, the oceanic uptake of anthropogenic CO_2 leads to a decreasing CO_2 gradient to the south. The interhemispheric gradient in the O_2 component predicted by POBM-TM2 has an equatorial bulge with a small depression at the equator, which results from the combined biological and thermal effects also discussed above. The POBM-TM2 CO_2 and O_2 components combine to form a large equatorial peak in APO. The predicted APO structure in the southern hemisphere appears to result from the meridional separation of O_2 sources and sinks in the Southern Ocean as illustrated in Figure 2.3b. As Figure 2.4a shows, the thermally driven outgassing of N_2 near the equator leads to an apparent decrease in APO.

Figure 2.4b shows the interhemispheric variation in APO and its components as predicted by HAMOCC3.1-TM2. The fossil fuel component is identical, and the CO_2 and N_2 components are very similar to those predicted by POBM-TM2. The

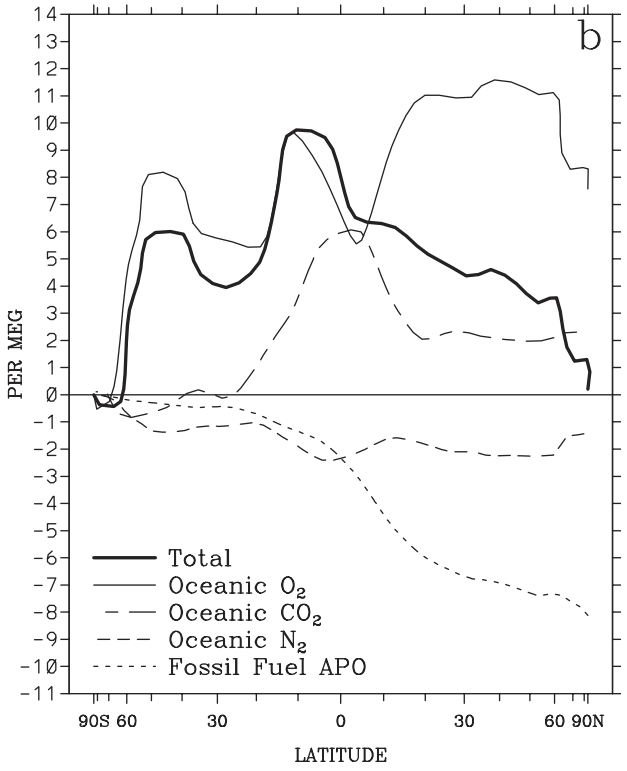

Figure 2.4. (continued)

primary differences between the interhemispheric APO variations predicted by POBM-TM2 and HAMOCC3.1-TM2 are due to differences in the O_2 component.

Most noticeably, the HAMOCC3.1-TM2 O_2 concentrations are lower around the equator and do not decrease as strongly toward the north. The equatorial O_2 depression seen in HAMOCC3.1-TM2 appears to be the result of both a stronger sink and seasonal covariations between air-sea O_2 fluxes and atmospheric mixing, as discussed below. Similar to POBM-TM2, HAMOCC3.1-TM2 predicts a small APO peak near 45°S with a significant decrease immediately to the south. This feature in

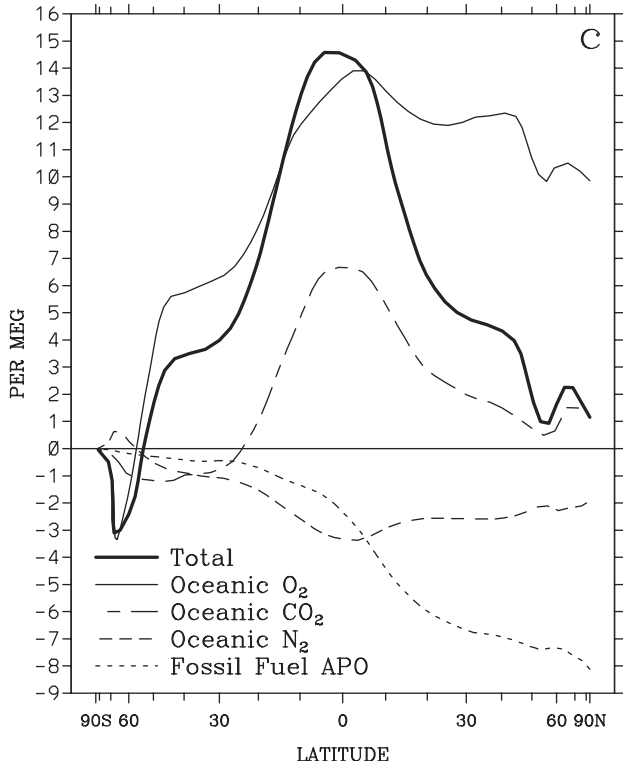

Figure 2.4. (continued)

HAMOCC3.1-TM2 also appears to be related to a pattern of O_2 sources in the northern half of the Southern Ocean and sinks in the southern half, including the strong sink in the Weddell Sea.

Figure 2.4c shows the interhemispheric variation in APO and its components as predicted by LLOBM-TM2. The shape of the total curve, with a large equatorial peak, is very similar to that of POBM-TM2. In the northern hemisphere, the LLOBM-TM2 O_2 component drops off less steeply than in POBM-TM2, indicating weaker O_2 sinks at high northern latitudes. However, the effect of this on APO is countered by

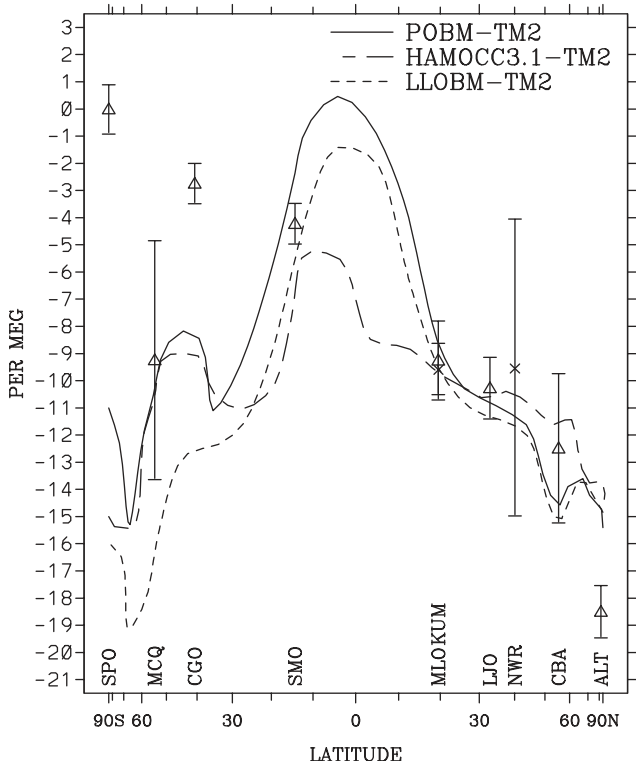

Figure 2.5. The observed latitudinal APO variations relative to South Pole (from Figure 2.2c) and the predictions of the three models (from Figure 2.4). The vertical scaling is the same as in Figure 4, but the model curves have been shifted to visually fit the northern midlatitude stations.

the CO_2 component dropping off more steeply than in POBM-TM2, apparently because of stronger CO_2 sinks at high northern latitudes. In the southern hemisphere, the LLOBM-TM2 APO gradient has less structure than the other two models between 40° and 50°S but shows a similarly strong dip around 70°S.

2.6 Model/Observation Comparisons

Figure 2.5 shows the interhemispheric variation in APO as determined from atmospheric observations (from Figure 2.2c) and as predicted by POBM-TM2, HAMOCC3.1-TM2, and LLOBM-TM2 (from Figure 2.4). As described in section 2.3.3, variations in the observed APO values can only result from air-sea gas exchange and the relatively well-constrained fossil fuel effect. Thus the comparison in Figure 2.5 represents a direct test of the model predictions of the longitudinal variation of combined air-sea CO_2, O_2, and N_2 fluxes. While all three models produce reasonable fits to the observations between Samoa and Cold Bay, they disagree markedly outside of this region. None of the models produce the observed depression in APO at Alert, and all three of the models predict a decreasing gradient toward high southern latitudes which is not observed. Most significantly, the observations define a reasonably large decreasing gradient from South Pole Station to Alert, which is not reproduced by either model. We do not have any long-term records from near the equator, and therefore cannot test the various model predictions of an equatorial peak in APO.

Table 2.2 shows the modeled and observed relative differences in APO as calculated directly between selected stations. Because our station records coincide over various time periods (Table 2.1), this approach provides a more robust means of comparing to model predictions than that of relating all records to one station. The error values in Table 2.2 represent quadrature sums of the errors for each station as shown in Figure 2.2c, adjusted for the number of overlapping months between the

Table 2.2. Modeled and observed relative APO differences

Stations	POBM-TM2	HAMOCC3.1-TM2	LLOBM-TM2	Observed
CBA-ALT	0.1	2.1	0.0	4.6 ± 3.0
LJO-CBA	3.8	1.0	3.8	2.2 ± 3.5
KUM-LJO	2.2	1.0	1.7	1.0 ± 1.8
SMO-KUM	6.5	3.1	4.1	4.6 ± 1.5
CGO-SMO	-5.9	-2.2	-6.7	0.5 ± 1.2
MCQ-CGO	-2.1	-1.6	-4.0	-6.5 ± 4.3
SPO-MCQ	-0.7	-4.4	-0.3	10.8 ± 3.9
SPO-ALT	4.1	-0.9	-1.4	20.6 ± 1.4
LJO-ALT	4.0	3.1	3.8	8.2 ± 1.1
SPO-SMO	-8.6	-8.1	-11.0	4.2 ± 1.3

Values are per meg.

stations. The most conspicuous of the discrepancies between the models and observations is the underestimation of the South Pole - Alert APO difference by 16 to 22 per meg. Also significant are the underestimation of the La Jolla - Alert difference by 4 to 5 per meg and the large negative South Pole - Samoa difference in the models of -8 to -11 per meg compared to the significantly positive observed value of 4 per meg. The model curves in Figure 2.5 appear fairly symmetric about the equator; however, it is important to remember that these curves contain a fossil fuel component. If we derive a purely oceanic signal by subtracting the fossil fuel component from the observations rather than adding it to the ocean models, our observations indicate a South Pole - Alert difference of around -13 per meg, while the models predict values between +3 and +9 per meg.

There are a number of possible explanations for these discrepancies. One possibility that we must consider, particularly when calculating relative differences between stations, is that of systematic biases in our sampling or measurement procedures. The TAC measurements shown in Figure 2.2a agree well with those of other sampling programs [Keeling *et al.*, 1989a, Tans *et al.*, 1990], and the $(O_2/N_2)_{corr}$ measurements shown in Figure 2.2b, though unique, reveal no unreasonable interstation differences. For APO, the comparison of the relatively proximal stations of Mauna Loa, Kumukahi, La Jolla, Niwot Ridge, and Cold Bay (see Figure 2.2c) suggests that systematic errors are similar to or smaller than our estimated precision. Observationally, the most difficult station is South Pole, where flasks must be stored for months at low ambient temperature and pressure. To date, we have found no systematic errors that could explain the discrepancy of around 12 per meg between the observed and modeled South Pole - Samoa APO difference [Keeling *et al.*, 1998a]. If the value of 1.1 for the O_2:CO_2 ratio of terrestrial photosynthesis and respiration were incorrect by more than the error estimates of Severinghaus [1995] or if this value varies systematically with latitude, our observed and modeled APO values would both change. However, the largest discrepancies we see are in the southern hemisphere where the terrestrial effects on APO are very small. Outside of the observations, the only other possible sources of error are the atmospheric transport model and the ocean models, which we now discuss in turn.

2.7 Atmospheric Transport Uncertainties

As Law *et al.* [1992] point out, atmospheric transport models may underestimate the meridional mixing efficiency at high southern latitudes by not accurately reproducing convective processes and transient disturbances in this region. While TM2 has been tested against Krypton 85 (^{85}Kr) and Radon 222 (^{222}Rn) and the model gives reasonable predictions of southern hemisphere meridional CO_2 gradients [Heimann and Keeling, 1989], none of these gases has strong southern hemisphere sources as O_2 does. However, as Figure 2.5 shows, enhanced meridional mixing in the southern hemisphere would only flatten the predicted gradients; it could not change their sign, which is necessary to bring them into agreement with the observations.

A transport problem that could potentially have a more significant effect on latitudinal APO gradients is the uncertainty in resolving the effects of seasonal covariations between surface fluxes and atmospheric mixing, known as rectifier effects. During summer at high latitudes, the marine boundary layer is stably stratified and the O_2 efflux due to surface warming and biological productivity is trapped near the surface, whereas during winter, strong vertical mixing in the atmosphere dilutes the surface O_2 deficit caused by cooling and deep ventilation. At low latitudes, seasonal variations in the Intertropical Convergence Zone cause the tropics to receive air preferentially from the winter hemisphere, where O_2 uptake is occurring. The net effect, as predicted by HAMOCC3.1-TM2 and shown in Figure 2.6, is that the purely seasonal O_2 flux component produces annual mean peaks of 1 to 2 per meg at the

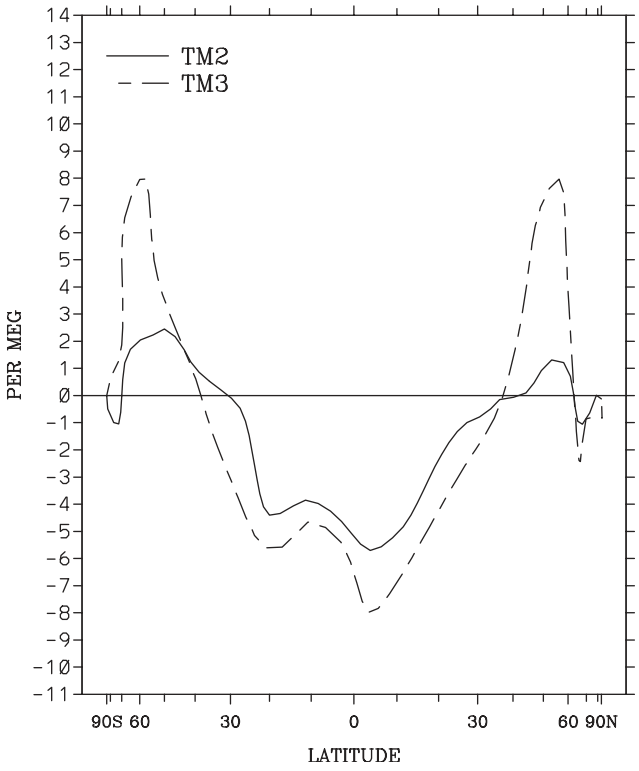

Figure 2.6. The latitudinal $\delta(O_2/N_2)_{corr}$ variations predicted by TM2 (solid curve) and TM3 (dashed curve) when driven by the purely seasonal component of the HAMOCC3.1 air-sea O_2 fluxes. The predictions are for the transect shown in Figure 2.1, where the TM3 values are taken from the second model level (approximately 170 m) to approximate selective sampling during well-mixed conditions. The vertical scaling is the same as for Figures 2.4 and 2.5.

surface around 50° latitude in each hemisphere and a trough of 4 to 6 per meg at the surface within 20° of the equator. The relatively smaller equatorial APO bulge in HAMOCC3.1-TM2 compared to the other two models (Figure 2.5) may be partially explained by this effect.

To explore the uncertainty in the simulated rectifier effects, we ran the same sources on a 4° by 5° by 18-level version of the transport model (TM3) which

produces significantly greater rectifier effects as shown in Figure 2.6. In the purely seasonal HAMOCC3.1-TM3 runs, the annual mean equatorial O_2 trough was slightly greater, while the peaks at 50° in each hemisphere were increased significantly to 8 per meg. This has the effect of bringing the HAMOCC3.1-TM3 Cold Bay - Alert APO difference (7.9 per meg) into agreement with the observations. However, this model also makes the La Jolla - Cold Bay prediction (-2.7 per meg) much worse. In addition, because the Cold Bay station is located inland, we do not expect its APO value to be as sensitive to marine boundary layer variations as TM3 predicts, and the improved agreement relative to Alert may be fortuitous. The HAMOCC3.1-TM3 predictions are also worse for the South Pole - Samoa difference (-12.5 per meg) and almost unchanged with respect to the most significant South Pole - Alert difference. While rectifier effects are clearly a large source of uncertainty in modeled latitudinal APO gradients, neither the TM2 nor the TM3 rectifier patterns can be scaled to consistently resolve the discrepancies shown here.

2.8 Ocean Model Uncertainties

The similarity among the model predictions in Figure 2.5 suggests that if the discrepancies with observations are due to the ocean models, the problems are likely fundamental to all three models. One aspect of coarse-resolution ocean models that has received considerable attention is that of the parameterization of subgrid-scale isopycnal eddy mixing [Veronis, 1975; Gent and McWilliams, 1990; Duffy *et al.*,

1997]. The three models tested here all simulate this process through horizontal diffusion. However, as pointed out by Veronis [1975], in regions of steeply sloping isopycnals this method can lead to artificial water, heat, and tracer transports. The feature consisting of a peak in APO around 45°S and a trough to the south (Figure 2.5), may be a result of such artificial transport in the Deacon cell, a meridional cell which appears in the zonally averaged mean velocity field as downwelling around 45°S and upwelling around 60°S [Döös and Webb, 1994]. In models which employ horizontal diffusion, advective transport in this cell results in a moderate air-to-sea heat flux at 45°S and a very strong sea-to-air heat flux at 60°S. By parameterizing the dynamical effect of subgrid-scale eddies through the diffusion of tracers and isopycnal thicknesses along isopycnals [Gent and McWilliams, 1990], Danabasoglu *et al.* [1994] showed that transport of heat and tracers by these eddies almost completely cancels the advective transport in the Deacon cell. Their model also produced less convection in the Southern Ocean and a confinement of the region of deep water formation in the North Atlantic.

These results, as they pertain to the meridional overturning of dissolved O_2, DIC, and heat, have potentially significant implications for model predictions of air-sea APO flux. The parameterization of Gent and McWilliams [1990] has been shown to significantly improve some ocean model simulations [Boning *et al.*, 1995; McDougall *et al.*, 1996], but also to worsen others [Duffy *et al.*, 1997]. To investigate the sensitivity of modeled APO variations to this parameterization, we have used output from a version of LLOBM which incorporated the Gent and McWilliams

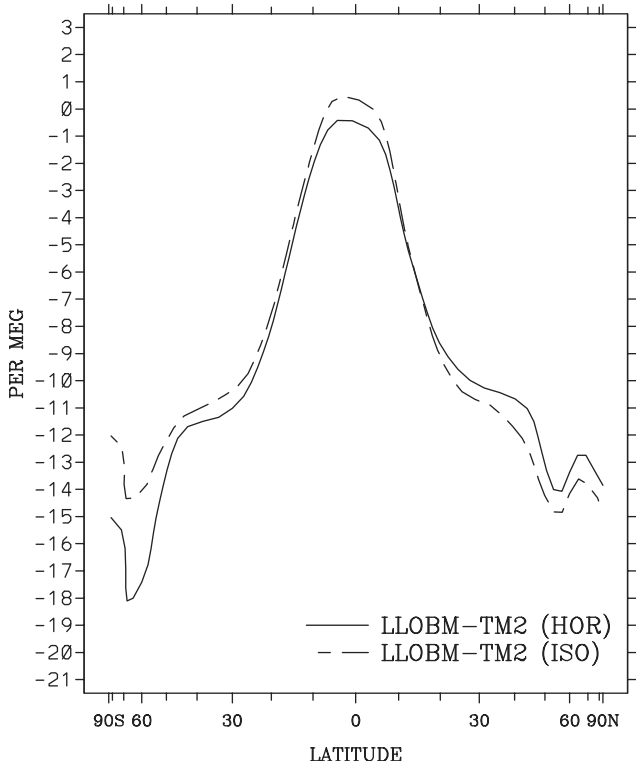

Figure 2.7. The latitudinal APO variations predicted by two versions of LLOBM-TM2, using horizontal diffusion (solid curve) (from Figure 2.4c) and using the parameterization of Gent and McWilliams [1990] (dashed curve). The vertical scaling is the same as for Figures 2.4-2.7.

[1990] mixing scheme. Figure 2.7 shows a comparison between the meridional APO gradients predicted by this version of LLOBM-TM2 and the previous version (Figure 2.4c) which used horizontal diffusion. Incorporating the Gent and McWilliams [1990] scheme produced a decrease in APO in the northern hemisphere and an increase and flattening of APO in the southern hemisphere. As Figures 2.5 and 2.7 show, these changes are of the right sense to bring the predicted APO variations into better agreement with the observations; however, the magnitude of change is much too

small. While this suggests that the Gent and McWilliams [1990] parameterization cannot resolve the large discrepancy with observations, it does not rule out the possibility that isopycnal eddy mixing is a large source of model error or that including this parameterization in other models might produce a more significant change.

Another limitation of POBM, HAMOCC3.1, and LLOBM related to their coarse resolution is that they do not simulate subgrid-scale vertical convection. This is potentially significant in the Southern Ocean where convection cells on scales of tens to hundreds of meters may be responsible for stabilizing the surface layer. Observations of salinity and O_2 saturation both show strong stratification in the upper 250 m of the Southern Ocean [Levitus, 1982]; however, GFDL- and LSG-based models produce no such halocline [Maier-Reimer *et al.*, 1993; Toggweiler and Samuels, 1995] or oxycline [Six and Maier-Reimer, 1996]. These models appear to be convecting too effectively and too deeply, which may be a result of only being allowed to convect on the grid scale of several degrees in latitude and longitude. The excessive deep convection in these models produces unrealistic inputs of O_2-depleted and relatively warm waters to the surface of the Southern Ocean, which is likely to produce an anomalously high uptake of APO and release of heat in this region.

The treatment of sea-ice formation is another aspect of physical ocean models which may contribute to the problem of excessive deep convection in the Southern Ocean. Toggweiler and Samuels [1995] showed that ocean circulation models form Antarctic bottom water (AABW) by cooling and salinizing southward flowing Antarctic surface waters until they convect and that to match observed deep water

salinities most models include brine inputs that are much higher than those expected from realistic sea-ice formation. They presented evidence from $\delta^{18}O$ and salinity measurements that deep water is actually formed by a sinking mixture of shelf water and southward flowing circumpolar deep water (CDW), which requires much smaller brine inputs to match observed deep salinities. The implication of this result for APO predictions is that converting CDW into AABW requires a much smaller heat flux and would thus take up less O_2 and CO_2 than the conversion of surface waters in present models.

In a related discussion in an earlier paper, Toggweiler and Samuels [1993] used ^{14}C measurements to argue that present ocean circulation models are fundamentally misrepresenting the global overturning of deep waters. Ocean models tend to agree with the classical view [Broecker, 1991] that deep waters upwell through the main thermocline in the Pacific and Indian Oceans and are carried poleward at the surface. However, in agreement with Wunsch *et al.* [1983], Toggweiler and Samuels [1993] found that the relationship between ^{14}C values in the deep North Pacific and the Antarctic surface indicate that most of the oceans' deep waters return to the Southern Ocean in a strong middepth outflow before being upwelled. The expected effect of Toggweiler and Samuels' [1993] reconfigured global conveyor on APO is that deep waters would upwell in a region where their preformed nutrients were the same and their temperatures were very close to those of the surface waters, resulting in less equatorial outgassing and high-latitude ingassing of APO. In addition, the surface

waters in the Southern Ocean would flow northward in a wind-driven cell, further reducing the modeled poleward heat transport in the Southern Ocean.

The cause of the excessive low-latitude upwelling in the models may be the heating of deep waters due to anomalously high vertical diffusivities in the main thermocline (R. Toggweiler, personal communication, 1997). These diffusivities are currently set as low as numerical considerations will allow; however, they may still overestimate mixing. To get a model to produce realistic middepth outflows, it is necessary to artificially cool the deep ocean south of the Antarctic Circumpolar Current so that advective heat loss to the south can replace low-latitude upwelling as the dominant heat sink for the deep Pacific and Indian Oceans (R. Toggweiler, personal communication, 1997). While this improves the pattern of the flow, it results in even higher sea-to-air heat fluxes near Antarctica. This excessive throughput of heat by the abyssal ocean may continue to be a source of uncertainty in APO simulations until its apparent cause, low-latitude inputs of heat from excessive vertical mixing, is resolved.

Improvements in any of the just described model deficiencies, lack of subgrid-scale eddies, lack of subgrid-scale vertical convection, too high salt inputs to Southern Ocean, and too high vertical diffusivities in the main thermocline, all have the potential to reduce the heat flux out of the Southern Ocean and the poleward transport of heat by the southern hemisphere oceans. These changes are in the right sense to bring the model predictions into agreement with the observations (Figure 2.5), and as previously mentioned, we expect APO to be particularly sensitive to heat flux-driven

solubility changes. Toggweiler and Samuels [1995] point out that sea-to-air heat fluxes in the Weddell and Ross Seas predicted by GFDL- and LSG-based models can be twice as large as indicated by observations. Whether the result shown in Figure 2.5 is symptomatic of solely a problem with the physical ocean models or not, efforts to improve the models' representation of heat fluxes are needed to improve their chemical flux predictions.

While potential problems in the physical ocean models fit with the observed discrepancies, the biological parameterizations themselves may also contribute to the disagreement. In the case of HAMOCC3.1, basing the calculation of primary productivity on one nutrient, PO_4, may lead to an overestimation of production in high-nutrient, low-chlorophyll regions where other nutrients have a limiting effect. In the case of the POBM and LLOBM parameterizations, if the model-predicted regions of upwelling are spatially offset from those in the real ocean, forcing model PO_4 concentrations to agree with local observations will lead to spurious production in these regions. Also, Six and Maier-Reimer [1996] have shown that the inclusion of a plankton model in HAMOCC3.1, which the tested versions of POBM and LLOBM are without, significantly altered the distribution of export production. Misrepresentation of hemispheric biological biases, such as enhanced iron fertilization in the northern hemisphere, could also lead to errors in the predicted meridional CO_2 and O_2 variations (Weber et al., manuscript in preparation, 1998). However, because of the counteracting effect of biological CO_2 and O_2 fluxes on APO, errors in the biological

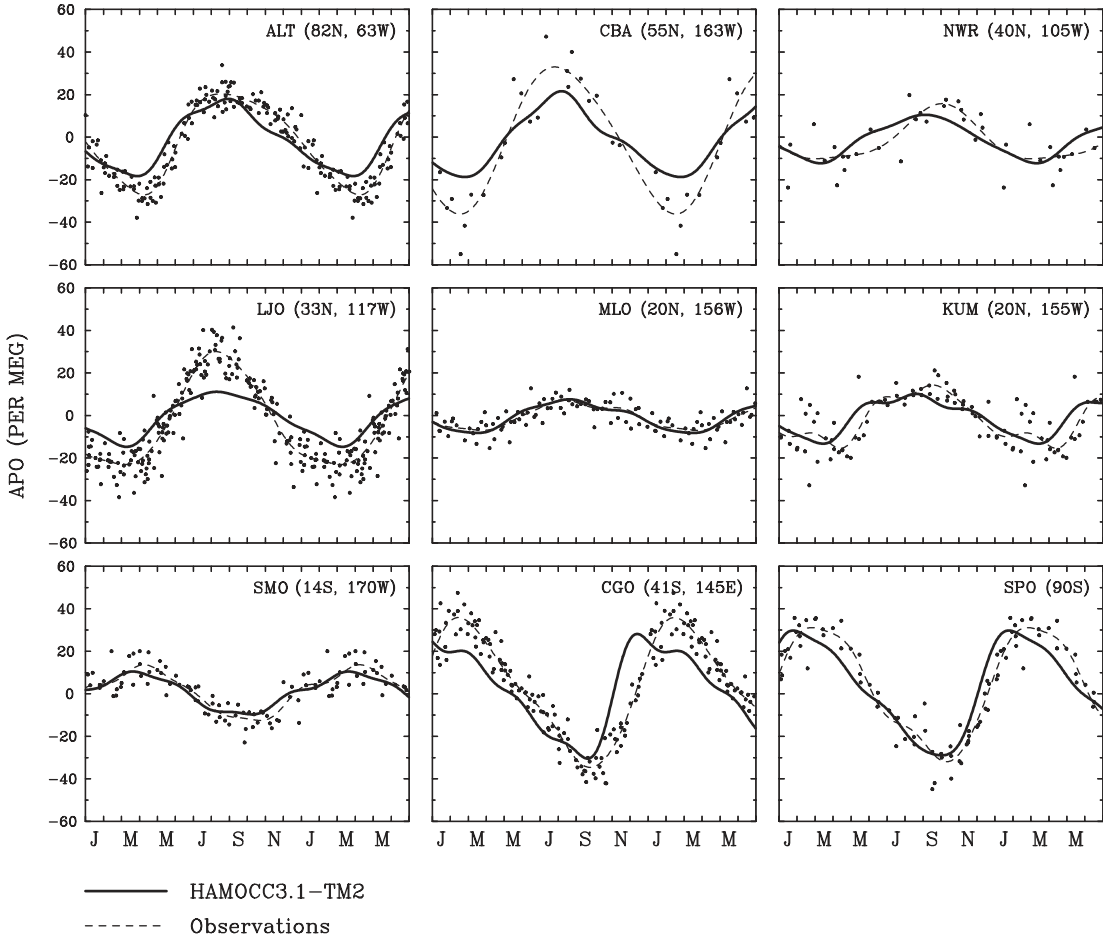

Figure 2.8. Seasonal variations in APO observed and predicted by HAMOCC3.1-TM2 for all of the stations except Macquarie Island. Observations from several years are plotted in one climatological year and have not been corrected for CO and CH_4. Lines are four-harmonic fits to the observations and HAMOCC3.1-TM2 predictions, except at Cold Bay and Niwot Ridge, where two-harmonic fits are used.

components of these models are less likely to produce the large discrepancies seen in Figure 2.5.

We can further test HAMOCC3.1 by comparing the predicted seasonal variations in APO to those observed at our stations. Figure 2.8 shows this comparison for all of the stations except Macquarie Island. As Figure 2.8 shows, the combined HAMOCC3.1-TM2 model does a remarkably good job of reproducing the phase and amplitudes of the observed cycles. Figure 2.8 confirms the favorable O_2/N_2 comparison at Cape Grim presented by Six and Maier-Reimer [1996]. The model predicts a slightly advanced phase at Alert, Niwot Ridge, Kumukahi, Cape Grim, and South Pole, and underestimates the amplitude at Cold Bay. The discrepancies seen at La Jolla are possibly related to the selective sampling procedure used at this station which is not duplicated in the model [Keeling *et al.*, 1998b]. The results shown in Figure 2.8 indicate that HAMOCC3.1-TM2 can place good constraints on seasonal oceanic new production and suggest that the APO discrepancies between HAMOCC3.1-TM2 and the observations shown in Figure 2.5 are not due to the seasonal representation of the plankton model.

2.9 Conclusion

We have presented observations of atmospheric potential oxygen, a derived tracer based on the sum of O_2 and CO_2, which show a strong interhemispheric gradient decreasing to the north. Our use of an atmospheric transport model to test air-sea

fluxes from global ocean carbon cycle models has shown that the current versions of three ocean models, POBM, HAMOCC3.1, and LLOBM, are underestimating the southward transport of the sum of CO_2 and O_2 in the oceans. Although uncertainties in modeled atmospheric transport and the representation of ocean biological fluxes may be significant, the discrepancies between modeled and observed APO variations appear most consistent with deficiencies in the underlying physical ocean models. Coarse-resolution ocean models such as POBM, HAMOCC3.1, and LLOBM are known to inadequately represent subgrid-scale isopycnal eddy mixing and subgrid-scale vertical convection and to overestimate brine inputs to the Southern Ocean and vertical diffusivities in the main thermocline. These deficiencies are thought to contribute to the unrealistic formation and overturning of deep waters in the models, which leads to significant discrepancies with observationally derived estimates of ocean heat transport.

The large disagreement shown in Figure 2.5 may be less surprising when one considers that climate simulations, using similar ocean models coupled to atmospheric global climate models, have required significant air-sea energy flux adjustments to maintain a realistic model state [Manabe *et al.*, 1991]. In this study, we have coupled ocean and atmosphere models chemically and appear to require analogous chemical flux adjustments to reproduce the observed state. The excessive uptake of APO by the Southern Ocean and too low uptake in the far Northern Oceans indicated in Figure 2.5 has implications for estimates of regional uptake of anthropogenic CO_2. Our results are consistent with those of Gruber *et al.* [1998], who found that POBM significantly

overestimates the observed inventory of anthropogenic CO_2 south of 50°S. A decrease in the Southern Ocean CO_2 uptake would also improve agreements with atmospheric CO_2 observations which indicate a CO_2 source in this region [Tans *et al.*, 1990].

Efforts are currently underway to improve simulations of large-scale ocean circulation and deep water formation and their effect on heat and tracer transports. Future comparisons to APO will benefit from the extension of our current O_2 measurement records and the addition of O_2 measurements targeting sensitive regions. Especially helpful would be additional stations south of 40°S, across the Equatorial Pacific, and closer to the North Atlantic region. If uncertainties in the physical components of the ocean models can be reduced, the comparison to APO observations will provide an even better test of the models' biological parameterizations. Global ocean carbon cycle models which accurately predict spatial and temporal variations in APO have the potential to significantly advance our understanding of regional and global carbon budgets.

This chapter appeared in full as

Stephens, B. B., R. F. Keeling, M. Heimann, K. D. Six, R. Murnane, and K. Caldeira, Testing global ocean carbon cycle models using measurements of atmospheric O_2 and CO_2 concentration, *Global Biogeochemical Cycles*, *12*, 213-230, 1998.

I was the primary investigator and lead author for this paper, and conducted all of the analyses presented therein. Chapter 7 includes an update to the discussion and conclusions of this chapter based on more recent observations.

2.10 References

Anderson, L. A., and J. L. Sarmiento, Global ocean phosphate and oxygen simulations, *Global Biogeochem. Cycles, 9,* 621-636, 1995.

Andres, R. J., G. Marland, T. Boden, and S. Bischoff, Carbon dioxide emissions from fossil fuel combustion and cement manufacture 1751-1991 and an estimate of their isotopic composition and latitudinal distribution, in *1993 Global Change Institute,* edited by T. Wigley and D. Schimel, in press, Cambridge Univ. Press, New York, 1999.

Bacastow, R., and E. Maier-Reimer, Dissolved organic carbon in modeling oceanic new production, *Global Biogeochem. Cycle*s, *5,* 71-85, 1991.

Boning, C. W., W. R. Holland, F. O. Bryan, G. Danabasoglu, and J. C. McWilliams, An overlooked problem in model simulations of the thermohaline circulation and heat transport in the Atlantic Ocean, *J. Clim., 8,* 515-523, 1995.

Brewer, P. G., C. Goyet, and D. Dyrssen, Carbon dioxide transport by ocean currents at 25° N latitude in the Atlantic Ocean, *Science, 246,* 477-479, 1989.

Broecker, W. S., The great global conveyor, *Oceanography, 2,* 79-89, 1991.

Broecker, W. S., and T.-H. Peng, Interhemispheric transport of carbon dioxide by ocean circulation, *Nature, 356,* 587-589, 1992.

Danabasoglu, G., J. C. McWilliams, and P. R. Gent, The role of mesoscale tracer transports in the global ocean circulation, *Science, 264,* 1123-1126, 1994.

Dlugokencky, E. J., P. M. Lang, K. A. Masarie and L. P. Steele, Atmospheric CH_4 records from sites in the NOAA/CMDL air sampling network, in *Trends '93: A Compendium of Data on Global Change,* edited by T. A. Boden, et al., *ORNL/CDIAC Rep. 65,* pp. 274-350, Carbon Dioxide Inf. Anal. Cent., Oak Ridge Nat. Lab., Oak Ridge, Tenn., 1994.

Döös, K., and D. J. Webb, The Deacon cell and the other meridional cells of the Southern Ocean, *J. Phys. Oceanogr., 24,* 429-442, 1994.

Duffy, P. B., K. Caldeira, J. Selvaggi, and M. I. Hoffert, Effects of subgrid-scale mixing parameterizations on simulated distributions of natural ^{14}C, temperature, and salinity in a three-dimensional ocean general circulation model, *J. Phys. Oceanogr., 27,* 498-523, 1997.

Enting, I. G., and J. V. Mansbridge, Seasonal sources and sinks of atmospheric CO_2: Direct inversion of filtered data, *Tellus, Ser. B, 41*, 111-126, 1989.

Enting, I. G., C. M. Trudinger, and R. J. Francey, A synthesis inversion of the concentration and $\delta^{13}C$ of atmospheric CO_2, *Tellus, Ser. B, 47*, 35-52, 1995.

Erickson, D. J., P. J. Rasch, P. P. Tans, P. Friedlingstein, P. Ciais, E. Maier-Reimer, K. Six, C. A. Fischer, and S. Walters, The seasonal cycle of atmospheric CO_2: A study based on the NCAR Community Climate Model (CCM2), *J. Geophys. Res., 101*, 15079-15097, 1996.

Gent, P. R., and J. C. McWilliams, Isopycnal mixing in ocean circulation models, *J. Phys. Oceanogr., 20*, 150-155, 1990.

Gruber, N., J. L. Sarmiento, and T. F. Stocker, An improved method for detecting anthropogenic CO_2 in the oceans, *Global Biogeochem. Cycles, 10*, 809-837, 1996.

Gruber, N., Anthropogenic CO_2 in the Atlantic Ocean, *Global Biogeochem. Cycles, 12*, 165-191, 1998.

Heimann, M., The global atmospheric tracer model TM2, *Tech. Rep. 10*, 53 pp., Dtsch. Klimarechenzentrum, Hamburg, Germany, 1995.

Heimann, M., and C. D. Keeling, A three-dimensional model of atmospheric CO_2 transport based on observed winds, 2, Model description and simulated tracer experiments, in *Aspects of Climate Variability in the Pacific and Western Americas, Geophys. Monogr. Ser.*, vol. 55, edited by D. H. Peterson, pp. 237-275, AGU, Washington D. C., 1989.

Heimann, M., and E. Maier-Reimer, On the relations between the oceanic uptake of CO_2 and its carbon isotopes, *Global Biogeochem. Cycles, 10*, 89-110, 1996.

Keeling, C. D., R. B. Bacastow, A. F. Carter, S. C. Piper, T. P. Whorf, M. Heimann, W. G. Mook, and H. Roeloffzen, A three-dimensional model of atmospheric CO_2 transport based on observed winds, 1, Analysis of observational data, in *Aspects of Climate Variability in the Pacific and Western Americas, Geophys. Monogr. Ser.*, vol. 55, edited by D. H. Peterson, pp. 165-236, AGU, Washington D. C., 1989a.

Keeling, C. D., S. C. Piper, and M. Heimann, A three-dimensional model of atmospheric CO_2 transport based on observed winds, 4, Mean annual gradients and interannual variations, in *Aspects of Climate Variability in the Pacific and Western Americas, Geophys. Monogr. Ser.*, vol. 55, edited by D. H. Peterson, pp. 305-363, AGU, Washington D. C., 1989b.

Keeling, R. F., Development of an interferometric oxygen analyzer for precise measurement of the atmospheric O_2 mole fraction, Ph.D. thesis, 178 pp., Harvard Univ., Cambridge, Mass., 1988.

Keeling, R. F., and T.-H. Peng, Transport of heat, CO_2 and O_2 by the Atlantic's thermohaline circulation, *Philos. Trans. R. Soc. London Ser. B, 348*, 133-142, 1995.

Keeling, R. F., and S. R. Shertz, Seasonal and interannual variations in atmospheric oxygen and implications for the global carbon cycle, *Nature*, *358*, 723-727, 1992.

Keeling, R. F., R. G. Najjar, M. L. Bender, and P. P. Tans, What atmospheric oxygen measurements can tell us about the global carbon cycle, *Global Biogeochem. Cycles*, *7*, 37-67, 1993.

Keeling, R. F., S. C. Piper, and M. Heimann, Global and hemispheric CO_2 sinks deduced from changes in atmospheric O_2 concentration, *Nature*, *381*, 218-221, 1996.

Keeling, R. F., A. C. Manning, E. M. McEvoy, S. R. Shertz, Methods for measuring changes in atmospheric O_2 concentration and their application in southern hemisphere air, *J. Geophys. Res.*, *103*, 3381-3397, 1998a.

Keeling, R. F., B. B. Stephens, R. G. Najjar, S. C. Doney, D. Archer, and M. Heimann, Seasonal variations in the atmospheric O_2/N_2 ratio in relation to the kinetics of air-sea gas exchange, *Global Biogeochem. Cycles*, 12, 141-163, 1998b.

Law, R. M., I. Simmonds, and W. F. Budd, Application of an atmospheric tracer model to high southern latitudes, *Tellus Ser. B*, *44*, 358-370, 1992.

Levitus, S., Climatological atlas of the world ocean, *NOAA Prof. Pap. 13*, 173 pp., U.S. Dep. of Comm., Washington, D. C., 1982.

Maier-Reimer, E., Geochemical cycles in an ocean general circulation model: Preindustrial tracer distributions, *Global Biogeochem. Cycles*, *7*, 645-677, 1993.

Maier-Reimer, E., U. Mikolajewicz, and K. Hasselmann, Mean circulation of the Hamburg LSG OGCM and its sensitivity to the thermohaline surface forcing, *J. Phys. Oceanogr.*, *23*, 731-757, 1993.

Maier-Reimer, E., U. Mikolajewicz, and A. Winguth, Future ocean uptake of CO_2: Interaction between ocean circulation and biology, *Clim. Dyn.*, *12*, 711-721, 1996.

Manabe, S., R. J. Stouffer, M. J. Spelman, and K. Bryan, Transient response of a coupled ocean-atmosphere model to gradual changes of atmospheric CO_2, I, Annual mean response, *J. Clim.*, *4*, 785-818, 1991.

Marland, G., R. M. Rotty, and N. L. Treat, CO_2 from fossil fuel burning: Global distribution of emissions, *Tellus Ser. B*, *37*, 243-258, 1985.

McDougall, T. J., A. C. Hirst, M. H. England, and P. C. McIntosh, Implications of a new eddy parameterization for ocean models, *Geophys. Res. Lett.*, *23*, 2085-2088, 1996.

Najjar, R.G., Simulations of the phosphorous and oxygen cycles in the world ocean using a general circulation model, Ph.D. thesis, 190 pp., Princeton Univ., Princeton, N. J., 1990.

Najjar, R. G., J. L. Sarmiento, and J. R. Toggweiler, Downward transport and the fate of organic matter in the ocean: Simulations with a general circulation model, *Global Biogeochem. Cycles*, *6*, 45-76, 1992.

Novelli, P. C., L. P. Steele, and P. P. Tans, Mixing ratios of carbon monoxide in the troposphere, *J. Geophys. Res.*, *97*, 20731-20750, 1992.

Sarmiento, J. L., and C. Le Quéré, Oceanic carbon dioxide uptake in a model of century-scale global warming, *Science*, *274*, 1346-1350, 1996.

Sarmiento, J. L., J. R. Toggweiler, and R. Najjar, Ocean carbon-cycle dynamics and atmospheric pCO_2, *Philos. Trans. R. Soc. London Ser. A*, *325*, 3-21, 1988.

Sarmiento, J. L., R. D. Slater, M. J. R. Fasham, H. W. Ducklow, J. R. Toggweiler, and G. T. Evans, A seasonal three-dimensional ecosystem model of nitrogen cycling in the North Atlantic euphotic zone, *Global Biogeochem. Cycles*, *7*, 417-450, 1993.

Sarmiento, J. L., R. Murnane and C. Le Quéré, Air-sea CO_2 transfer and the carbon budget of the North Atlantic, *Philos. Trans. R. Soc. London Ser. B*, *348*, 211-219, 1995.

Severinghaus, J. P., Studies of the terrestrial O_2 and carbon cycles in sand dune gases and in Biosphere 2, Ph.D. thesis, 148 pp., Columbia Univ., New York, 1995.

Six, K., and E. Maier-Reimer, Effects of plankton dynamics on carbon fluxes in an ocean general circulation model, *Global Biogeochem. Cycles*, *10*, 559-583, 1996.

Takahashi, T., T. T. Takahashi, and S. C. Sutherland, An assessment of the role of the North Atlantic as a CO_2 sink, *Philos. Trans. R. Soc. London Ser. B, 348*, 143-152, 1995.

Tans, P. P., I. Y. Fung, and T. Takahashi, Observational constraints on the atmospheric CO_2 budget, *Science*, *247*, 1431-1438, 1990.

Toggweiler, J. R., and B. Samuels, New radiocarbon constraints on the upwelling of abyssal water to the ocean's surface, in *The Global Carbon Cycle*, edited by M. Heimann, *NATO ASI Ser.*, vol. I 15, pp. 333-366, 1993.

Toggweiler, J. R., and B. Samuels, Effect of sea ice on the salinity of Antarctic bottom waters, *J. Phys. Oceanogr., 25*, 1980-1997, 1995.

Toggweiler, J. R., K. Dixon, and K. Bryan, Simulations of radiocarbon in a coarse-resolution world ocean model, 1, Steady state prebomb distributions, *J. Geophys. Res., 94*, 8217-8242, 1989a.

Toggweiler, J. R., K. Dixon, and K. Bryan, Simulations of radiocarbon in a coarse-resolution world ocean model, 2, Distribution of bomb-produced carbon 14, *J. Geophys. Res., 94*, 8243-8264, 1989b.

Veronis, G., The role of models in tracer studies, in *Numerical Models of the Ocean Circulations*, pp. 133-146, Natl. Acad. of Sci., Washington, D. C., 1975.

Volk, T., and M. I. Hoffert, Ocean carbon pumps: Analysis of relative strengths and efficiencies in ocean-driven atmospheric CO_2 changes, in *The Carbon Cycle and Atmospheric CO_2: Natural Variations Archean to Present, Geophys. Monogr. Ser.*, vol. 32, edited by E. T. Sundquist and W. S. Broecker, pp. 99-110, AGU, Washington D. C., 1985.

Wunsch C., D. X. Hu, and B. Grant, Mass, heat, salt, and nutrient fluxes in the South Pacific Ocean, *J. Phys. Oceanogr., 13*, 725-753, 1983.

Chapter 3

Vacuum Ultraviolet Oxygen Analyzer

Abstract

I have developed an instrument for making continuous ppm-level measurements of atmospheric oxygen concentration, which has a precision comparable to existing laboratory instruments and can be transported to and operated from research ships and remote field stations. This instrument detects changes in oxygen by the absorption of vacuum ultraviolet (VUV) radiation as it passes through a flowing gas stream. To do this, it uses the 147 nm line produced by a radio-frequency powered xenon lamp, detected by solar-blind cesium iodide photodiodes. The instrument has a precision of 6 per meg O_2 for a discrete 10-second measurement, 1 per meg for a 5-minute average measurement, and agrees with other methods to ± 3 per meg. A moderate sensitivity of the instrument to motion results in an increase in the 5-minute precision to a typical at-sea value of 2.5 per meg. These high levels of precision are a result of establishing a large VUV absorption coefficient, very low-noise amplification of the consequently small photodiode signals, and rapid switching between sample and reference gases. The external reproducibility depends critically on careful gas handling to eliminate potential sources of fractionation. The precision and portability of this VUV analyzer give it many biogeochemical applications. In this chapter I describe the instrument and its development in detail and show laboratory and field results that demonstrate its performance.

3.1 Introduction

The development of an interferometric technique by Keeling [1988] provided a means of measuring atmospheric O_2 with a precision of a few per meg (see Equation 3.1), and first allowed the detection of spatial, seasonal, and interannual O_2 variations. More recently, Bender *et al.* [1994] have demonstrated measurements of a similar precision using a stable-isotope mass spectrometer. The use of these techniques on flask samples collected from a global network of stations has led to new insights into the carbon cycle that were not possible through measurements of CO_2 alone. The constraints placed by the observed atmospheric potential oxygen (APO) gradients presented in Chapter 2 are one such example. While the comparisons between these observations and models revealed significant discrepancies, there were large gaps in the long-term flask sampling network, particularly at equatorial and high southern latitudes, such that some of the more extreme model predictions could not be directly tested.

One limitation of the interferometric and mass-spectrometric methods is that the size of the instruments prohibits their field use, which consequently limits the spatial resolution of their measurements to that which is feasible through flask sampling. Field-based measurements from continuous analyzers have the potential to significantly extend the spatial and temporal resolution of existing atmospheric O_2 measurements, thus helping to refine the constraints in Chapter 2 and promising new insights into biogeochemical cycling on even smaller time and space scales. Manning

et al. [submitted to Global Biogeochemical Cycles, 1998] have recently developed a paramagnetic analyzer which is well-suited for continuous measurements at remote field-stations. This instrument is very motion-sensitive, however, so that it cannot make measurements from a moving platform such as a ship or airplane.

The VUV instrument described here has a precision comparable to, and a temporal resolution significantly higher than, these other methods. It is also relatively motion-insensitive, and can be shipped easily between field sites. This makes it particularly fit for improving upon the spatial resolution of existing flask measurements, specifically by filling in gaps in the meridional atmospheric O_2 gradient. With this goal in mind, I have successfully implemented the VUV instrument on ships in the equatorial Pacific and the Southern Ocean as described in Chapters 4 and 5. I have also used this instrument to measure atmospheric O_2 variations for a month during summer at Harvard Forest, Massachusetts [Stephens *et al*., manuscript in preparation, 1999]. After describing the instrument, I will show some data to illustrate its performance in these different field settings. I include developmental information where I feel it would benefit future investigators using this technique.

3.2 Instrument Theory

The absorption of VUV radiation was first used to measure atmospheric O_2 almost 30 years ago [Kaplan *et al.*, 1971]. However, there have been few

improvements to the technique since then [Wong, 1978; Kronick *et al.*, 1980, Wong, 1986], and its demonstrated precision is much larger than the geochemically interesting variations of ~0.0001%. Because of the high O_2 concentration in the atmosphere of 21%, ppm-level variations in O_2 mole fraction are much more difficult to measure than for trace gases. For example, a photosynthesizing tree that removes one CO_2 molecule per million molecules in an air parcel and releases an equivalent number of O_2 molecules will leave a 1/350 or 0.3% signal in the background CO_2 concentration, but only a 1/209500 or 0.00048% signal in O_2.

3.2.1 A Word on Units

Presently, it is not possible to determine the absolute mole fraction of O_2 to one ppm, whereas it is possible to measure relative changes in O_2 at this level. To accommodate these small signals, and to provide a framework that is insensitive to the diluting affects of CO_2, variations in atmospheric O_2 are commonly expressed as deviations in the O_2/N_2 ratio relative to a reference, where

$$\delta(\mathrm{O_2/N_2})\ (\text{per meg}) = \left(\frac{(\mathrm{O_2/N_2})_{sample}}{(\mathrm{O_2/N_2})_{reference}} - 1 \right) \times 10^6 \qquad (3.1)$$

Thus, for constant N_2, one per meg is approximately equivalent to a one-millionth relative change in O_2 mole fraction. All measurements presented here are referenced to a suite of gas cylinders, defined to have an average O_2/N_2 ratio of 0.0 per meg on the Scripps O_2 scale [Keeling *et al.*, 1998].

While mass spectrometers measure the O_2/N_2 ratio directly, interferometric, paramagnetic, and optical instruments all measure signals more directly related to the mole fraction of O_2, which is also sensitive to variations in other gases. The tree mentioned above would change the O_2 mole fraction in the parcel by 1 μmole $mole^{-1}$ or its O_2/N_2 ratio by 4.8 per meg. There is an important distinction to be made, however, when processes change both O_2 and the total number of molecules in an air parcel. If instead of being released during photosynthesis, the same number of O_2 molecules were outgassed from the ocean without an opposing CO_2 flux, the O_2 mole fraction would change by $(209501/1000001-209500/1000000) \times 10^6$ or 0.79 μmol mol^{-1}, whereas the change in per meg would be the same. Similarly, an equivalent outgassing of CO_2 would change the O_2 mole fraction by $(209500/1000000-209500/1000001) \times 10^6$ or -0.21 μmol mol^{-1}. To account for such diluting effects on O_2, it is necessary to simultaneously measure and make a correction for variations in CO_2 [Keeling *et al.*, 1998]. In addition to the effect of dilution, CO_2 has an additional interference effect on the VUV measurement. All per meg values reported here have been corrected for CO_2 interference and dilution to a reference concentration of 363.29 ppm, corresponding to the average CO_2 concentration in the primary Scripps O_2/N_2 reference cylinders [Keeling *et al.*, 1998]. Natural variations in argon and other species are small enough that they can be ignored in most applications.

Throughout this chapter, I refer to variations in instrument parameters, such as sample-cell pressure or detector output, in relative units of ppm. Variations in sample-cell pressure scale as 1 ppm-pressure = 1 per meg O_2. The scaling of the detector

output varies depending on the amount of light absorption, from 1.4 to 2.2 ppm-volts = 1 per meg O_2 for the conditions presented here (1 ppm-volt = $(V / V_{ave} - 1) \times 10^6$).

3.2.2 Detection Limits

Natural variations in atmospheric oxygen include interannual trends of around -10 per meg yr^{-1}, interhemispheric differences of 20 to 40 per meg, and seasonal cycle amplitudes of up to 100 per meg [Keeling *et al.*, 1993]. To resolve these features, and to distinguish their terrestrial and oceanic sources by comparison to CO_2 data, one must be able to measure O_2 at a precision of a few per meg. Consequently, any viable detection system must be sensitive to variations in O_2, and free of noise, at a relative level close to one ppm. The absorption of ultraviolet radiation is well-suited to this task, as light sources can be made stable, light levels can be measured and signals amplified, and pressure in a flowing gas stream can be maintained, all at the ppm level.

The O_2 analyzer that I have developed measures the absorption of VUV radiation as it passes through a flowing air stream. For a light source, I use a radio frequency (RF) powered xenon lamp, which has a strong emission line in the Schumann-Runge continuum at 147 nm [Sampson, 1967]. Figure 3.1 shows the absorption cross-sections for O_2, CO_2, and H_2O, and the xenon emission spectrum in this region. Because O_2 is the primary atmospheric absorber at 147 nm, variations in

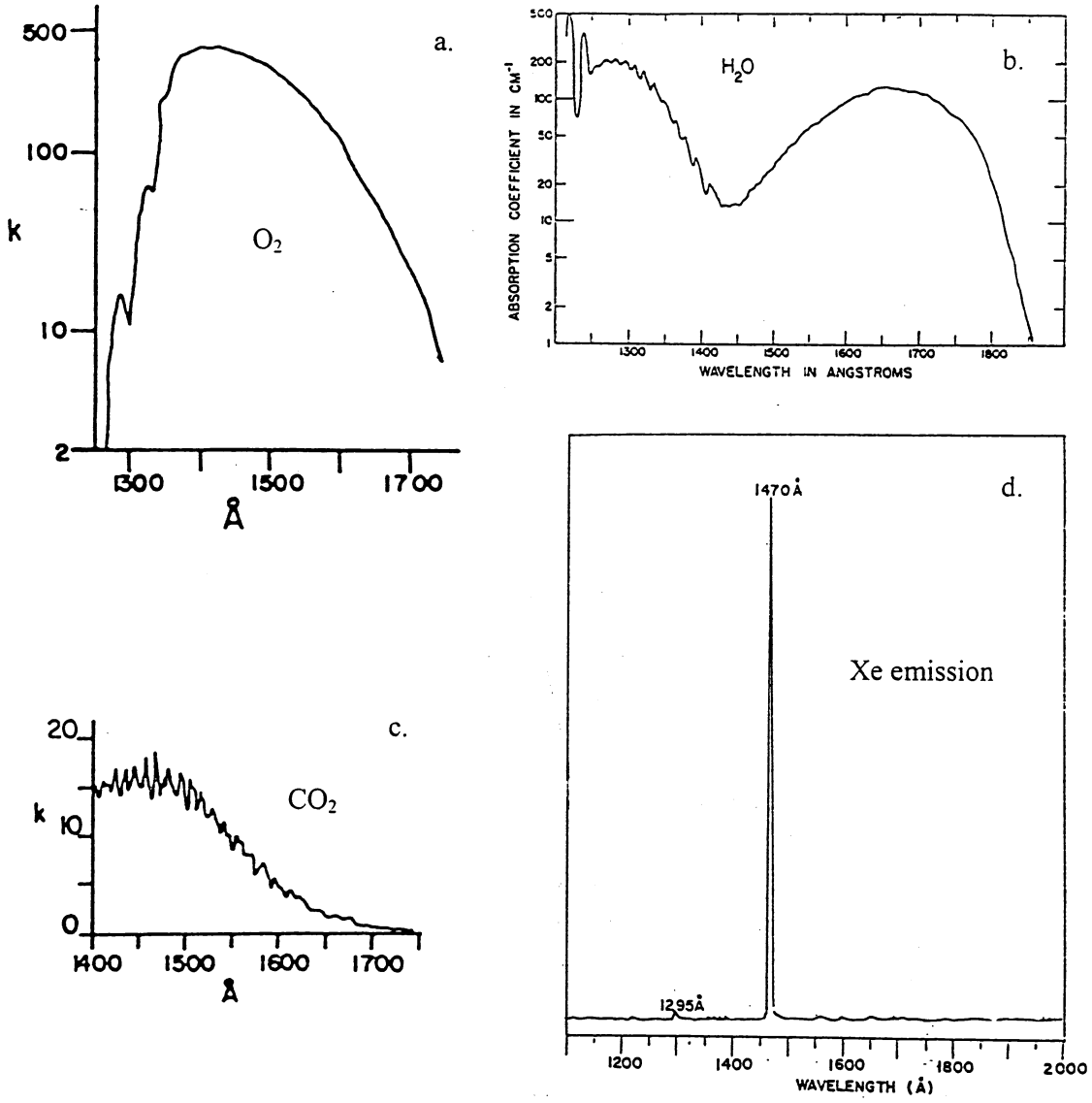

Figure 3.1 Vacuum ultraviolet absorption coefficients and xenon resonance lamp emission spectrum. Absorption coefficients are in units of atm^{-1} cm^{-1}, 0° C, base *e* and correspond to the value k in Equation 3.2. (a) O_2 from Watanabe *et al.* [1953], (b) H_2O from Watanabe and Zelikoff [1953], (c) CO_2 from Inn *et al.* [1953], and (d) emission spectrum from an electrodeless resonance xenon lamp, showing the intense resonance line at 1470 angstroms utilized by the VUV instrument [from Okabe, 1964].

absorption are related to the O_2 mole fraction (X_{O_2}) via the Beer-Lambert Law:

$$I = I_0 \exp[-k\ell P(T_0/T)X_{O_2}]$$

$$\text{or } I = I_0 \exp(-\alpha) \qquad (3.2)$$

which can also be expressed in differential form as

$$\Delta I/I = -\alpha(\Delta X_{O_2}/X_{O_2}) , \qquad (3.3)$$

where I is the transmitted light intensity, α the sensitivity, k the absorption coefficient of O_2 at one atmosphere, ℓ the path length, P the air pressure, T the air temperature, and $T_0 = 273.15$ K.

Equation 3.3 indicates that the response of the instrument to small changes in X_{O_2} will be linear. For O_2 absorption at 147 nm, departures from linearity over the natural range of variability are expected to be less than 0.1 per meg. However, there are potential interference effects from water vapor and CO_2, as shown in Figure 3.1. This published data indicates a CO_2 absorption coefficient at 147 nm that is approximately 5% of that for O_2. I have conducted independent measurements using the VUV instrument, which give a value of 4.9%. By pre-drying the sample air, I avoid having to correct for H_2O interference. However, after correcting for the CO_2 dilution effect, changes in CO_2 mole fraction will still appear to the VUV detector as changes in X_{O_2} of one twentieth the magnitude. I measure variations in the CO_2 concentration directly, and use these values to apply an interference correction to the O_2 measurements in addition to the CO_2 dilution correction.

To achieve the desired instrument sensitivity, it is necessary to use a path length and pressure corresponding to optically thick conditions. If $\alpha = 1$, then 63% of the light will be absorbed by the sample gas and a 1 ppm relative change (1 per meg) in X_{O_2} will result in a 1 ppm change in light intensity. Increasing the absorption to 86% will double the sensitivity, but there is a trade off with inherent noise at the resultantly low detector currents. In practice, available photodiodes have current limits around 100 nA, which translates into a ppm-precision detection requirement of 100 fA. Shot noise, which results from statistical uncertainty associated with counting a limited number of electrons, and Johnson noise, which results from random thermal motion in a resistor, can both be significant at these levels [Jenkins, 1987].

Figure 3.2 shows detector output under conditions of constant sample-gas flow for two different lamps described below. The sealed lamp curve (slope explained in Section 3.3.1) has a detrended root-mean-squared (rms) noise of 3.3 ppm at this 0.2 s resolution. In comparison, using the observed current of 64 nA gives a shot noise estimate of 3.4 ppm. This demonstrates that the detection and amplification circuitry, and the steady-state flow-control, are capable of performing near the shot noise limit. Johnson noise for these conditions should be less significant, at around 0.25 ppm.

For the 5-second switching scheme I employ, a critical statistic is the error on differences between 5-second means and the average for adjacent 5-second periods. To calculate these differences I use

$$\Delta_{5-\text{sec}} = \frac{\left[\overline{\mathrm{V}}_t - \left(\overline{\mathrm{V}}_{t-1} + \overline{\mathrm{V}}_{t+1}\right)/2\right]}{\overline{\mathrm{V}}_t} \tag{3.4}$$

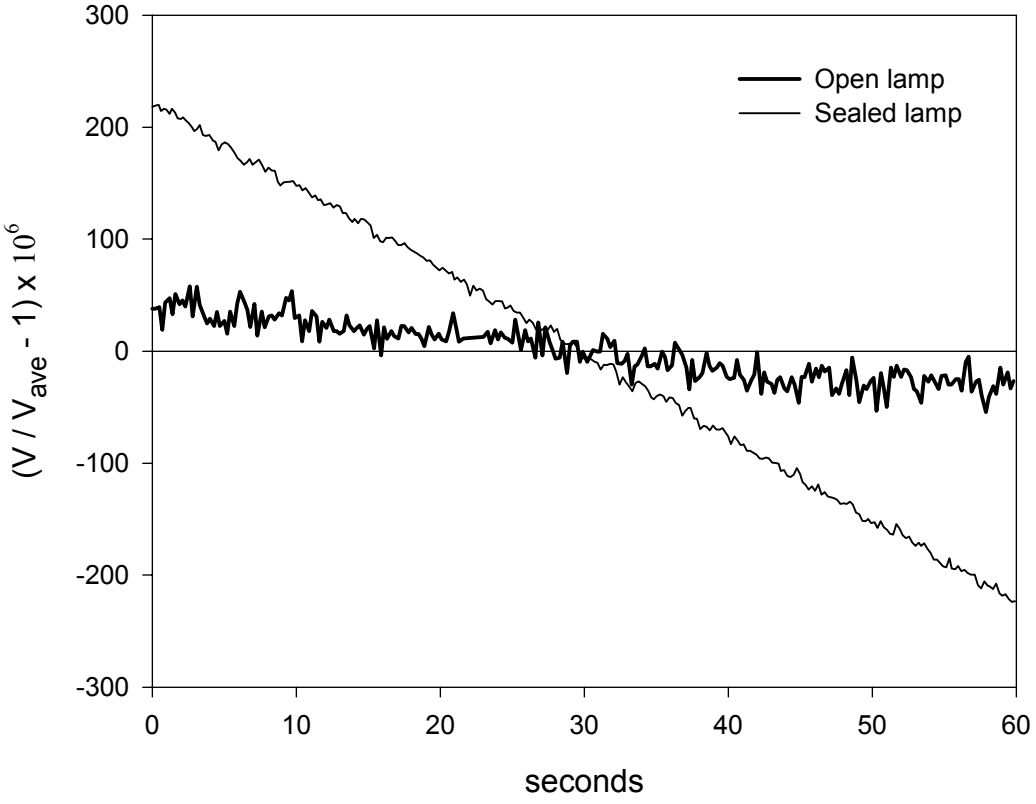

Figure 3.2 Output signals for sealed and open xenon lamps. For both curves, the light passed through a flowing gas stream before reaching a photodiode. The photodiode currents are amplified and converted to voltages using a feedback amplifier, then integrated over 0.2 s periods using a 6 1/2 digit voltmeter. Values are plotted as ppm-volts relative to the mean. The thin curve represents output using a sealed lamp and a sample-cell pressure of 50 torr ($\alpha = 1.4$). The mean signal for this curve is 8.0 V, corresponding to a photodiode current of 64 nA. The thick line represents output using an open lamp and sample-cell pressure of 80 torr ($\alpha = 2.2$), with a mean signal of 2.0 V, or 16 nA.

where the $\overline{V}$ terms represent consecutive 5-second means of the detector voltage. The sealed lamp curve in Figure 3.2 corresponds to an rms value for $\Delta_{5\text{-sec}}$ of 1.8 ppm. This value is significantly greater than the standard error of the intrinsic electrical noise of $3.3 / \sqrt{n} = 0.7$ ppm, indicating that other noise sources are important on this

longer time scale. This potential error of 0.7 ppm in signal, or 0.5 per meg O_2 for these conditions, is close to the theoretical limit for VUV absorption measurements at 10 second resolution. The actual $\Delta_{5\text{-sec}}$ rms error for the sealed lamp of 1.8 ppm, or 1.3 per meg O_2, is also only attainable under idealized conditions. The open lamp used for the field studies in Chapters 4 and 5 is considerably noisier, and under constant sample-gas flow conditions (Figure 3.2) produces a rms error on $\Delta_{5\text{-sec}}$ of 3.5 per meg O_2. As discussed below, pressure fluctuations from the switching scheme, and motion sensitivity in several components further increase this value.

3.3 Instrument Design

Because the desired instrument precision is very close to theoretical detection limits, the optical, electrical, and flow systems all must operate near their absolute performance limits. A considerable amount of testing was required to attain this optimization, and I describe the resulting configuration here. Without calibration gases, chiller, PC, and vacuum pumps, the current VUV instrument fits in a 6 feet × 19 inch instrument rack, and can be shipped without disassembly to any location. While this instrument design was successful in the field deployments presented in Chapters 4 and 5, there is still room for improvement and I outline several potential modifications later in this chapter.

3.3.1 Xenon Lamp

Producing resonance line emissions from a plasma lamp requires lamp-fill pressures on the order of a few torr. Low-pressure xenon lamps powered by direct current (DC) are commonly available, however earlier tests by W. Paplawsky (personal communication, 1996) showed that the short-term flicker in these lamps was greater than 50 ppm. An electrodeless lamp powered by a radio frequency (RF) field can be much quieter. The signals in Figure 3.2 are from RF lamps. The thin curve is from a sealed lamp containing 0.98 torr of helium and 0.02 torr of xenon, and gettered by a strip of activated zirconium/aluminum metal. The helium had improved the stability of the DC lamps, but I found later that it was unnecessary in an RF lamp.

This sealed lamp design had excellent output and stability characteristics, but it had a major drawback in its short lifetime. The thin curve in Figure 3.2 has a slope of -5 ppm s^{-1}. At this rate, the output from these sealed lamps decreased by a factor of 2 on a timescale of around 38 hours. This lamp degradation may have resulted from water or other contaminants outgassing from, or xenon attaching to, the glass walls. After failing to significantly improve upon the lamp lifetime using various gas fills, filling procedures, window sealing methods, and gettering devices, I switched to an open lamp with a continuous throughflow of xenon. The thick curve in Figure 3.2 is from this open lamp. Despite its increased short-term noise, this lamp is much better adapted for extended field work such as on an oceanographic cruise, because of its indefinite lifetime and the ability to control its output by adjusting the xenon pressure.

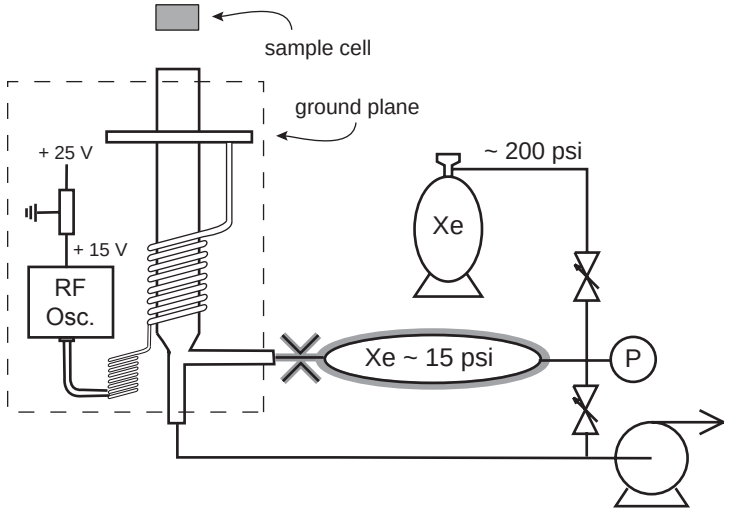

Figure 3.3 Xenon lamp gas-handling and power-supply schematic. Power-supply components shown include a 15 VDC voltage regulator, a 180 MHz RF oscillator and a coil of copper wire coupled to the lamp. The dashed line represents a 1/4-inch wall aluminum enclosure. The gas-handling components shown include a cylinder of xenon gas, two manual needle valves, a pressure gauge (P), a 250 ml storage volume and crimped capillary both insulated (grey shading), and a vacuum pump.

Figure 3.3 is a schematic of the gas handling and power supply configuration of the open xenon lamp. The lamp body consists of a 3" long by 1/2" diameter Pyrex tube fused to a sapphire window at one end, with two perpendicular 1/4" arms at the other end (Glass Contour, Laguna Beach, CA). To maintain a constant xenon pressure and flow, I bleed xenon from a 250 ml volume at ~ 15 psi, through a crimped capillary and into the lamp. A vacuum pump downstream of a needle valve pulls xenon from the lamp. I adjust this downstream needle valve so that the lamp pressure is ~ 0.3 torr. The capillary has a conductance such that the throughflow of xenon is ~ 0.02 ml STP min^{-1} at these pressures, corresponding to a flushing time of ~ 10 s. Although the

lamp output does exhibit a long-term drift resulting from the decreasing upstream xenon pressure, this is effectively removed by the switching and calibration scheme and the upstream volume can be occasionally refilled with xenon. It is necessary to insulate this volume and the capillary to avoid short-term lamp variability in response to temperature changes.

Figure 3.3 also illustrates the power supply for the lamp, which consists of a 15 W, 180 MHz RF oscillator (LCF Enterprises, Camarillo, CA) coupled to the lamp via a coil of copper magnet wire. I tuned the coil by varying the coil number, spacing, and orientation, and found an optimal shape similar to that used for chlorine lamps in ozone research (D. Toohey, personal communication, 1996) with 8 tightly spaced coils around the lamp and 8 smaller coils offset and parallel to the lamp. This double coil is connected between the RF oscillator output and a ground plane. To avoid potential problems of window degradation, I positioned the ground plane 2" from the lamp window to limit the forward advance of the plasma. I supply power to the RF oscillator from a 25 VDC power supply coupled to a 15 VDC voltage regulator, which I found significantly improved the short-term lamp stability. The lamp and RF oscillator are enclosed in an aluminum box that shields other instrument components from RF interference. This box has 1/4-inch thick walls, which provide adequate thermal inertia to the system without further insulation.

The cleanliness of the lamp with respect to VUV emission from non-xenon impurities can be checked by scanning over the O_2 pressure, $P \times X_{O_2}$. Figure 3.4 shows signal variations for a sealed and gettered lamp and for the open lamp, obtained

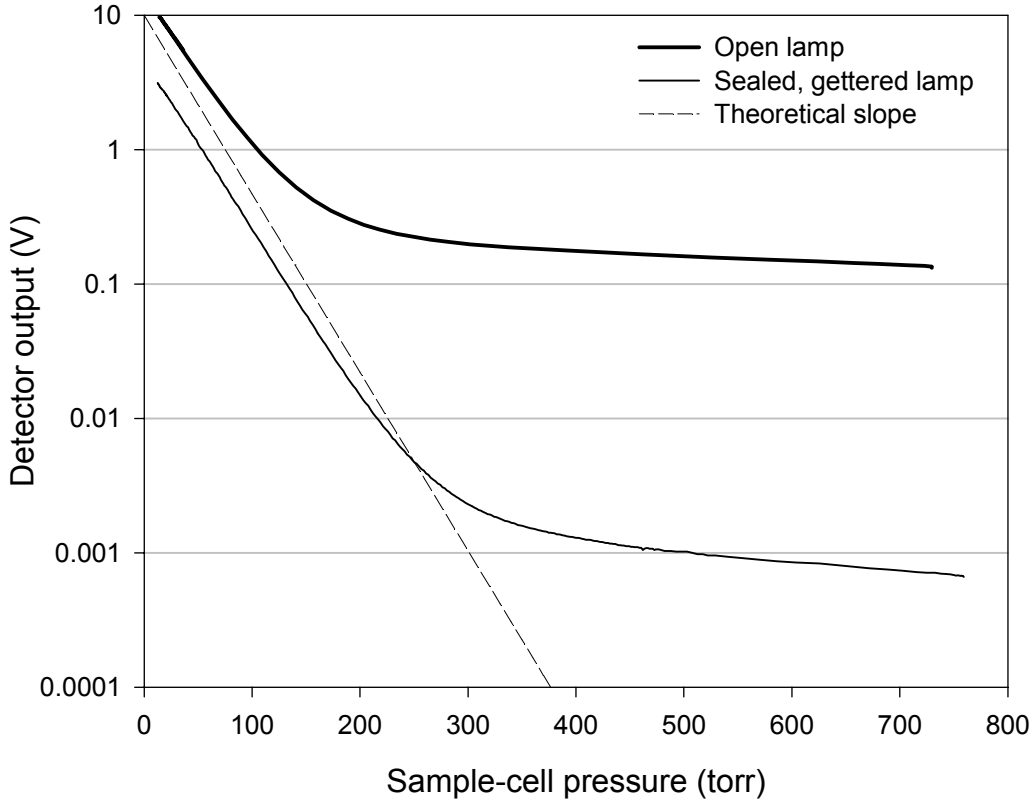

Figure 3.4 Pressure scan for sealed and gettered (thin curve) and open (thick curve) xenon lamps. The detector output signals decrease as the pressure in the air between the lamp and photodiode is increased. The open lamp output in this figure and in Figure 3.2 are from the same lamp, but the sealed lamp outputs are not. The straight line represents a theoretical slope generated using Equation 3.2 with I_0 = 10 V, k = 320 cm^{-1} atm^{-1}, and ℓ = 3 mm.

by varying the pressure of the air in the 3 mm sample cell between the lamp and detector. On a log plot, for emission at a single wavelength, these curves should be linear. As the pressure increases, the sealed/gettered curve decreases linearly over 3 orders of magnitude before it finally flattens out. This flattening at high pressure reflects a contribution to signal absorption at a smaller cross section, probably associated with emission from an impurity such as water or hydrogen. Because the

open lamp is without a getter, its I vs. P curve flattens out at a lower pressure, reflecting a greater source from impurities. These impurities result in a difference between the slope of the open-lamp curve and that of a theoretical curve for a 147 nm O_2 absorption coefficient of 320 atm^{-1} cm^{-1} [Watanabe *et al*., 1953] (Figure 3.4). However, as described in the following section the optical configuration confines this non-xenon emission between 140 and 220 nm, where O_2 is still the primary absorber. Based on the open-lamp curve in Figure 3.4, these lamp impurities should only increase the non-linearity of the O_2 response by 0.01 per meg over the range of natural variability.

3.3.2 Signal Detection and Amplification

The initial instrument design called for a magnesium fluoride window to pass a fraction of the lamp output through a sample cell and then onto a detector, while reflecting the rest of the output directly onto a reference photodiode. This beamsplitter and extra detector were included so that fluctuations in the lamp output could be removed by ratioing the sample and reference signals. In practice however, the short-term lamp variability observed by the two photodiodes is uncorrelated, possibly because the noise is related to plasma motion and the photodiodes do not see exactly the same lamp cross-section. The second photodiode is still useful for detecting occasional lamp glitches that result from unidentified electrical noise, allowing the removal of these periods from the record, thus I have left it in place.

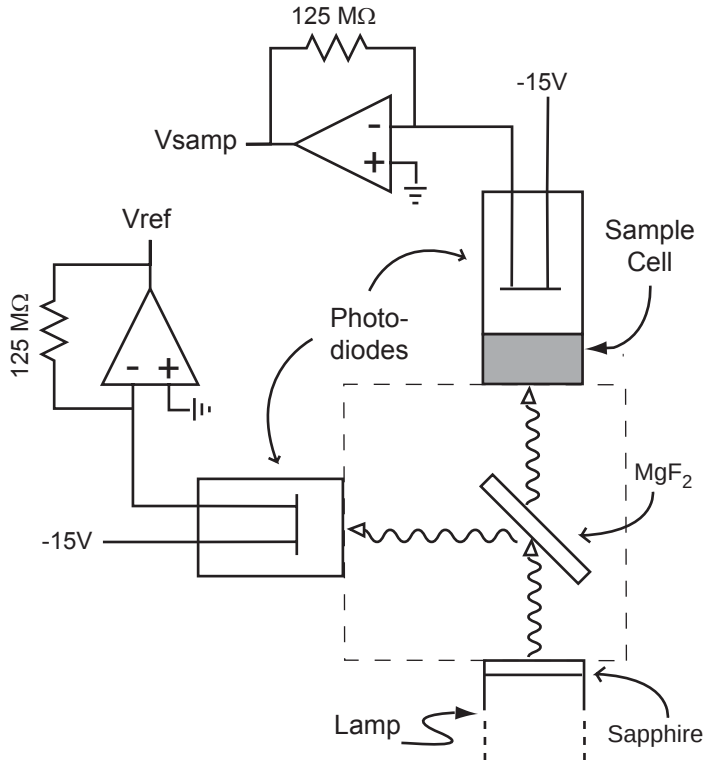

Figure 3.5 Optical and electronic signal-detection schematic. Optical components shown include the lamp with a sapphire window, a MgF_2 window used as a beamsplitter, and two photodiodes. The dashed line represents an evacuated space. The reference and sample photodiode currents are converted to voltages by two feedback amplifiers.

Figure 3.5 is a schematic of the optical and electrical configuration of the signal detection assembly. I use solar-blind cesium iodide photodiodes (Hamamatsu Corporation, Bridgewater, NJ) as detectors. These photodiodes are only sensitive to wavelengths between 110 and 220 nm and have a quantum efficiency of around 1% at 147 nm. The wavelength of the transmitted light is further constrained by the sapphire window on the lamp that effectively cuts out wavelengths shorter than 140 nm,

including the secondary xenon line at 130 nm (Figure 3.1d). At the operating sample-cell pressure, the photodiode currents are around 50 nA. To measure this signal to ppm-level precision using a conventional 6 1/2 digit voltmeter requires amplification by a factor of 10^8. To accomplish this, I use the feedback ammeter circuits shown in Figure 3.5. The low-noise op-amp (AD549LH) and the low temperature coefficient (5 ppm K^{-1}) of the 125 MOhm feedback resistor (Caddock Electronics, Riverside, CA) are critical in this design. As discussed above, this amplifier is capable of converting a 50 nA current to a 6.25 V signal with precision near the shot-noise limit for 0.2 second integrations. There is no filter capacitor in this circuit, as I found the inclusion of one did not improve the detector stability on the relevant time scales. Consequently, the amplifier has a very fast response time, with a RC constant around 0.05 seconds.

3.3.3 Gas Handling

The above components are all only stable to a ppm on relatively short time scales. Because of this, the instrument must rapidly switch between the sample and a reference gas to compensate for inherent signal drift, while at the same time maintaining pressure and flows in the sample cell constant to 1 ppm. Precision improves with shorter and shorter switching times, but pressure control eventually becomes too difficult and a higher fraction of signal is lost during the transitions. In consideration of these issues, I use a switching time of 5 seconds. The gas handling system must also provide for the cryogenic drying of air, for the automatic selection of multiple sample and calibration gases, and for greater flow rates through sample intake

tubes than through the instrument, all without producing any fractionation or transient surface effects. Figure 3.6 is a schematic of the gas handling system that I have designed to accomplish these tasks.

An absolute requirement for O_2 measurement stability is that all points in the gas handling system experience constant flow rates with unchanging pressure and moisture characteristics. This arrangement prevents transient surface adsorption-desorption effects, and the aliasing of diffusive O_2/N_2 gradients that form across temperature or pressure gradients such as through a cold trap or a needle valve [Keeling *et al*., 1998]. A diaphragm pump (Figure 3.6) pulls sample air at 2 L min^{-1} through multiple inlet lines, such as from the bow and stern of a ship or multiple heights in a forest. A set of solenoid valves selects air from one of these lines, which is delivered to the instrument by a separate diaphragm pump.

Desired field response times often require that gases be pulled through the intake lines at a rate much faster than that used by the instrument. To accommodate these rapid flows, a tee dumps most of the inlet gas out through a back-pressure regulator, and sends only 80 ml min^{-1} through the analyzer. Back-pressure regulators fractionate O_2 relative to N_2, so there is a 2 m loop of 1/4" tubing between the tee and the regulator to insure that any gradients resulting from this fractionation do not influence the small flow going to the analyzer. A. Manning (personal communication, 1998) has demonstrated that the combination of a tee and pump-induced air pulsations also fractionates O_2/N_2. As shown in Figure 3.6, there are two additional 2 m coils of

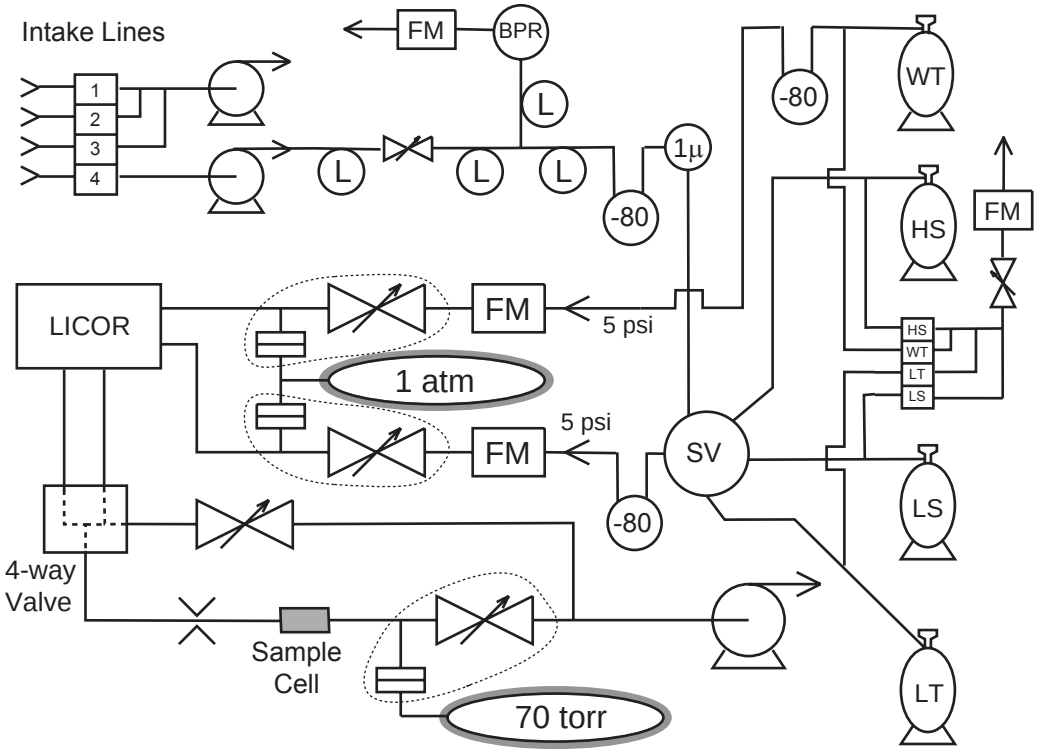

Figure 3.6 Gas handling schematic. From approximately upstream to downstream, the components shown include the intake solenoid valves (1-4), an exhaust pump and the instrument inlet pump, a 2 m loop of 1/4" tubing (L) and a needle valve after the inlet pump, a tee isolated by three additional 2 m loops of 1/4" tubing leading to a back-pressure regulator (BPR) and flowmeter (FM), four reference cylinders (WT, HS, LS, and LT) with solenoid purge valves leading to a needle valve and flowmeter, three cold-traps (-80), a 1 μm filter (1μ), a stream-selection valve (SV), two flowmeters, two feedback control valves and differential pressure gauges (within dotted loops) referenced to an insulated (grey shading) 1-atm volume, a LiCor NDIR CO_2 analyzer, a pneumatic 4-way valve, the sample cell with an upstream flow constriction and a downstream pressure control valve referenced to an insulated 70-torr volume, a bypass line with a manual needle valve, and an exhaust vacuum pump. The flow and pressure balancing scheme is further described in the text.

1/4" tubing and a needle valve between the diaphragm pump and the tee to minimize the magnitude of the air pulsations at the tee.

After this tee, the sample air passes through a preliminary cold trap, maintained at either -78 °C by dry ice or - 90 °C by a cryogenic chiller, and then through a 1.0 μm filter to remove any remaining particles. A rotary selector valve chooses between this sample air and several calibration gases. Immediately upstream of this valve, each calibration line is connected to a purge line and solenoid valve to allow flushing of the lines and regulators at times when they are not delivering air to the detector. Although at this point the sample air has been through one cold trap and the calibration gases have been chemically dried during preparation, they still have too much water for the VUV measurement (see Section 3.4.3 below), so the selected air stream is passed through a second cold trap before finally reaching the first active flow control assembly (Figure 3.6). A separate cylinder of reference gas, called the working tank (WT), continuously delivers air through another cold trap to a second flow control assembly. The back-pressure regulator and the reference cylinder regulators are set so that these two gas streams are at 5 psi. This pressure then drops to 1 atm as the gases pass through a pair of automatic needle valves that are adjusted by feedback flow controllers (MKS, Andover, MA). These flow controllers are referenced to 10-torr full scale differential pressure-gauges (MKS) which measure the difference in pressure between the sample lines and a pressure-reference volume held at 1 atm.

The sample or calibration gas and the WT gas next pass through the sample and reference cells, respectively, of a non-dispersive infrared (NDIR) CO_2 analyzer

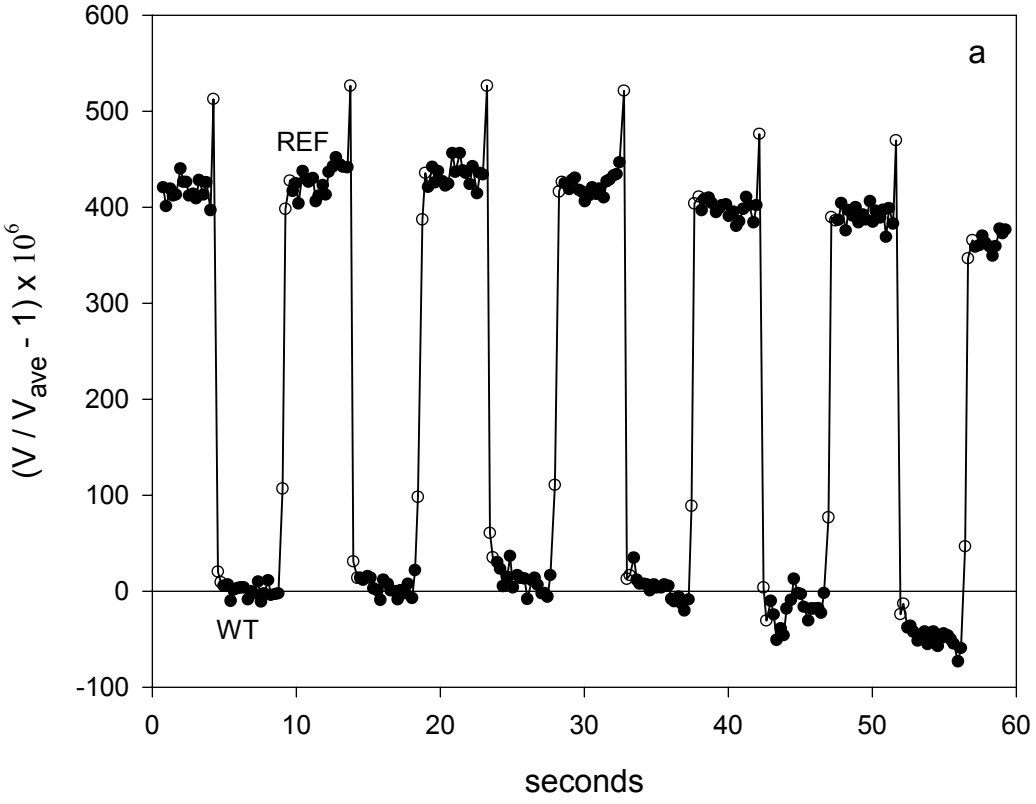

Figure 3.7 Example signals from 5-second switching scheme. (a) switching between WT and another reference gas (REF) on land, (b) switching between WT and sample gas on land (Harvard Forest), (c) switching between WT and sample gas at sea (equatorial Pacific), and (d) switching between WT and sample gas with the chiller temperature at -40°C, illustrating the potential problems from water contamination. In each figure, values are plotted in ppm-volts relative to the average signal for the first WT jog. Hollow symbols represent the first three points after each switch that are discarded in the standard data-workup program.

(LiCor, Lincoln, NE). These two gas streams are then pulled by a rotary-vane vacuum pump through a pneumatic 4-way valve (Micromass Ltd., UK). This valve directs one stream through the sample cell and the other through a bypass loop. A third pressure-reference, feedback-controller assembly adjusts a downstream needle valve to hold the sample cell pressure at 80 torr, while a manual needle valve on the bypass loop can be

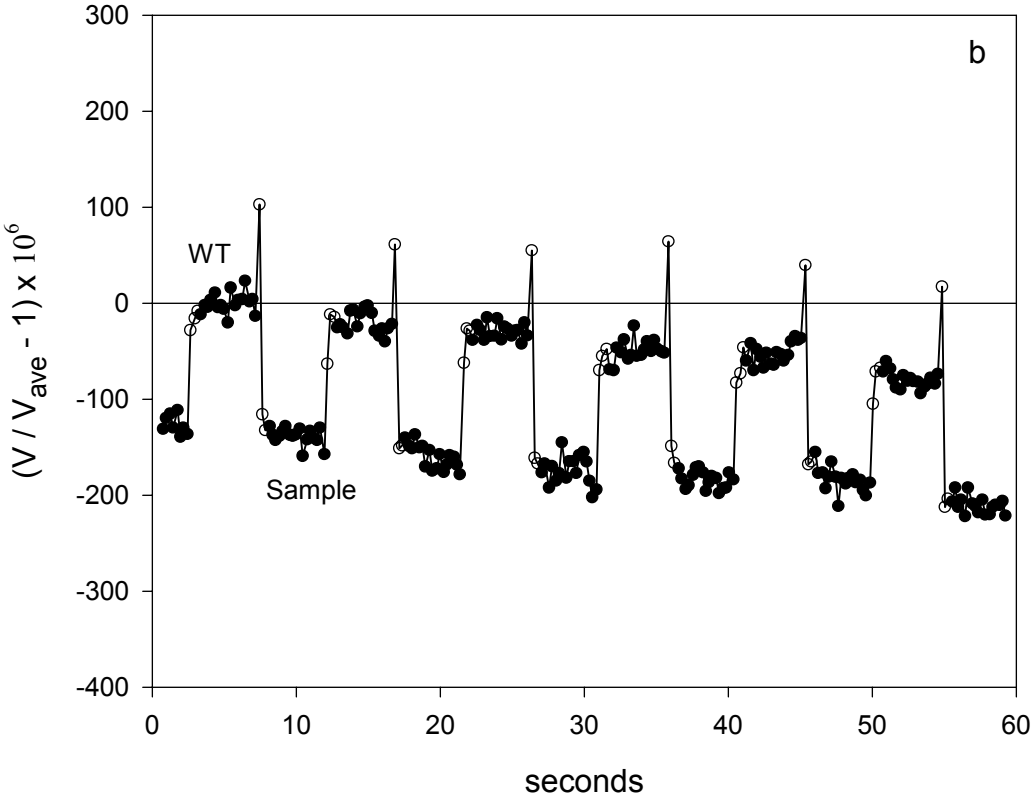

Figure 3.7 (continued)

adjusted to match the flows. This feedback assembly uses a 1-torr full scale differential pressure gauge (MKS) that allows short-term control to better than 10^{-4} torr. The 80 torr cell pressure corresponds to an instrument sensitivity α of 2.2 ppm-volts / per meg O_2. The two pressure-reference volumes (Figure 3.6), at 1 atm and 80 torr, are insulated against short-term temperature fluctuations.

Figure 3.7a shows the VUV signal while switching every 5 seconds between two calibration gases with an O_2/N_2 difference of ~ 250 per meg. The small internal volume and rapid switching capability of the 4-way valve are critical to the fast

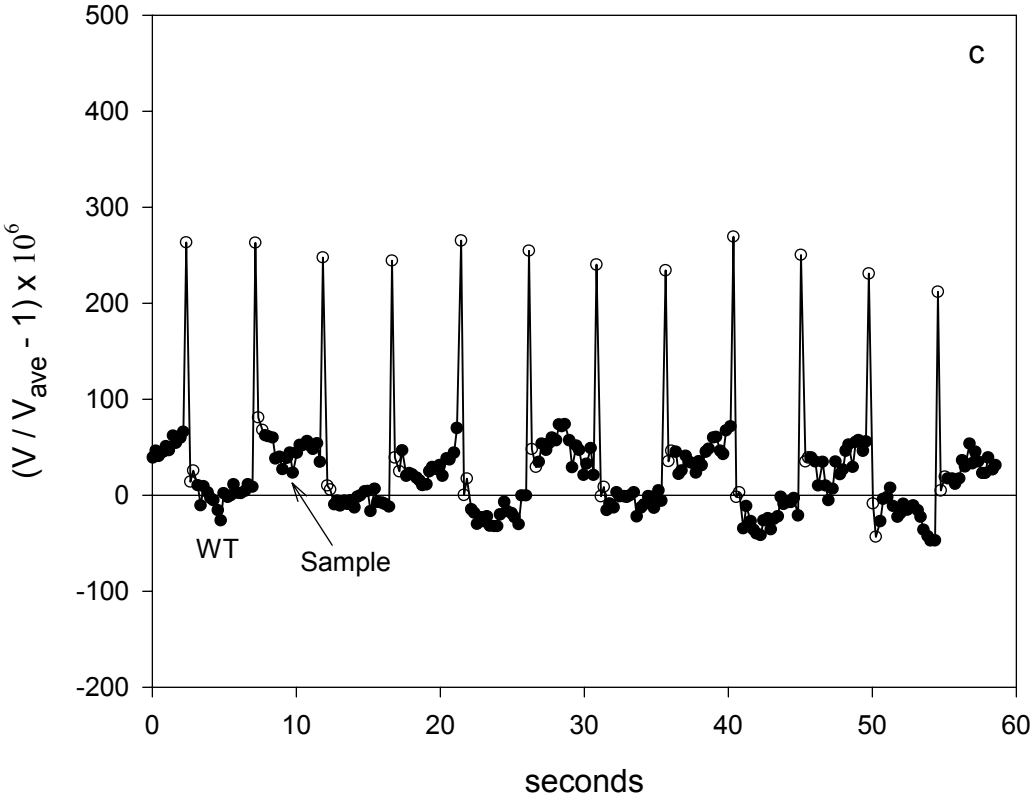

Figure 3.7 (continued)

recovery times shown in this figure. This valve must also be able to endure over 17,000 switches per day. The 100-ppm spikes at the end of each step correspond to a temporary drop in cell pressure resulting from the switching of the 4-way valve. The residence time of the gas in the sample cell is 0.2 seconds. To allow for pressure equilibration and sweepout of the sample cell, I reject the first three 0.2 second integrations after each switch. Figure 3.7b shows a similar data series for switching between WT and sample air at Harvard Forest. The sample gas at this time had an O_2/N_2 ratio that was ~ 100 per meg greater than the WT value. The downward trends

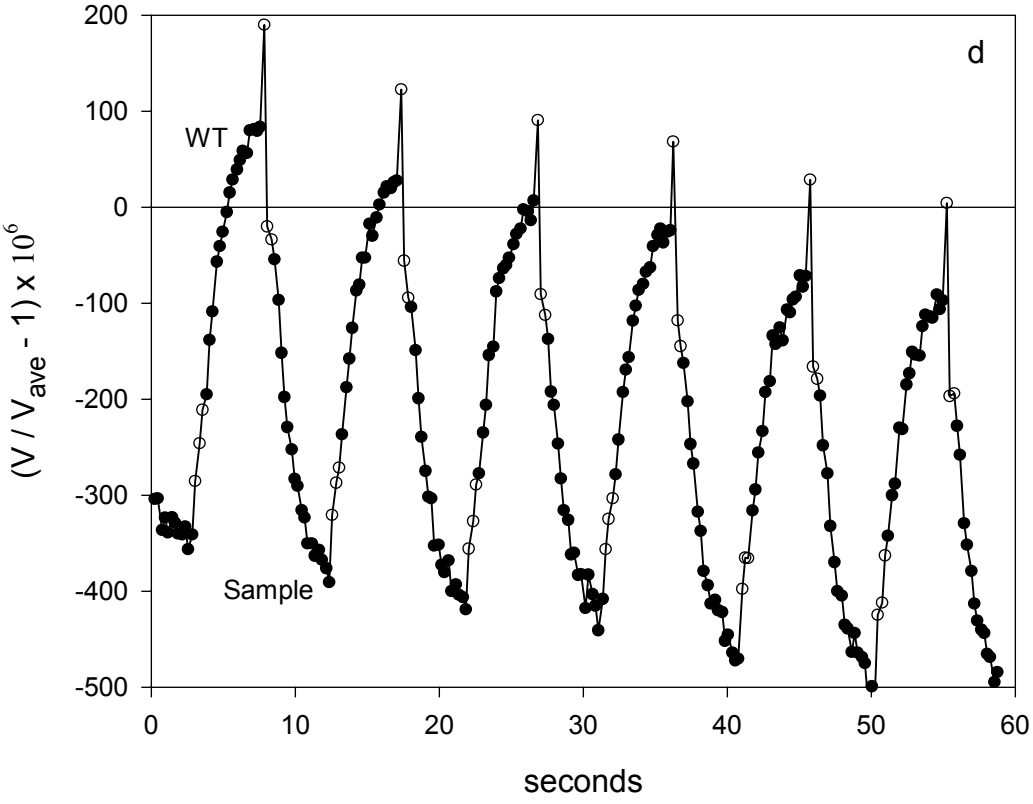

Figure 3.7 (continued)

at the end of the period in Figure 3.7a and for the whole period in Figure 3.7b are examples of the type of lamp variability that is compensated by the 5-second switching.

3.4 Instrument Performance

As the basis of the O_2 measurement, I use Equation 3.4 where time t corresponds to a period of sample gas analysis, and t-1 and t+1 to the adjacent periods of WT analysis. The pressure and flow fluctuations introduced by the rapid switching

scheme increases the instrument noise somewhat. By comparing two reference gases, as in Figure 3.7a but for much longer periods, I estimate a rms error on $\Delta_{5\text{-sec}}$ of 6 per meg compared to 3.5 per meg without any switching. Averaging these differences over 5-minute periods results in a precision of 1 per meg.

To determine actual oxygen concentrations, it is necessary to compare the differences between a sample and reference gas (Figure 3.7b) to those between the same reference gas and other known standards. It is also necessarily to do a similar comparison for the absolute NDIR signal to calculate the CO_2 concentration, and then to apply the CO_2 dilution and interference corrections to the O_2 signal. The VUV signal differences between WT and the reference gases can drift by several ppm in an hour. In the following section I describe the calibration scheme I use to compensate for this drift, and to relate the VUV measurements to the O_2/N_2 reference scale.

3.4.1 Absolute Calibration

In addition to the WT gas, I use high span (HS) and low span (LS) calibration gases which have O_2/N_2 ratios ~200 per meg higher and lower than ambient air. Once during every 80 minutes of measurement (Figure 3.8) I analyze these gases for 7 minutes each. For 5 minutes prior to introducing these gases to the detector, I purge their lines and regulators at a flow rate of 300 ml min^{-1}. I then reject the first 3.5 minutes of data after switching gas lines, and calculate HS and LS signal values using the last 3.5 minutes. These values have an estimated precision in O_2 of 1.3 per meg.

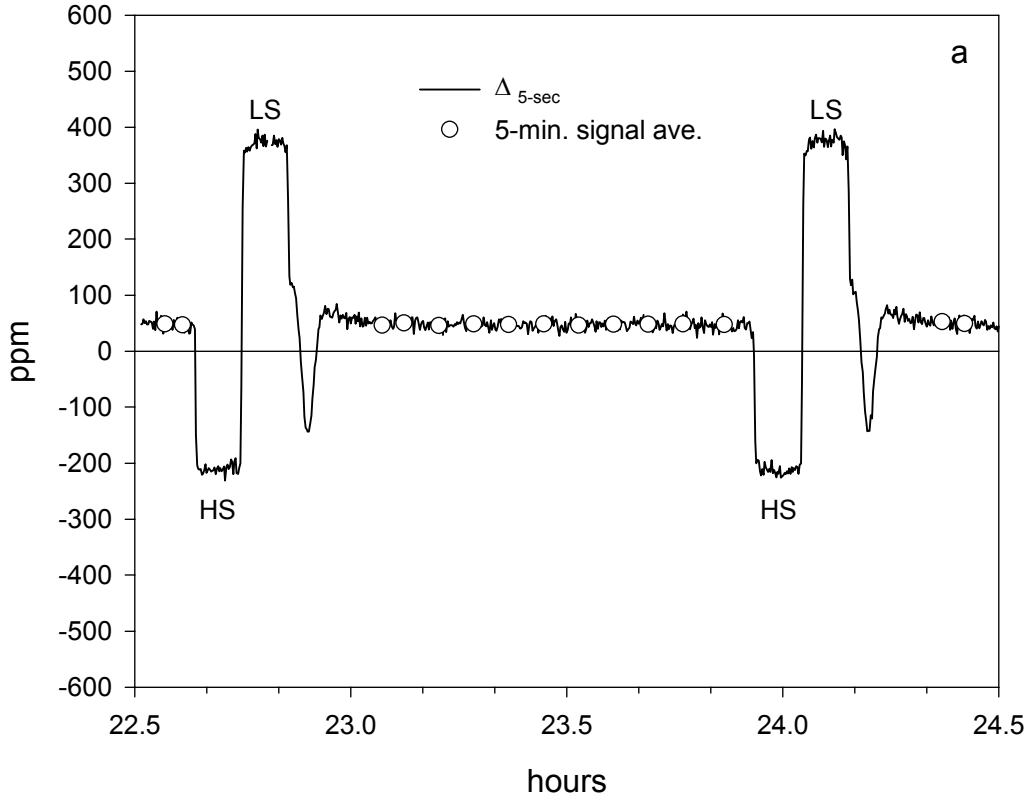

Figure 3.8 Example of data over hourly calibration cycle. The O_2 data is plotted as $\Delta_{5\text{-sec}}$ from Equation 3.4 multiplied by 10^6, and is inversely related to concentration. (a) 5-second differences for O_2 from Lawrence M. Gould during calm conditions among pack-ice. Sequence is 7 minutes of high span (HS), 7 minutes of low span (LS), and 66 minutes of sample gas. (b) 5-second differences for O_2 (thick curve) and 10-second signal averages for CO_2 (thin curve) from Harvard Forest during early morning. The high span gas has high O_2 concentration, but low CO_2 concentration. The steps in (b) correspond to switching among 4 heights on the tower (30 m, 25m, 18m, and 5m). Circles represent 5-minute averages in (a) and 12-minute averages for each tower level in (b). The dip in the O_2 signal after the LS-sample switch results from the rotary valve passing the HS port on its way to the sample port.

Because the rotary selector valve must pass by another calibration gas port to get back to the sample air position, it takes longer for the signal to restabilize (see Figure 3.4). Consequently, I reject the first 7 minutes of sample signal after this switch. To calculate O_2/N_2 ratios over the 60 minutes of usable sample signal, I first

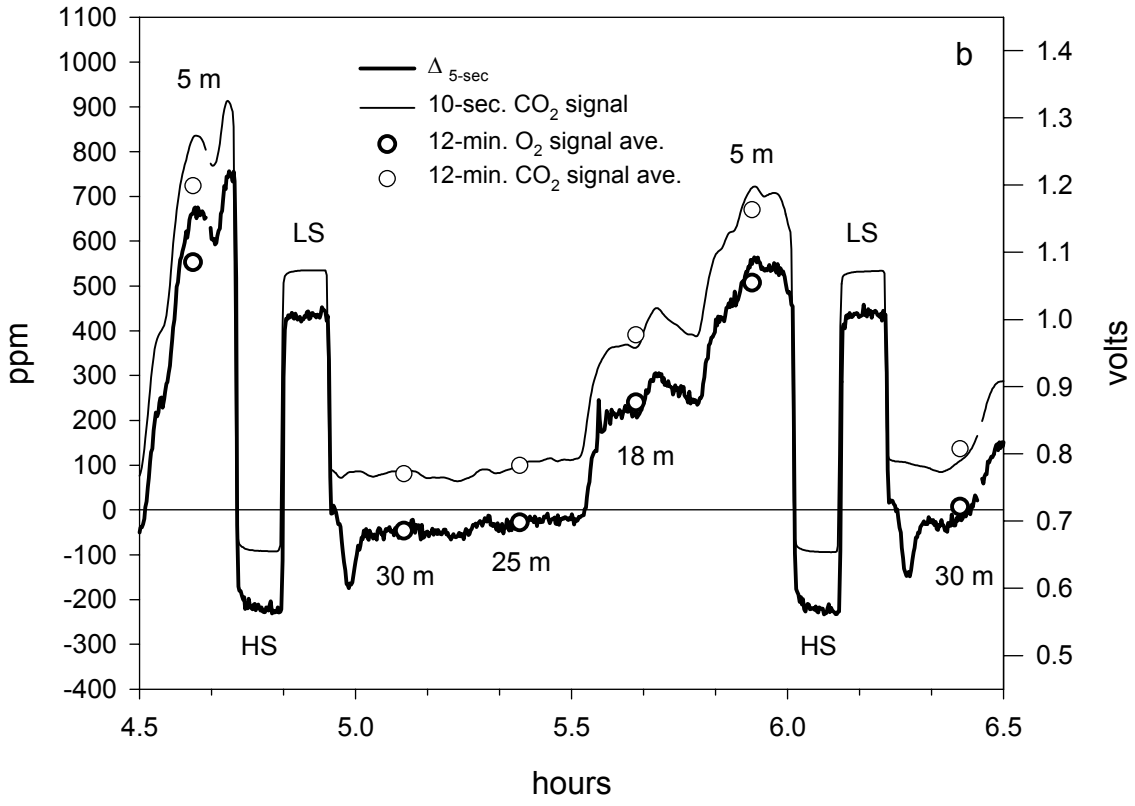

Figure 3.8 (continued)

determine concurrent HS and LS signals along linear trendlines fit to the preceding and following calibrations, then I use these HS and LS values to linearly interpolate the sample signals. I initially compare the sample and calibration gases on the basis of changes in apparent O_2 mole fraction at constant CO_2. To convert between deviations in apparent mole fraction to deviations in per meg, I use equation 4 from Keeling *et al*. [1998], and correct for the actual CO_2 concentrations:

$$\delta X_{O_2} = \delta(O_2/N_2) \times X_{O_2} (1 - X_{O_2}) - ([CO_2] - 363.29) \times (X_{O_2} - 0.05) \qquad (3.5)$$

where [CO_2] is the CO_2 concentration in ppm for the calibration or sample gas and 363.29 is the average CO_2 concentration of the reference cylinders defining zero on the Scripps O_2 scale. Multiplying this CO_2 deviation by X_{O_2} corrects for the diluting effect of CO_2 on the apparent mole fraction, and multiplying by -0.05 corrects for the CO_2 interference effect intrinsic to the VUV measurement.

For one hour during every day of measurement, I analyze a fourth calibration gas. This long-term reference (LT) gas provides a daily check of the measurement stability, and it allows direct comparisons between measurements made in different environments and using different HS and LS cylinders. I determine the O_2/N_2 ratio in the 4 reference gases to within ~ 1 per meg by repeated measurements on our laboratory interferometer [Keeling, 1988; Keeling *et al.*, 1998]. Figure 3.9 shows a comparison between LT O_2/N_2 ratios determined daily by the VUV instrument at sea and between cruises by our laboratory interferometer. The end points correspond to the HS and LS values, and are set to be the same on both scales. The average difference between the VUV and interferometer LT values is 0.7 ± 2.2 per meg. Figure 3.9 also includes shipboard flask samples analyzed on the interferometer and compared to adjacent VUV measurements. With the exception of one flask outlier, these data agree to within ± 3.5 per meg. These differences are well within the combined uncertainties associated with the two techniques. This demonstrates the external reproducibility, as well as the linearity of the VUV measurements.

Estimating the precision of 5-minute averages relative to values in another calibration cycle, or the precision of hourly averages relative to one another, is not

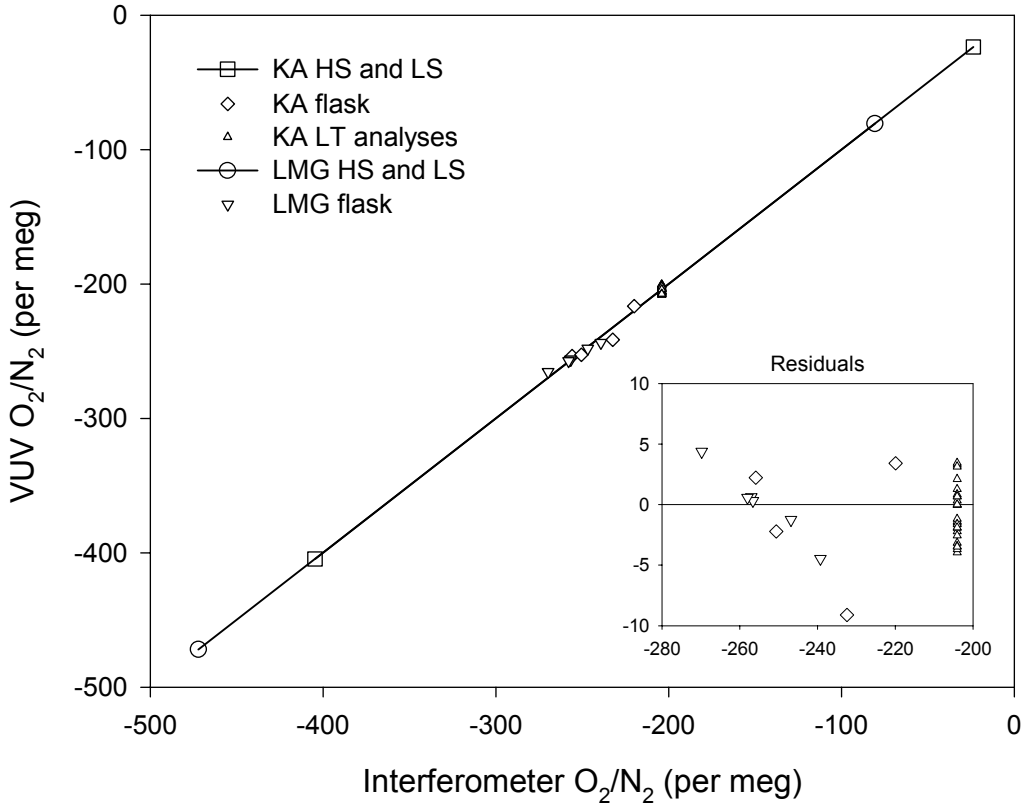

Figure 3.9 Comparison between VUV and interferometric measurements. The values for the high-span (HS) and low-span (LS) endpoints were determined on the interferometer and prescribed in the VUV calculation. A straight line is fit between these points. The 25 daily 1-hour VUV measurements on the long-term (LT) reference gas (upward triangles) are plotted against the average of four interferometer analyses spaced over 7 months. The diamonds represent flasks collected aboard the NOAA ship Ka'imimoana (KA) in the equatorial Pacific and analyzed on the interferometer, while the downward triangles represent flasks from the NSF ship Lawrence M. Gould (LMG) in the Soutehern Ocean. These values are plotted against the average of VUV measurements made during the hour before and hour after the flask was collected. The one flask value that lies noticeably off the line was likely influenced by leaks during sampling or storage (see Section 4.2).

straightforward. The net influence of uncertainties in the two HS and two LS values used in each concentration calculation is a 1.3 per meg contribution to the between-cycle precision. The statistical error associated with summing twelve 5-minute means

is rather small, but this does not account for signal drift on time scales between 5 minutes and 1 hour. Based on the repeated LT measurements shown in Figure 3.9, I estimate a precision on hourly measurements using different calibration periods, such as those presented in Chapters 4 and 5, of 2.2 per meg O_2.

For the ancillary CO_2 measurements, I use the same calibration scheme as for O_2 with several exceptions. Because rapid switching is not necessary for CO_2, the NDIR analyzer is upstream of the 4-way valve and I use 10-second average signals instead of $\Delta_{5\text{-sec}}$ values as the base measurement. The NDIR signal is not linear with CO_2 concentration. I have used a quadratic fit to the 4 reference gases as a calibration curve. In comparison to laboratory measurements, I obtain a CO_2 precision of 0.05 ppm, and an external reproducibility of 0.4 ppm.

3.4.2 Field Implementation

The primary challenge to using the VUV instrument on a ship is its motion sensitivity. In theory, an optical instrument could be designed to be very insensitive to motion. In practice a number of effects, including the inertial sensitivity of the differential pressure gauges, sloshing of heat-transfer fluid in the chiller perturbing thermal gradients, and small motions in the RF coil and lamp geometry contribute additional noise to shipboard VUV measurements. Occasionally during the cruises discussed in Chapters 4 and 5, such as near the Equator, in the lee of Hawaii, and in the pack ice around Antarctica, the conditions at sea were calm enough that the instrument performed as well as it did in the laboratory, with an rms error on $\Delta_{5\text{-sec}}$ of 6

per meg. However, this was not always the case. Figure 3.7c shows VUV signals recorded in the equatorial Pacific on the NOAA ship Ka'imimoana at a time when there was an 8-10 ft swell. This sample air had an O_2/N_2 ratio that was ~ 35 per meg lower than the WT value. The apparent increase in short-term signal variability (Figure 3.7c) at this moderate amount of motion corresponds to an increase in the rms error on $\Delta_{5\text{-sec}}$ to 10 per meg O_2. Tests comparing two calibration gases under these conditions indicated a precision on 5-minute averages of these differences of 2.5 per meg.

Under conditions of extreme motion, such as while in Drake Passage aboard the NSF ship Lawrence M. Gould at a time when there were 40 kt winds and 25 ft seas coming from 45° off the bow, the instrument error grew to 17 per meg on $\Delta_{5\text{-sec}}$, and 4 per meg on 5-minute averages of these differences. The data in Figure 3.8a come from the same cruise, but during calm sampling conditions experienced as the ship passed through loosely consolidated pack ice near shore. The ship motion at this time was minimal and the composition of the outside air very constant. The standard deviation of the twelve 5-minute averages from this hour of measurement is 1.1 per meg O_2. As shown in Figure 3.9 and discussed in Chapters 4 and 5, these O_2/N_2 values determined from the equatorial Pacific and Southern Ocean VUV measurements also compared well with concurrent shipboard and marine boundary layer station flask samples.

The main challenges in implementing the VUV instrument at a remote forest field site were logistical and stemmed from leaving the instrument unattended for longer periods of time than aboard a ship. Without the motion problems, the

instrument performance was similar to that in the laboratory. In addition, the natural variations in O_2 and CO_2 were enormous compared to those at sea, and thus much easier to resolve. The $\Delta_{5\text{-sec}}$ values for O_2 and signals for CO_2 shown in Figure 3.8b reflect switching every 17 minutes among intake lines at different heights on the sampling tower. The data from this figure show that there were vertical gradients on this morning of ~ 335 per meg in O_2 and ~ 68 ppm in CO_2. Over a period of several weeks, O_2:CO_2 ratios determined from vertical gradients, diurnal cycles at different heights, and soil and leaf chambers were very consistent at 1.03 ± 0.03 mol O_2:mol CO_2. This value is significantly lower than earlier respiration quotient (RQ) estimates from compositional and incubation studies, of 1.1-1.2 mol O_2:mol CO_2 [Keeling, 1988, Severinghaus, 1995]. I will prepare the complete results of this field study for publication elsewhere.

3.4.3 Potential Sources of Error

The sharpness of the square waves shown in Figure 3.7 depend significantly on the amount of water vapor in the sample and calibration gases. To illustrate this, I have shown a signal in Figure 3.7d that is from a period when a compressor on the cryogenic chiller failed and the temperature of the traps climbed to -40°C. The large amount of rollover after switching probably reflects a pressure-pulse induced adsorption or desorption of water on the optical surfaces, which could significantly affect their transmissivity. Although undesirable, at lesser magnitudes this rollover

does not appear to significantly affect the measurements, as it influences the calibration and sample signals similarly. For a period of LT analysis during which the rollover was approximately half as great as in Figure 3.7d, the measured concentration was only 2 per meg higher than its long-term mean. This problem is also easy to avoid with reliable chilling of the air.

A much more significant potential problem is that associated with fractionation effects. Any division of flow, restricted vent, or unintentional leak can fractionate O_2 relative to N_2 [Keeling *et al*., 1998]. The first week of measurements on the equatorial Pacific cruise discussed in Chapter 4 produced O_2 values that were consistent but ~ 70 per meg higher than expected from extrapolations based on earlier background station flask measurements. Fortunately, it was possible to debug this problem in the field, and I eventually traced it to fractionation at the tee upstream of the back-pressure regulator and downstream of the pump (Figure 3.6), resulting from an insufficient length of tubing upstream of the regulator and an insufficient constriction downstream of the pump.

At the beginning of the Ka'imimoana cruise, the VUV instrument's signal was found to be sensitive to variations in sample flow rate, the back-pressure regulator setting, and whether I used a 1.0 or a 0.1 μm filter. After putting two 2 m loops of 1/4" tubing separated by a needle valve upstream of the tee, and additional 2 m loops on both downstream legs of the tee (Figure 3.6), the signal was no longer sensitive to these flow and pressure variations, and closer to expected values. The presence or lack of flow and pressure sensitivity is an important diagnostic for identifying fractionation

effects, but without a means of absolutely determining O_2 concentrations at these levels it is not possible to entirely rule them out. By repeatedly changing between the original and improved instrument configurations while at sea, I was able to independently calculate a fractionation offset factor of +68 per meg. I have adjusted the data from the first week of the Ka'imimoana cruise, and selected data from the debugging period, for this offset and include an additional ± 10 per meg in my estimate of their absolute uncertainty.

3.4.4 Future Improvements

After establishing that the VUV instrument was able to reliably measure O_2 at a precision of a few per meg, I directed most of my efforts towards using it in the field. Consequently, I have yet to pursue a number of potential modifications that could significantly improve its present performance. For example, at present only the components that are grossly temperature sensitive are insulated, yet the lamp, electronics, and pressure gauges are probably also influenced by thermal variability. Putting the analyzer in a temperature controlled enclosure could improve its precision. In addition, it might be possible to reduce the motion sensitivity illustrated in Figure 3.7c through more rigid supports for the lamp and RF coil, and possibly by the identification of more robust pressure sensors. The optical configuration might also be improved. By removing the beamsplitter, which proved unnecessary, the transmitted light intensity could be increased, which could improve detector performance. However, the benefit of this modification is limited by the maximum photodiode

current, which is only a factor of 2 greater than that associated with the present light levels.

I have also tested a commercial Xenon lamp (Opthos, Rockville, MD), which has excellent noise and optical characteristics, similar to those shown for the sealed and gettered lamp in Figures 3.2 and 3.4. Although rated for 1000 hours of service using a microwave power supply, preliminary RF tests showed a rapid signal decline and therefore I did not use it in the field. However, at the point when I turned it off to save it for a field spare, its signal appeared to be leveling. For certain applications, the benefits of less noise and less hardware gained from using a sealed lamp might outweigh the costs of frequently replacing the lamp. The compactness of the instrument could be further improved by replacing prepackaged electronics such as voltmeters, flow controllers, and power supplies with custom built circuitry. Finally, considering recent developments in our awareness of fractionation effects, using an instrument that pulled sample air at the same rate as the analyzer throughflow, and thus had no tees, might be worth the sacrifice in temporal resolution due to the lower sample flow (A. Manning, personal communication, 1999). I estimate based on theoretical limits and the results shown above that a future VUV instrument could easily be capable of measuring O_2 to a precision of several per meg at 10-second resolution and 0.5 per meg at 5-minute resolution, and made small enough for light-aircraft deployments.

3.5 Applications

The precision and portability of the VUV instrument lend it to many geochemical studies. Repeated ocean transects, similar to those presented in the next two chapters, have the potential to greatly increase the spatial resolution and extent of the current network of background O_2 measurements. This would improve our ability to partition terrestrial and oceanic CO_2 sources on global and hemispheric scales [Keeling *et al.*, 1996]. Shipboard atmospheric O_2 measurements over several years in the equatorial Pacific promise new insights into the biogeochemical responses to El Niño variability, while repeated measurements in the Southern Ocean would allow us to monitor biological and dynamical changes in a region that is expected to be particularly sensitive to future climate change.

Another aspect of ocean geochemistry that the VUV instrument could address is improving theories and formulations for air-sea gas exchange. Eddy techniques for measuring air-sea CO_2 fluxes are continuously improving [Oost *et al.*, 1995]. The VUV instrument could be applied to make complementary measurements of air-sea O_2 fluxes using gradient techniques. Because O_2 and CO_2 have very different solubilities, measuring simultaneous fluxes of both gases would provide a new constraint on the solubility dependence of air-sea gas exchange. A stable vessel such as the Scripps Floating Instrument Platform (FLIP) would be ideal for such a study.

The VUV instrument has a number of interesting applications on land as well. Before taking the VUV instrument to Harvard Forest (see Figure 3.8c), observations of

respiratory and photosynthetic quotients were limited to laboratory measurements on the scale of a leaf or a dirt sample [Bloom *et al.*, 1989, Severinghaus, 1995]. Future VUV measurements from forest towers and *in situ* leaf and soil chambers could significantly advance our understanding of the relationships between plant O_2, CO_2, and nutrient cycling on a range of time and space scales. The VUV instrument could also be particularly helpful in determining net primary productivity at free-air carbon enrichment (FACE) sites. Because the intentional emission of CO_2 at these sites prevents the use of eddy-correlation CO_2-flux measurements, variations in productivity currently must be estimated by mass-balance techniques.

The VUV instrument described here is suitable for airborne measurements on very large aircraft such as the NCAR C-130, and could be repackaged to fly on light aircraft. Because oceanic, terrestrial, and industrial processes have inherently different O_2:CO_2 ratios, VUV measurements of vertical O_2 profiles would aid the interpretation of their relative influences on CO_2. Separately identifying the terrestrial component of vertical and longitudinal CO_2 variations would help to constrain terrestrial rectification processes, and indicate how to best measure continental scale CO_2 exchange [Stephens *et al.*, 1999]. Identifying the industrial contribution to CO_2 variations, using airborne VUV O_2 measurements, could prove valuable in future attempts at emission verification.

A final area of scientific pursuit where the VUV instrument may be applicable is animal physiology. In the laboratory, commercially available instruments are sensitive enough to measure the respiration of even the smallest vertebrates.

Nonetheless, the high-precision of the VUV instrument could be helpful in studying the respiration of individuals or groups of animals in the field by detecting changes in ambient O_2 concentrations, or in studying the respiration of very small animals in the laboratory. Ellington *et al.* [1990] used a modified commercial electrolytic analyzer to measure the oxygen consumption of bumblebees. Because the VUV instrument has a precision some 15 times better than that used by these authors, measurements of oxygen consumption may be possible for much smaller animals.

3.6 Conclusion

In this chapter, I have described the design and performance of a new technique for measuring variations in atmospheric O_2. On land, this VUV instrument has a precision of 6 per meg O_2 at 10-second resolution and 1 per meg for a 5-minute average. The motion-sensitivity characteristics of the instrument are good, and for typical conditions at sea these values only increase to 10 and 2.5 per meg for 10-second resolution and a 5-minute average, respectively. By comparison to flask and reference-cylinder concentrations determined by our laboratory interferometer, I have shown that the external reproducibility of the VUV measurements is ± 3 per meg.

The keys to attaining the high levels of precision are a light source, signal detection, and signal amplification stable to near their theoretical limits, as well as a gas-handling system that can switch between two gases every 5 seconds with very small and short-lived pressure and flow perturbations. The external reproducibility is

potentially very sensitive to the gas-handling configuration, but the design described here does not appear to suffer from fractionation problems. Further work on improving lamp stability, in identifying and minimizing the remaining motion sensitivity, and in further comparisons to laboratory interferometric and mass-spectrometric techniques promise even greater instrument performance. The successful field demonstrations presented in Chapters 4 and 5 of the present VUV instrument will likely lead to its future use in a wide range of biogeochemical studies.

3.7 References

Bender, M. L., P. P. Tans, J. T. Ellis, J. Orchardo and K. Habfast, A high precision ratio mass spectrometry method for measuring the O_2/N_2 ratio of air, *Geochimica et Cosmochimica Acta*, *58*, 4751-4758, 1994.

Bloom, A. J., R. M. Caldwell, J. Finazzo, R. L. Warner, and J. Weissbart, Oxygen and carbon dioxide fluxes from barley shoots depend on nitrate assimilation, *Plant Physiol.*, *91*, 352-356, 1989.

Ellington, C. P., K. E. Machin, T. M. Casey, Oxygen consumption of bumblebees in forward flight, *Nature, 347*, 472-473, 1990.

Inn, E. C. Y., K. Watanabe, and M. Zelikoff, Absorption coefficients of gases in the vacuum ultraviolet. Part III. CO_2, *J. Chem. Phys.*, *21*, 1648-50, 1953.

Jenkins, T. E., *Optical Sensing Techniques and Signal Processing*, 243 pp., Prentice-Hall, Englewood Cliffs, NJ, 1987.

Kaplan, A., C. Jurgens, and K. Yu, Ultraviolet oxygen sensor, *Instrument and Control Systems*, 113-114, February 1971.

Keeling, R. F., Development of an interferometric oxygen analyzer for precise measurement of the atmospheric O_2 mole fraction, Ph.D. thesis, 178 pp., Harvard Univ., Cambridge, Mass., 1988.

Keeling, R. F., R. G. Najjar, M. L. Bender, and P. P. Tans, What atmospheric oxygen measurements can tell us about the global carbon cycle, *Global Biogeochem. Cycles, 7*, 37-67, 1993.

Keeling, R. F., S. C. Piper and M. Heimann, Global and hemispheric CO_2 sinks deduced from changes in atmospheric O_2 concentration. *Nature*, 381, 218-221, 1996.

Keeling, R. F., A. C. Manning, E. M. McEvoy, S. R. Shertz, Methods for measuring changes in atmospheric O_2 concentration and their application in southern hemisphere air, *J. Geophys. Res.*, *103*, 3381-3397, 1998.

Kronick, M. N., C. E. Bryson, J. A. Bridgham, and S. H. Eletr, Measurement of oxygen by differential absorption of UV radiation, U.S. Patent No. 4192996, 1980.

Oost, W. A., W. Kohsiek, G. de Leeuw, G. J. Kunz, S. D. Smith, B. Anderson, and O. Hertzman, On the discrepancies between CO_2 flux measurement methods, in Air-Water Gas Transfer, edited by B. Jähne and E. C. Monahan, pp. 723-733, AEON Verlag and Studio, Hanau, 1995.

Sampson, J. A. R., *Techniques of Vacuum Ultraviolet Spectroscopy*, 348 pp., Wiley, New York, 1967.

Severinghaus, J. P., Studies of the terrestrial O_2 and carbon cycles in sand dune gases and in Biosphere 2, Ph.D. thesis, 148 pp., Columbia Univ., New York, 1995.

Stephens, B. B., S. C. Wofsy, R. F. Keeling, P. P. Tans, and M. J. Potosnak, The CO_2 budget and rectification airborne study: Strategies for measuring rectifiers and regional fluxes, accepted to the AGU Monograph, *Inverse Methods in Global Biogeochemical Cycles*, 1999.

Watanabe, K., E. C. Y. Inn, and M. Zelikoff, Absorption coefficients of oxygen in the vacuum ultraviolet, *J. Chem. Phys.*, *21*, 1026-30, 1953.

Watanabe, K., and M. Zelikoff, Absorption coefficients of water vapor in the vacuum ultraviolet, *J. Opt. Soc. Am.*, *43*, 753-755, 1953.

Wong, J. Y., Measuring gaseous oxygen with U.V. absorption, U.S. Patent No. 4096388, 1978.

Wong, J. Y., Oxygen analysis employing absorption spectroscopy, U.S. Patent No. 4591721, 1986.

Chapter 4

Shipboard Atmospheric O_2 Measurements in the Equatorial Pacific

Abstract

I have used the VUV instrument described in Chapter 3 to measure atmospheric O_2 in the eastern equatorial Pacific between April 18 and May 20, 1998, aboard the NOAA ship Ka'imimoana. In this chapter, I present results from the atmospheric O_2 measurements and from concurrent atmospheric CO_2, dissolved O_2, and meteorological observations. The VUV measurements from this cruise agree with laboratory analyses of concurrent shipboard and background-station flask samples, and represent both the first successful field-based measurements of atmospheric O_2 and the first extensive measurements of atmospheric O_2 in the equatorial region. These measurements reveal a southward-increasing latitudinal trend and significant small-scale variability in atmospheric O_2. Variations in atmospheric O_2 near the Equator correlate with wind-direction, air-mass properties, and air-mass origins as determined by back-trajectory analyses. Thus, the observations in this region appear to predominantly reflect variable sampling across the relatively strong interhemispheric O_2 gradient rather than local variations in air-sea O_2 flux. On a regional scale, the observed O_2 concentrations are close to the predictions of the HAMOCC3.1-TM2 model, but are significantly lower than those of POBM-TM2 and LLOBM-TM2. The model-observation differences may result from errors in the amount of equatorial O_2 and CO_2 outgassing in these models, the lack of a seasonal marine O_2 rectifier in these models, or interannual variability in the observations associated with the large El Niño event during this cruise.

4.1 Introduction

The modeling results shown in Chapter 2 predict that the equatorial Pacific is a region of significant spatial variation in atmospheric O_2. As discussed in Section 2.2, the upwelling of DIC and preformed nutrients and the strong air-sea heat fluxes lead to a net outgassing of O_2 and CO_2 from this region. Two of the models, POBM-TM2 and LLOBM-TM2, predict peaks on the order of 10 per meg in the derived tracer APO between 20°N and 20°S, while the third model, HAMOCC3.1-TM2, predicts a smaller and southward-shifted APO peak (see Figure 2.5). In Chapter 2, I attributed much of the difference between models to the inclusion or exclusion of the marine O_2 rectifier, but also speculated that all of the models' equatorial predictions were sensitive to their overprediction of low-latitude deep-water upwelling. It is not possible to test models near the Equator using the available background O_2 flask data because of gaps in the sampling network. The measurements presented in this chapter represent a step toward filling in these gaps, and provide direct evidence of the controls on low-latitude atmospheric O_2 over a range of time and space scales.

The NOAA ship Ka'imimoana is dedicated to servicing the Tropical Atmosphere Ocean (TAO) array of moored buoys. These buoys are located within 8° of the Equator between 135°E and 95°W longitude in the Pacific (Figure 4.1), and provide temperature, salinity, current, and wind data that are critical to the prediction and observation of El Niño climate variability [McPhaden, 1999]. Ka'imimoana visits each of these buoys approximately twice a year, thus providing an excellent platform

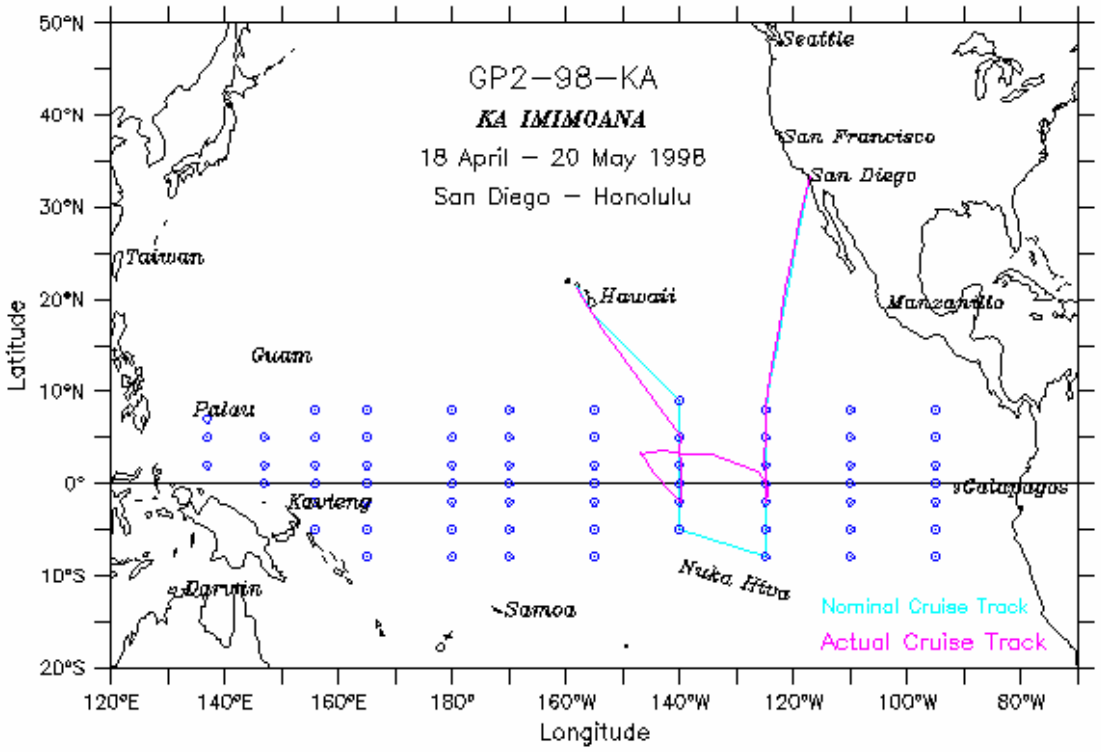

Figure 4.1 Map showing the cruise track for Ka'imimoana leg GP2-98. The dark line shows the actual ship track, which diverted from the intended track (light line), to capture a drifting buoy. The circles represent the locations of the TAO array buoys. Figure obtained from http://rho.pmel.noaa.gov/atlasrt/kaimi.html.

for conducting repeatable geochemical surveys of this region. The data presented here are from leg GP2-98, which departed San Diego on April 18, 1998, included maintenance along the 125°W and 145°W buoy lines, and then returned to Honolulu on May 20. As the ship track in Figure 4.1 shows, after reaching 2°S, 125°W the ship diverted from its scheduled course to pursue a buoy that had broken free from its anchor and was steadily drifting westward. After capturing this buoy near 3°N, 147°E, the ship returned to 2°S, 140°W and continued north along the 140°W buoy line. The two southernmost turnaround points were within or just south of the

Intertropical Convergence Zone (ITCZ). Material presented in Section 4.4 below indicates that both the position of the ship relative to the ITCZ at these times, and the latitudinal history of the sampled air during the rest of the cruise had significant consequences for the measured O_2 concentrations.

I have combined these shipboard O_2 and CO_2 data, to calculate APO concentrations as for the flask data in Chapter 2. The resulting APO values for this particular region and time of year can be directly compared to coupled ocean-atmosphere models that explicitly resolve the seasonal cycle, such as HAMOCC3.1-TM2. Also, because the seasonal cycle in atmospheric O_2 is relatively small at low-latitudes, annual-mean APO values can be estimated from these observations and used to constrain aseasonal models. Material presented in Section 4.5 shows that these comparisons are relatively favorable for HAMOCC3.1-TM2, but that POBM-TM2 and LLOBM-TM2 appear to overpredict equatorial APO concentrations. This discrepancy could result from the presence of too much low-latitude outgassing of O_2 and CO_2, or the lack of seasonal rectification effects in these models. However, because all of the models represent climatologically average conditions, their comparisons to the observations may also be impacted by the large El Niño event that took place up to and during this cruise.

4.2 Atmospheric O_2 and CO_2 Data

The VUV instrument drew air from one of two sample lines: on a bow mast approximately 20 m above the water and at a high point on the aft control tower

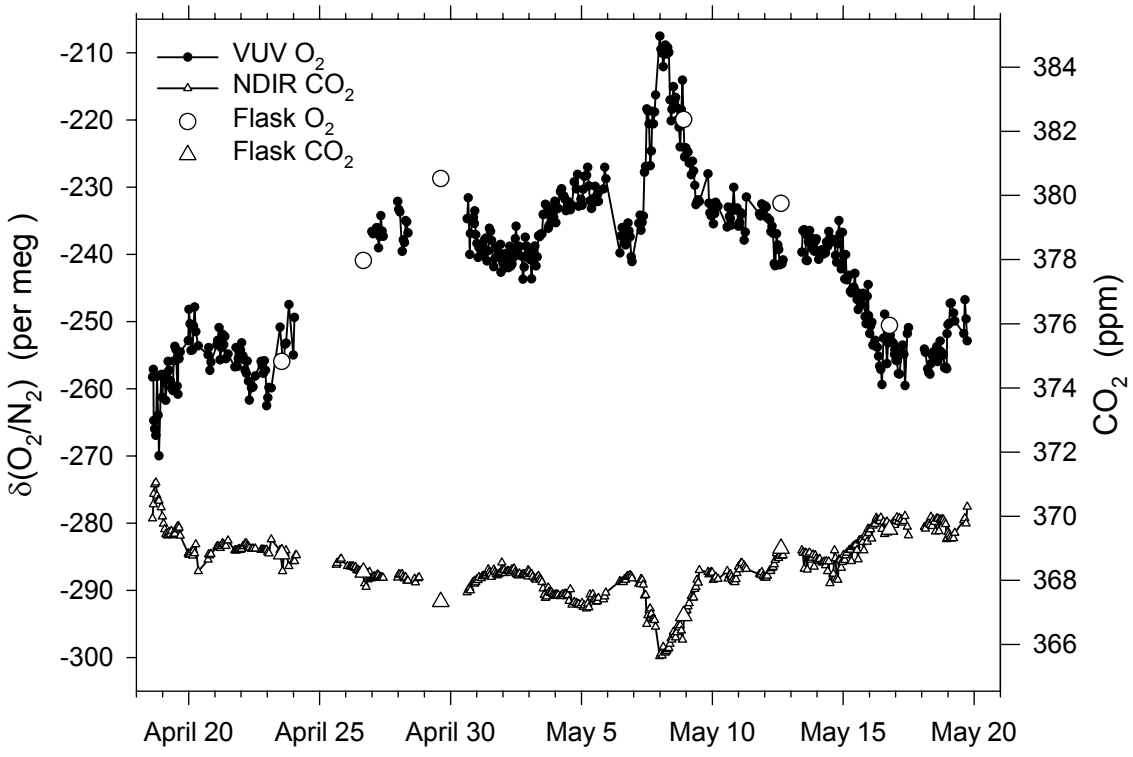

Figure 4.2 Hourly-mean concentrations of atmospheric O_2 and CO_2 plotted versus time. The O_2 and CO_2 vertical axes are scaled to be equivalent in moles. The ticks on the x-axis correspond to midnight local time and are labeled with the date of the following day. The large symbols represent 5-liter flask samples collected aboard the ship and analyzed on the Scripps interferometer. The O_2 values were determined as described in Section 3.4 from data similar to that in Figure 3.8. After April 30, the O_2 values have an uncertainty of ± 3 per meg. Prior to April 30, the O_2 values have been shifed down by 68 per meg to account for an independently-quantified fractionation effect and consequently have a higher uncertainty of ± 10 per meg (see Section 3.4.3). The overall accuracy of the CO_2 measurements is ± 0.4 ppm.

approximately 15 m above the water. I measured CO_2 in this same gas stream using a non-dispersive infrared gas analyzer, as described in Chapter 3. I manually switched between the fore and aft sample lines according to the prevailing winds to avoid sampling air from the engine exhaust stacks located amidships. However, it was still necessary to filter the data for times when exhaust air did occasionally get in the

sample lines, which were easily identifiable by strong O_2 and CO_2 excursions. I show the resulting O_2 and CO_2 data, averaged over hourly periods and plotted versus time, in Figure 4.2. I have adjusted the O_2 data before April 30 to account for fractionation effects, as described in Section 3.4.3. The gaps in this figure correspond to times when I was modifying and testing the instrument to quantify and eliminate these effects.

The large symbols in Figure 4.2 represent six 5-liter flask samples that I collected on the ship, and which were analyzed by E. McEvoy on the Scripps O_2 laboratory interferometer. The flask sample taken on May 12 is 8 per meg higher than the adjacent VUV O_2 values. However, because the O_2:CO_2 ratio in this flask sample is also anomalous (see Figure 4.6 below), it is likely that a problem during flask collection or storage, rather than VUV instrument error, is the cause of this discrepancy. The other three flasks that overlap VUV data give O_2 values that are in good agreement with the *in situ* measurements, and do not reveal any consistent offsets. The differences of ± 2-3 per meg are within the combined errors for these two techniques. One of these flasks overlaps the early fractionation-adjusted VUV data, however I calculated this adjustment independent of the flask result. The two flask samples taken when continuous data are not available give O_2 values that appear reasonable in comparison to the nearby VUV data and trends.

Figure 4.3 shows the same continuous data plotted versus latitude. Together, Figures 4.2 and 4.3 show coherent O_2 variations on time scales of hours to weeks and space scales of tens to hundreds of kilometers. I will briefly describe these variations

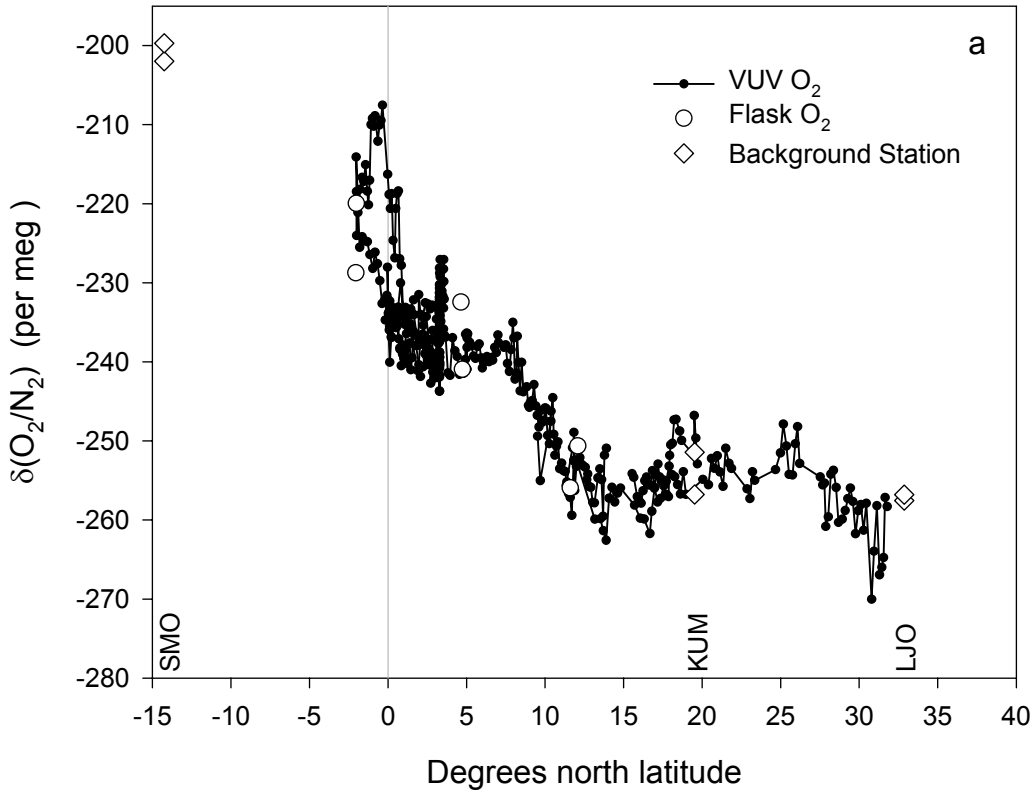

Figure 4.3 Hourly-mean shipboard O_2 and CO_2 plotted versus latitude. Data is the same as in Figure 4.2 for (a) O_2 concentrations and (b) CO_2 concentrations. The diamonds represent measurements on flask trios collected on April 23rd and May 6th at La Jolla (LJO), on May 4th and 19th at Samoa Observatory (SMO), and on May 12th and 26th at Cape Kumukahi (KUM).

here then discuss their likely causes in more detail in the following sections. For the first several days steaming south from San Diego, O_2 concentrations increased by ~10 per meg and CO_2 concentrations decreased by ~2 ppm. However, at around 25°N these trends shifted as CO_2 leveled off and O_2 began a slight decrease (Figure 4.3). Then, on the morning of April 23 near 14°N, these trends underwent another larger shift as O_2 concentrations began a steady climb, and CO_2 a steady decline, that continued all the way to the Equator. On the first pass across the Equator along

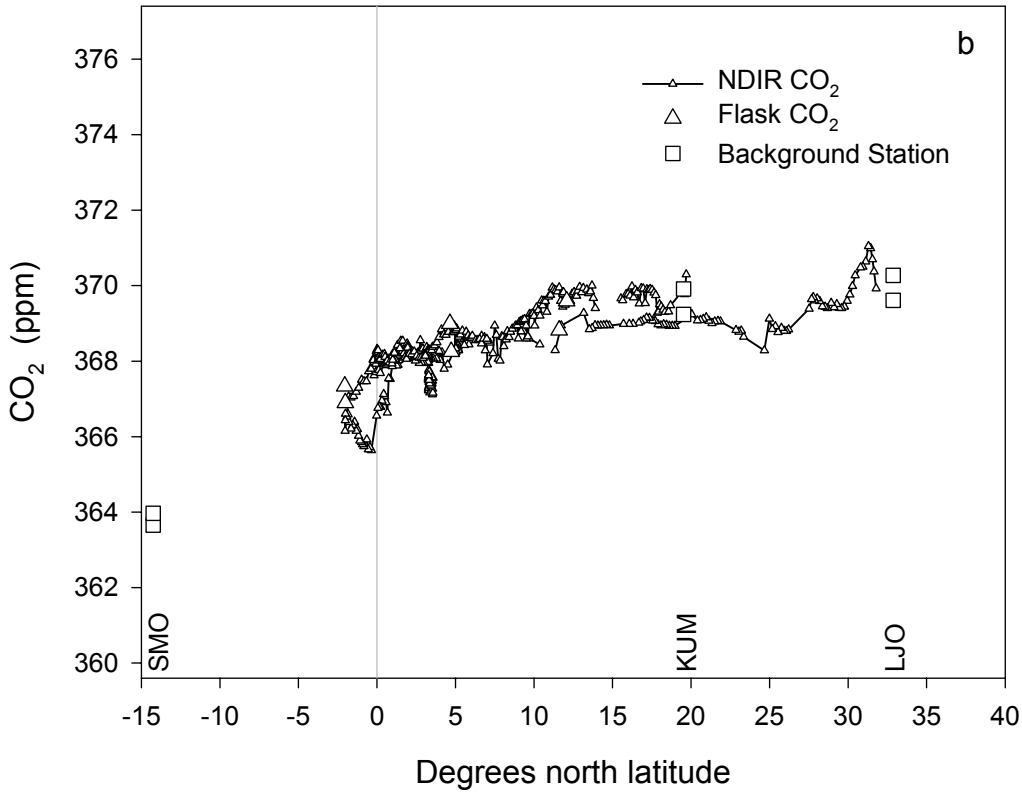

Figure 4.3 (continued)

125°W, O_2 concentrations increased by a total of ~10 per meg and CO_2 decreased by ~1 ppm as indicated by the flask sample taken at 2°S on April 29 (Figure 4.2). I observed a much larger jump across the Equator on the second pass just over a week later and 15 degrees further west, when O_2 increased by ~30 per meg and CO_2 decreased by ~3 ppm. These concentration excursions along 145°W longitude actually diminished by a factor of 2 by the time the ship reached its southernmost point at 2°S. From this point to the end of the cruise in Honolulu, I observed the reverse of the general trends seen earlier from San Diego to the Equator. Again at

around 14°N I observed a leveling-off of CO_2 and a shift to slightly increasing O_2 concentrations.

The overall latitudinal gradients shown in Figure 4.3 are consistent with the larger scale interhemispheric differences in O_2 and CO_2 at this time of year. I have also included points in this figure representing background-station flask trios collected near the beginning of the cruise at La Jolla, California (LJO), near the middle of the cruise at American Samoa (SMO), and near the end of the cruise at Cape Kumukahi, Hawaii (KUM). The LJO and KUM measurements agree well with the adjacent continuous values, and the southward trends are generally in line with the SMO concentrations at 14°S. Figure 4.4 compares the shipboard O_2 and CO_2 data to flask data from SMO and LJO over the past 5 years. This figure shows that the interhemispheric O_2 and CO_2 gradients reverse every summer and winter, and that this cruise happened to take place at the time of year with the greatest interhemispheric O_2 and CO_2 differences.

The observed latitudinal CO_2 gradient resulted from a combination of terrestrial respiration occurring during the boreal winter preceding this cruise and the large industrial source in the northern hemisphere. The observed latitudinal O_2 gradient was oppositely affected by the corresponding industrial and terrestrial O_2 sinks in the north. In addition, the O_2 gradient was steepened by oceanic outgassing in the southern hemisphere resulting from net productivity, and by oceanic ingassing in the northern hemisphere resulting from enhanced vertical mixing of O_2-depleted waters, which occurred throughout the boreal winter.

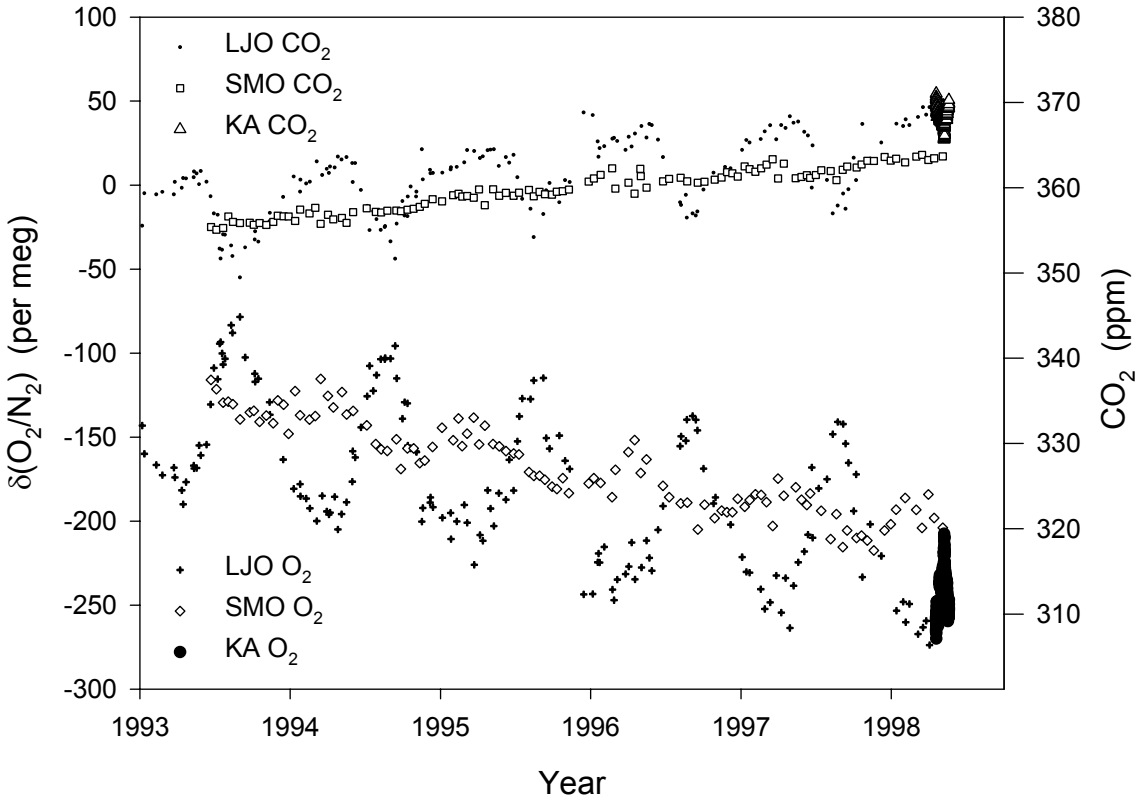

Figure 4.4 Hourly-mean shipboard (KA) O_2 and CO_2 data compared to flask data from La Jolla (LJO) and Samoa Observatory (SMO) over the past 5 years. The O_2 and CO_2 vertical axes are scaled to be equivalent in moles.

An indication of the relative terrestrial and oceanic contributions to the latitudinal gradients presented here can be obtained by directly comparing the O_2 and CO_2 data. Figure 4.5 shows a plot of the observed O_2 versus CO_2 concentrations. These data correlate well, with an average slope of -2.3 mol O_2:mol CO_2. By comparison, fossil fuel burning alone would produce a slope of around -1.4 mol O_2:mol CO_2 [Keeling, 1988], and terrestrial exchange would produce a slope of around -1.1 mol O_2:mol CO_2 [Keeling, 1988; Severinghaus, 1995]. The more negative observed slope reflects the influence of oceanic O_2 exchange, which has very little

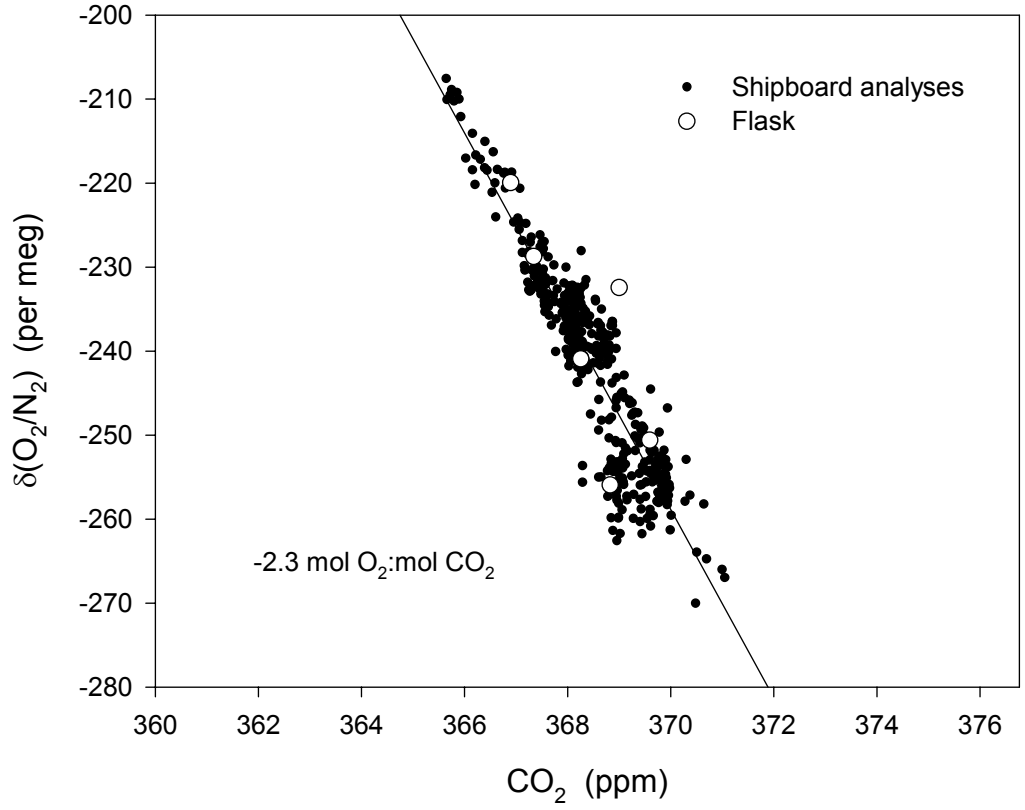

Figure 4.5 Hourly-mean shipboard O_2 versus CO_2 concentrations. The line and reported slope are from a least squares fit to the shipboard data. The O_2 and CO_2 vertical axes are scaled to be equivalent in moles.

corresponding CO_2 flux. The value of -2.3 mol O_2:mol CO_2 is consistent with approximately equal oceanic and terrestrial influences on the interhemispheric O_2 gradient at this time.

The tight relationship between the shipboard O_2 and CO_2 observations is further illustrated in Figure 4.6. The one time when O_2 does not closely track CO_2 at a consistent ratio is from April 20 to around April 24, as the ship steamed from 25°N to 13°N near 120°W longitude. During this period, O_2 dropped by ~10 per meg while CO_2 remained fairly constant. Although instrument error must be considered for this

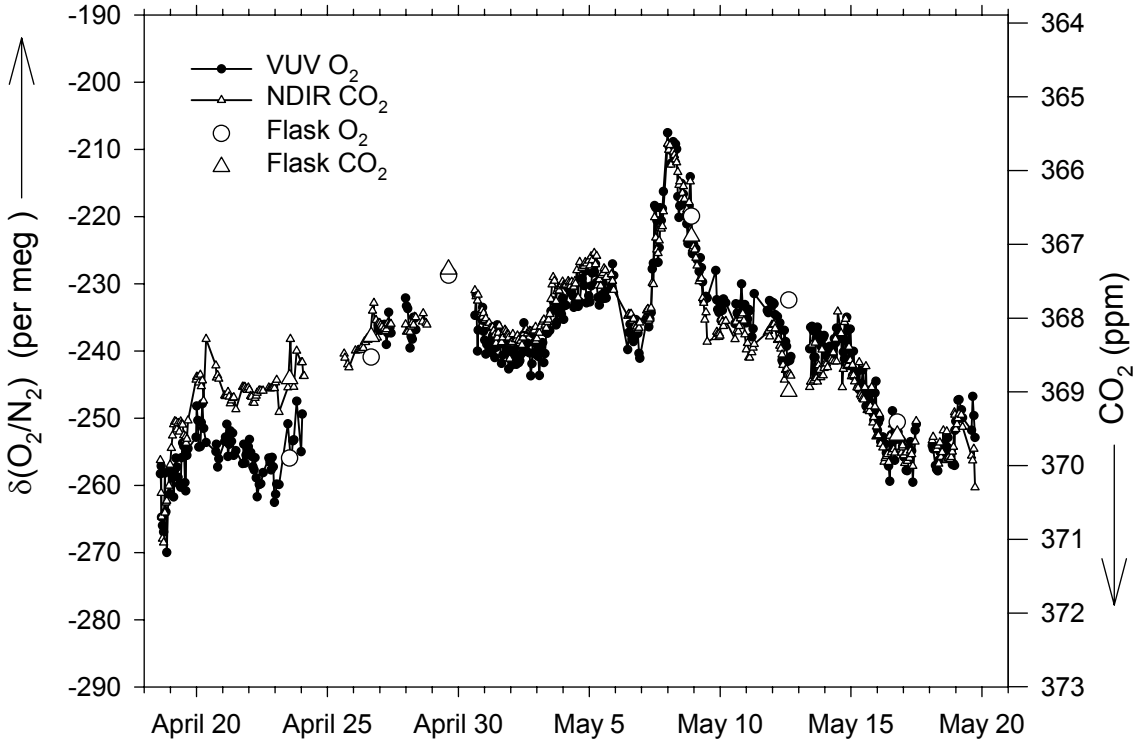

Figure 4.6 Hourly-mean shipboard O_2 and scaled CO_2 data. Same as Figure 4.2, but with the CO_2 axis flipped and scaled by -2.3 mol O_2:mol CO_2.

period of known fractionation problems, the O_2 values determined from the adjusted VUV signal on April 23 are very close to the independently determined flask concentration. An alternative explanation is that this O_2 divergence represents the influence of northern oceanic O_2 uptake, as discussed below in Section 4.4.

4.3 Dissolved O_2 Data

In addition to atmospheric O_2 and CO_2, I also measured the dissolved oxygen concentration of surface waters. I collected water samples four times per day from the

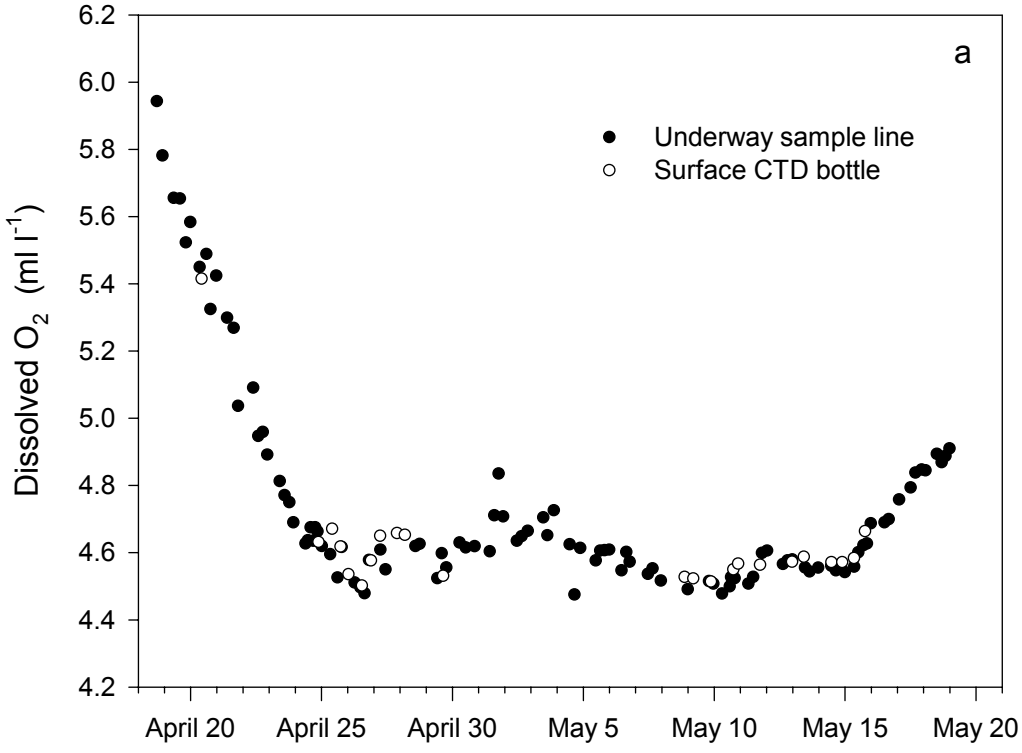

Figure 4.7 Dissolved O_2 measurements made using the Winkler titration method. Samples were collected from the underway sample line and from surface CTD bottles. Plotted versus (a) time and (b) latitude.

ship's underway sampling system, and from the surface bottle on every CTD cast. The purpose of these samples was to explore possible regional correlations between surface-water and atmospheric O_2, and to aid in the interpretation of the atmospheric measurements with respect to interannual variability in the equatorial Pacific. Resolving correlations between atmospheric O_2 and diurnal or sharp-frontal surface O_2 variations, if they existed, would require a much higher dissolved-O_2 sampling frequency. I analyzed the water samples using a Winkler titration apparatus [Carpenter, 1965] obtained from the Scripps Oceanographic Data Facility, which has a

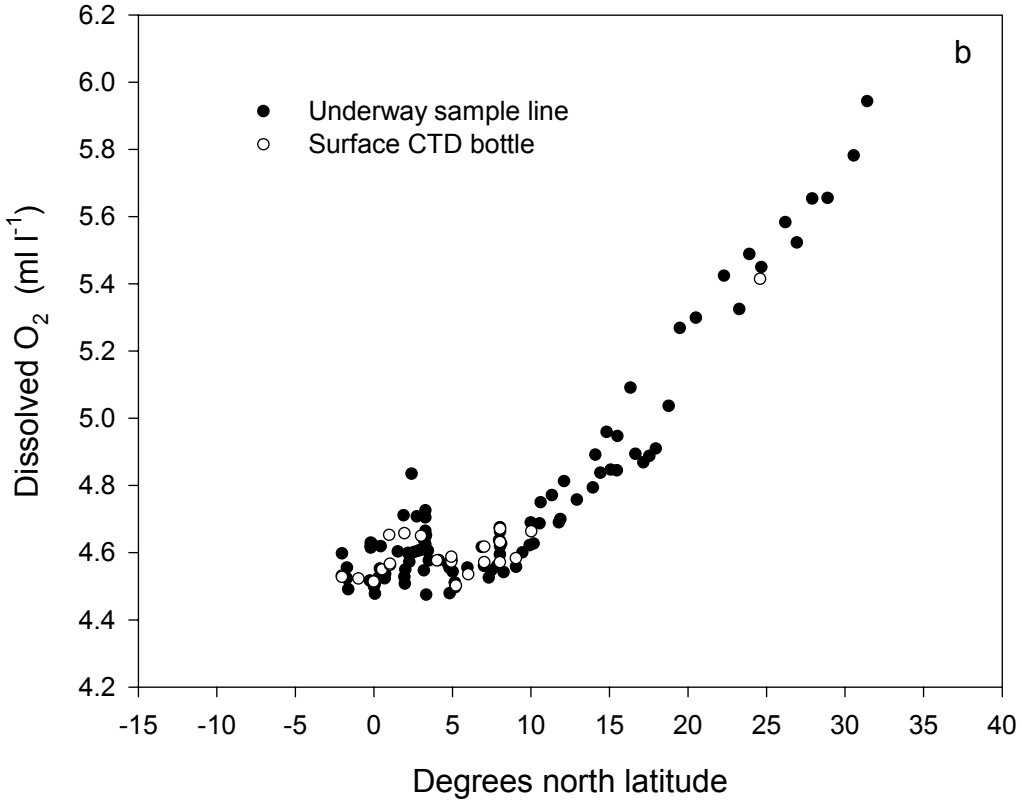

Figure 4.7 (continued)

potential precision of 0.01 ml l^{-1}. Of 125 underway samples and 26 CTD samples collected, I have discarded 23 either because bubbles were inadvertently introduced during pickling or storage, or because of problems with sampling from the underway line while the ship was on station. The dissolved O_2 concentrations for the remaining 128 samples are shown in Figure 4.7.

The agreement between the underway line and the CTD samples appears good, and as expected the O_2 concentration is less in warmer water, where O_2 is less soluble. Figure 4.8 shows the dissolved O_2 saturation anomaly (ΔO_2). These data reveal a moderate amount of scatter that appears to increase close to the Equator. More

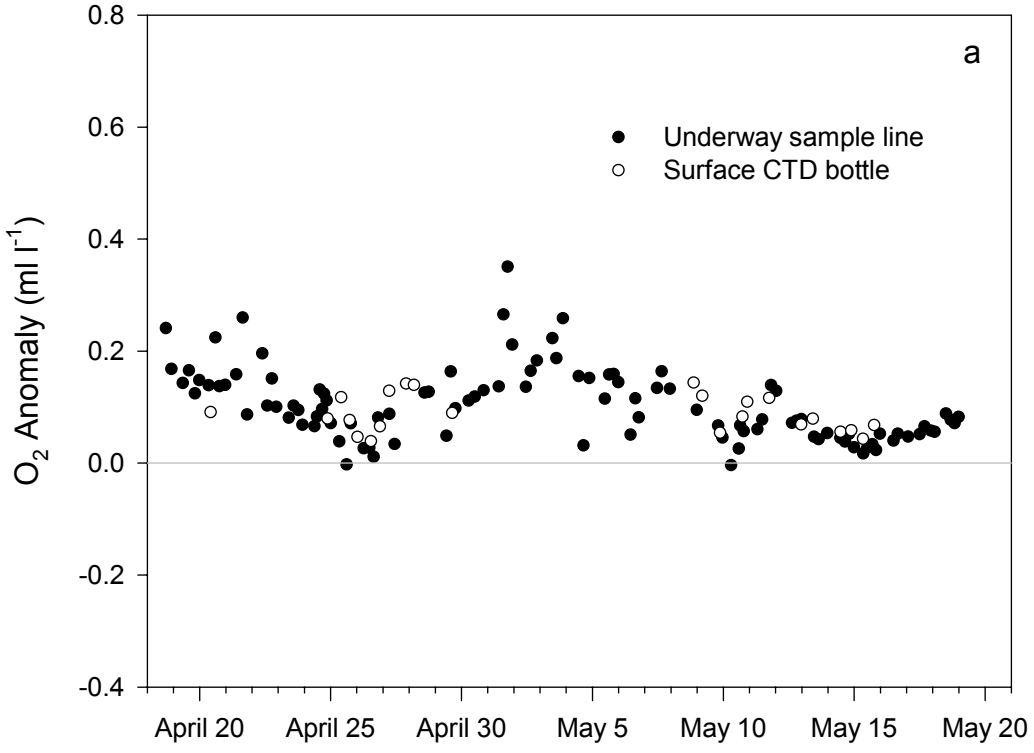

Figure 4.8 Dissolved O_2 anomaly (ΔO_2) plotted versus (a) time and (b) latitude.

importantly, they indicate that the eastern equatorial Pacific was consistently supersaturated during the time of this cruise. This is not normally the case. Figure 4.9 compares the ΔO_2 measurements from this cruise to those made by NOAA scientists along 125°W and 140°W during the US JGOFS Equatorial Pacific Process Study (EQPAC) cruises [Wanninkhof *et al*., 1995] in the boreal spring and fall of 1992, and to monthly ΔO_2 values for this region from the climatology of Najjar and Keeling [1997]. The fall EQPAC measurements were made during post-El Niño conditions, and show a strong understaturation in O_2 along the Equator that reflects local upwelling produced by Ekman divergence in this region. In contrast, the spring

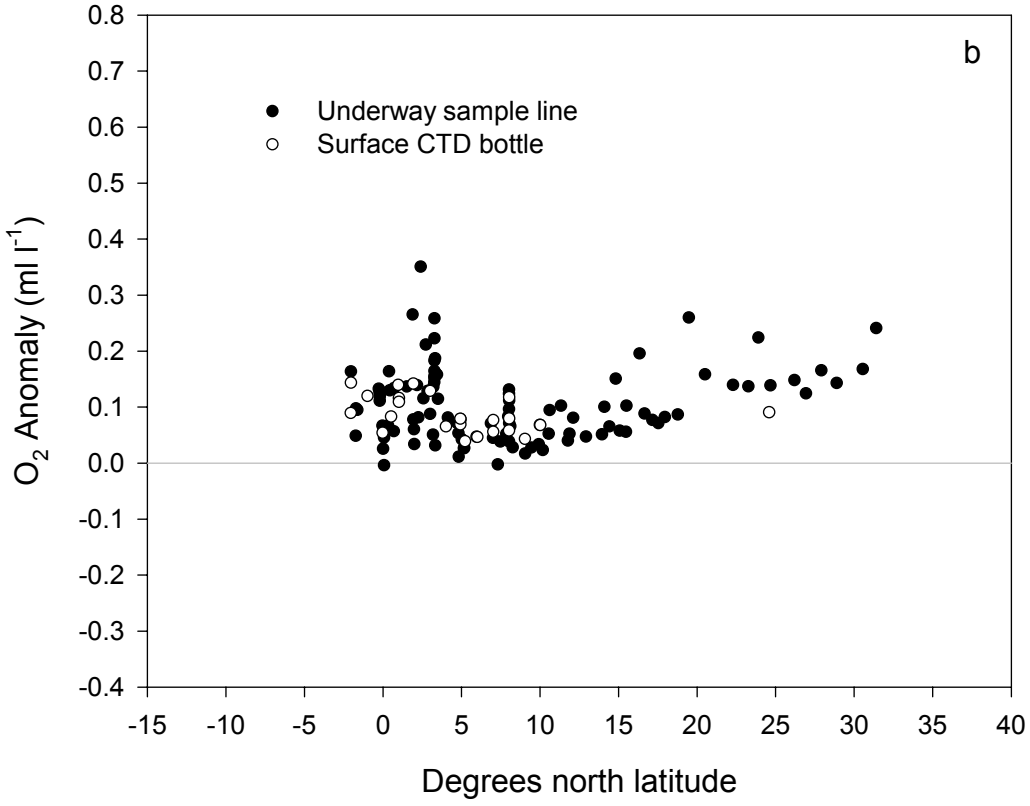

Figure 4.8 (continued)

EQPAC measurements were made during a moderate El Niño, when this upwelling was shut off. Similar to my observations, these spring El Niño data lack a strong undersaturation at the Equator.

However, the 1992 El Niño ΔO_2 values are still lower than I observed, possibly reflecting the fact that the 1997-98 El Niño event was much larger than the one in 1992 (see Section 4.6 below). Overall, these previous measurements indicate that the variability in my dissolved O_2 data is not uncommon. As illustrated by Feely *et al.* [1994] and Murray *et al.* [1994], such variability can be produced by the passage of tropical instability waves. The climatology of Najjar and Keeling [1997] is based on

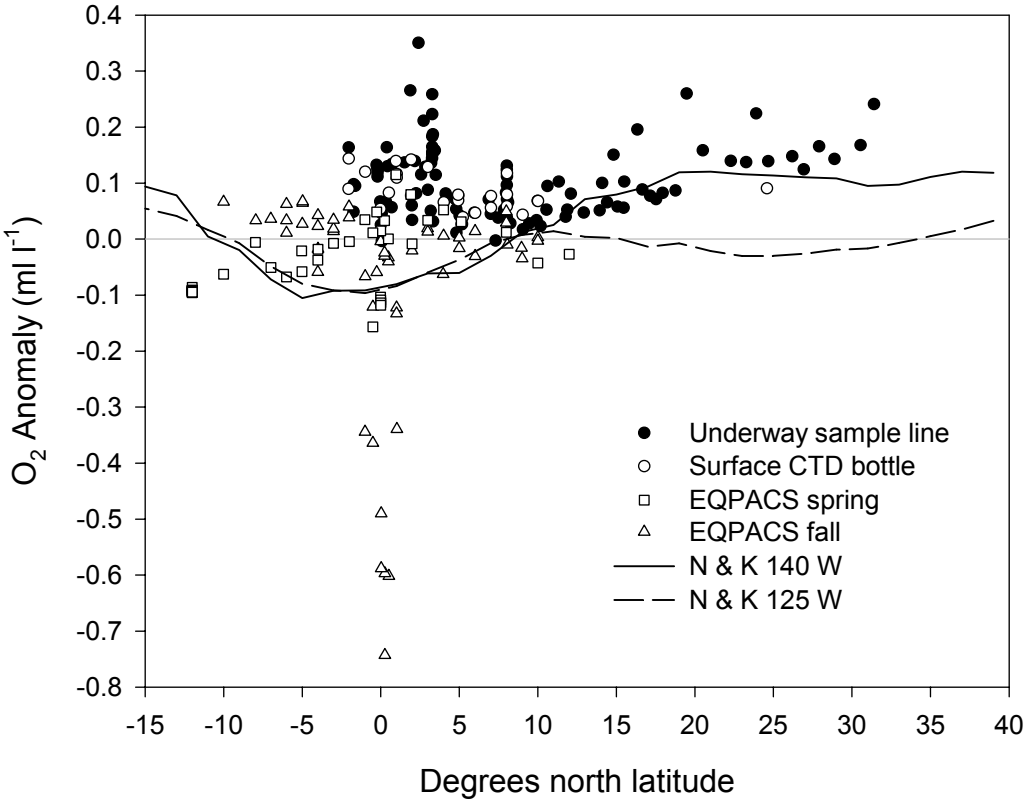

Figure 4.9 Dissolved O_2 anomaly (ΔO_2) compared to measurements during the 1992 EQPAC cruises [Wanninkhof *et al*., 1995] and the climatology of Najjar and Keeling [1997]. The spring EQPAC measurements were made during a moderate El Niño, while the fall measurements were made during non-El Niño conditions.

over 90 years of observations, and thus smooths over these waves and any interannual variability. This climatology predicts a general undersaturation of O_2 near the Equator, indicating either that the equatorial dip during non-El Niño times is on average more persistent than the supersaturation during El Niños, or an aliasing of non-El Niño periods during generation of the climatology. The saturation levels observed during this cruise along 125°W are closer to the climatology values for

140°W, again possibly reflecting the vast amount of warm, O_2-rich waters pushed eastward during the 1997-98 El Niño.

The coherent dip in ΔO_2 observed on May 1st corresponds to a northward pass across the Equator and may be a sign of a small amount of renewed local upwelling. However, it is not possible to find any correspondence between the small-scale ΔO_2 variations in Figure 4.8 and the atmospheric O_2 variations in Figures 4.2 and 4.3. It is clear that at least during this cruise, the equatorial O_2 source was too homogenous relative to the interhemispheric atmospheric gradient to imprint strong signals on the atmosphere.

4.4 Origin of Sampled Air

Manning and Keeling [1994] found that the aliasing of meridional gradients at MLO was a significant source of observed O_2 variability, and predicted that this effect would be greater at lower latitudes. The indication from Figures 4.3-4.5, that selective sampling across the strong interhemispheric gradient was the dominant source of variability in these measurements, confirms their prediction and is borne out by further meteorological analyses. To help identify the origin of the sampled air, I have calculated 72-hour back-trajectories for daily ship locations using the HYbrid Single-Particle Lagrangian Integrated Trajectory model version 4 (HYSPLIT4), developed by the NOAA Air Resources Laboratory [HYSPLIT4, 1997; Draxler and Hess, 1998]. For input fields, this model uses 1° meteorological analyses from the National Centers for Environmental Prediction. These analyses are based on a global set of

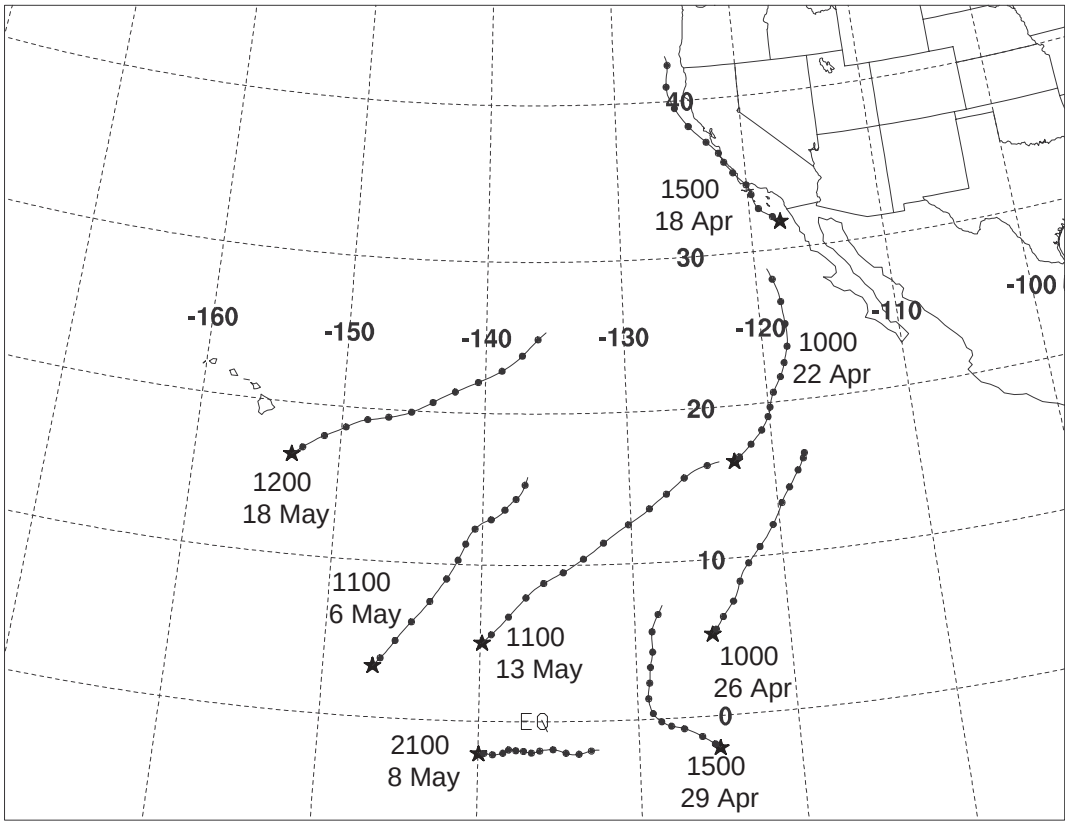

Figure 4.10 Back-trajectories calculated using the HYSPLIT4 model [HYSPLIT4, 1997; Draxler and Hess, 1998]. Trajectories were run for 72 hours, and the symbols are plotted every 12 hours UT. The end points for the trajectories (stars) correspond to actual ship positions, and are labeled in local time to facilitate comparison to the other figures.

observations, which over the ocean consist of satellite scatterometer winds and direct observations from ships, including observations made on Ka'imimoana during this cruise. The HYSPLIT4 back-trajectories (Figure 4.10) predict that the VUV instrument sampled air almost exclusively of northern hemisphere origin, but that there were significant variations in the origin of the air within the eastern Pacific

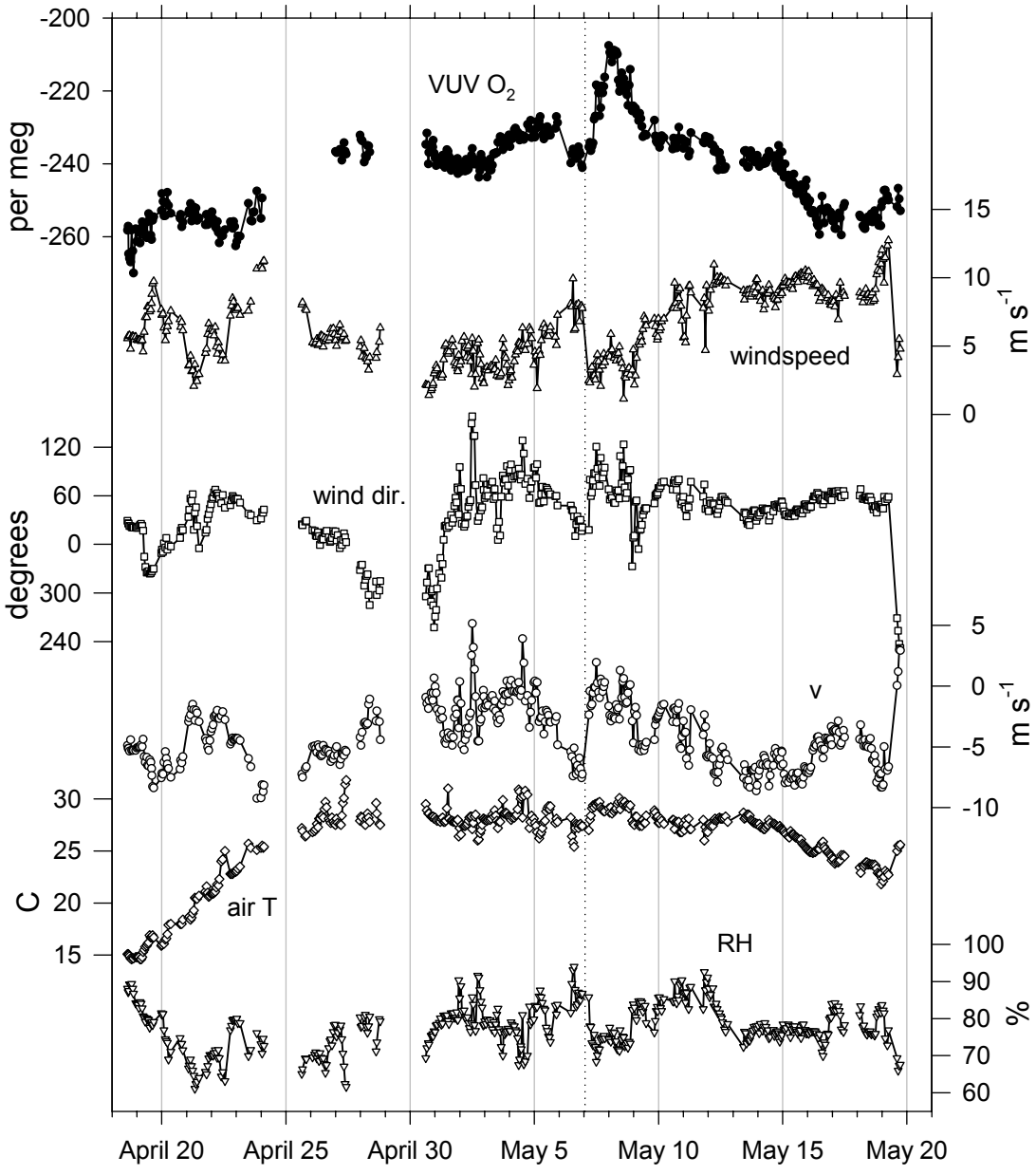

Figure 4.11 Hourly-mean shipboard meteorological data. The VUV O_2 data is the same as in Figure 4.2. This plot also includes wind speed, wind direction, northward wind component (v), air temperature, and relative humidity (RH). Vertical reference lines are plotted every 5 days at local midnight, and at 0112 local time on May 7th.

basin. These variations correspond to variations in the measured O_2 and CO_2 concentrations.

Figure 4.11 shows the O_2 data of Figure 4.6 along with concurrent measurements of wind speed, wind direction, northward wind component (v), air temperature, and relative humidity. As Figures 4.10 and 4.11 show, the air sampled near the Equator was primarily delivered by the northeasterly trades, with a few exceptions at the southern extensions of the cruise track. By the turnaround point at 2°S, 125°W, where only a flask sample is available, the winds had shifted to a northwesterly direction (Figure 4.10). This point also appears to have been a temporal peak in O_2. The GOES-9 satellite image in Figure 4.12a indicates that the ITCZ was relatively indistinct at this time. However the ship was directly under a thin line of high clouds that did exist, suggesting that it was sampling a convergent mixture of northern and southern air.

On the return back across the Equator, the winds shifted back to the northeast and O_2 decreased (Figure 4.11). During the transect to capture the drifting buoy, the ship's latitude remained relatively constant, yet on May 3rd I observed a +10 per meg and -1 ppm step in O_2 and CO_2 respectively. The back trajectories for this longitudinal transect (not shown) indicate that the observed concentration shifts correspond to a change in the origin of the air from the northeast to the east. At the end of this transect on May 6th, before the ship turned to the south, the winds increased in speed and returned to the northeast while O_2 and CO_2 returned to values close to those observed 20° to the west (Figure 4.11). Variations in the efficiency of

a.

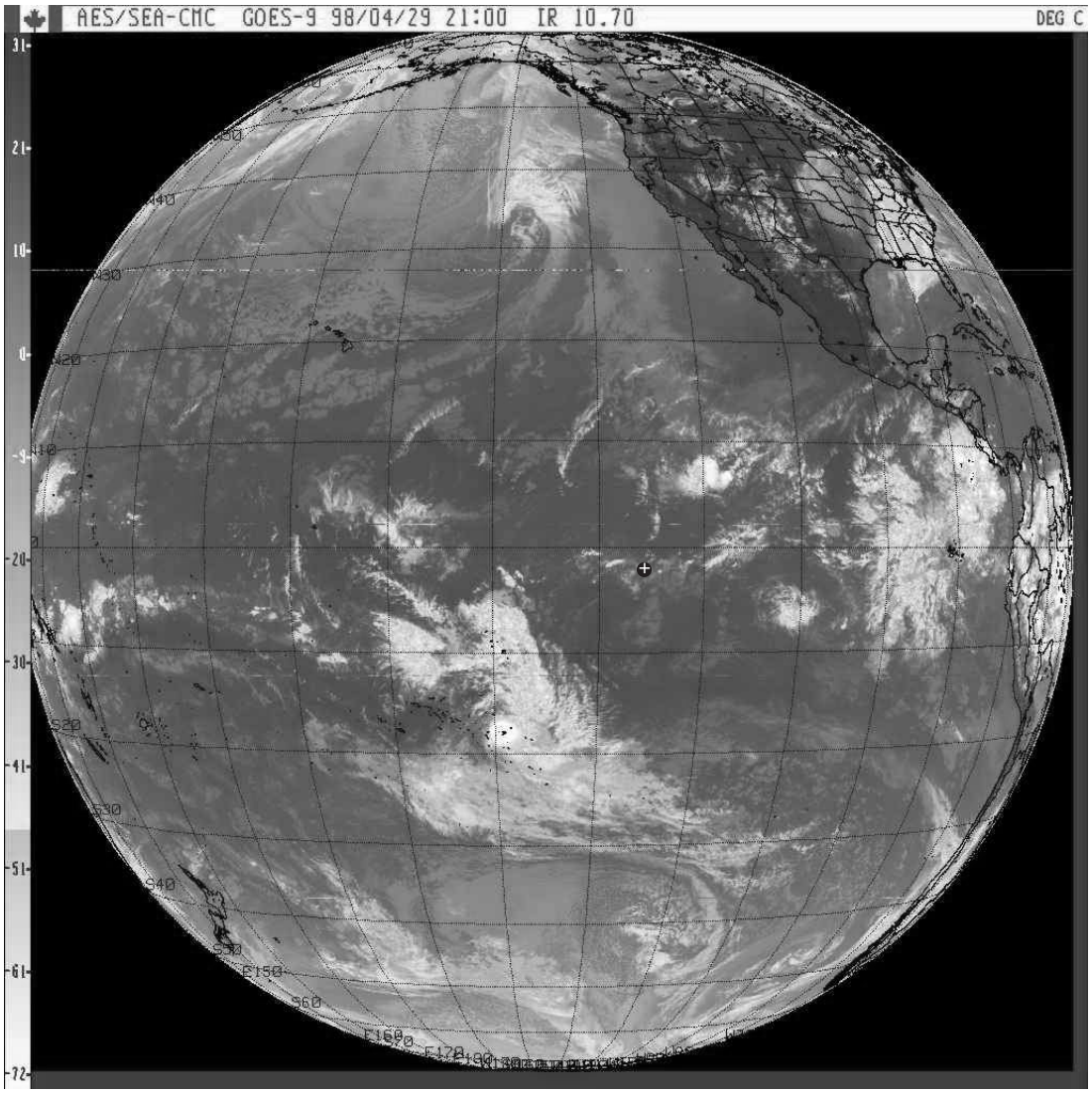

Figure 4.12 GOES-9 infrared satellite images. Selected images corresponding to (a) 1300 local time on April 29th, close to the ships furthest extent south along 125°W, (b) 1200 local time on May 7th, corresponding to the O_2 maximum measured while the ship was on its way south towards 2°S 140°W and (c) 0000 local time on May 9th, corresponding to relatively lower O_2 concentrations while the ship was near 2°S 140°W. The ship position is marked in each image by a black dot with a white hatch. Images obtained from the Canadian Meteorological Centre archives.

b.

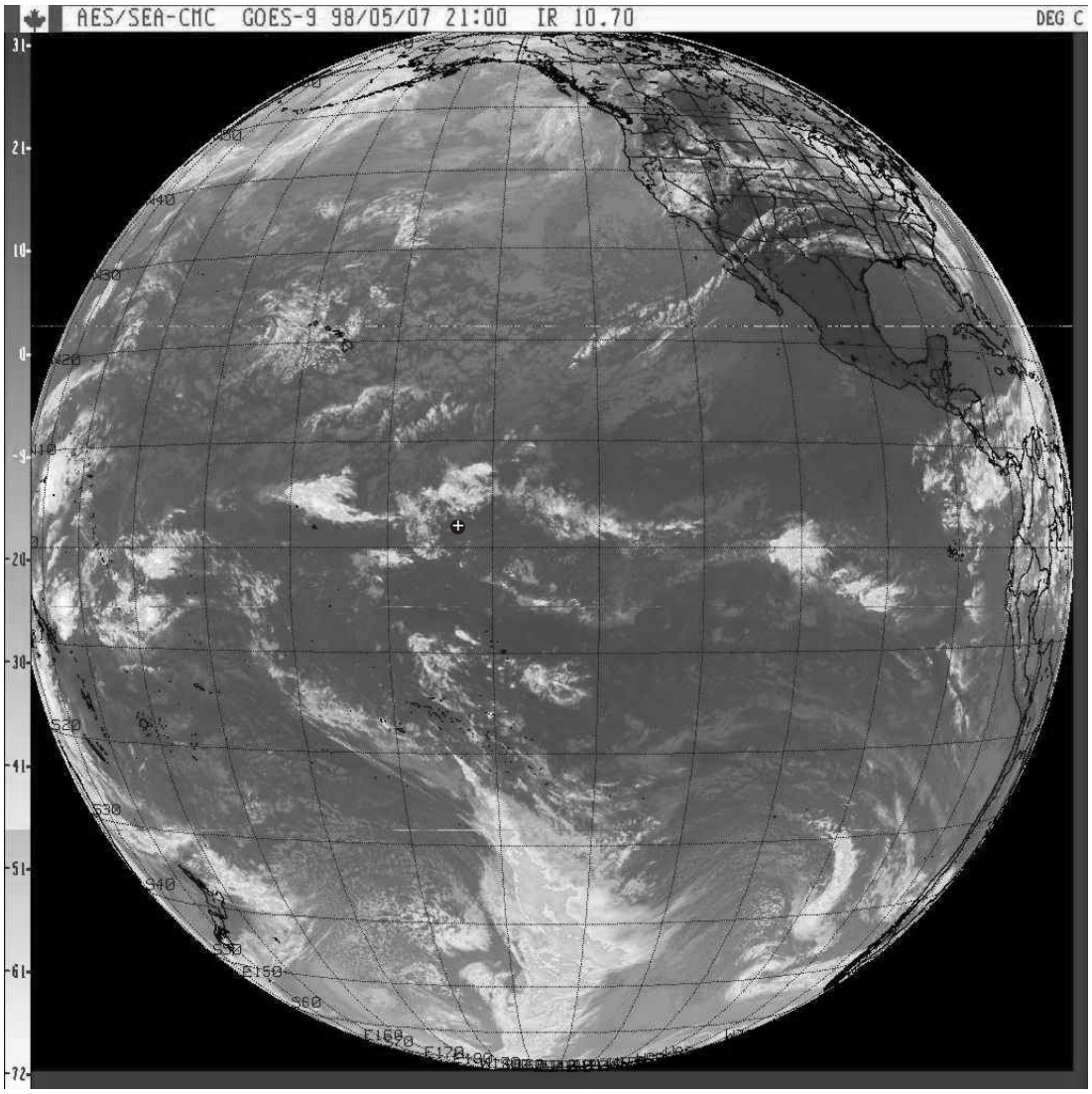

Figure 4.12 (continued)

c.

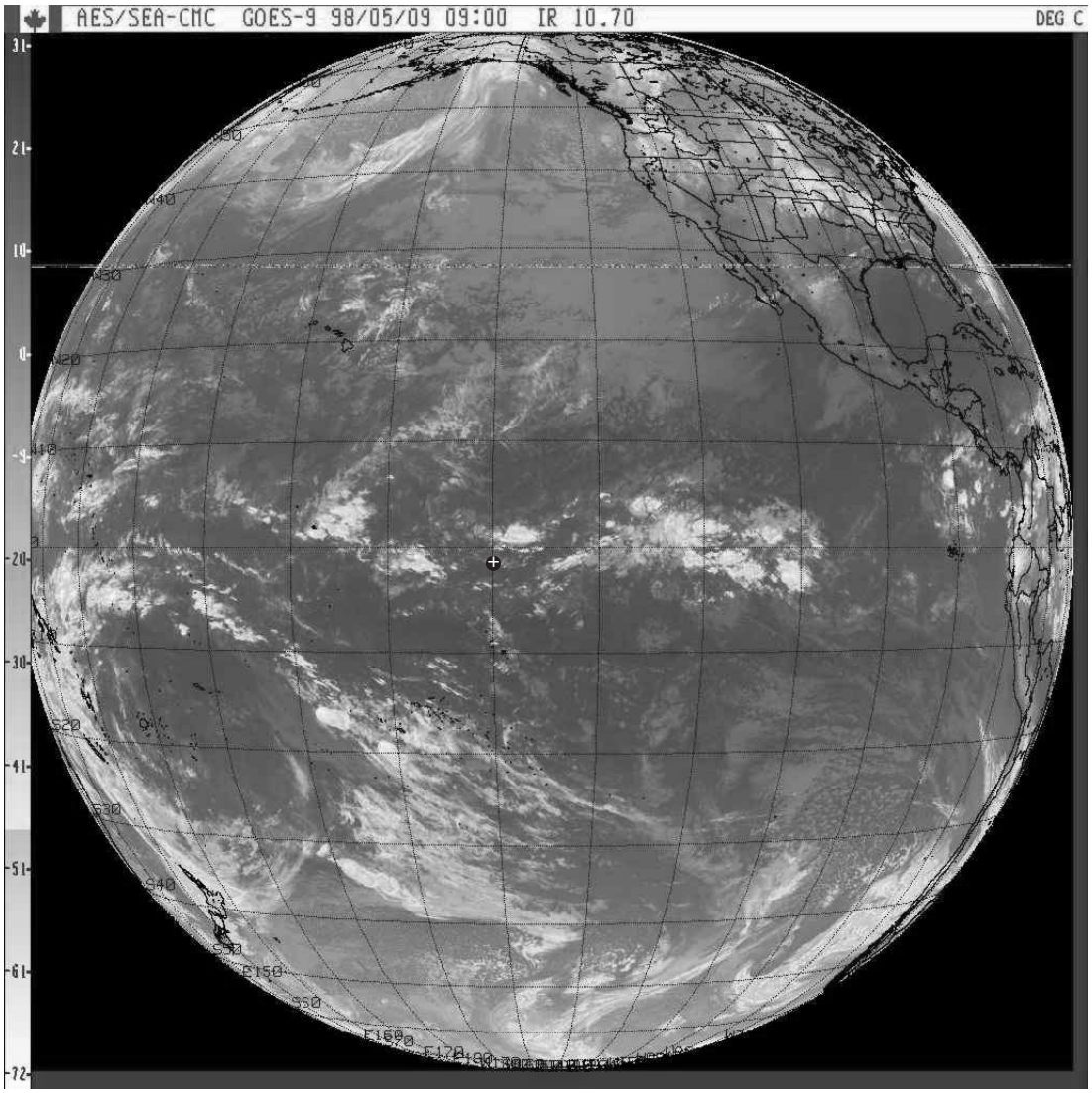

Figure 4.12 (continued)

atmospheric transport from the north appears to have produced these changes in the observed concentrations, with more efficient southward transport corresponding to low O_2 and high CO_2.

The sharpest observed change in O_2 and CO_2 occurred on May 7th as the ship headed south across the Equator. This change was coincident with a sharp slackening of the winds, a shift to a less northerly wind direction, a decrease in relative humidity, an increase in air temperature, and a change from almost complete cloud cover to mostly clear skies (Figures 4.11 and 4.12). The GOES-9 satellite image in Figure 4.12b shows that the ITCZ was relatively distinct at this time, and that the ship had just penetrated south of the main line of high clouds centered near 5°N. The ship remained under the patch of clear sky between this and a southern branch of clouds throughout most of May 8th. The O_2 and CO_2 concentrations observed aboard the ship on this day are close to those from a flask sample taken on May 5th at SMO (see Figure 4.3), suggesting that the ship was in fact sampling air primarily of southern hemisphere origin. The HYSPLIT4 model predicts that the sampled air at this time ultimately originated to the north (not shown), but this may be a model artifact resulting from the limited observations in this region. The lack of clouds could indicate descending air conditions, and it is possible that the high-O_2, low-CO_2 air moved north at a higher altitude before descending upon the ship.

The easterly back-trajectory at 2° S, 140° W in Figure 4.10 actually corresponds to a time when the O_2 and CO_2 concentrations were closer to their more northerly values (Figure 4.3). By the time the ship reached this point, the winds had

shifted back to the north, relative humidity and cloud cover had increased, and temperature had decreased (Figure 4.11). Satellite imagery from early on May 9th (Figure 4.12c) shows that the band of high clouds had shifted southwards by ~ 5° and were now effectively surrounding the ship. This combination of meteorological observations suggest that the O_2 and CO_2 concentrations observed near the Equator were highly sensitive to the position of the ship relative to the ITCZ and local synoptic weather systems. These observations highlight the difficulty of measuring seasonal and interannual variations in low-latitude O_2 using background-station or shipboard flask measurements. Discrete samples taken at biweekly or longer intervals could alias synoptic variations such as those presented here. Further evidence of this atmospheric transport uncertainty can be seen in Figure 4.4, which shows that the greatest O_2 and CO_2 variability in the SMO flask data occurs when the interhemispheric gradients are largest.

The HYSPLIT4 back-trajectories shown in Figure 4.10 may also provide clues as to the source of the observed O_2 variations at higher latitudes. The higher O_2 and lower CO_2 concentrations at the beginning and end of the cruise are as expected associated with sampling air from further north. However, as previously mentioned the variations near the beginning of the cruise are anomalous with respect to their O_2:CO_2 ratio. The back-trajectories show that during this period the sampled air was travelling from far to the north along the coast of California. The northern Pacific and California coast are both regions of relatively strong vertical mixing at this time of year, which delivers a greater O_2-deficit to the surface than local productivity can

accommodate. The resulting O_2 uptake in these regions might explain the observed drop in O_2 with constant CO_2 from April 20th to the 23rd. In support of this hypothesis, when the ship began sampling air from much further south and off the coast on the 23rd the atmospheric O_2 concentrations began a steady climb.

4.5 Comparison to Model Estimates

While the O_2 and CO_2 variations discussed thus far appear to be consistent with interhemispheric mixing superimposed by synoptic variability, with little influence from local air-sea gas exchange, I have yet to address the broader implications of the average concentrations. Considering the large disparity among the equatorial O_2 patterns predicted by the three models in Chapter 2 (Figure 2.4) these VUV measurements have the potential to shed some light on the actual air-sea O_2 exchange in this region. To compare the observations to model estimates, I have calculated atmospheric potential oxygen concentrations according to

$$\text{APO (per meg)} = \delta(O_2/N_2) + (CO_2 - 363.29) \times 1.1 / X_{O_2} \quad (4.1)$$

This equation differs from Equation 2.4 in that it does not include CO or CH_4 corrections, and it establishes an arbitrary reference point that corresponds to the reference cylinders used to define zero on the Scripps O_2/N_2 scale. The resulting latitudinal APO variations observed during this cruise are shown in Figure 4.13.

The southwards-increasing gradient in APO results from the industrial and seasonal-oceanic influences discussed in Section 4.2 above. In addition, the APO values between 10°N and 20°N in Figure 4.13 reveal a longitudinal/temporal

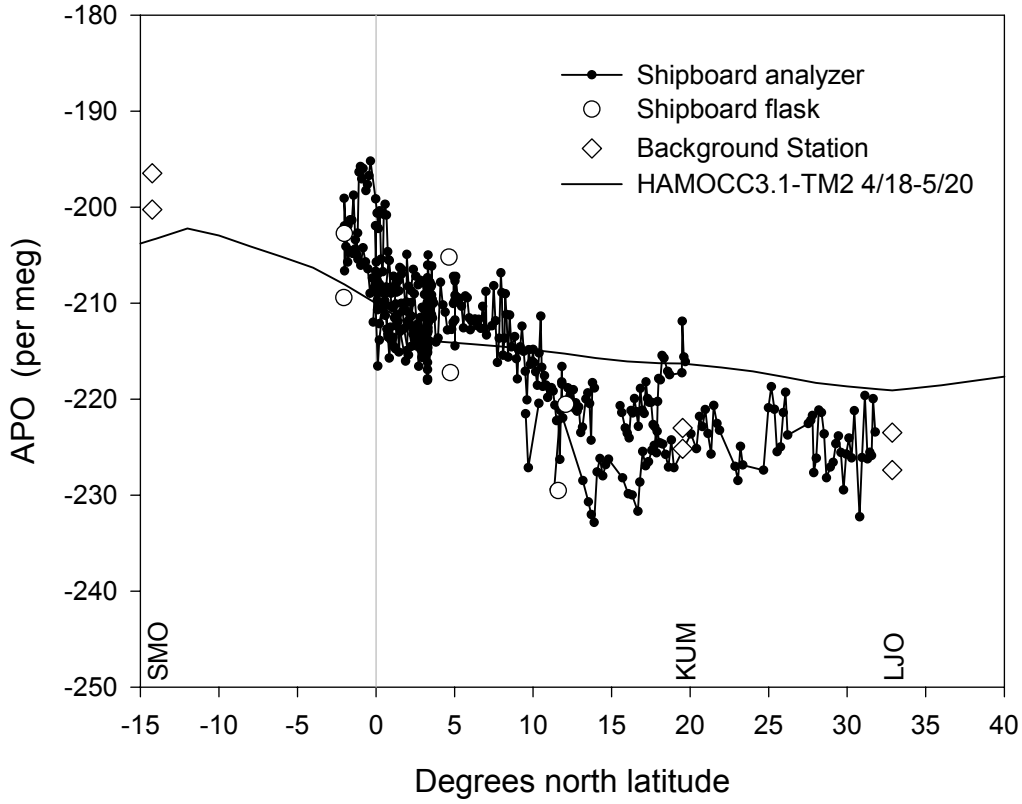

Figure 4.13 Hourly-mean shipboard concentrations of the derived tracer APO compared to HAMOCC3.1-TM2. The flask samples from SMO, LJO, and KUM are the same as in Figure 4.3. The model prediction corresponds to a mean from April 18th to May 20th, interpolated along the track in Figure 7.1, and adjusted vertically to optimize its fit to the background sites.

difference of 5-10 per meg that is larger than that for O_2 or CO_2 alone. The temporal nature of this difference is consistent with the rapidly increasing APO concentrations in the northern hemisphere at this time of year (see Figure 2.8). However, it may also include an oceanic signal resulting from greater uptake, or less release, of O_2 and CO_2 in the eastern Pacific, and in fact HAMOCC3.1-TM2 predicts a longitudinal APO gradient of 2.5 per meg for this time and these locations. Of the models used in Chapter 2, only HAMOCC3.1-TM2 has seasonal variations that can be directly

compared to these measurements. LLOBM has a seasonal cycle, but because its biological parameterization does not accurately reproduce seasonal air-sea O_2 flux variations (see discussion in Section 2.4) I have only used its annual mean fluxes here.

The curve in Figure 4.13 represents the predictions of HAMOCC3.1-TM2 averaged over the time of year of the cruise, along a track from SMO to KUM passing through the Equator near the area of this cruise (see Figure 7.1). There are two features of low-latitude atmospheric O_2 that should be matched by such a model: the absolute difference across the Equator as measured between locations such as SMO and KUM or LJO, and the curvature of the gradient between these points. The absolute low-latitude interhemispheric O_2 difference is likely determined by processes outside the tropics, while the local curvature of the gradient should be sensitive to Equatorial outgassing or ingassing.

The HAMOCC3.1-TM2 model is unable to reproduce the total LJO-SMO difference at this time (Figure 4.13), or for the long-term mean (see Table 2.2), thus making it difficult to compare the predicted curvature. However, if I shift the model-predicted gradient to minimize the total error at these two stations, its predictions at the Equator are in fairly good agreement with the shipboard observations. It does not produce an APO minimum as observed near 15°N, but it does predict a large jump in APO at the Equator, as observed.

Although seasonal predictions are not available from the other two models used in Chapter 2, it is possible to derive an annual mean estimate from the measurements. The seasonal data shown in Figure 2.8 indicate that APO at low

latitudes has a relatively small seasonal cycle and that at this time of year it is close to its annual-mean value. To avoid having to make large seasonal corrections, I have excluded the clearly trending APO values south of the Equator and north of 8°N (see Figure 4.13) and have simply averaged the observations between these two latitudes. I have also excluded observations before the fractionation problem was resolved, and thus include only data from April 30th - May 15th. The resulting mean value is -210.8 per meg.

The HAMOCC3.1-TM2 model, which is successful at reproducing the seasonal cycles in Figure 2.8, predicts that in this region APO has a seasonal peak-to-peak amplitude of 15 per meg, and that at this time its value is only 1.1 per meg above the annual mean. I have therefore subtracted 1.1 per meg from the calculated average, and obtain a value of -211.9 per meg at a mean position of 2° 56' N, 137° 42' W. I have calculated an error of ± 5.0 per meg for this annual mean estimate by geometrically summing the statistical error from averaging 213 hourly observations (± 3.3 per meg), the absolute accuracy estimate from Chapter 3 (± 3 per meg), and a value equal to 200% of the seasonal adjustment (± 2.2 per meg). As in Chapter 2, I have not attempted to estimate the uncertainty due to interannual variability, however as discussed in the next section it may be significant.

Figure 4.14 compares the annual-mean equatorial estimate to the model predictions along the track in Figure 7.1. I have also included annual means from SMO and KUM centered on May 1, 1998 in this figure, and have adjusted the model gradients to minimize their error relative to these two background-station values.

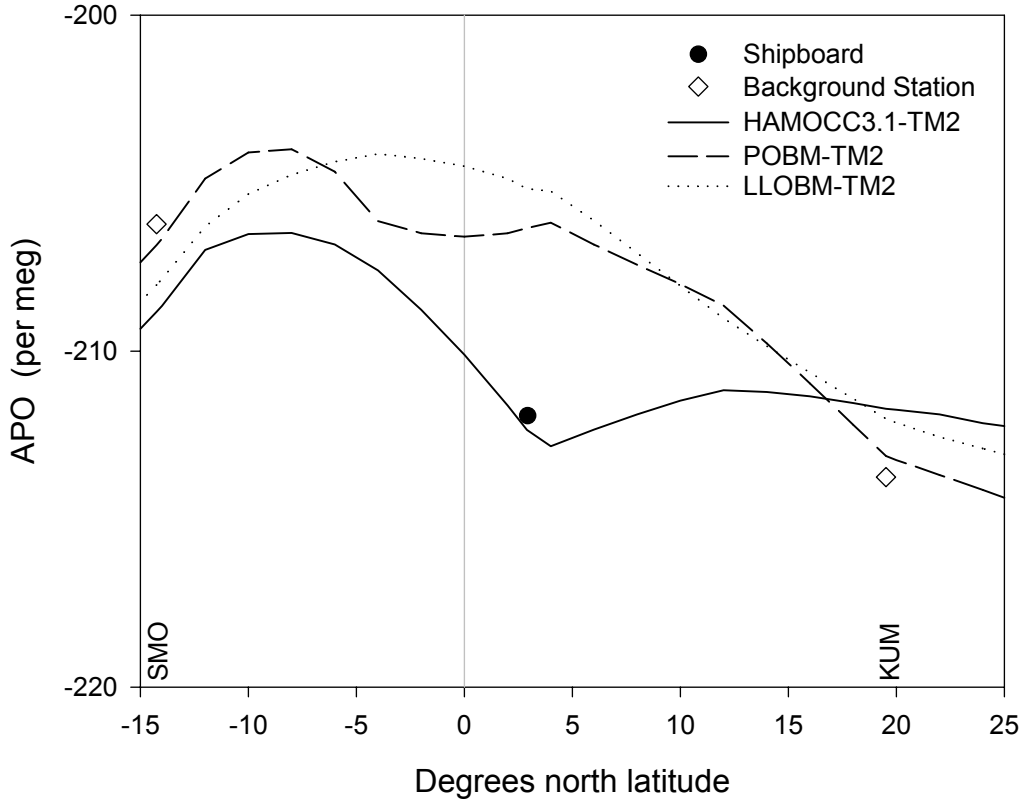

Figure 4.14 Annual-mean APO estimate compared to HAMOCC3.1-TM2, POBM-TM2, LOBM-TM2 predictions. The flask-station values for SMO, KUM are annual means centered on the time of the cruise. The model predictions have been interpolated along the track in Figure 7.1 and vertically adjusted to optimize their fits to the background sites.

Similar to the direct comparison in Figure 4.13, HAMOCC3.1-TM2 underpredicts the overall gradient but gets the relative position of the equatorial value approximately correct. The other two models, POBM-TM2 and LLOBM-TM2, predict a large equatorial APO peak that is not supported by these *in situ* observations. It is apparent from Figure 2.3d, that the HAMOCC3.1 model predicts less equatorial outgassing of O_2 than the other two models. Although not as apparent in Figure 2.3c, this is also the case for CO_2. These differences in annual mean O_2 and CO_2 outgassing could explain

much of the gap between the models' equatorial APO predictions, as well as the POBM-TM2 and LLOBM-TM2 discrepancies with the observations of 5-6 per meg (Figure 4.14).

Another factor that may be involved is the seasonal marine O_2 rectifier, which I have hypothesized (Section 2.7) could cause equatorial surface stations to preferentially see air from the winter hemisphere. The two aseasonal models, POBM-TM2 and LLOBM-TM2, can not account for such an effect. Because the ship was primarily sampling air from the northern hemisphere that carried a strong winter signal, the lack of seasonal resolution in these models may explain some of their disagreement with the observations and with HAMOCC3.1-TM2. However, the TM2 curve in Figure 2.6 indicates that adding the predicted marine O_2 rectifier to the other models would degrade their prediction of the SMO-KUM difference by 2 per meg while only improving their equatorial predictions relative to these two background stations by 3 per meg. Although large uncertainties still exist with respect to the numerical representation of rectifier effects, this limited analysis suggests that other effects must contribute to the discrepancies in Figure 4.14.

4.6 The Effect of El Niño

Because the predictions of the three models in Figure 4.14 represent climatological means, interannual variability such as that associated with El Niño events could affect their success at matching observations. This month-long cruise coincided with the end of the largest El Niño event on record. At the midpoint of the

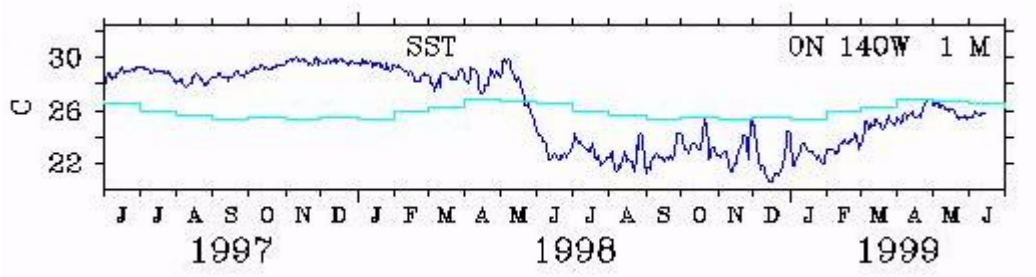

Figure 4.15 Sea surface temperatures measured at the 0°N 140°W TAO buoy. Figure obtained from the TAO realtime web display [TAO, 1999]. The dark curve represents the SST measurements and the light curve the climatological means.

cruise the sea surface temperature (SST) on the Equator at 140°W was 3°C above average, at the end of the cruise it was average, and two weeks later it was 3°C below average (Figure 4.15). This sudden collapse of the El Niño event requires a certain amount of caution in interpreting coincident equatorial Pacific measurements. However, if the response of atmospheric gas concentrations to oceanic perturbations were slower than ~ one week, these measurements would represent close to full El Niño conditions.

Feely *et al.* [1994], Murray *et al.* [1994], Feely *et al.* [1995], and Wanninkhof *et al.* [1995] provide in-depth discussions of the marine biogeochemical responses to El Niño, as characterized by their EQPAC measurements during and after the moderate 1991-1992 El Niño event. This study found O_2 undersaturation anomalies along the Equator at 125°W as large as -0.75 ml l^{-1} during the boreal autumn post-El Niño period compared to smaller than -0.2 ml l^{-1} during the spring El Niño period [Wanninkhof *et al.*, 1995] (Figure 4.9). In addition, these scientists found surface pCO_2 levels that were 15 to 55 μatm lower during El Niño conditions than during

post-El Niño conditions, and inferred a reduction in the annual sea-air CO_2 flux from this region of 0.5-0.7 Gt C [Feely *et al.*, 1995]. They attributed these marked changes to the advection of CO_2-depleted, O_2-enriched water from the west and the locally reduced upwelling of CO_2-enriched, O_2-depleted water.

The ΔO_2 measurements (Figure 4.9) from this cruise clearly show that these effects were present and probably greater in magnitude than for the 1991-1992 El Niño. The implications of the combined O_2 and CO_2 effects for APO fluxes are complex. During the initial stages of an El Niño a local O_2 outgassing, or reduced ingassing, may result from the decreased upwelling of O_2-depleted waters, followed at a slightly longer response time by an associated CO_2 ingassing signal. Eventually however, as the broader equatorial Pacific region comes into equilibrium with the reduced input of preformed nutrients from below, an O_2 ingassing signal will result (see discussion in Section 2.2). Furthermore, the reduced air-sea heat flux in this region during El Niño will result in less outgassing of both O_2 and CO_2. Le Quéré *et al.* [1999] have investigated these effects using a version of the Océan Parallélisé (OPA) model that has high equatorial resolution and is forced by meteorological and oceanic observations over the period January 1979 through December 1997. This model qualitatively reproduces the timing of events outlined above for CO_2 [Le Quéré *et al.*, 1999] and O_2 (C. Le Quere, personal communication, 1999). The net effect of El Niño on APO in this model is an ingassing signal that lags the Southern Oscillation Index by approximately one year.

I have used these results to get an indication of the potential sensitivity of the observations to El Niño variability. By extrapolating the OPA model predictions, I obtained an estimate for an anomalous APO sink at the time of this cruise of 1.0 ± 0.5 mol m^{-2} yr^{-1} from 15°S to 15°N in the Pacific. I have not included the effect of thermal N_2 fluxes in this estimate, which would have a small compensating effect on the apparent APO flux. Using this flux estimate as a lower boundary condition for the TM2 atmospheric transport model (S. Piper, personal communication, 1999) produces a steady-state APO concentration at the Equator that is 3 per meg lower than at SMO and KUM. This implies that the shipboard observations might be an underestimate of the climatological values represented by the models. However, the O_2 ingassing prediction of the OPA model requires that dissolved O_2 concentrations be lower than average. In contrast, the observations (Figure 4.9) from this cruise suggest that they were significantly higher than average. This suggests an anomalous APO outgassing, which would imply that the shipboard observations were actually an overestimate of climatological conditions.

Another potentially significant El Niño influence on these observations is through altered wind patterns. The winds on the Equator at 140°W were much more northerly and much less easterly during the 1997-98 El Niño event, which at the time of year of this cruise would have led to anomalously low APO concentrations. However, by the time of the cruise the wind had already returned to close to its normal velocity and direction, in advance of the SST shift [McPhaden, 1999; TAO, 1999].

Many of these issues could be resolved by future equatorial Pacific O_2 measurements during non-El Niño conditions.

4.7 Conclusion

In this chapter, I have presented the first field-based measurements of atmospheric O_2 variations and the first extensive measurements of atmospheric O_2 in the equatorial region. Comparisons between these measurements and concurrent shipboard and background-station flask measurements demonstrate that a shipboard VUV instrument is capable of accurately detecting meaningful changes in atmospheric O_2 on time scales of hours to weeks and on space scales of tens to hundreds of kilometers. Comparisons with atmospheric CO_2, dissolved O_2, and meteorological measurements from this cruise show that equatorial atmospheric O_2 concentrations at this time of year are strongly influenced by atmospheric mixing processes. As a result of the strong oceanic, terrestrial, and industrial influences on the latitudinal gradients, O_2 concentrations were lower and CO_2 concentrations higher when the ship sampled air from further north. Likewise, I observed the highest O_2 and lowest CO_2 concentrations when the ship briefly sampled air that was primarily of southern hemisphere origin.

The dissolved O_2 measurements from this cruise indicate that the equatorial surface was consistently supersaturated with respect to O_2, an anomalous condition tied to the large El Niño event at this time. The uncertainties associated with the effect of El Niño on equatorial atmospheric O_2 and CO_2 somewhat limit the ability of these

measurements to constrain climatological-mean model simulations. Nonetheless, I have made preliminary comparisons between these measurements and the predictions of three chemically-coupled atmosphere-ocean carbon cycle models, based on the derived tracer APO. These comparisons suggest that both the amount of equatorial outgassing of O_2 and the representation of the marine O_2 rectifier are important to predictions of low-latitude meridional atmospheric O_2 gradients.

These comparisons also provide a framework for using future measurements to investigate the seasonal and interannual controls on equatorial atmospheric O_2. Because atmospheric O_2 is more sensitive to oceanic perturbations than is atmospheric CO_2, equatorial O_2 measurements have the potential to significantly improve our understanding of the response of the ocean carbon cycle to natural and anthropogenic climate perturbations. Initially resolving the influence of rectification effects on annual-mean concentrations will require repeated measurements at several different times of year. Then, rigidly constraining the amount of equatorial O_2 outgassing in models, and quantifying its interannual variability, will require repeated measurements over several years.

Recently M. Bender has undertaken a Pacific atmospheric O_2 measurement program based on flask samples collected from a north-south transecting commercial ship. This program promises many insights into global biogeochemical cycling. However, as noted above, the flask samples taken near the Equator during spring and fall are likely to be highly variable due to selective sampling across the interhemispheric gradient. High-resolution continuous field-based measurements,

such as the VUV measurements presented here, can provide additional information on the sources of O_2 variability and improved estimates of mean concentrations. The NOAA ship Ka'imimoana is an advantageous platform for future VUV O_2 measurements because of its repeatable transects over a wide range of longitudes, and the extended periods of time spent near the Equator.

4.8 References

Carpenter, J. H., The Chesapeake Bay Institute technique for the Winkler dissolved oxygen method, *Limnol. Oceanog.*, *10*, 141-3, 1965.

Draxler, R. R., and G. D. Hess, An overview of the HYSPLIT_4 modelling system for trajectories, dispersion, and deposition, *Aust. Met. Mag.*, *47*, 295-308, 1998.

Feely, R. A., R. Wanninkhof, C. E. Cosca, M. J. McPhaden, R. H. Byrne, F. J. Millero, F. P. Chavez, T. Clayton, D. M. Campbell, and P. P. Murphy, The effect of tropical instability waves on CO_2 species distributions along the equator in the eastern equatorial Pacific during the 1992 ENSO event, *Geophys. Res. Lett.*, *21*, 277-280, 1994.

Feely, R. A., R. Wanninkhof, C. E. Cosca, P. P. Murphy, M. F. Lamb, and M. D. Steckley, CO_2 distributions in the equatorial Pacific during the 1991-1992 ENSO event, *Deep-Sea Res. II*, *42*, 365-386, 1995.

HYSPLIT4, HYbrid Single-Particle Lagrangian Integrated Trajectory Model, Web address: http://www.arl.noaa.gov/ready/hysplit4.html, NOAA Air Resources Laboratory, Silver Spring, MD, 1997.

Keeling, R. F., Development of an interferometric oxygen analyzer for precise measurement of the atmospheric O_2 mole fraction, Ph.D. thesis, 178 pp., Harvard Univ., Cambridge, Mass., 1988.

Keeling, R. F., and S. R. Shertz, Seasonal and interannual variations in atmospheric oxygen and implications for the global carbon cycle, *Nature*, *358*, 723-727, 1992.

Le Quéré, C., J. C. Orr, P. Monfray, O. Aumont, and G. Madec, Interannual variability of the oceanic sink of CO_2 from 1979 to 1997, submitted to Global Biogeochemical Cycles, 1999.

Manning A. C., and R. F. Keeling, Correlations in short-term variations in atmospheric oxygen and carbon dioxide at Mauna Loa Observatory, in *Climate Monitoring and Diagnostics Laboratory No. 22 Summary Report*, edited by J. T. Peterson, pp. 121-123, NOAA ERL, Boulder, CO, 1994.

McPhaden, M. J., Genesis and evolution of the 1997-1998 El Niño, *Science*, *283*, 950-954, 1999.

Murray, J. W., R. T. Barber, M. R. Roman, M. P. Bacon, and R. A. Feely, Physical and biological controls on carbon cycling in the equatorial Pacific, *Science*, *266*, 58-65, 1994.

Najjar, R. G., and R. F. Keeling, Analysis of the mean annual cycle of the dissolved oxygen anomaly in the World Ocean, *J. Marine Res.*, *55*, 117-151, 1997.

Severinghaus, J. P., Studies of the terrestrial O_2 and carbon cycles in sand dune gases and in Biosphere 2, Ph.D. thesis, 148 pp., Columbia Univ., New York, 1995.

TAO, The Tropical Atmosphere Ocean Array, Web address: http://www.pmel.noaa.gov/toga-tao, NOAA Pacific Marine Environmental Laboratory, Seattle, WA, 1999.

Wanninkhof, R., R. A. Feely, D. K. Atwood, G. Berberian, D. Wilson, P. P. Murphy, and M. F. Lamb, Seasonal and lateral variations in carbon chemistry of surface water in the eastern equatorial Pacific during 1992, *Deep-Sea Res. II*, *42*, 387-409, 1995.

Chapter 5

Shipboard Atmospheric O_2 Measurements in the Southern Ocean

Abstract

I have measured atmospheric O_2 using the VUV instrument aboard the NSF ship Lawrence M. Gould in the Southern Ocean. The cruise took place in early October of 1998, and crossed Drake Passage from Palmer Station, Antarctica to Punta Arenas, Chile over a period of 7 days. The data presented here reflect the strong austral winter and early-spring Southern Ocean O_2 sink, with very low atmospheric O_2 concentrations in Drake Passage increasing to the north. In addition, I observed significant small-scale variability in O_2, including a 20 per meg step increase that occurred over several hours. This feature appears to have corresponded to the passage of an atmospheric front, which resulted in the delivery to the ship of air less influenced by the Southern Ocean O_2 sink. These O_2 measurements allow the differentiation between oceanic and industrial influences on simultaneous atmospheric CO_2 measurements. The clean-air O_2 variations were anticorrelated with CO_2 concentrations at a slope of -5 mol O_2:mol CO_2. This implies an influence from CO_2 outgassing on the atmospheric gradients at this latitude and time of year. This CO_2 outgassing is in contrast to the HAMOCC3.1 model, which predicts CO_2 ingassing at this time of year, and with the coupled HAMOCC3.1-TM2 model, which predicts positive correlations between O_2 and CO_2 gradients. Overall, the measured O_2 concentrations are in agreement with recent flask measurements initiated at Palmer Station, and significantly lower than flask measurements at Cape Grim and the South Pole. The annual-mean O_2 difference between Palmer Station and the South Pole may be significantly influenced by a seasonal rectification process.

5.1 Introduction

The Southern Ocean may be particularly sensitive to potential future climate change, and will likely play a critical role in the amount of anthropogenic CO_2 absorbed by the oceans in the next 100 years [Sarmiento and Le Quéré, 1996]. Despite a long recognition of the region's global importance, its harsh conditions have allowed only limited oceanographic and atmospheric observations, leaving much unknown about local biogeochemical processes. As discussed in Chapter 2, flask samples collected at the South Pole (SPO) and Cape Grim, Tasmania (CGO) reveal much higher O_2 concentrations than predicted by coupled atmosphere-ocean carbon cycle models. In addition, comparisons between these stations lead to the perplexing conclusion that annual-mean O_2 concentrations are higher at SPO than at CGO, without any known annual-mean O_2 sources at high southern latitudes [Keeling *et al.*, 1998].

Recent measurements in our laboratory on flask samples from Palmer Station (PSA, 64° 46' S, 64° 3' W) show O_2 concentrations that are much closer to the predictions of the three coupled ocean-atmosphere models in Chapter 2, but which make the annual-mean SPO values even harder to explain with a steady source/sink distribution. These measurements suggested that either the meridional O_2 gradients at high southern latitudes are much stronger than observed for other atmospheric species, or that some unknown systematic bias might be affecting the SPO flask measurements. To address these growing questions, I implemented the VUV O_2 analyzer described in Chapter 3 aboard the NSF ship Lawrence M. Gould in the Southern Ocean. The

resulting measurements presented here show short-term variations in O_2 and CO_2 that are traceable to oceanic and industrial influences. In addition, these measurements confirm the low O_2 concentrations at Palmer Station (PSA). The discussion in Section 5.7 provides a possible explanation for the relatively higher annual-mean O_2 concentrations observed at SPO.

The Lawrence M. Gould conducts research cruises throughout the Southern Ocean, but during the spring and fall of each year it makes several rapid transits from Punta Arenas, Chile to PSA in order to resupply the station and change personnel. Similar to the NOAA ship Ka'imimoana (Chapter 2), this vessel provides an excellent opportunity for conducting atmospheric and oceanographic surveys that can be closely repeated in the future. The spring and fall also happen to be interesting times to measure atmospheric O_2 at these latitudes, as they correspond to the trough and peak of the relatively large O_2 seasonal cycle (see Figure 2.8). I participated on cruise leg 98-8a, the second resupply cruise of the austral spring, which left Punta Arenas on September 27th and returned on October 8th, 1998.

Unfortunately, the VUV equipment was mistakenly loaded onto the previous cruise and then mistakenly offloaded at PSA. Consequently, I was only able to make measurements during the return leg. Figure 5.1 shows the cruise track during this period. The ship left PSA on October 2, spent most of October 4th off King George Island while equipment and crew were offloaded at the Copa summer field station, and then steamed back to Punta Arenas passing to the east of Tierra del Fuego. Despite the shortened measurement period, the 7 days of measurements that I did obtain

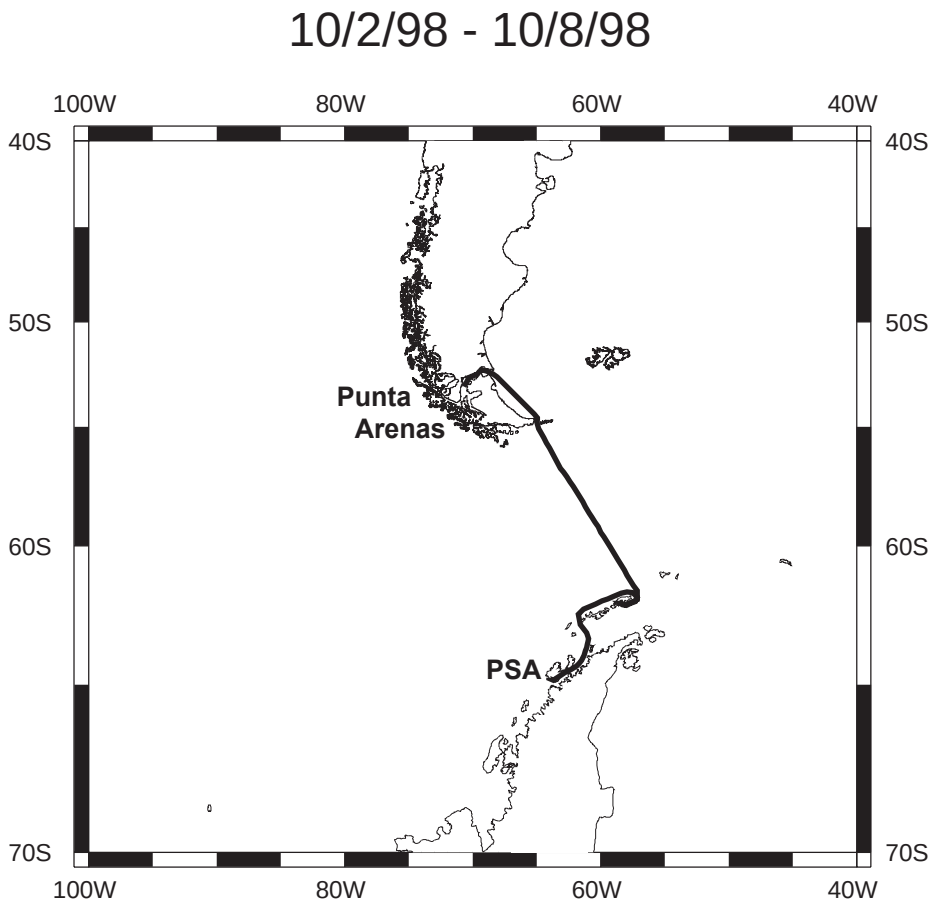

Figure 5.1 Map showing the cruise track for the return leg of Lawrence M. Gould cruise 98-8A.

provide a good measure of the background atmospheric O_2 concentrations, and insights into the causes of their variability at these latitudes and this time of year.

Most background flask-sampling stations are located in the marine boundary layer and downstream of large ocean areas, for the primary reason of avoiding the

influence of strong terrestrial and industrial CO_2 sources. However, this places them very close to the strong oceanic O_2 sources and sinks. Thus, we expect to see stronger gradients and short-term variability in O_2 than in CO_2 at these locations. The marine boundary-layer data presented here, for example, show short-term O_2 variations that were approximately 5 times greater than anticorrelated CO_2 variations on a molar basis.

In addition, meteorological analyses show that the short-term variations, similar to those shown in Chapter 4, resulted from variations in the origin of the sampled air, with higher O_2 concentrations and lower CO_2 concentrations associated with air from more northern latitudes. The observed O_2:CO_2 ratio probably represents the ratio between air-sea O_2 and CO_2 exchange integrated over several months and a relatively large area of the Southern Ocean. In austral winter and early spring, the ocean around Antarctica is a strong sink for O_2, because of the low biological productivity and vigorous vertical mixing of O_2-depleted waters. Thus, the observed anticorrelation between O_2 and CO_2 implies a Southern Ocean CO_2 source, which conflicts with a HAMOCC3.1-predicted CO_2 sink at this time of year. Because of the dominant effect of synoptic atmospheric variations, the passage of the ship over the strong oceanographic fronts in Drake Passage did not appear to significantly affect the measured O_2 concentrations.

I have combined the O_2 and CO_2 data to compare these measurements to the seasonal predictions of the HAMOCC3.1-TM2 model on the basis of the derived tracer atmospheric potential oxygen (APO). This model appears to slightly

underestimate the APO measurements of this cruise relative to those at CGO at this time of year. I have also used the seasonal-cycle amplitudes measured at PSA to place these APO measurements in an annual mean context for comparison to predictions of the POBM-TM2 and LLOBM-TM2 models. The estimated annual-mean concentrations relative to CGO are close to the prediction of LLOBM-TM2, but below the prediction of POBM-TM2. However, the large seasonal-cycle limits the annual-mean constraints that can be placed by these measurements.

The VUV O_2 measurements are in good agreement with simultaneous shipboard flask samples, subsequently analyzed on the Scripps interferometer [Keeling *et al*., 1998], as well as with projections based on PSA flask samples. The shipboard data show O_2 concentrations that were 6 per meg lower than concentrations projected at SPO for this time. Closer examination of the SPO and PSA flask values reveal that the O_2 concentration at PSA is in fact only lower than that at SPO during winter and spring, and that the two locations have the same concentration during summer. This may result from a seasonal variation in the efficiency of atmospheric transport between the stations, which may be caused by the isolation of SPO under the wintertime Antarctic inversion. I hypothesize below that the seasonal correlation between atmospheric transport and the oceanic O_2 source, referred to as a rectifier effect, produces the high annual-mean O_2 concentrations observed at SPO. Similar effects with terrestrial origins plague model-observation comparisons of CO_2, and improvements in atmospheric transport modeling will be required to further reduce uncertainties in these comparisons. Shipboard O_2 observations such as those

presented here may be very helpful in this regard, as marine O_2 rectifiers appear to be larger than terrestrial CO_2 rectifiers, and associated with more homogeneous sources.

5.2 Atmospheric O_2 and CO_2 Data

The VUV O_2 and infrared CO_2 instruments analyzed air pulled from a bow mast on the ship, approximately 15 m above the water. A second, aft inlet was available, however as the relative wind was always from the bow, this inlet was not used and stack air was only detected while the ship was on station. Figure 5.2a shows the measured O_2 and CO_2 concentrations presented as hourly mean values. The gap on October 5th represents data lost due to a power outage on the ship, and corresponds to the time period when the ship was on station at King George Island. The vertical axes in this figure are scaled to be equal on a mole to mole basis, and it is clear that the O_2 variations are significantly greater than the CO_2 variations.

The most salient features in the O_2 data are 1) a gradual decreasing trend during the first day and a half to a minimum of -270 per meg early on October 3rd, 2) a gradual rise and fall over the next three days, superimposed with shorter variations, 3) a step increase of 20 per meg in the afternoon of the 6th, followed by another 5 per meg jump and a 10 per meg drop later that evening, and 4) a brief dip down and up 15 per meg just before the end of the cruise. The CO_2 concentrations were very steady for the first five days of the cruise, though varying slightly in opposition to the O_2 variations. Beginning with the drop in O_2 and jump in CO_2 late on the 6th, the CO_2 variations were much larger than during the earlier period. The last point of very high

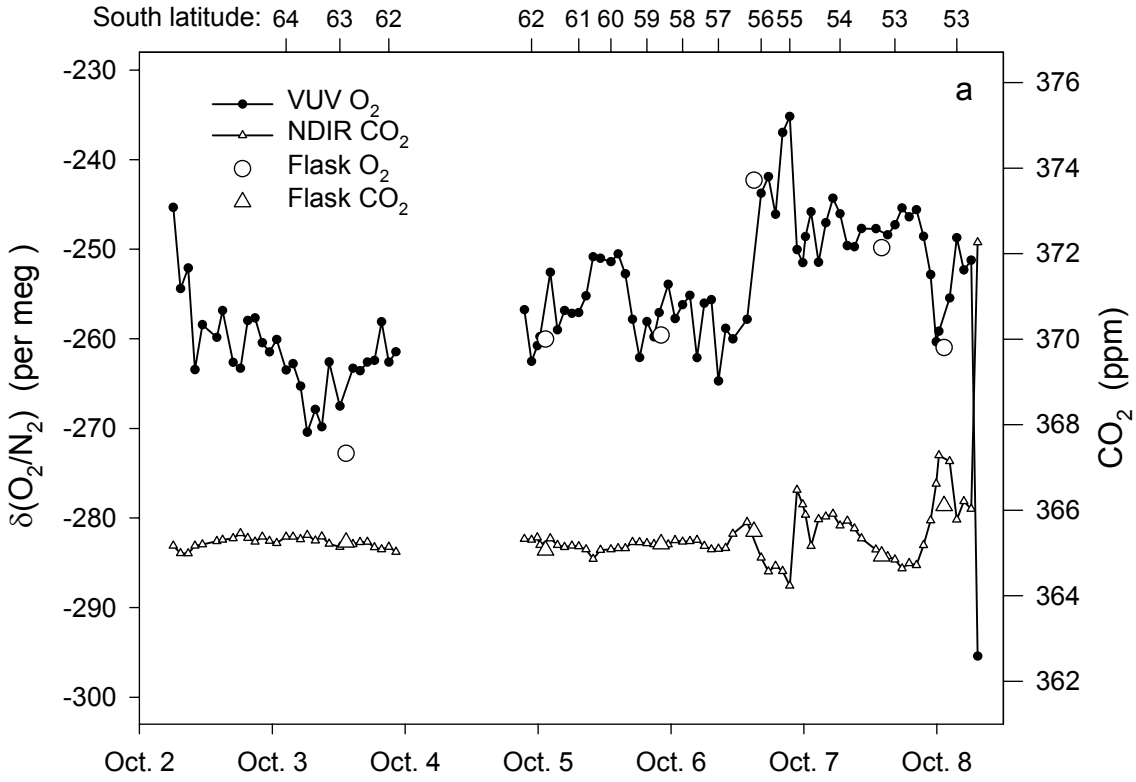

Figure 5.2 Concentrations of atmospheric O_2 and CO_2 potted versus time, with the corresponding latitude indicated at the top of the plot. (a) Hourly-mean values, (b) 5-minute mean values. The O_2 and CO_2 vertical axes are scaled to be equivalent in moles. The ticks on the bottom x-axis correspond to midnight local time and are labeled with the date of the following day. The large symbols represent 5-liter flask samples collected aboard the ship and analyzed on the Scripps interferometer. The gap on October 4th corresponds to data lost during a ship power-outage.

CO_2 and very low O_2 was measured in the Straight of Magellan. It was clearly influenced by fossil fuel burning, and I include it in the analyses to help identify industrial signals in the earlier data.

The large symbols in Figure 5.2 represent 6 flask samples collected on the ship and later analyzed by E. McEvoy on our laboratory interferometer. The flask O_2 values are in good agreement with the proximate VUV measurements (see Section

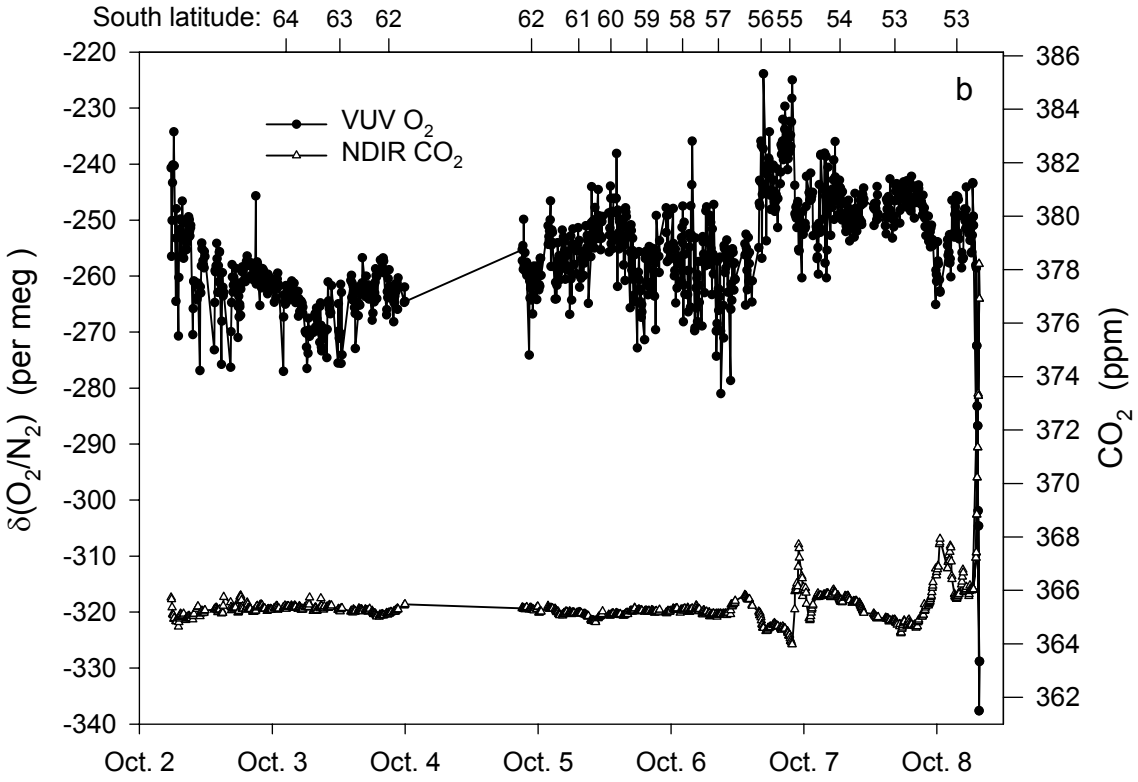

Figure 5.2 (continued)

3.4.1, Figure 3.9), and independently support the large positive and negative O_2 excursions observed by the VUV instrument on the 6th and early on the 8th, respectively. With the exception of an unexplained discrepancy with the last flask, the CO_2 values are also in good agreement. The hourly means shown in Figure 5.2a are derived from averaging ~360 values at 10-second resolution. In Figure 5.2b, I show the same data averaged over 5-minute intervals. As discussed in Chapter 3, these 5-minute values are subject to greater noise than the hourly means, yet they are still precise enough to clearly resolve all of the above-mentioned features. This figure also illustrates the residual motion sensitivity of the instrument. The relatively smooth

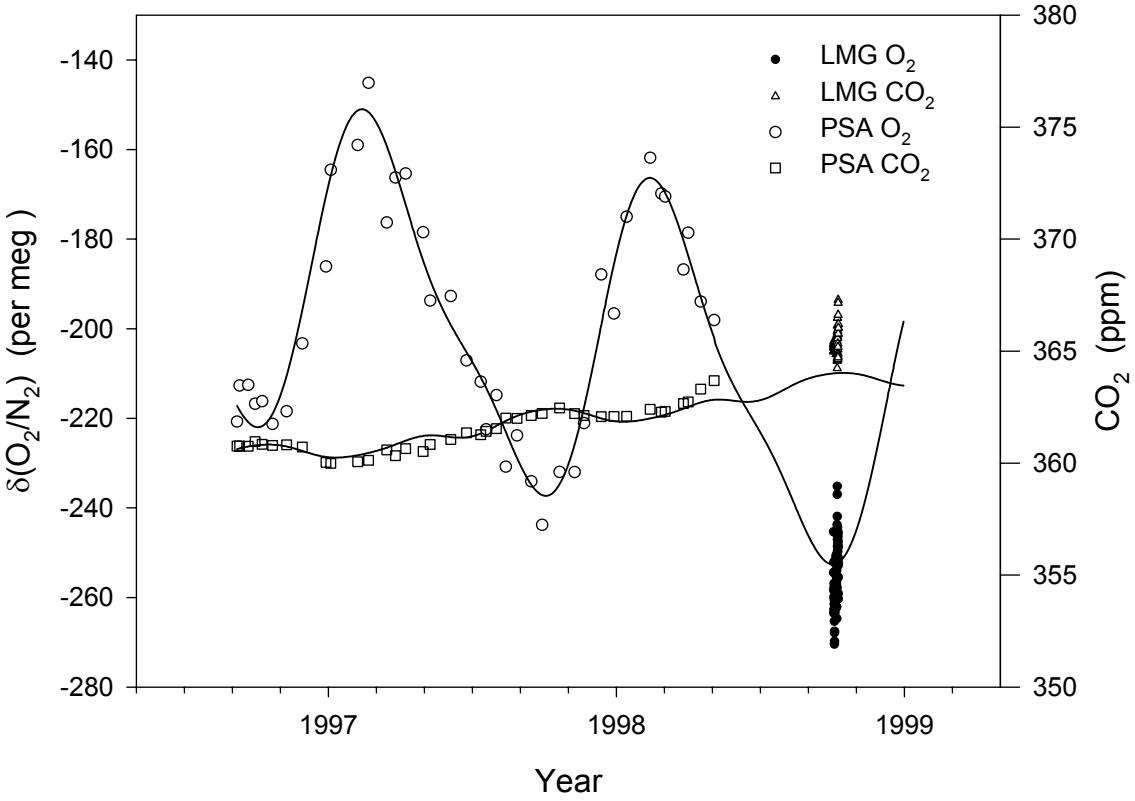

Figure 5.3 Hourly-mean shipboard O_2 and CO_2 data (LMG) compared to the existing flask data from PSA. The O_2 and CO_2 vertical axes are scaled to be equivalent in moles. The curves represent a combined fit to the PSA data using a 2-harmonic seasonal cycle and a linear interannual trend, then extended to the time of the cruise.

period late on the 2nd and early on the 3rd corresponds to very calm conditions encountered in loose pack-ice. The following day of data was collected in moderate 5-10 ft seas, and the data from the 5th and 6th in more extreme 15-25 ft seas.

Our laboratory's biweekly flask collection program at PSA was initiated in September of 1996. Figure 5.3 shows the 1-hour average values again, plotted along with the available PSA flask data which extends through May, 1998. Because of the time required for flask shipment, analysis, and data processing, PSA flask data is not yet available for the time of this cruise. To obtain temporary projected values for

comparison to the VUV measurements, I have extended a fit to the existing PSA data based on a 2-harmonic seasonal cycle and a linear interannual trend. I obtain projected values for SPO and CGO similarly, but use a 4-harmonic seasonal cycle and a stiff-spline interannual trend to fit these longer records. The O_2 concentrations observed during this cruise are in good agreement with the projected PSA values (Figure 5.3). The CO_2 values are significantly higher than the PSA projections, however they are consistent with observations from the Scripps CO_2 network (T. Whorf, personal communication, 1999), which show a global increase in the rate of CO_2 rise following the recent El Niño event. Isotope data indicate that this trend shift is primarily the result of a release of terrestrial CO_2 (S. Piper, personal communication, 1999). The fact that I did not observe a corresponding down-shift of the O_2 trend may indicate an oceanic O_2 outgassing associated with El Niño, however this requires further investigation with a more complete global data set.

5.3 Origin of Sampled Air

Relationships between the O_2 and CO_2 concentrations provide information, independent of any meteorological analyses, on the sources for the observed O_2 variations. Plotting O_2 versus CO_2 (Figure 5.4), reveals a division of the data into two modes. Up to and including the peak O_2 value late on the 6^{th}, O_2 and CO_2 varied at an average ratio of -4.8 mol O_2:mol CO_2. In contrast, including and after the peak O_2 value, O_2 and CO_2 varied at an average ratio of -1.4 mol O_2:mol CO_2. The trace in

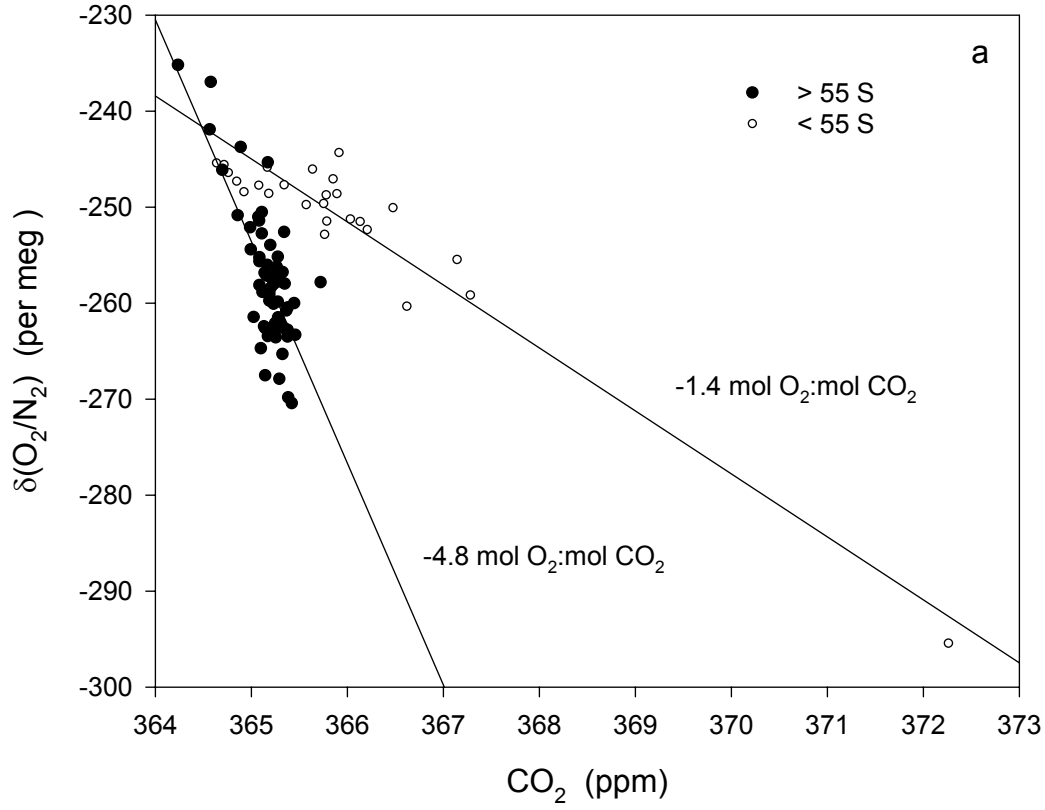

Figure 5.4 Shipboard O_2 versus CO_2 concentrations. (a) Hourly mean values with a linear fit to the measurements made up to and including the maximum O_2 value on October 6th (filled circles) and a linear fit to the measurements including and after this point (open circles). (b) A curve representing 5-hour running means of the data, plotted on enlarged axes. The large dot represents a mean of the first 5 hours of data while the ship was on station at PSA, and the arrow indicates the direction of the last hourly value measured in the Straight of Magellan.

Figure 5.4b indicates that the early period could actually be further subdivided into periods with slopes slightly greater than and less than -4.8.

Flask measurements from the same time of year in 1996 and 1997 indicate that the PSA O_2 concentration was lower and the PSA CO_2 concentration slightly higher than the respective concentrations at SPO and CGO. These austral-spring atmospheric gradients result from the ingassing of O_2 and outgassing of CO_2 associated with the

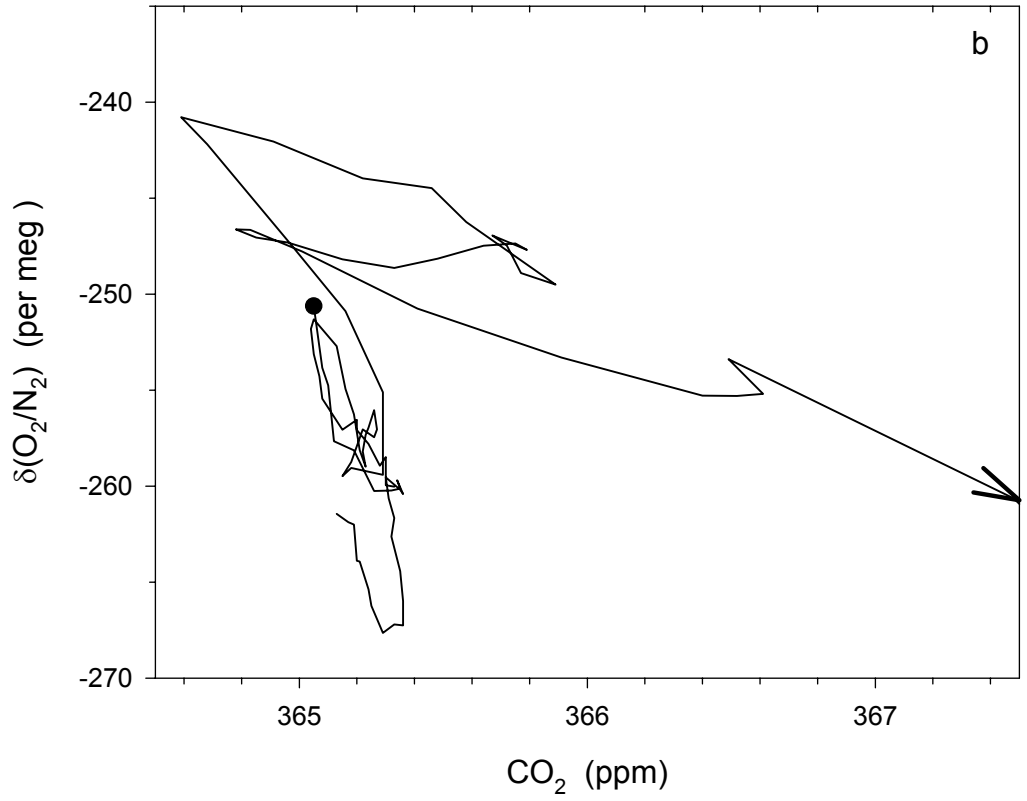

Figure 5.4 (continued)

strong wintertime vertical mixing of O_2-depleted and CO_2-enriched waters in the Southern Ocean. Although the biological imprint from deep respiration on these upwelling waters has a ratio of around -1.4 mol O_2:mol C, the buffering chemistry of CO_2 results in greater air-sea fluxes for O_2 than for CO_2. The SPO-PSA and PSA-CGO differences in October, 1996 had ratios of -15.3 and -8.8 mol O_2:mol CO_2, respectively, while in October, 1997 they both had a ratio of -4.3 mol O_2:mol CO_2 (see Table 5.1).

The ratio observed during the first part of this cruise of -4.8 is within the range of these earlier flask-station values, and indicates that the major source of O_2

variability during this period was probably the result of sampling across the large-scale meridional O_2 gradient. Furthermore, because of the relatively small terrestrial and industrial influences on the meridional gradient in this region, this ratio likely represents an oceanic signal. The ratio of -1.4 observed during the last two and a half days of the cruise is very close to that expected from the combustion of liquid fossil fuels [Keeling, 1988]. The division between these two periods is coincident with the passage of the ship into the lee of Tierra del Fuego, suggesting that the ship at this point began sampling air that had recently been influenced by anthropogenic processes. The consistency of the O_2:CO_2 ratio as Punta Arenas was approached (Figure 5.4), confirms that industrial emissions had the dominant influence on O_2 and CO_2 variability during this latter period.

The large increase in O_2 on the 6th however, does not appear to be an industrial signal, as it occurred some 5 hours before the ship passed behind Tierra del Fuego, in the direction of higher not lower O_2, and at a molar ratio close to -5. Meteorological observations from this cruise provide some clues to the origin of this feature. Figure 5.5 shows the hourly-mean O_2 data plotted along with hourly-mean measurements of wind speed, wind direction, barometric pressure, air temperature, and short-wave radiation. At the time of the 20 per meg O_2 jump, the wind was backing from the northwest to the southwest and the barometric pressure passed through a local nadir. This indicates that that a center of low pressure passed eastward just to the south of the ship. The sharpness of the barometric pressure change, and the sudden decrease in cloud cover recorded by the short-wave radiometer, suggest that the ship may have

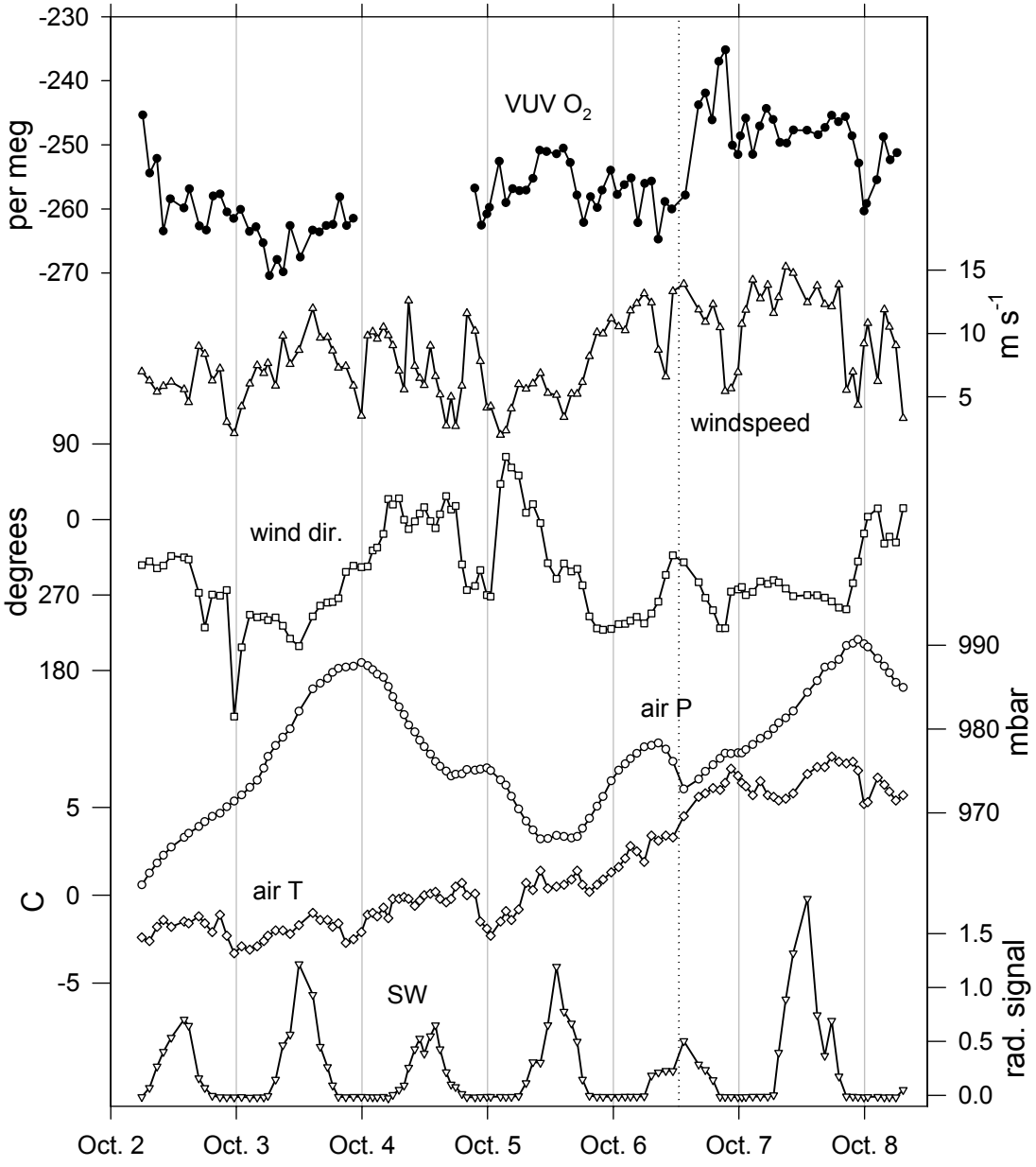

Figure 5.5 Hourly-mean shipboard meteorological observations. The VUV O_2 data is the same as in Figure 5.2. This plot also includes wind speed, wind direction, barometric pressure, air temperature, and short-wave incoming radiation. Vertical reference lines are plotted every day at local midnight, and at 1248 local time on October 6th.

passed through a front separating two distinct airmasses. Although the wind shifted to the south, it is possible that this newly sampled airmass had originally migrated from the north and had spent less time over the Southern Ocean than the previously sampled airmass. The fact that atmospheric temperature increased by 2-3°C at this point supports this hypothesis.

Although back-trajectory analyses have the potential to clarify such issues, meteorological reanalyses may be subject to large uncertainties in this region, because of the lack of direct observations. I have run the HYSPLIT4 model [HYSPLIT4, 1997], for various times and locations during this cruise, and the results are plotted in Figure 5.6. While they do indicate a shift to more northerly air late on the 6th (Figure 5.6g) the wind direction does not agree with that observed on the ship and the air is predicted to have passed over Tierra del Fuego, which probably would have introduced a detectable pollution signal. This model does however clearly show the influence of a low pressure center to the south early on the 6th (Figure 5.6f), as well as the passage of another low as the ship was moving up the Peninsula on the 2nd and 3rd (Figures 5.6a-c). This earlier low resulted in a shift in the sampling of air from relatively far north to air from the south. This appears to correspond to the steady decrease in O_2 and increase in CO_2 observed during the first 2 days of measurements. Half of this 10 per meg drop in O_2 occurred while the ship was still on station at PSA, indicating a potential sensitivity to wind direction for the biweekly flask samples taken for O_2 analyses in our laboratory.

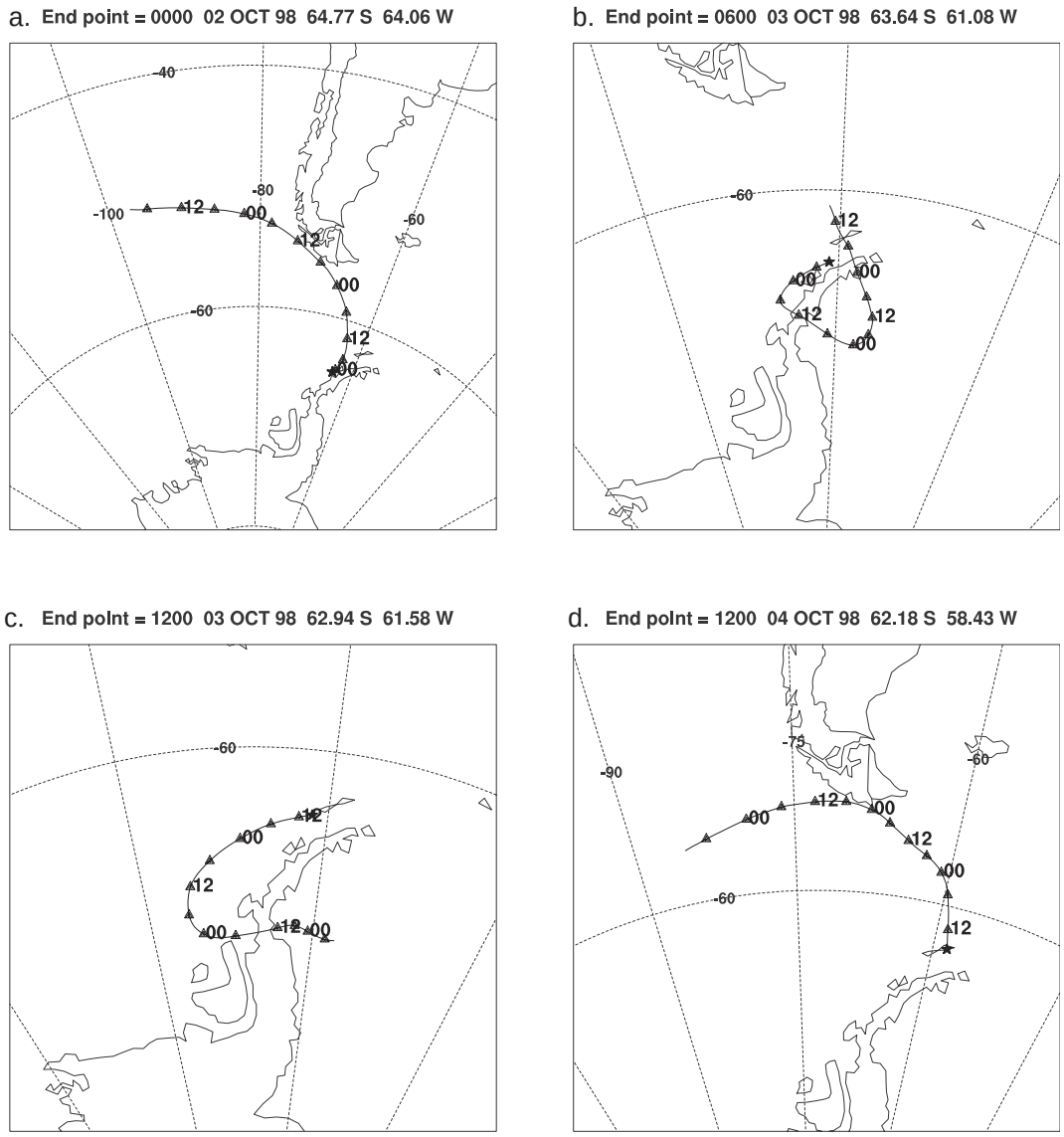

Figure 5.6 Back-trajectories calculated using the HYSPLIT4 model [HYSPLIT4, 1997]. Trajectories were run for 72 hours, and the symbols are plotted every 12 hours UT. The end points for the trajectories (stars) correspond to actual ship positions, and are labeled above each plot in local time to facilitate comparison to the other figures.

e. End point = 1800 05 OCT 98 59.31 S 60.16 W

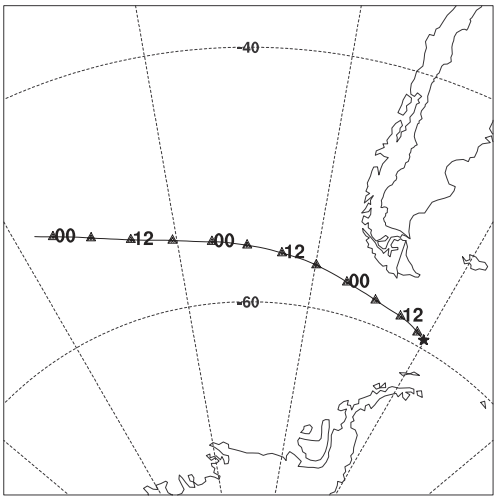

f. End point = 0300 06 OCT 98 58.35 S 61.25 W

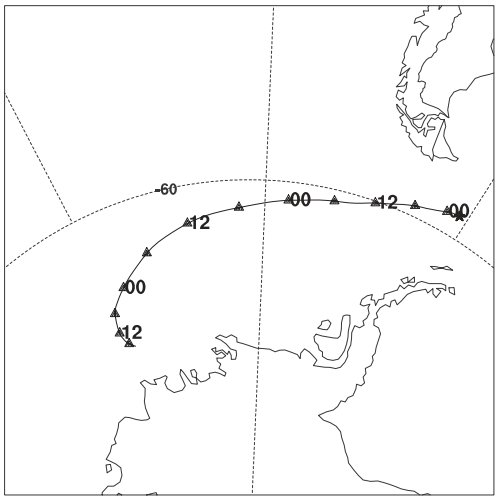

g. End point = 2100 06 OCT 98 55.63 S 64.30 W

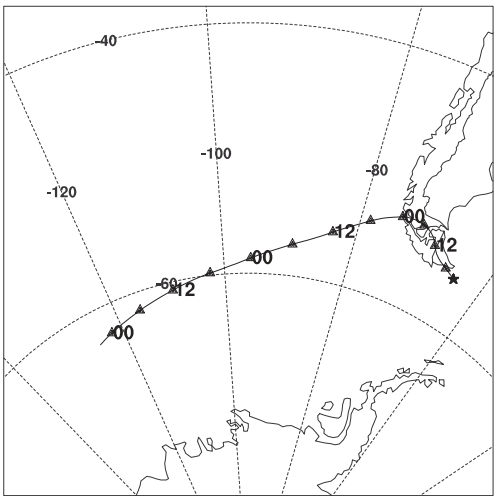

Figure 5.6 (continued)

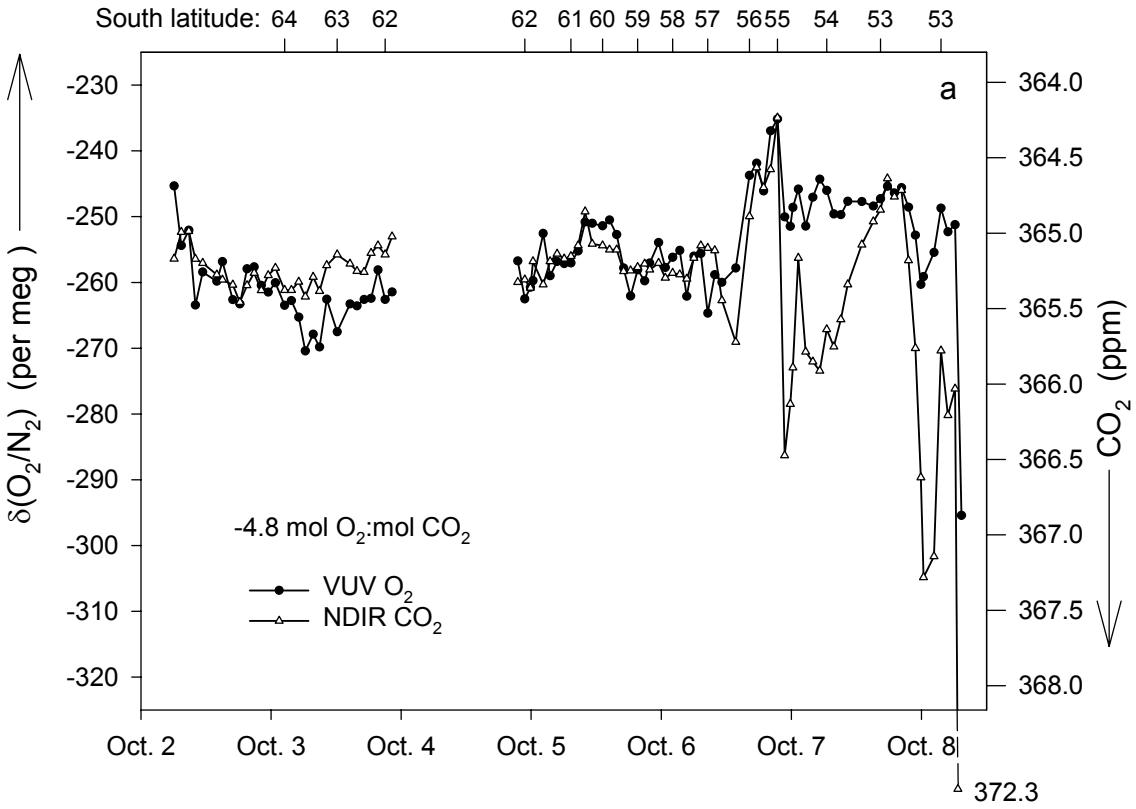

Figure 5.7 Hourly-mean shipboard O_2 and scaled CO_2 data. Same as Figure 5.2, but with the CO_2 axis flipped and scaled by (a) -4.8 mol O_2:mol CO_2 and (b) -1.4 mol O_2:mol CO_2.

This feature is shown more clearly in Figure 5.7a, in which the CO_2 curve has been scaled by the apparent oceanic ratio of -4.8 relative to the O_2 curve. Similarly, the gradual increase in O_2 on the 5th and decrease on the 6th are associated with a shift in the origin of sampled air first to the north and then back to south, which can be seen both in the back-trajectories (Figures 5.6d-f) and measured winds (Figure 5.5). The overlapping curves in Figure 5.7a show that these features, and the sharp jump in O_2 on the 6th, occurred at similar ratios to CO_2. Figure 5.7b is a similar plot, but with CO_2 scaled by the apparent fossil fuel ratio of -1.4. These plots illustrate that as the ship

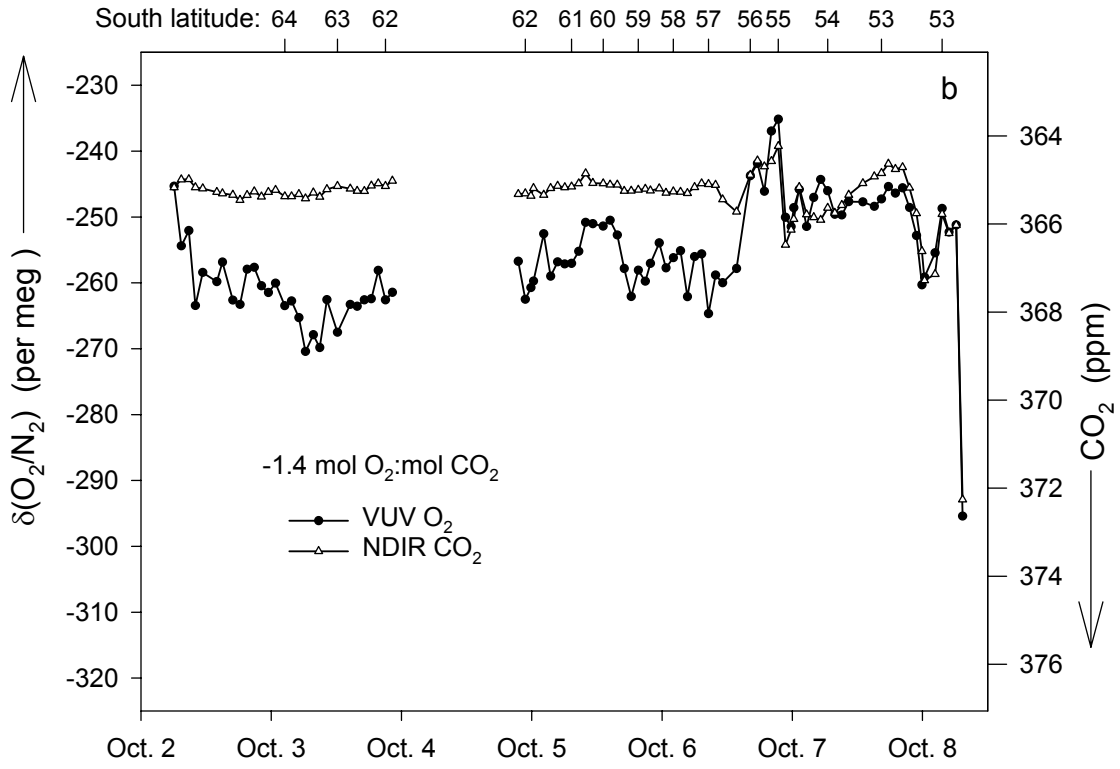

Figure 5.7 (continued)

passed into the lee of Tierra del Fuego several hours after the 20 per meg O_2 increase, the CO_2 curve switched from the oceanic to the industrial O_2 relationship. Less than 12 hours later, CO_2 began a steady decrease, during which O_2 curiously remained relatively constant. Figure 5.7a and Figure 5.4b demonstrate that the O_2 and CO_2 concentrations returned to their oceanic relationship during this period. The relatively flat slope corresponding to this transition period in Figure 5.4b probably results from a gradual combination of less industrial and greater oceanic influence on the observed concentrations. The CO_2 concentration increased again by the end of the 7th, and the

variability during the remainder of the cruise was consistent with industrial forcing (Figure 5.7b).

5.4 Oceanographic Data

One point of interest in analyzing these data was to see if the influence of the relatively strong oceanographic fronts in Drake Passage might be detectable in the local atmospheric O_2 concentrations. The zonal wind patterns at these latitudes lead to several convergences and divergences in the surface ocean [e.g. Tomczak and Godfrey, 1994]. The waters that upwell along the Antarctic Divergence around 65°S and spread north with the Ekman drift should have much lower dissolved O_2 concentrations than the surface waters north of the Antarctic Polar Front (APF) and Subantarctic Front (SAF). These two zonal features, which normally lie between 60°S and 50°S, are crowded together through Drake Passage, as reflected in the surface temperature gradients at 59°S (APF) and 55°S (SAF) shown in Figure 5.8. Unfortunately, the ship's underway temperature and salinity instrumentation only worked intermittently during this cruise. However, we dropped XBT and XCTD probes on the leg down to PSA and these data (D. Roemmich, personal communication, 1999) give a clear picture of the frontal locations on the 29th and 30th of September (Figure 5.8).

There is not a clear connection between the local oceanographic properties and the atmospheric concentrations. In fact, as the SST increased across the APF the atmospheric O_2 concentration steadily decreased, in contrast to the expected solubility

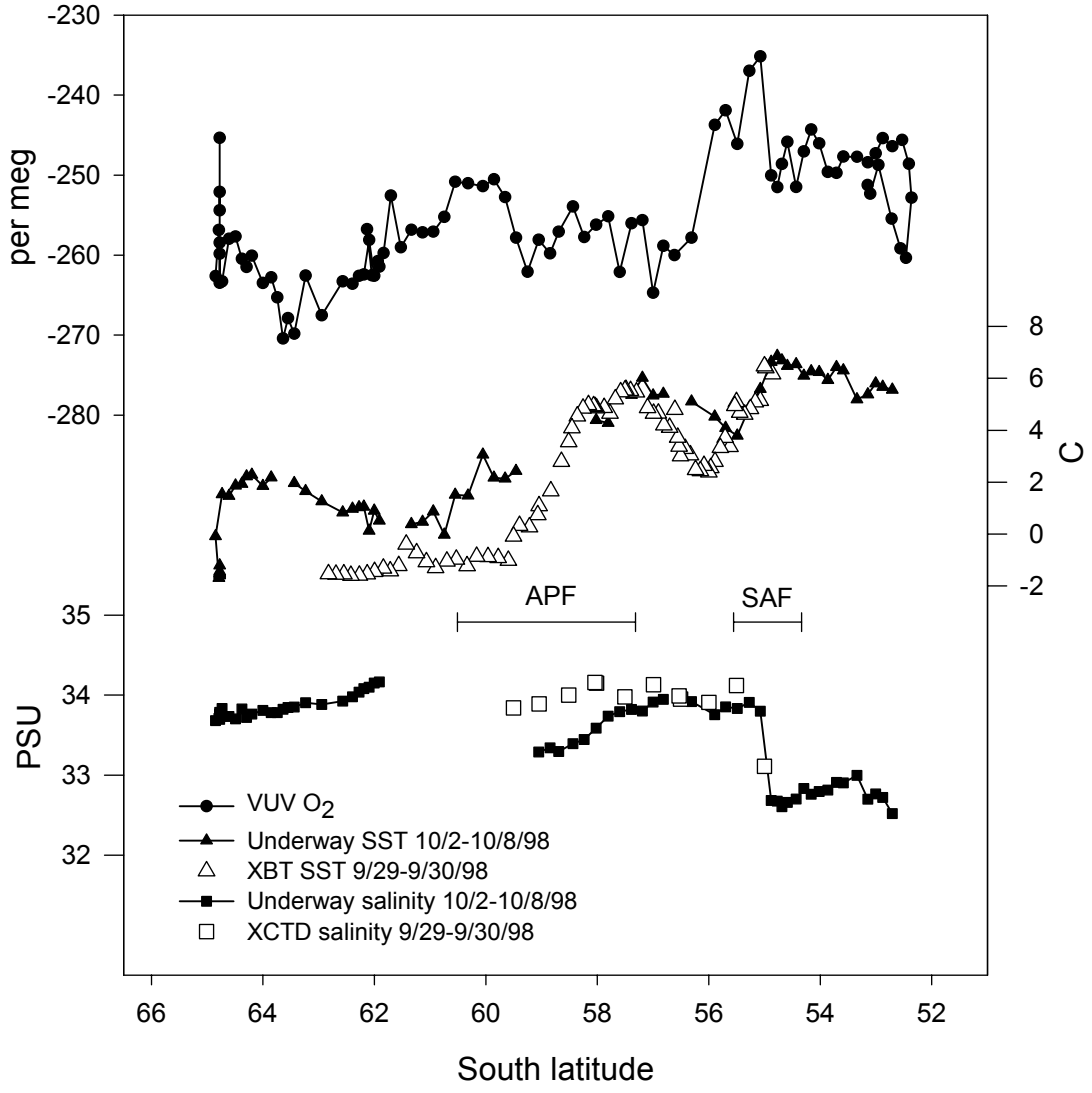

Figure 5.8 Oceanographic data plotted versus latitude. The VUV O_2 data is the same as in Figure 5.2. The O_2 data gap is not apparent, as it corresponded to the time when the ship was on station at King George Island. This plot includes hourly-mean sea surface temperature (SST) and surface salinity measured by the ship's underway analysis system from October 2nd-8th. Problems with this system resulted in significant data gaps. This plot also includes SST and surface salinity data from XBT and XCTD casts from the southward cruise leg on September 29th and 30th. The approximate positions of the Antarctic Polar Front (APF) and Subantarctic Front (SAF) during the return leg, determined by the SST gradients at 59°S and 55°S, are indicated by horizontal bars.

influence but in accord with the southerly wind shift discussed above. The atmospheric O_2 increase on the 6th is close to the XBT temperature increase indicative of the SAF position 7 days earlier, however it is almost half a degree south of the apparent position of this same front at the time of the O_2 measurements. Although the synoptic weather variations appear to have had more influence on atmospheric O_2 than local oceanographic properties during this cruise, it is ultimately the regional oceanographic properties associated with these zonal frontal systems that give the meridional air-origin shifts such influence.

5.5 Comparison to Model Estimates

Because of the lack of strong terrestrial or industrial sources at high southern latitudes, the background variations in O_2 and CO_2 observed during this cruise should primarily reflect oceanic influences. As such, they provide a good opportunity for examining the predictions of ocean carbon cycle models. An initial comparison can be made on the basis of the O_2:CO_2 ratio of the observations. With an accurate representation of thermal and biological forcing at this time of year in the Southern Ocean, a model should predict air-sea fluxes at something close to the observed ratio of -4.8 mol O_2:mol CO_2, or allowing for interannual variability close to the range of -4.3 to -15.3 mol O_2:mol CO_2 defined by the flask-station gradients observed in October 1996 and 1997, as shown in Table 5.1. The HAMOCC3.1 model predicts the opposite, a positive relationship between O_2 and CO_2 fluxes at this time of year.

Table 5.1. Modeled and observed O_2:CO_2 relationships at high southern latitudes

Source	O_2:CO_2 ratio
VUV observations from 10/2/98 - 10/6/98	-4.8
Flask measurements from October 1997:	
PSA-SPO	-4.3
PSA-CGO	-4.3
Flask measurements from October 1996:	
PSA-SPO	-15.3
PSA-CGO	-8.8
HAMOCC3.1 air-sea fluxes for October:	
South of 55 °S	+38.4
Between 55°S and 65°S	+13.6
Between 55°S, 65°S, 60°W, and 120°W	+7.6
HAMOCC3.1-TM2 atmospheric gradients:	
October 2nd - October 8th	
PSA-SPO	+13.1
PSA-CGO	+15.1
September 20th - October 20th	
PSA-SPO	+24.1
PSA-CGO	+39.3

The large positive ratios shown for HAMOCC3.1 fluxes in Table 5.1 result from the model prediction of small but positive air-to-sea fluxes of CO_2 during October. Most of this CO_2 ingassing results from the uptake of anthropogenic carbon, however the model predicts small positive preindustrial air-to-sea CO_2 fluxes at this time as well. For the upwind ocean region bounded by 55°S, 63°S, 65°W, and 115°W, HAMOCC3.1 predicts an ingassing of 1.5×10^{12} mol O_2 and an ingassing of 2.0×10^{11} mol CO_2 during the month of October. Integrating over the entire Southern Ocean south of 55°S, these values go to 3.7×10^{13} mol O_2 and 9.6×10^{11} mol CO_2.

HAMOCC3.1 predicts similar ingassing fluxes in September, and it is only in August and earlier that this model predicts wintertime CO_2 outgassing in oppostion to O_2 ingassing. In contrast, these VUV measurements appear to indicate Southern Ocean CO_2 outgassing in October. This inference is supported by the existing flask measurements, which show that in October 1996, CO_2 at PSA was symmetrically 0.2 ppm higher than at SPO and CGO, while in October 1997 it was 0.4 ppm higher.

It is difficult to estimate the spatial and temporal scales represented by these measurements because of their interdependence. For example, the O_2:CO_2 ratio observed during this cruise could reflect large-scale gradients due to air-sea gas exchange over the whole Southern Ocean during the preceding several months, or regional gradients resulting from strong local variations in air-sea gas exchange during the preceding few days. Thus, an atmospheric model must be used to make direct comparisons to ocean model predictions. From the coupled simulations presented in Chapter 2, HAMOCC3.1-TM2 predicts ratios for the SPO-PSA and PSA-CGO gradients during the period of this cruise of +13 and +15 mol O_2:mol CO_2, respectively (Table 5.1), which like the flux predictions are opposite in sign to the observations. Because this model only resolves the seasonal cycle at monthly resolution, it may be more appropriate to average the predictions on this time scale. Averaging over a 30 day period centered over the time of year of this cruise results in values of +24 and +39 mol O_2:mol CO_2, respectively. I speculate that the O_2:CO_2 ratio observed during the first part of this cruise represents an air-sea gas-exchange signal integrated over several thousand kilometers and a period on the order of 1-2

months, based on (a) the consistency with ratios determined from the large-scale gradients between SPO, PSA, and CGO, (b) the intrahemispheric mixing times that affect these gradients, and (c) the correspondence predicted by HAMOCC3.1-TM2 between these gradients and air-sea fluxes over large scales and several months (see Table 5.1).

It is the upwelling of biologically O_2-depleted and CO_2-enriched waters that is responsible for the observed opposition of O_2 and CO_2 fluxes at this time of year in the Southern Ocean (see discussion in Section 2.2). Air-sea fluxes of CO_2 and O_2 would only go in the same direction if solubility forcing were dominant. For the HAMOCC3.1 model to predict CO_2 ingassing at this time of year, it must either underestimate the biological upwelling signal, or overestimate the cooling of southward-flowing surface or upwelling deep waters. In Chapter 2 (Section 2.8), I discussed several reasons why this latter hypothesis might be true for coarse-resolution ocean models, including excessive inputs of heat to the low-latitude deep waters requiring excessive sea-to-air heat fluxes at high latitudes, and the formation of Antarctic Bottom Water by open ocean convection rather than shelf mixing. Thus, the disagreement between the O_2:CO_2 ratio observed during this cruise and that predicted by HAMOCC3.1 may be related to the annual-mean interhemispheric gradient discrepancies discussed in Chapter 2.

Ocean model uncertainties can also be investigated by comparing the gradients between these shipboard measurements and those at nearby flask stations to the gradients predicted by the coupled models. For consistency, I do these comparisons

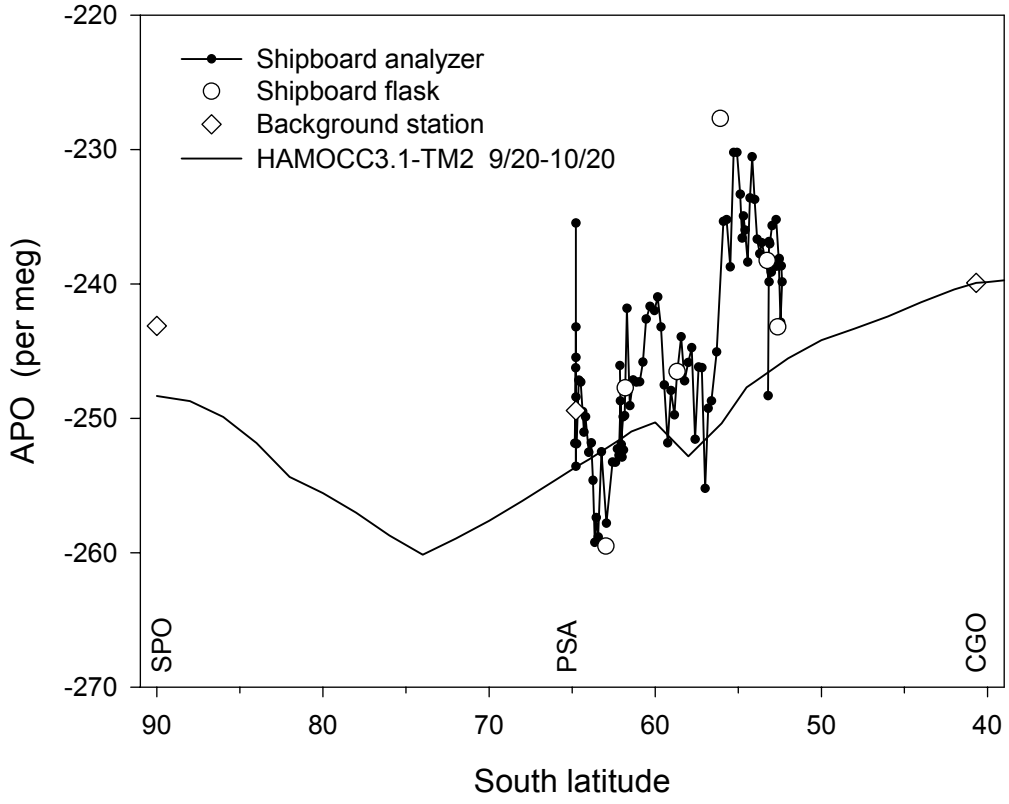

Figure 5.9 Hourly-mean shipboard concentrations of the derived tracer APO compared to HAMOCC3.1-TM2. The flask-station values for SPO, PSA, and CGO were determined by extrapolating combined seasonal-interannual fits to the existing data to the time of the cruise. The model prediction corresponds to a mean from September 20th to October 20th, interpolated along the track in Figure 7.1 and adjusted vertically to optimize its fit to the projected CGO value.

based on the derived tracer atmospheric potential oxygen (APO), even though the same analyses could be done on O_2 alone because of the lack of strong terrestrial signals at these latitudes. Figure 5.9 shows APO calculated by Equation 4.1 for the hourly measurements. This figure also includes projected flask-station values for SPO, PSA, and CGO and the HAMOCC3.1-TM2 prediction for a 30-day period centered on the time of year of this cruise for a transect from CGO, across the Southern Pacific to Drake Passage, then south through PSA to SPO (see Figure 7.1).

The APO values north of 55°S show a decreasing trend due to the negative influence of fossil fuel combustion. In relation to the APO concentration at CGO, the high values just south of 55°S and at the beginning of the cruise indicate either higher APO in the eastern South Pacific relative to the west, or that the sampled air was coming from latitudes even further north than that of CGO.

Similar to the annual-mean comparisons in Chapter 2, the HAMOCC3.1-TM2 simulation at this time of year fails to reproduce the observed gradients between the high southern latitude flask stations, which somewhat limits comparison to these shipboard data. Because of uncertainties in the numerical representation of atmospheric transport between PSA and SPO (see Section 5.6), I have not shifted the model curve to fit these stations, but simply set it to agree at CGO. With this constraint, the model underestimates the APO concentration observed during this cruise by around 6 per meg. The trough and peak between 55°S and 60°S correspond to variability across the longitudinal transect from CGO to Drake Passage, and its similarity to the observations is likely fortuitous. The minimum predicted around 75°S results from large O_2 undersaturations in the Weddell and Ross Seas, and the fact that seasonal ice cover does limit O_2 fluxes in the model. This was intended by the model developers to reflect the rapid air-sea equilibration time for O_2 and the year-round presence of leads and polynyas in the ice (see discussion in Chapter 6). Sensitivity tests with ice-masking of O_2 shifted the greatest fluxes northward but did not significantly effect the total magnitude or seasonality of the Southern Ocean O_2 fluxes (M. Heimann, personal communication, 1999).

To obtain an average APO value for the whole cruise, I have included data up to and including the peak value on the 6th, but exclude the later data as clearly influenced by local pollution. This produces a value of -247 per meg, corresponding to an average position of 61° 0' S, 61° 9' W, as shown in Figure 5.9. The statistical error on this mean is ± 6 per meg, which when quadrature summed with the instrument uncertainty of ± 3 per meg gives a net uncertainty of ± 6.7 per meg. However, uncertainty on the representativeness of this mean with respect to seasonal and synoptic variability may be significantly larger. Because of the magnitude of the seasonal O_2 cycle at this latitude, and uncertainties in representing the amplitude of this cycle in HAMOCC3.1-TM2, it is not possible to use this model to make a seasonal correction as done for the equatorial data in Chapter 4. However, we do have seasonal flask observations at the nearby latitude of PSA. These observations (see Figure 5.11) indicate that the PSA APO concentration at this time of year is approximately 33 per meg below its annual mean.

In Figure 5.10, I show the annual-mean APO predictions of HAMOCC3.1-TM2, POBM-TM2, and LLOBM-TM2 at these latitudes, along with projected annual means at SPO, PSA, and CGO, and the average value from this cruise adjusted upwards by 33 per meg. The two aseasonal models include ice-masking of O_2 fluxes, and thus predict flatter meridional APO gradients at these high-southern latitudes. In addition, the annual-mean HAMOCC3.1-TM2 prediction of the 50°S to 75°S difference is increased ~ 3 per meg by the rectification effect shown in Figure 2.6. The difference between the POBM-TM2 and LLOBM-TM2 predictions may result

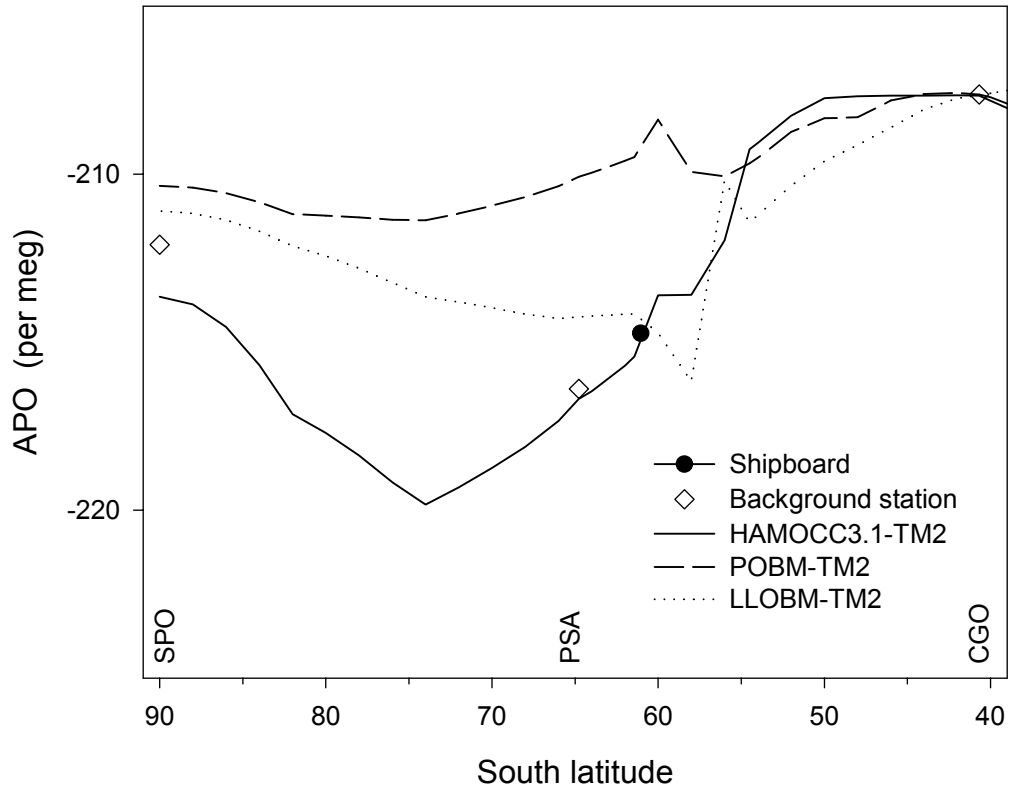

Figure 5.10 Annual-mean clean-air APO estimate compared to HAMOCC3.1-TM2, POBM-TM2, LOBM-TM2 predictions. The flask-station values for SPO, PSA, and CGO were determined by extrapolating fits to the existing deseasonalized data. The seasonal adjustment to the shipboard observation consisted of adding 33 per meg, based on seasonal observations at PSA. The model predictions have been interpolated along the track in Figure 7.1 and vertically adjusted to optimize their fits to the projected CGO value.

from the O_2 source in POBM and sink in LLOBM immediately upwind of the cruise track (see Figure 2.3). However, the zonal mean air-to-sea APO fluxes at this latitude are also greater for LLOBM than for POBM, so it is unclear which spatial scale is responsible for the differences in Figure 5.10. The VUV observations do not provide a rigid constraint on these annual-mean predictions, but are suggestive that the APO concentrations in Drake Passage relative to CGO are close to the LLOBM-TM2 and

HAMOCC3.1-TM2 predictions, but lower than the POBM-TM2 predictions. The SPO APO values for the most recent year of available data used to produce the value in Figure 5.10 are lower than those at CGO. Consequently, the CGO-SPO discrepancies with model-predictions are not as great as for the long-term means (see Figures 2.5 and 7.2).

5.6 Antarctic Marine O_2 Rectifier

Differences between the observed meridional O_2 gradients at high southern latitudes and those predicted by coupled ocean-atmosphere models may result in part from the misrepresentation of temporal correlations between atmospheric transport and surface fluxes. Such correlations can produce average concentration gradients from zero-average fluxes, and are known as rectifier effects in analogy to electronic rectifiers that convert an alternating current into a direct current. In the case of seasonally varying atmospheric boundary-layer mixing and seasonally varying but annually balanced terrestrial CO_2 fluxes, rectifier effects may generate annual-mean interhemispheric gradients of up to 2 ppm [Denning *et al*., 1995]. In Chapter 2, I showed that the HAMOCC3.1-TM2 model predicted significant rectifier effects on meridional O_2 gradients (Figure 2.6). These gradients appeared to result from seasonal correlations of air-sea O_2 fluxes with low-latitude horizontal atmospheric transport, as well as with high-latitude vertical atmospheric mixing.

The measurements presented in Chapter 4 suggest that the low-latitude marine O_2 rectifier is in fact an important influence on annual-mean O_2 gradients. However,

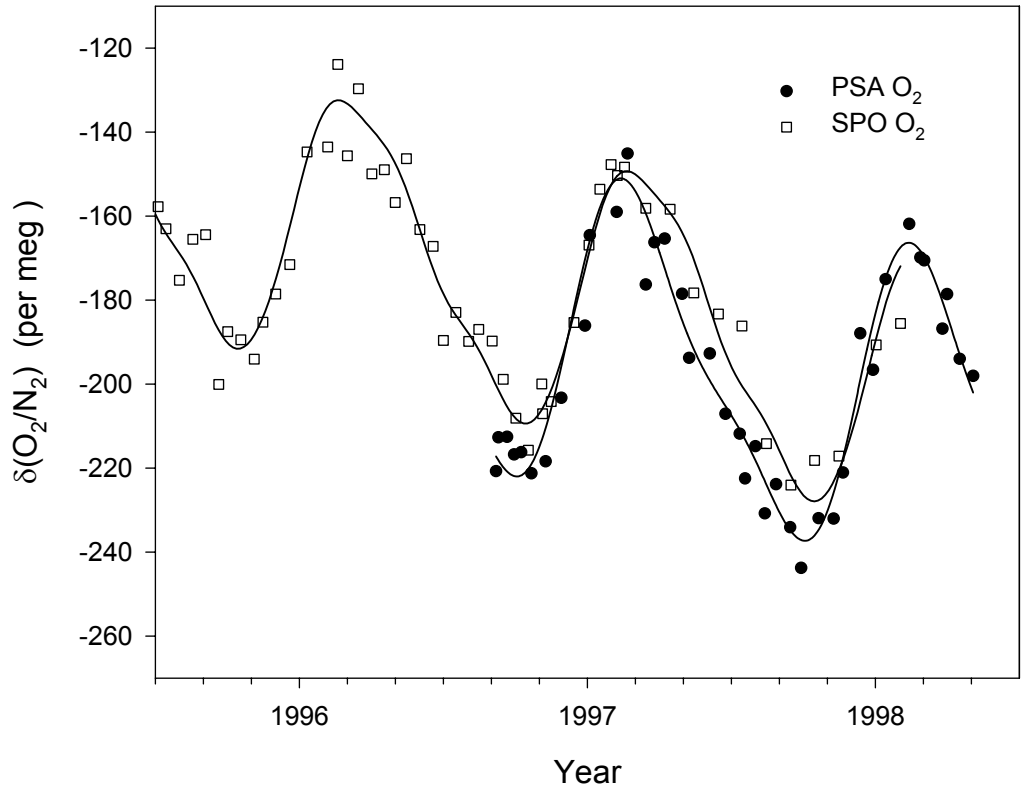

Figure 5.11 Comparison between background O_2 records at PSA and SPO, as measured in the Scripps atmospheric O_2 laboratory using an interferometric technique.

the high-latitude O_2 peak predicted by HAMOCC3.1-TM2 is in the opposite direction of the observed O_2 trough at high southern latitudes. Nonetheless, close examination of the flask data suggests that a different seasonal rectification process may be at work. Figure 5.11 shows flask O_2 data from our laboratory for SPO and PSA. It is apparent from this figure that the O_2 concentrations at these stations are very similar from November through February during the austral summer, but that the concentrations at PSA are systematically lower by about 15 per meg during the rest of the year. I speculate that this reflects enhanced atmospheric transport between PSA and SPO during summer and reduced transport during winter.

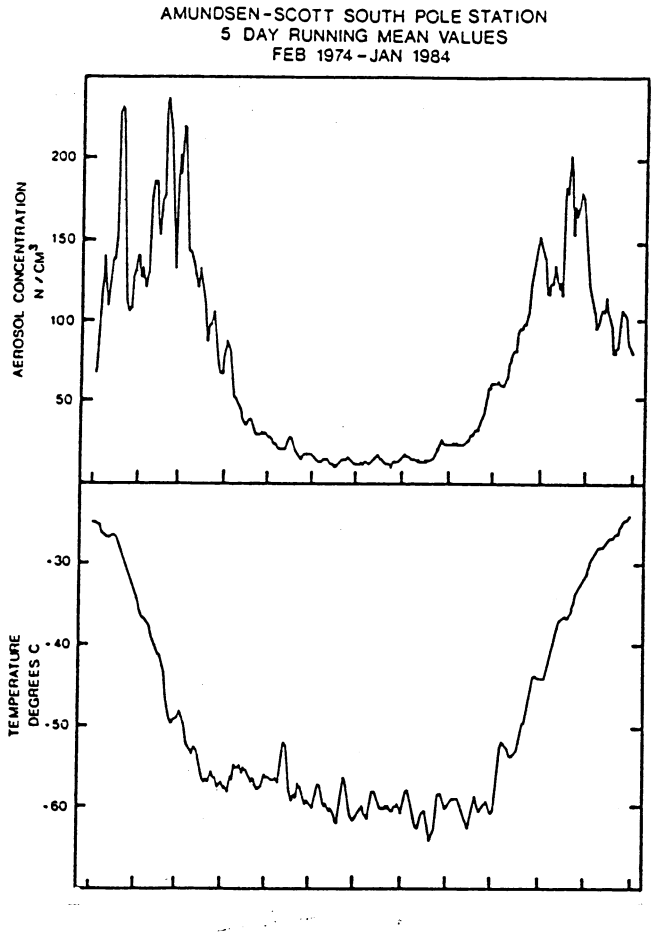

Figure 5.12 Average seasonal cycle in aerosol concentrations and temperature at SPO from 1974 to 1984 [from Sampson *et al*., 1990].

Studies of the meteorology around SPO indicate the presence of a wintertime inversion over the South Pole which results from the strong radiative cooling of the surface in the absence of sunlight [e.g. Parish, 1988]. Hogan *et al*. [1982] show that this inversion, as well as the katabatic influence of the polar high, work to isolate SPO from more northerly air for much of the winter season. This isolation can clearly be

seen in the seasonal cycle of aerosols at SPO [Hogan *et al*., 1982, 1990; Samson *et al*., 1990]. As shown in Figure 5.12, aerosol concentrations are close to zero throughout the winter and jump up sharply in October. Because the time of isolation corresponds to O_2 uptake by the oceans around Antarctica, whereas the time of greater mixing corresponds to O_2 outgassing, there may be a net effect on the annual mean difference between SPO and PSA of as much as 10 per meg. In this mechanism, the summertime Southern Ocean O_2 source elevates the concentration at SPO and PSA alike, but the wintertime O_2 sink draws the concentration down much more significantly at PSA. It appears from Figure 5.11, that during some winters this isolation breaks down and the concentration at SPO occasionally dips by 10-15 per meg.

Because of its coarse resolution, and the general lack of validation data for meteorological analyses over the Antarctic continent, it is likely that the TM2 model does not accurately represent the seasonality of horizontal and vertical transport to SPO. This would not necessarily be noticeable in the gases typically used to validate tracer transport models, as they do not have strong seasonally varying southern hemisphere sources. Unfortunately, it is difficult to estimate the potential magnitude of this rectifier effect on the modeled APO gradients without a transport model that can be verified at high southern latitudes. How much the model predictions at SPO would increase with an Antarctic rectifier depends on the relative volume of air represented by the SPO and PSA measurements. Of potential relevance is the fact that a similar relationship is seen between the limited O_2 observations at MacQuarie Island (MCQ) and those at CGO, with similar concentrations between these stations during

summer and much lower concentrations at MCQ during winter (data not shown). This may be the cause of the strong annual-mean MCQ-CGO difference shown in Chapter 2, and suggests that the Antarctic rectifier might more accurately be viewed as a wintertime isolation of the Southern Ocean marine-boundary layer from regions both north and south rather than just the isolation of SPO. The inclusion of such an effect in the existing models might improve their prediction of the long-term PSA-SPO difference (see Figure 7.2). However, it would also reduce their predicted APO concentrations at PSA, which would increase model-observation disagreements between PSA and stations north of CGO (see Figure 7.2).

5.7 Conclusion

In this chapter, I have presented the results from VUV atmospheric O_2 measurements during a one-week austral-spring cruise in the Southern Ocean. The advantage of continuous measurements is apparent in the amount of information that can be obtained from this relatively short and highly variable time series. Covariations between observed O_2 and CO_2 concentrations allow the differentiation between anthropogenic and oceanic influences on the observations. Comparisons to meteorological data indicate that these O_2 and CO_2 variations were the combined result of variable atmospheric transport and the strong large-scale concentration gradients, and that they were relatively insensitive to local oceanographic changes. The observed clean-air ratio of -4.8 mol O_2:mol CO_2 thus probably represents the relationship between air-sea O_2 and CO_2 fluxes integrated over a relatively large area

of the Southern Ocean at this time of year. As such, it provides valuable information on the seasonality of thermal and biological forcing of these fluxes and quantitative tests for seasonal ocean carbon cycle models.

HAMOCC3.1, and possibly other models, predict Southern Ocean CO_2 ingassing at this time of year, in contrast to the VUV observations which indicate CO_2 outgassing. Future work on coarse-resolution ocean models may be needed, along the lines of improving the representation of processes responsible for the formation of Antarctic Bottom Water and the global overturning of deep waters, to reproduce these observations. Although the results presented here support inferences made in Chapter 2 regarding uncertainties in the models' meridional carbon transports, the large seasonal cycle in atmospheric O_2 at these latitudes limits the annual-mean constraints that can be placed. Future measurements such as these, made at different times of year, would significantly improve our understanding of the present fluxes of carbon and oxygen into and out of the Southern Ocean.

I have also presented a theory in this chapter that attempts to explain the high annual-mean O_2 concentrations at SPO through a seasonal rectification process. Although this theory matches well with existing flask measurements, without improved atmospheric transport models, it is difficult to estimate its implications for coupled atmosphere-ocean model predictions such as those examined in Chapter 2. Further investigations of the Antarctic marine O_2 rectifier promise insights into other atmospheric rectification processes as well.

5.8 References

Denning, A. S., I. Y. Fung, and D. A. Randall, Latitudinal gradient of atmospheric CO_2 due to seasonal exchange with land biota, *Nature*, 376, 240-243, 1995.

Hogan, A., S. Barnard, J. Samson, and W. Winters, The transport of heat, water vapor and particulate material to the South Polar Plateau, *J. Geophys. Res., 87*, 4287-4292, 1982.

Hogan, A. W., W. G. Egan, J. A. Sampson, S. C. Barnard, D. M. Riley, and B. B. Murphey, Seasonal variation of some constituents of Antarctic tropospheric air, *Geophys. Res. Lett.*, 17, 2365-2368, 1990.

HYSPLIT4, HYbrid Single-Particle Lagrangian Integrated Trajectory Model, Web address: http://www.arl.noaa.gov/ready/hysplit4.html, NOAA Air Resources Laboratory, Silver Spring, MD, 1997.

Keeling, R. F., Development of an interferometric oxygen analyzer for precise measurement of the atmospheric O_2 mole fraction, Ph.D. thesis, 178 pp., Harvard Univ., Cambridge, Mass., 1988.

Keeling, R. F., A. C. Manning, E. M. McEvoy, S. R. Shertz, Methods for measuring changes in atmospheric O_2 concentration and their application in southern hemisphere air, *J. Geophys. Res.*, *103*, 3381-3397, 1998.

Parish, T. R., Surface winds over the Antarctic continent: A review, *Rev. Geophys., 26*, 169-180, 1988.

Tomczak, M., and J. S. Godfrey, *Regional Oceanography: An Introduction* (Pergamon, Oxford, 1994), pp. 67-87.

Samson, J. A., S. C. Barnard, J. S. Obremski, D. C. Riley, J. J. Black, and A. W. Hogan, On the systematic variation in surface aerosol concentration at the South Pole, *Atmos. Res.*, *25*, 385-396, 1990.

Sarmiento, J. L., and C. Le Quéré, Oceanic carbon dioxide uptake in a model of century-scale global warming, *Science*, *274*, 1346-1350, 1996.

Chapter 6

The Influence of Antarctic Sea Ice on Glacial-Interglacial CO_2 Variations

Abstract

The robust observation of an 80 ppm drop in atmospheric CO_2 during glacial times is without a satisfactory explanation. There is growing evidence that ocean models previously used to investigate this problem significantly overestimate the amount of deep water upwelling at low latitudes. Here we use a box model that has no low-latitude deep-water upwelling to investigate the linkages between glacial-interglacial temperature and atmospheric CO_2 variations. This model allows us to explore the possibility that atmospheric CO_2 responds to temperature through effects on air-sea gas exchange resulting from variations in Antarctic sea ice. Operating from the simple assumptions that deep waters only significantly outcrop south of 55°S, and that sea ice covered most of this region during glacial times, our model reproduces 67 ppm of the observed glacial-interglacial CO_2 difference. Unlike other mechanisms put forward to explain this difference, our model is consistent with estimates of glacial deep O_2 concentrations, Antarctic surface $\delta^{13}C$ ratios, and lysocline depths, and also with estimates of the timing of events during deglaciation.

6.1 Introduction

Measurements of deuterium in ice and CO_2 in air bubbles from Antarctic ice cores reveal a tight correlation between Antarctic temperatures and atmospheric CO_2, with glacial CO_2 concentrations approximately 80 ppm lower than their preindustrial value of 280 ppm [Barnola *et al*., 1987; Petit *et al*., 1999] (Figure 6.1). Most theories put forth to explain low glacial atmospheric CO_2 levels rely on one of two mechanisms: an increase in the strength of the biological pump as a result of changes in the supply or utilization of nutrients or light [Broecker, 1982; Sarmiento and Toggweiler, 1984; Siegenthaler and Wenk, 1984; Knox and McElroy, 1984; Martin, 1990; Broecker and Henderson, 1998], or an increase in the ocean's alkalinity via coral reef dissolution [Berger, 1982; Opdyke and Walker, 1982] or carbonate sediment interactions [Boyle, 1988; Archer and Maier-Reimer, 1994]. Biological pump scenarios are generally inconsistent with the magnitude and/or direction of glacial-interglacial changes in $^{13}C/^{12}C$ ratios and nutrients [Charles and Fairbanks, 1990; Mortlock *et al*., 1991; Boyle, 1992], and with the lack of widespread glacial deep-water anoxia. On the other hand, scenarios invoking alkalinity changes predict large increases in the depth of the glacial lysocline which are not observed.

The trend over the past fifteen years has been toward the proposal of increasingly complex scenarios in the face of continuing observations which have made enhanced biological productivity or whole ocean alkalinity more and more difficult to accommodate. Here, we present a scenario that is not based on productivity or alkalinity increases, but rather on changes in the rate of air-sea gas

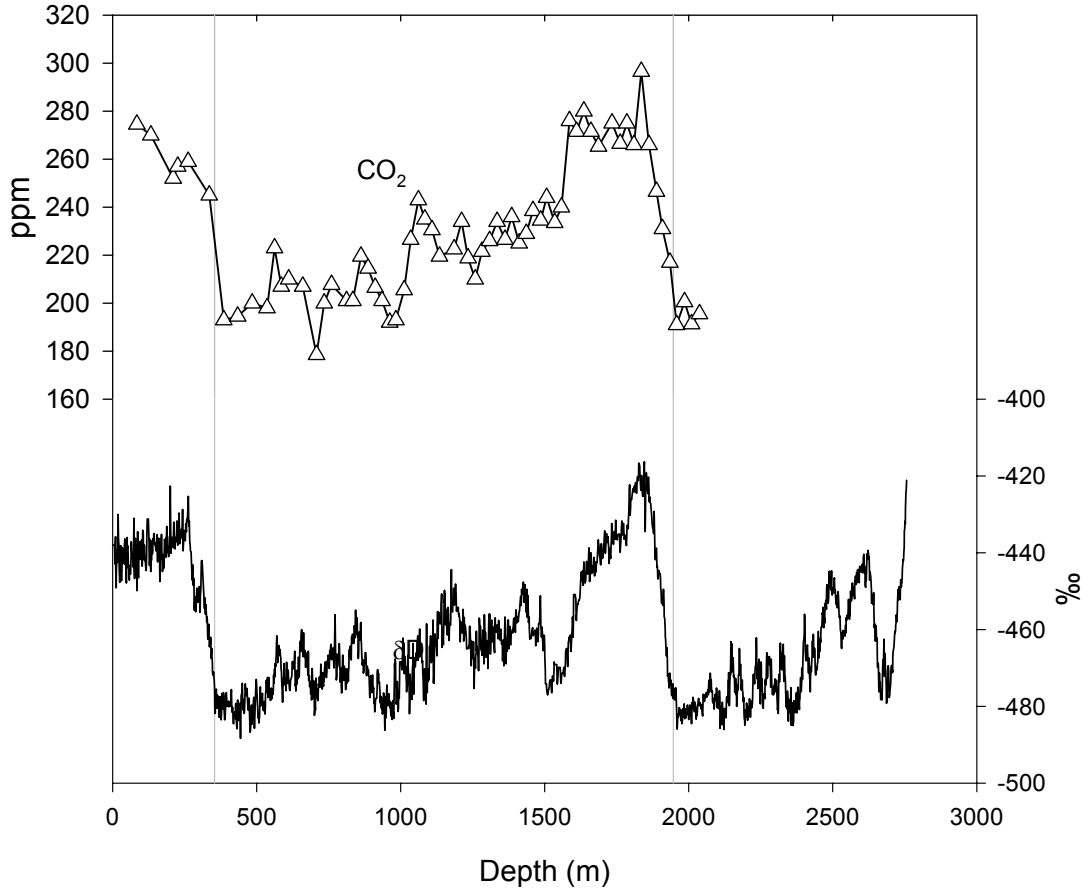

Figure 6.1 Measurements of deuterium (solid line) and CO_2 (triangles) from the Vostok ice-core [Petit *et al*., 1999], extending past the penultimate termination. The data are plotted versus depth with the CO_2 data shifted up by 40 m to account for the lag due to bubble closure.

exchange as a result of increased sea-ice cover at high southern latitudes. By significantly limiting the sea-to-air CO_2 flux in the primary region for deep-water ventilation, expanded Antarctic sea ice during glacial times may trap relatively more carbon in the deep ocean, thereby reducing atmospheric CO_2. This mechanism would enhance the effect of the biological pump without actually increasing productivity, and thus would not necessarily require changes in nutrient concentrations or utilization

efficiencies. Because dissolved O_2 equilibrates more rapidly with the atmosphere than CO_2, as a result of its lack of buffering chemistry, the limitation imposed by glacial sea ice would have a lesser effect on O_2 entering the deep ocean than on CO_2 leaving and thus would not produce deep anoxia. Furthermore, because this gas-exchange limitation would not directly affect alkalinity, a large lysocline shift is not required. Finally, the direct connections between Antarctic temperature and sea-ice cover provide a possible explanation for the observed synchroneity between Antarctic temperature and atmospheric CO_2 during deglaciation (see Figure 6.1).

The influences of Antarctic sea ice on glacial atmospheric CO_2 through reduced oceanic convection [Toggweiler and Sarmiento, 1985; François *et al*., 1997], and on glacial ^{13}C values through a reduced air-sea disequilibrium flux [Broecker, 1993] have been previously investigated. Of particular relevance to this work, Leuenberger *et al*. [1992] parenthetically mentioned the potential for sea ice to increase the effect of the biological pump without increasing productivity. Increases in Antarctic sea ice have even been included in 3-dimensional ocean model simulations, but their potential to significantly affect atmospheric CO_2 in these models may be limited by defects involving excessive low-latitude upwelling of deep water.

Toggweiler and Samuels [1993b] have demonstrated from ^{14}C comparisons, and Gnanadesikan and Toggweiler [1999] from silica flux comparisons, that coarse-resolution ocean models all overestimate the amount of deep water upwelling across the main thermocline at low-latitudes in the Indian and Pacific Oceans. This artifact may be related to uncertainties in simulating the downward penetration of heat

associated with diapycnal mixing in the open ocean [Ledwell *et al*., 1993; Toole *et al*., 1994] and along boundaries [Lueck and Mudge, 1997] in coarse-resolution models. Previous box models used to explore paleo-CO_2 controls [Sarmiento and Toggweiler, 1984; Siegenthaler and Wenk, 1984; Knox and McElroy, 1984; Toggweiler and Sarmiento, 1985; Marino *et al*., 1992] also overestimate deep-water upwelling at low latitudes. These models have from 15 to 40 Sv (1 Sv = 10^6 m^3 sec^{-1}) of upwelling directly from the deep to the warm surface box, which is much greater than the combined upper limit of ~7 Sv indicated by tracer and transect studies in the Pacific [Toggweiler and Samuels, 1993b] and Indian [Robbins and Toole, 1997] Oceans.

A consistent picture of the global thermohaline circulation is possible without significant low-latitude upwelling if we assume that deep waters predominantly upwell around Antarctica, as in the reconfigured global conveyor of Toggweiler and Samuels [1993b]. As demonstrated elsewhere by these authors [Toggweiler and Samuels, 1993a; 1998] and by Gnanadesikan [1999], this overturning circulation is consistent with forcing associated with the open channel and zonal winds in the latitudes of Drake Passage. By investigating the limit of no deep-water low-latitude upwelling using a simple box model, Keeling and Stephens [1999] are able to reproduce a number of paleocirculation features that have previously been unexplained. A key hypothesis of the Keeling and Stephens study is that expanded Antarctic sea ice during glacial times reversed the freshwater balance of the Southern Ocean south of Drake Passage, and thus allowed the ocean-climate system to flip between on and off modes of North Atlantic Deep Water (NADW) circulation. To

further investigate the implications of expanded Antarctic sea ice for atmosphere-ocean carbon partitioning, we employ a biogeochemical version of the Keeling and Stephens [1999] model. We find that in the absence of low-latitude deep-water upwelling, the Antarctic-ice mechanism has the potential to produce large changes in atmospheric CO_2.

6.2 Box Model Description

We start by adopting the same temperature, salinity, and flow patterns of Keeling and Stephens [1999], but make several modifications (Figure 6.2) to optimize the model's geochemical rather than dynamical representativeness. We divide the upper ocean into a warm, low-nutrient surface (S) box and a cooler, higher-nutrient thermocline (T) box. We also separate the upwelling that feeds the Antarctic Bottom Water (AABW) formation (B) box from that which flows north in the Antarctic surface (A) box to allow for higher nutrient concentrations in AABW. In addition, we enlarge the deep box to represent the full chemical storage capacity of the deep ocean, and increase the flux of AABW to 15 Sv to be consistent with this larger volume and the estimate of Broecker *et al*. [1998].

We allow for surface exposure of Antarctic Intermediate Water (AAIW) in the Subantarctic (SA) box (Figure 6.2) to investigate model sensitivities to uncertainties in the fate of northward flowing Antarctic surface waters. Deep waters that upwell along the Antarctic Divergence (~65°S), mix with surface waters, and then flow north are generally thought to sink again at the Antarctic Polar Front (APF) (~55°S) as part of

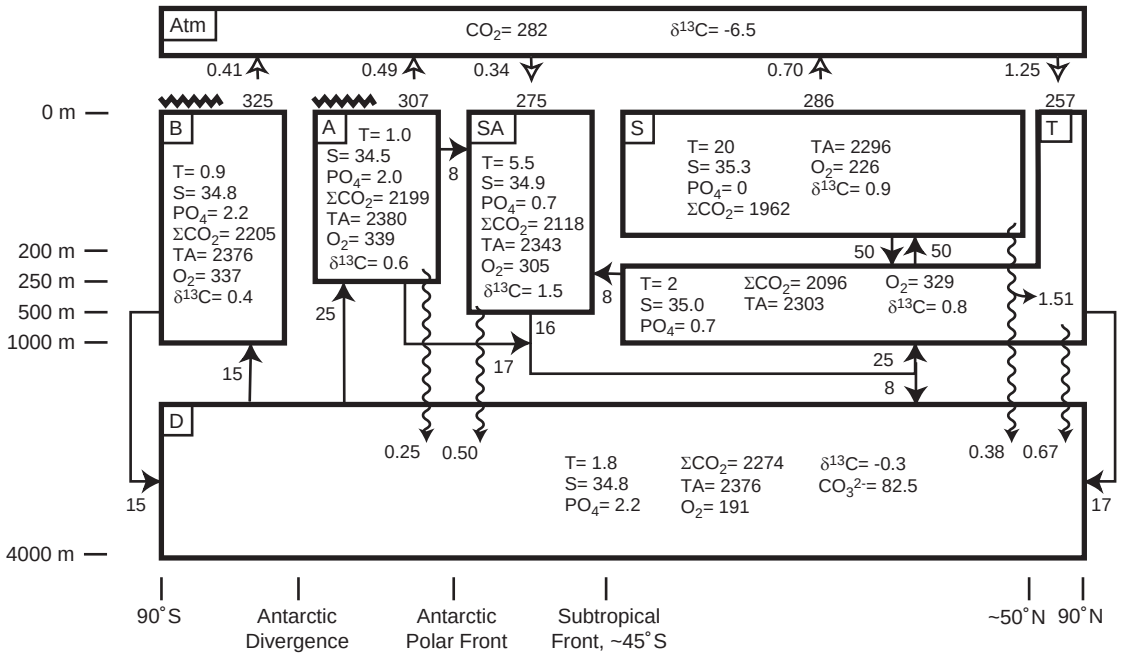

Figure 6.2 Atmosphere-ocean model solution for a best-guess modern-preindustrial state in which $F_a = 0.3$. This model consists of an atmosphere and six ocean boxes: a main surface box (S) representing the upper 200 m of water between approximately 50°N and the Southern Subtropical Front (STF), a main thermocline box (T) representing waters between 200 and 1000 m depth with a surface outcrop north of the main surface box, an Antarctic Bottom Water formation box (B) representing the upper 1000 m of water south of the Antarctic Divergence (AD) (~ 65°S today), an Antarctic surface box (A) representing the upper 250 m Ekman layer of the Southern Ocean south of the Antarctic Polar Front (APF) (~ 55°S today) and north of the AD, a Subantarctic box (SA) representing the upper 500 m of water north of the APF and south of the STF, and a deep box (D) representing the remainder of the world's oceans. We use a total ocean volume of 1.29×10^{18} m^3 and a total ocean surface area of 3.49×10^{14} m^2. We assume volume percentages for the boxes (S:T:B:A:SA:D) of 4:17:0.5:0.5:1:77, and surface area percentages of 75:8:3:6:8:0. We assume that 50 % of the ocean in boxes B and A is covered by sea-ice (represented by jagged lines), leaving a combined area of 1.6×10^{13} m^2 open for the ventilation of upwelled deep waters. Solid straight arrows denote water fluxes and are labeled in Sv. Solid wavy arrows indicate sinking fluxes of organic material and hollow arrows indicate air-sea CO_2 fluxes, and both are labeled in Gt C yr^{-1}. Numbers above the surface boxes denote CO_2 partial pressures in μatm. Values for PO_4, ΣCO_2, TA, dissolved O_2, and CO_3^{2-} are indicated in μmol kg^{-1}, $\delta^{13}C$ in per mil, T in °C, S in PSU, and atmospheric CO_2 in ppm.

the low salinity AAIW [Tomczak and Godfrey, 1994]. Although there is considerable uncertainty [McCartney, 1977; Molinelli, 1978; 1981], it appears that some of this recent deep water remains near the surface north of the APF where it convectively mixes with surface waters of low-latitude origin before sinking.

We prescribe surface phosphate concentrations in the A, SA, S, and T boxes (Figure 6.2), and the total ocean phosphate concentration. The model consumes excess phosphate in these four surface boxes at revised Redfield proportions of -175 O_2:127 C:16 N:1 P [Broecker *et al*., 1985; Peng and Broecker, 1987]. As the resulting organic matter sinks, 80% of the main surface flux is oxidized in the thermocline box and the remainder of all three fluxes in the deep box. We assume inorganic to organic carbon production ratios of 0, 1:20, 1:10, and 1:3 in the A, SA, S, and T boxes respectively. The model remineralizes all of the sinking calcium carbonate in the deep box, such that the effective inorganic to organic production ratio for the S box is 1:2. We use ^{13}C fractionation factors of -22‰ and 1.0‰ for the production of organic carbon and calcite shells respectively.

We calculate fluxes across the air-sea interface assuming a perfectly mixed atmosphere and using CO_2 invasion rates of 0.15 (B, A, SA, T) and 0.05 (S) mol m^{-2} yr^{-1} μatm^{-1}, and O_2 gas transfer velocities of 45 (B, A, SA, T) and 15 (S) cm hr^{-1}. Net air-to-sea CO_2 fluxes fractionate ^{13}C by -1.8 ‰ in the model. We calculate the sea-to-air fractionation as a function of temperature according to Lesniak and Sakai [1989] and Mook *et al*. [1974]. We maintain a constant CO_3 concentration in the deep box by dissolving or precipitating an appropriate amount of $CaCO_3$. We have chosen total

atmosphere-ocean carbon (35900 Gt), total atmosphere-ocean ^{13}C (3.324×10^{16} moles), and average ocean alkalinity (2360 μeq kg^{-1}) values to best fit modern preindustrial atmospheric CO_2 and $\delta^{13}C$ values. These totals are within 1% of estimates based on GEOSECS/TTO data [Toggweiler and Sarmiento, 1985]. We calculate the solubility of oxygen using equations from Garcia and Gordon [1992], and the partitioning of the ocean carbon system using the algorithms of Peng *et al*. [1987].

After prescribing temperatures, salinities, water transports, and surface nutrients, and parameterizing the effects of biological production, air-sea gas exchange, and carbonate sediment interaction as described above, we integrate the model to calculate the steady-state distribution of total CO_2 (ΣCO_2), the $^{13}C/^{12}C$ ratio ($\delta^{13}C$), total alkalinity (TA), dissolved O_2, and the atmospheric CO_2 concentration. Figure 6.2 depicts a solution to this model using input parameters representing the modern preindustrial state. We have adjusted the surface nutrient field such that the model reproduces the observed deep preformed phosphate (PO_4^o) concentration of 1.4 μmol kg^{-1} and the PO_4^o concentration of intermediate waters penetrating the deep ocean, also equal to 1.4 μmol kg^{-1} [Broecker *et al*., 1985].

Preformed nutrients, which are created when waters leave the surface after experiencing air-sea gas exchange but not complete nutrient utilization, are inversely proportional to the efficiency of the biological pump [Knox and McElroy, 1984; Toggweiler and Sarmiento, 1985]. Thus any model attempting to simulate glacial changes in biological pump efficiency must accurately reproduce their modern distributions. Because ice cover in our model decouples air-sea CO_2 and O_2

exchanges, the standard definition of PO_4^o is not a useful diagnostic for our glacial-interglacial comparisons. Instead, we define the biogical pump efficiency (BPE) as the ratio between the actual surface to deep ΣCO_2 difference and the potential difference:

$$BPE = \frac{\Sigma CO_2(D) - \Sigma CO_2(S)}{PO_4(D) - PO_4(S)} \times \frac{1}{R_{C:P}} \quad (6.1)$$

where $R_{C:P}$ is the Redfield carbon to phosphorous ratio. In a world with no air-sea gas exchange, no solubility pump, and no alkalinity pump, this ratio would be 1. Our model, when run with modern-preindustrial parameters and constant temperatures, salinities, and alkalinities has a BPE of 0.45, indicating that transfer of carbon from the high to low latitudes through the atmosphere is reducing the effect of the biological pump on low-latitude surface ΣCO_2 by 55 %. When the solubility and alkalinity pumps are included, the apparent BPE is close to 1.0.

One of the distinct results of assuming deep water only outcrops at high southern latitudes is that the modern-preindustrial Southern Ocean south of 45°S becomes a source of 0.55 Gt C yr^{-1} to the atmosphere. This positive value is in disagreement with the predictions of 3-dimensional ocean carbon-cycle models [Sarmiento *et al*., 1995], but is consistent with atmospheric [Keeling *et al*., 1989; Tans *et al*., 1990] and oceanographic [Broecker and Peng, 1992; Keeling and Peng, 1995] observations. A key observation for evaluating this prediction is the difference in gas-exchange derived CO_2 ($\Delta\Sigma CO_2$, as defined by Broecker and Peng [1992]) between southward flowing deep waters and northward flowing intermediate waters. The

solution shown in Figure 6.2 gives a value for this difference of 51 μmol kg^{-1} which is lower than the observed value of 80 μmol kg^{-1} [Broecker and Peng, 1992; Keeling and Peng, 1995] indicating that our model may actually underestimate the southward oceanic transport and Antarctic outgassing of carbon.

6.3 Sensitivity to Increased Antarctic Sea Ice

To assess the sensitivity of our model to variations in Antarctic ice cover, we have calculated steady state solutions using modern-preindustrial parameters and varying the ice-free surface area south of the APF from 1.6×10^{13} m^2 down to zero. Figure 6.3a shows the atmospheric CO_2 concentration for these solutions for 4 cases with different proportions of AAIW sinking south and north of the APF. To achieve this, we held the low-latitude contribution to AAIW constant and adjusted the fraction (F_a) of northward flowing remnant Antarctic surface waters entering the Subantarctic box. Based on the evidence of Molinelli [1978; 1981] showing the importance of subsurface transport of Antarctic waters relative to vertical mixing as the Subantarctic source of AAIW, we have chosen a relatively low F_a value of 0.3 to use as a best-guess case. We use 1.6×10^{13} m^2 as a modern estimate of the effective ice-free area south of the APF, and 1.6×10^{11} m^2 to illustrate a possible glacial value. Using these F_a and area values produces an atmospheric CO_2 response to the ice variation in Figure 6.3a of 67 ppm.

The case with all northward flowing waters sinking at the APF ($F_a = 0$) shows the greatest change of 78 ppm over this range of surface exposures, while the case of

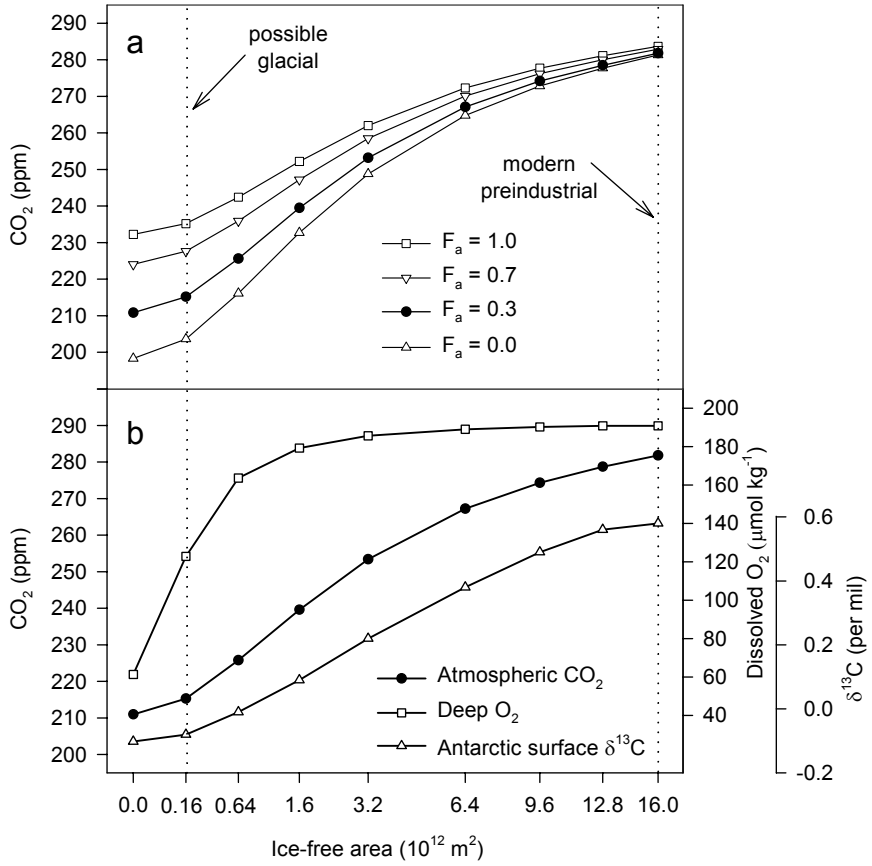

Figure 6.3 Steady-state solutions of the model for different ice coverages south of the APF. We vary the exposed sea surface in the B and A boxes such that the same fraction of total surface is ice-free in each. The x-axis values represent the sum of exposed area in these two boxes, and are scaled by their square root to expand the left side of the plot. (a) Atmospheric CO_2 using modern-preindustrial parameters and different values of F_a. (b) Atmospheric CO_2, deep O_2, and Antarctic surface $\delta^{13}C$ using $F_a = 0.3$.

all northward flowing waters contacting the surface in the Subantarctic zone before sinking ($F_a = 1.0$) shows the smallest change of 49 ppm. The high F_a case still responds to ice cover south of the APF because once north of the APF the recent deep waters no longer see the surface in their pure state, but as in the real ocean are mixed with a contribution of low-latitude, low ΣCO_2 water. The decreases in atmospheric

CO_2 with increasing ice cover shown in Figure 6.3a result from increases in the efficiency of the biological pump. From the modern to the possible-glacial ice-cover estimates, the constant temperature, salinity, and alkalinity BPE increases from 0.45 to 0.75.

The 67 ppm decrease in the best-guess case is associated with a 92% decrease in the sea-to-air CO_2 flux south of the APF and a 1.8% increase in the deep ΣCO_2 concentration, with no change in the nutrient distribution. The deep ΣCO_2 increase contributes to the dissolution of 2.5×10^{16} moles of $CaCO_3$, which produces a 1.6% increase in the whole ocean alkalinity and 13 ppm of the total atmospheric CO_2 effect. Although not enough to produce large changes in glacial lysocline depths, this alkalinity-ice relationship is consistent with observations of a global carbonate-sediment preservation spike during deglaciation [Berger, 1977].

In contrast to atmospheric CO_2, as shown in Figure 6.3b, the model deep O_2 concentration is not sensitive to ice coverage except when the outcrop area becomes very small. The change in deep O_2 from a modern-preindustrial estimate of 191 μmol kg^{-1} to a possible glacial value of 123 μmol kg^{-1} (Figure 6.3b) would not produce deep anoxia. This decoupling of O_2 and CO_2 through their contrasted air-sea equilibration times is a unique feature of this scenario, which allows it to leverage the biological pump to produce a decrease in atmospheric CO_2 without a correspondingly large decrease in deep O_2.

The Antarctic surface $\delta^{13}C$ predictions also shown in Figure 6.3b highlight another aspect of this model that agrees well with observations. The net sea-to-air flux

of CO_2 and the disequilibrium flux of ^{13}C in the model both work to make the Antarctic surface box heavier in ^{13}C. As these fluxes decrease with increasing ice cover, the Antarctic surface $\delta^{13}C$ value decreases by 0.7 ‰. This decrease is similar to that inferred from measurements on planktonic foraminifera [Charles and Fairbanks, 1990], and is consistent with earlier hypotheses [Charles and Fairbanks, 1990; Broecker, 1993]. In contrast, scenarios that invoke increases in high-latitude nutrient utilization or decreases in high-latitude vertical mixing predict increased glacial Antarctic-surface $\delta^{13}C$ values.

6.4 Evidence for Increased Glacial Antarctic Sea Ice

Is it possible that Antarctic sea ice effectively blocked air-sea gas exchange over most of the region south of the APF during glacial times? Sediment proxies indicate significant increases in Southern Ocean ice cover during the Last Glacial Maximum (LGM) [Cooke and Hays, 1982; Burckle *et al*., 1982]. Cooke and Hays [1982] estimate an increase in Southern Ocean summer ice coverage from 2.5×10^{12} m^2 at present to 2.5×10^{13} m^2 at the LGM, and in winter ice coverage from 2.0×10^{13} m^2 to 4.0×10^{13} m^2. By comparison, the total ocean area south of the modern APF is approximately 3×10^{13} m^2 (see Figure 6.4). Burckle *et al*. [1982] and Crosta *et al*. [1998] used modern comparisons to satellite data to argue that the glacial summer ice limits of Cooke and Hays [1982] were overestimated. However, all of these studies agree upon a glacial extension of winter sea ice beyond the modern APF.

For our purposes, we expect the winter ice extent to have the dominant impact on deep-water ventilation, as stratification and biological productivity during summer independently limit the outgassing of CO_2 and ingassing of O_2. Furthermore, open leads and polynyas in summer ice would be even more stratified because of locally increased surface heat and freshwater inputs. Thus the effective summer ice cover, in terms of blocking ventilation, may have been significantly greater than the actual ice area. Increased glacial ice cover would affect Southern Ocean productivity: negatively under the ice by reducing light levels, and positively in leads or polynyas where the ice did melt by increasing stratification. These hypotheses are in agreement with interpretations based on sediment $\delta^{15}N$, opal, and $\delta^{13}C$ data that the region of maximum air-sea gas exchange [Charles and Fairbanks, 1990] and biological production [Mortlock *et al*., 1991; François *et al*., 1997] shifted north of the modern APF during the LGM, and that the regions where production occurred south of the APF were more stratified [François *et al*., 1997].

6.5 Sensitivity to Model Parameters

Although the atmospheric CO_2 decrease shown in Figure 6.3 for the case in which $F_a = 0.3$ represents only one potential realization of this mechanism, the significance of its effect is relatively insensitive to the assumed parameters. For example, keeping all other parameters the same and quadrupling the Antarctic Ocean ice-free area only decreases the net effect on atmospheric CO_2 by 10 ppm, whereas completely blocking gas-exchange south of the APF increases the effect by 4 ppm

(Figure 6.3). Varying F_a to 0.7 or 0.0 changes the net effect by -12 and +10 ppm, respectively (Figure 6.3a), while doubling or reducing to zero the entrainment of low-latitude waters in AAIW changes the effect by -9 and +10 ppm, respectively. While the model illustrates the behavior of the ocean in the limit of no low-latitude deep-water upwelling, it is likely that there is some finite amount of diapycnal flow through the main thermocline in the real ocean. However, if we include a high-latitude sinking, low-latitude upwelling term of 10 Sv in the model, the total atmospheric CO_2 difference decreases only 8 ppm to a total of 59 ppm.

In addition, we have not tried to simulate increases in nutrient utilization in the Subantarctic, yet in the reconfigured conveyor such changes could significantly affect the amount of CO_2 entering the deep ocean. If we reduce Subantarctic surface nutrients after increasing Antarctic sea ice to generate a 1.5 to 2.8 mol C m^{-2} yr^{-1} increase in Subantarctic export production, slightly less than that proposed by Francois *et al*. [1997], the CO_2 drawdown increases by 15 ppm to a total of 82 ppm. With Subantarctic nutrients low, turning NADW off decreases atmospheric CO_2 by another 19 ppm, as fewer preformed nutrients enter the deep ocean. In the reverse of this effect, our model predicts a 19 ppm increase associated with the glacial NADW-on mode flips simulated by Keeling and Stephens [1999], which may provide an explanation for the transient atmospheric CO_2 increases observed during Dansgaard-Oeschger (D-O) events [Stauffer *et al*., 1998]. However, the magnitude and direction of this mode-flip response are not well constrained, as they are sensitive to the temperature and nutrient concentrations in the Subantarctic box. Another possible

cause of the D-O CO_2 shifts is the warming-induced reduction in Antarctic ice-cover that is invoked by Keeling and Stephens [1999] to trigger the NADW turn-on.

A final perturbation to consider is that of temperature driven solubility changes. After reducing surface temperatures by a maximum of 5°C, and less in boxes that are already near the freezing point, our model predicts an additional CO_2 drawdown of 27 ppm. Most of this effect, 17 ppm, results from temperature changes in the high-latitude boxes. The ratio between the actual atmospheric CO_2 change and the potential change due to cooling of the low-latitude surface box, known as the Harvardton-Bear Index [Bacastow, 1996; Broecker and Peng, 1998], is 0.2 for this model, in agreement with those of the original Harvardton Bear models [Sarmiento and Toggweiler, 1984; Siegenthaler and Wenk, 1984; Knox and McElroy, 1984]. The combined effects of ice cover, Subantarctic productivity, circulation, and temperature simulated by our model are large enough that even after including the counteracting effects of terrestrial biomass changes and salinity driven solubility effects [Broecker and Peng, 1998], an 80 ppm decrease in glacial atmospheric CO_2 can still be attained.

6.6 Conclusion

Broecker and Henderson [1998] recently argued based on Antarctic $\delta^{18}O$ measurements over Termination II that the trigger mechanisms for many of the proposed scenarios actually post-date the rise in atmospheric CO_2. We expect Antarctic air temperatures to have a direct effect on Antarctic sea ice, and vice versa as a result of albedo feedbacks. This close connection between temperature and ice

cover accommodates the timing requirement of Broecker and Henderson [1998], and may help to explain the virtual overlap between deuterium and CO_2 observed in Antarctic ice cores during deglaciation [Petit *et al*., 1999] (Figure 6.1). Furthermore, Cooke and Hayes [1982] estimate that lithologic changes associated with the advance and retreat of Antarctic sea ice occurred over huge areas in less than 200 years, and that these changes predate shifts in northern hemisphere climate. In this context, Antarctic sea ice might also provide a strong positive feedback on climate during glacial-interglacial transitions. Decreased ice cover decreases the albedo of the ocean surface. If it also generates the circulation changes proposed by Keeling and Stephens [1999], which in turn would produce warming and decreased albedo in the north, and if it increases atmospheric CO_2 as simulated here, then Antarctic sea ice cover could represent an important non-linear amplifier of Milankovitch insolation forcing.

Because our intent is to demonstrate the existence of a potentially important phenomenon and not to explicitly model the glacial or interglacial states, we have not attempted to include other mechanisms that have been previously presented as significant factors in determining atmospheric CO_2. While we feel the striking repeatability of the paleo-CO_2-temperature correlation begs a simple explanation, it is likely that the full cause is a combination of several effects. Toggweiler [1999] recently developed a scenario that similarly invokes a reduction in deep-water ventilation to explain the low glacial CO_2 levels. Whereas he generates reduced ventilation by decreasing the vertical exchange between deep and Antarctic surface waters, we hypothesize that reduced ventilation was driven by limitations to air-sea

gas exchange imposed by increased sea-ice in this region. We have constructed a simple box model of the ocean-atmosphere carbon cycle with the constraint of no low-latitude upwelling of deep-waters across the main thermocline, and have found that the Antarctic ice mechanism has the potential to explain most of the observed glacial-interglacial CO_2 difference.

Portions of this chapter have been submitted as

Stephens, B. B., and R. F. Keeling, The influence of Antarctic sea ice on glacial-interglacial CO_2 variations, submitted to *Nature*, 1999.

I was the primary investigator and lead author for this paper, and conducted all of the analyses presented therein.

6.7 References

Archer, D., and E. Maier-Reimer, Effect of deep-sea sedimentary calcite preservation on atmospheric CO_2 concentration, *Nature, 367*, 260-263, 1994.

Bacastow, R. B., The effect of temperature change of the warm surface waters of the oceans on atmospheric CO_2, *Global Biogeochem. Cycles, 10*, 319-333, 1996.

Barnola, J. M., D. Raynaud, Y. S. Korotkevitch, and C. Lorius, Vostok ice core provides 160,000-year record of atmospheric CO_2, *Nature*, *329*, 408-414, 1987.

Berger, W. H., Deep-sea carbonate and the deglaciation preservation spike in pteropods and foraminifera, *Nature, 269*, 301-304, 1977.

Berger, W. H., Increase of carbon dioxide in the atmosphere during deglaciation: The coral reef hypothesis, *Naturwissenschaften, 69*, 87-88, 1982.

Boyle, E. A., Vertical oceanic nutrient fractionation and glacial/interglacial CO_2 cycles, *Nature, 331*, 55-56, 1988.

Boyle, E. A., Cadmium and $\delta^{13}C$ paleochemical ocean distributions during the Stage 2 glacial maximum, *Ann. Rev. Earth Planet. Sci., 20*, 245-287, 1992.

Broecker, W. S., Glacial to interglacial changes in ocean chemistry, *Prog. Ocean., 11*, 151-197, 1982.

Broecker, W. S., An oceanographic explanation for the apparent carbon isotope-cadmium discordancy in the glacial Antarctic? *Paleoceanography*, *8*, 137-139, 1993.

Broecker, W. S., and G. M. Henderson, The sequence of events surrounding Termination II and their implications for the cause of glacial-interglacial CO_2 changes, *Paleoceanography, 13*, 352-364, 1998.

Broecker, W. S., and T.-H. Peng, Interhemispheric transport of carbon dioxide by ocean circulation, *Nature, 356*, 587-589, 1992.

Broecker, W. S., and T.-H. Peng, *Greenhouse Puzzles,* 2nd ed., pp. M6-M16, Eldigio Press, Palisades, 1998.

Broecker, W. S., S. L. Peacock, S. Walker, R. Weiss, E. Fahrbach, M. Schroeder, U. Mikolajewicz, C. Heinze, R. Key, T.-H. Peng, and S. Rubin, How much deep water is formed in the Southern Ocean? *J. Geophys. Res., 103*, 15833-15843, 1998.

Broecker, W. S., T. Takahashi, and T. Takahashi, Sources and flow patterns of deep-ocean waters as deduced from potential temperature, salinity, and initial phosphate concentration, *J. Geophys. Res., 90*, 6925-6939, 1985.

Burckle, L. H., D. Robinson, and D. W. Cooke, Reappraisal of sea-ice distribution in Atlantic and Pacific sectors of the Southern Ocean at 18,000 yr BP, *Nature, 299*, 435-437, 1982.

Charles, C. D., and R. G. Fairbanks, Glacial to interglacial changes in the isotopic gradients of Southern Ocean surface water, in *Geological History of the Polar Oceans: Arctic Versus Antarctic*, edited by U. Bleil and J. Thiede, pp. 519-538, Kluwer Academic Publishers, Netherlands, 1990.

Cooke, D. W., and J. D. Hays, Estimates of Antarctic Ocean seasonal sea-ice cover during glacial intervals, in *Antarctic Geoscience: Symposium on Antarctic Geology and Geophysics,* edited by C. Craddock, pp. 1017-1025, University of Wisconsin Press, Madison, 1982.

Crosta, X., J.-J. Pichon, and L. H. Burckle, Application of modern analog technique to marine Antarctic diatoms: Reconstruction of maximum sea-ice extent at the Last Glacial Maximum, *Paleoceanography*, *13*, 284-297, 1998.

François, R., M. A. Altabet, E.-F. Yu, D. M. Sigman, M. P. Bacon, M. Frank, G. Bohrmann, G. Bareille, and L. D. Labeyrie, Contribution of Southern Ocean surface-water stratification to low atmospheric CO_2 concentrations during the last glacial period, *Nature, 389*, 929-935, 1997.

Garcia, H. E., and L. I. Gordon, Oxygen solubility in seawater: Better fitting equations, *Limnol. Oceanogr., 37*, 1307-1311, 1992.

Gnanadesikan, A., A simple predictive model for the structure of the oceanic pycnocline, *Science, 283*, 2077-2079, 1999.

Gnanadesikan, A., and J. R. Toggweiler, Constraints placed by silicon cycling on vertical exchange in general circulation models, submitted to *Geophys. Res. Lett.*, 1999.

Keeling, C. D., S. C. Piper, and M. Heimann, A three-dimensional model of atmospheric CO_2 transport based on observed winds, 4, Mean annual gradients and interannual variations, in *Aspects of Climate Variability in the Pacific and Western Americas, Geophys. Monogr. Ser.,* vol. 55, edited by D. H. Peterson, pp. 305-363, AGU, Washington D. C., 1989.

Keeling, R. F., and T.-H. Peng, Transport of heat, CO_2, and O_2, by the Atlantic's thermohaline circulation, *Philos. Trans. R. Soc. London Ser. B*, *348*, 133-142, 1995.

Keeling, R. F., and B. B. Stephens, Antarctic control of Pleistocene climate variability, submitted to *Nature,* 1999.

Knox, F., and M. B. McElroy, Changes in atmospheric CO_2: Influence of the marine biota at high latitude, *J. Geophys. Res., 89*, 4629-4637, 1984.

Ledwell, J. R., A. J. Watson, and C. S. Law, Evidence for slow mixing across the pycnocline from an open-ocean tracer-release experiment, *Nature, 364*, 701-703, 1993.

Lesniak, P. M., and H. Sakai, Carbon isotope fractionation between dissolved carbonate (CO_3^{2-}) and CO_2(g) at 25° and 40°C, *Earth Planet. Sci. Lett., 95*, 297-301, 1989.

Leuenberger, M., U. Siegenthaler, and C. C. Langway, Carbon isotope composition of atmospheric CO_2 during the last ice age from an Antarctic ice core, *Nature, 357*, 488-490, 1992.

Lueck, R. G., and T. D. Mudge, Topographically induced mixing around a shallow seamount, *Science, 276*, 1831-1833, 1997.

Marino, B. M., M. B. McElroy, R. J. Salawitch, and W. G. Spaulding, Glacial-to-interglacial variations in the carbon isotopic composition of atmospheric CO_2, *Nature, 357*, 461-466, 1992.

Martin, J. H., Glacial-interglacial CO_2 change: The iron hypothesis, *Paleoceanography, 5*, 1-13, 1990.

McCartney, M. S., Subantarctic Mode Water, in *A Voyage of Discovery*, edited by M. Angel, pp. 103-119, Pergamon Press, Oxford, 1977.

Molinelli, E. J., Isohaline thermoclines in the southeast Pacific Ocean, *J. Phys. Oceanogr., 8*, 1139-1145, 1978.

Molinelli, E. J., The Antarctic influence on Antarctic Intermediate Water, *J. Marine Res., 39*, 267-293, 1981.

Mook, W. G., J. C. Bommerson, and W. H. Staverman, Carbon isotope fractionation between dissolved bicarbonate and gaseous carbon dioxide, *Earth Planet. Sci. Lett., 22*, 169-176, 1974.

Mortlock, R. A., C. D. Charles, P. N. Froelich, M. A. Zibello, J. Saltzman, J. D. Hays, and L. H. Burckle, Evidence for lower productivity in the Antarctic Ocean during the last glaciation, *Nature, 351*, 220-223, 1991.

Opdyke, B. N., and J. C. G. Walker, Return of the coral reef hypothesis: Basin to shelf partitioning of $CaCO_3$ and its effect on atmospheric CO_2, *Geology, 20*, 733-736, 1982.

Peng, T.-H., and W. S. Broecker, C/P ratios in marine detritus, *Glob. Biogeochem. Cycles, 1*, 155-161, 1987.

Peng, T.-H., T. Takahashi, W. S. Broecker, and J. Olafsson, Seasonal variability of carbon dioxide, nutrients and oxygen in the northern North Atlantic surface water: observations and a model, *Tellus, 39B*, 439-458, 1987.

Petit, J. R., J. Jouzel, D. Raynaud, N. I. Barkov, J.-M. Barnola, I. Basile, M. Bender, J. Chappellaz, M. Davis, G. Delaygue, M. Delmotte, V. M. Kotlyakov, M. Legrand, V. Y. Lipenkov, C. Lorious, L. Pépin, C. Ritz, E. Saltzman, and M. Stievenard, Climate and atmospheric history of the past 420,000 years from the Vostok ice core, Antarctica, *Nature*, *399*, 429-436, 1999.

Robbins, P. E., and J. M. Toole, The dissolved silica budget as a constraint on the meridional overturning circulation of the Indian Ocean, *Deep-Sea Res., 44*, 879-906 1997.

Sarmiento, J. L., and J. R. Toggweiler, A new model for the role of the oceans in determining atmospheric pCO_2, *Nature, 308*, 621-624, 1984.

Sarmiento, J. L., R. Murnane and C. Le Quéré, Air-sea CO_2 transfer and the carbon budget of the North Atlantic, *Philos. Trans. R. Soc. London Ser. B*, *348*, 211-219, 1995.

Siegenthaler, U., and T. Wenk, Rapid atmospheric CO_2 variations and ocean circulation, *Nature*, *308*, 624-626, 1984.

Stauffer, B., T. Blunier, A. Dällenbach, A. Indermühle, J. Schwander, T. F. Stocker, J. Tschumi, J. Chappellaz, D. Raynaud, C. U. Hammer, and H. B. Clausen, Atmospheric CO_2 concentration and millennial-scale climate change during the last glacial period, *Nature, 392*, 59-62, 1998.

Tans, P. P., I. Y. Fung, and T. Takahashi, Observational constraints on the atmospheric CO_2 budget, *Science*, *247*, 1431-1438, 1990.

Toggweiler, J. R., Variation of atmospheric CO_2 by ventilation of the ocean's deepest water, in press *Paleoceanography,* 1999.

Toggweiler, J. R., and B. Samuels, Is the magnitude of the deep outflow from the Atlantic Ocean actually governed by southern hemisphere winds? in *The Global Carbon Cycle,* edited by M. Heimann, *NATO ASI Ser.,* vol. I 15, pp. 303-331, 1993a.

Toggweiler, J. R., and B. Samuels, New radiocarbon constraints on the upwelling of abyssal water to the ocean's surface, in *The Global Carbon Cycle,* edited by M. Heimann, *NATO ASI Ser.,* vol. I 15, pp. 333-366, 1993b.

Toggweiler, J. R., and B. Samuels, On the ocean's large-scale circulation near the limit of no vertical mixing, *J. Phys. Oceanogr., 28*, 1832-1852, 1998.

Toggweiler, J. R., and J. L. Sarmiento, Glacial to interglacial changes in atmospheric carbon dioxide: The critical role of the ocean surface water in high latitudes, in *The Carbon Cycle and Atmospheric CO_2: Natural Variations Archean to Present*, edited by E. T. Sundquist and W. S. Broecker, pp. 163-184, AGU, Washington, D. C., 1985.

Tomczak, M., and J. S. Godfrey, *Regional Oceanography: An Introduction,* pp. 67-87, Pergamon Press, Oxford, 1994.

Toole, J. M., K. L. Polzin, and R. W. Schmitt, Estimates of diapycnal mixing in the abyssal ocean, *Science, 264*, 1120-1123, 1994.

Chapter 7

Conclusion

Our understanding of the global carbon cycle is continuously evolving. Developing technologies and ongoing research efforts continue to provide new and highly informative data, which can be used to validate earlier hypotheses and to support new ones. This is particularly true for studies of atmospheric O_2, whose short measurement history results in relatively large increases in available information each year. In the two years since the manuscript presented in Chapter 2 was submitted for publication, I have conducted the shipboard measurements presented in Chapters 4 and 5, and the Scripps atmospheric O_2 laboratory has collected substantial data from the new flask station at Palmer Station. In addition, the existing background records have grown, thus reducing uncertainties in the long-term interstation differences. It is thus worth briefly updating the results from Chapter 2 before presenting a final summary.

7.1 Update to Figure 2.5

The primary results in Chapter 2 were based upon Figure 2.5, in which the observed meridional APO gradient was compared to the predictions of three chemically-coupled ocean-atmosphere models. The observations showed a generally southward-increasing APO trend, which contrasted the more meridionally-symmetric model gradients. To include the recent data in this comparison, it is necessary to slightly modify the transect used to interpolate the model predictions. Figure 7.1 shows a new transect that passes through the locations of the mean APO values determined from the cruises in Chapters 4 and 5, and through PSA, but is otherwise

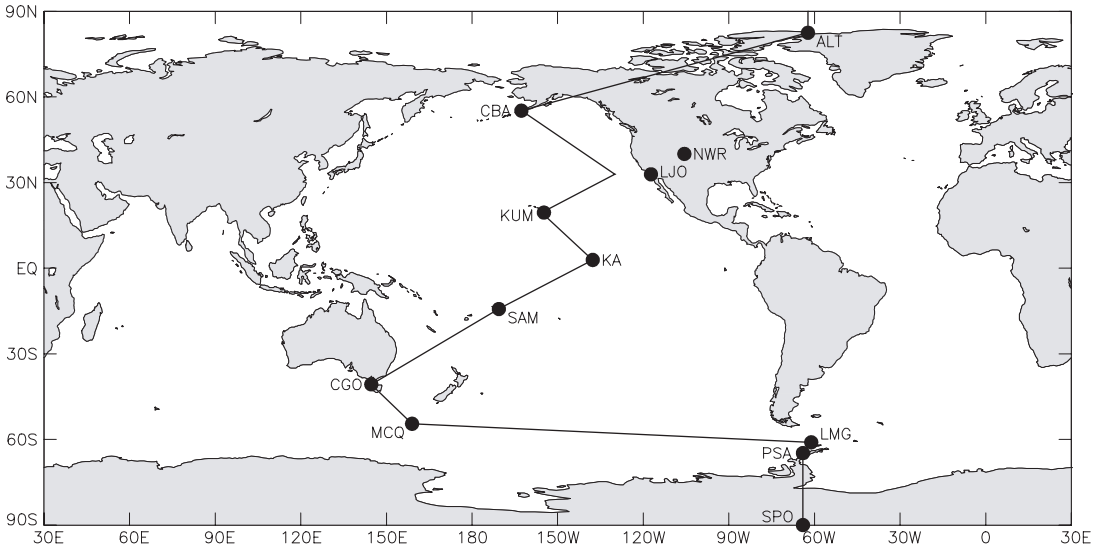

Figure 7.1 Showing the locations of the stations in the Scripps O_2/N_2 sampling network (see Table 2.1) including Palmer Station, Antarctica (PSA, 64° 46' S, 64° 3' W), and the locations corresponding to the average values determined for the Ka'imimoana (KA, 2° 56' N, 137° 42' W) and Lawrence M. Gould (LMG, 61° 0' S, 61° 9' W) cruises presented in Chapters 4 and 5, respectively. The solid line indicates the surface transect used to present the model predictions in Figures 4.13, 4.14, 5.9, 5.10, and 7.2.

the same as that shown in Figure 2.1. Figure 7.2 shows the model APO predictions along this transect, compared to the updated background and shipboard data.

To update the observations in this figure, I have added data up to September, 1998 for ALT, CBA, LJO, KUM, SMO, and CGO, and up to February, 1998 for SPO (see Table 2.1). I have also included data from September, 1996 through May, 1998 at PSA. No new data have been collected at NWR and MCQ. I have left MLO out of this new comparison pending the resolution of potential problems with the air inlet system at this station, though this does not affect any of the Chapter 2 conclusions. I

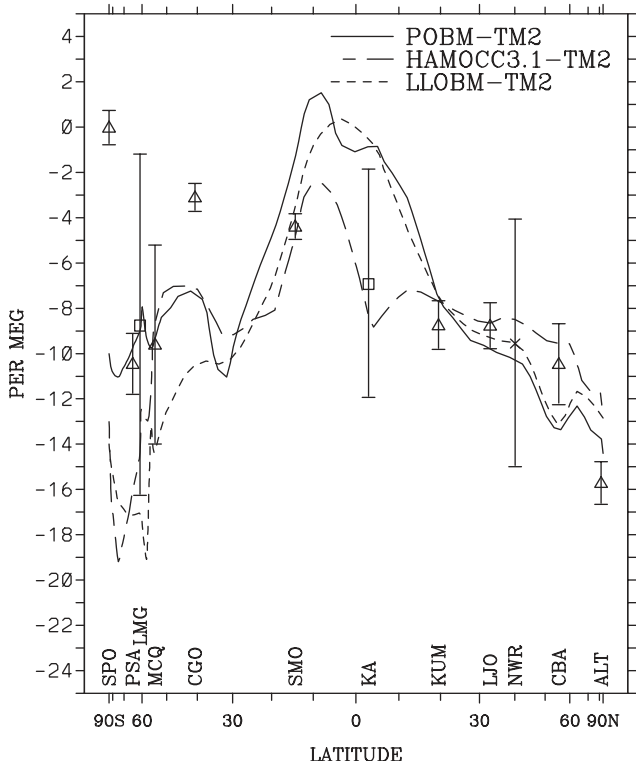

Figure 7.2 The observed latitudinal APO variations relative to the South Pole, and the predictions of the three chemically coupled ocean-atmosphere models. The triangles represent background flask stations that lie along the model transect shown in Figure 7.1. The × represents the value at NWR, which is not directly predicted by the model transect. The squares represent the KA and LMG cruise-average APO values. As in Figure 2.5, the model curves have been vertically shifted to visually fit the northern mid-latitude stations.

have calculated the interstation differences for the updated records as described in Section 2.3. To place the shipboard data on this figure, I have used the annual-mean APO estimates and errors derived for the Ka'imimoana (Figure 4.14) and Lawrence M. Gould (Figure 5.10) cruises and their differences relative to KUM and PSA, respectively. The difference between the Ka'imimoana (KA) value and the KUM

value shown in Figure 7.2 is equal to that between an annual mean for KUM centered on the time of the cruise and the mean of the cruise data with a +1 per meg seasonal correction (see Section 4.5). The difference shown between the Lawrence M. Gould (LMG) value and that at PSA is simply equal to the difference between the mean of the cruise data and the projected value for PSA at the time of the cruise (see Section 5.5).

Extending the existing data records reduced the error estimates for the annual-mean APO concentrations, most notably at CBA, but did not significantly change the interstation differences. The LJO-KUM difference is now almost zero and the total SPO-ALT difference is slightly less at 16 per meg. However, this SPO-ALT difference is still very different from the model predictions, which range from 4 to -1 per meg. The new shipboard data obtained in the equatorial Pacific falls on a linear trend between the northern and southern mid-latitude background concentrations. These results are close to the predictions of HAMOCC3.1-TM2, but do not support the large equatorial peaks predicted by POBM-TM2 and LLOBM-TM2. As discussed in Chapter 4, seasonal atmospheric effects might account for about half of this discrepancy, but the remaining disagreements suggest an oceanographic explanation. The new background and shipboard data obtained in the Southern Ocean confirm the earlier indication from MCQ of low O_2 levels at these latitudes relative to both SPO to the south and CGO to the north. These results are close to those predicted by POBM-TM2, but still considerably higher than the HAMMOCC3.1-TM2 and LLOBM-TM2 predictions.

None of the models are able to reproduce the apparent 10 per meg increase in APO from 60°S to SPO. The Antarctic rectifier mechanism presented in Chapter 5 may be responsible for much of this discrepancy, yet including such a mechanism in the models would actually make their predictions at PSA relative to lower latitudes worse. In a best case scenario in which the predicted concentrations at PSA did not change, the gradients between 0° and 60°S from the various models would range from 9 to 17 per meg, as shown in Figure 7.2. In contrast, the shipboard VUV measurements presented in Chapters 4 and 5 give an observational estimate for this annual-mean APO gradient of 2 per meg. Using the PSA flask data instead of the Lawrence M. Gould VUV data gives a gradient of 4 per meg. More robust comparisons, in the sense of being less affected by potential rectification effects, can be made between mid-latitudes in both hemispheres. The observed CGO-LJO APO difference of 6 per meg is in disagreement with the model predictions ranging from 2 to -2 per meg.

All of these comparisons reinforce the hypotheses presented in Chapter 2, that the coarse-resolution ocean models overestimate the upwelling of deep water at low latitudes, and that this leads to excessive outgassing of O_2 and CO_2 at low latitudes and excessive uptake of O_2 and CO_2 at high southern latitudes. If these models produced an overturning circulation similar to the reconfigured conveyor proposed by Toggweiler and Samuels [1993], or the box model developed in Chapter 6, they would likely predict a greater APO gradient between LJO and CGO and a lesser gradient between KA and LMG, in closer agreement with the observations. In addition to these

APO constraints, surface ^{14}C measurements [Toggweiler and Samuels, 1993] and recent work on dissolved silica budgets [Robbins and Toole, 1997; Gnanadesikan and Toggweiler, 1999] similarly indicate much less low-latitude deep-water upwelling than produced in the models. Furthermore, Toggweiler and Samuels [1998] and Gnanadesikan [1999] have recently shown that a global overturning circulation does not require vertical penetration of heat at low latitudes, and that a circulation with all deep-water upwelling south of the open channel in Drake Passage can be supported by the driving force of strong zonal winds at these latitudes. Finally, the success of the simple box model presented in Chapter 6, and those used by Keeling and Stephens [1999] and Toggweiler [1999], in explaining features of the glacial oceans, is suggestive that such a circulation may in fact be more realistic.

7.2 Concluding Remarks

Numerical models of ocean circulation and biology are potentially very powerful tools for studying ocean carbon cycling. Their ability to integrate and extend upon limited data sets gives them great explanatory and investigative powers, yet it also opens the potential for incorrect predictions if any of the assumptions required in making the models are invalid. Components of this dissertation relate to both edges of this modeling sword. In Chapter 2, I presented discrepancies between observations and model predictions of meridional atmospheric O_2 and CO_2 gradients, which call into question the amount of low-latitude deep-water upwelling in coarse-resolution 3-dimensional ocean models. Then in Chapter 6, I used a simple box model with no

low-latitude deep-water upwelling to argue that if such a circulation exists, the large glacial-interglacial CO_2 difference might be explained by the influence of Antarctic sea ice on the ventilation of deep waters.

One may question the ability of a simple 7-box model with a prescribed circulation to give a more realistic simulation of the ocean than a 3-dimensional model with a circulation based on the equations of fluid dynamics. It is true that most of the parameters in a box model must be assumed. However, these assumptions can be made freely and in agreement with existing observations and current thinking. In constrast, many of the assumptions that go into a 3-dimensional ocean model are forced by the discretization of the physical equations on a coarse-resolution grid, and these assumptions may not be correct.

Examples of incorrect, but forced, assumptions in coarse-resolution ocean models include high diapycnal diffusivities in the open ocean and grid-scale convection as the means of forming Antarctic Bottom Water. As discussed in Chapter 2, both of these model artifacts may affect the predictions of oceanic carbon transport and CO_2 uptake. While model extrapolations will always be subject to some uncertainty, numerical methods can be confidently used as a means of identifying potential areas of sensitivity for future research, as I have done in Chapter 6.

The bulk of the work represented by this dissertation, however, is concerned not with numerical modeling, but with the development and implementation of a new instrumental technique for making field-based measurements of atmospheric O_2. The VUV analyzer described in Chapter 3 has a precision as good or better than existing

laboratory methods, and can be transported to and operated from research ships and remote field stations. I have successfully implemented the VUV analyzer during cruises in the equatorial Pacific and in the Southern Ocean, as described in Chapters 4 and 5, respectively. In addition to providing the regional constraints outlined in Section 7.1, these measurements reveal significant short-term variations in marine-boundary layer O_2 that contain additional biogeochemical information. Future shipboard O_2 measurements using the VUV technique have the potential to significantly advance our understanding of the ocean carbon cycle and its regional and interannual variability.

7.3 References

Gnanadesikan, A., A simple predictive model for the structure of the oceanic pycnocline, *Science,* 283, 2077-2079, 1999.

Gnanadesikan, A. and J. R. Toggweiler, Constraints placed by silicon cycling on vertical exchange in general circulation models, submitted to *Geophys. Res. Lett.* (1999).

Keeling, R. F., and B. B. Stephens, Antarctic control of Pleistocene climate variability, submitted to *Nature*, 1999.

Robbins, P. E., and J. M. Toole, The dissolved silica budget as a constraint on the meridional overturning circulation of the Indian Ocean, *Deep-Sea Res.,* 44, 879-906, 1997.

Toggweiler, J. R., Variation of atmospheric CO_2 by ventilation of the ocean's deepest water, in press *Paleoceanography,* 1999.

Toggweiler, J. R., and B. Samuels, New radiocarbon constraints on the upwelling of abyssal water to the ocean's surface, in *The Global Carbon Cycle,* edited by M. Heimann, *NATO ASI Ser.,* vol. I 15, pp. 333-336, 1993.

Toggweiler, J. R., and B. Samuels, On the ocean's large-scale circulation near the limit of no vertical mixing, J. Phys. Ocean., 28, 1832-1852, 1998.

Errata

p. 70, lines 11-12. The quantity within the parentheses should be (209500/1000001-209500/1000000).

p. 73, line 15. The measured CO_2 interference was 4.7%, not 4.9%.

p. 102, last line. The referenced figure should be 3.8b, not 3.8c.

p. 107, line 5. “Sampson” should be spelled “Samson”

p. 107, line 12. The Stephens et al. reference is from 2000, not 1999.

p. 134, lines 15-16. “higher O_2 and lower CO_2” should read “lower O_2 and higher CO_2.”

p. 135, line 15. The referenced equation should be 2.3, not 2.4.

p. 166, line 2 of caption. The symbols are plotted every 6 hours, not 12.

p. 173, Table 5.1. Southern boundary of HAMOCC3.1 fluxes in rows 7 and 8 is 63˚S not 65˚S.

p. 173, Table 5.1. The preliminary October flask measurement ratios have been revised slightly after further data processing to -10.1, -6.3, -10.1, and -9.5 for PSA-SPO 1997, PSA-CGO 1997, PSA-SPO 1996, PSA-CGO 1996, respectively.

p. 201, line 17. There is no Figure 6.4.

p. 210, line 6. The Opdyke and Walker reference is from 1992, not 1982.